The Pennsylvania State University

The Graduate School

# FULLY NON-CONTACT LASER ULTRASOUND SYSTEM AND METHODS FOR MONITORING METAL ADDITIVE MANUFACTURING PROCESS

A Dissertation in

Engineering Science and Mechanics

by

Chaitanya Bakre



Submitted in Partial Fulfillment
of the Requirements
for the Degree of

Doctor of Philosophy

August 2022

The dissertation of Chaitanya Bakre was reviewed and approved by the following:

Cliff Lissenden
Professor of Engineering Science and Mechanics
Dissertation Co-Advisor, Chair of Committee

Abdalla Nassar
Associate Professor of Engineering Science and Mechanics
Dissertation Co-Advisor

Yun Jing
Associate Professor of Acoustics

Christopher Kube
Assistant Professor of Engineering Science and Mechanics

Victor Sparrow
United Technologies Corporation Professor of Acoustics

Albert Segall
Professor and Graduate Program Officer
Department of Engineering Science & Mechanics

**ABSTRACT**

This research contributes to the development of an in-situ laser ultrasonic inspection system to ensure a defect-free fabrication of additive manufacturing (AM) parts. AM process is hailed as one of the most innovative technologies of industry 4.0. due to the many unique advantages over the subtractive manufacturing methods. The increased design freedom due to the layer-wise manufacturing also allows significant weight reductions and enhanced component performance with little or no specialized tooling. However, the lack of understanding of the process makes it prone to defects inhibiting its use in safety-critical applications such as power generation and aerospace industries. In the absence of defects, subtle changes in the process parameters can lead to undesired microstructure that can be detrimental to the part performance. Thus, in-situ material state monitoring techniques are urgently needed to realize the full benefits of additive manufacturing.

The majority of the current process monitoring systems are vision-based, limiting them from monitoring the internal defects, and are incapable of providing information about the mechanical properties. X-ray computed tomography is being used extensively to detect volumetric AM defects, but it is not amenable for in-situ inspections and is limited by size. Thus, laser ultrasound is considered as a viable solution for in-situ monitoring of AM as it is non-contact and offers benefits of ultrasonic testing, such as detecting volumetric defects and estimating strength-related properties.

This research presents a laser ultrasonic system integrated into a directed-energy-deposition additive manufacturing system and demonstrates the in-situ detection of realistic AM defects and microstructural sensing. Laser generation of both narrowband and broadband Rayleigh waves is exploited to detect localized defects created by altering the process parameters in Ti-6Al-4V depositions. Furthermore, the nonlinear waveform distortion of broadband Rayleigh waves is used to detect changes instilled by marginally varying the process parameters for Ti-6Al-4V and IN718 depositions. The AM surface roughness is a key challenge for laser ultrasound-based in-situ monitoring because it affects both wave reception and the Rayleigh wave propagation. Results demonstrate the influence of AM surface roughness and unique microstructure on nonlinear distortions of Rayleigh waves. Furthermore, the capability of the laser ultrasonic system to carry out artificial flaw detection using narrowband and broadband Rayleigh waves and microstructure monitoring using nonlinear distortion of broadband Rayleigh waves is demonstrated for Ti-6Al-4V and IN-718 specimens within the directed energy deposition additive manufacturing chamber.

# TABLE OF CONTENTS

# LIST OF FIGURES



Figure **2-3**. Schematic showing the Rayleigh waves generated from (a) point source, (b) line source, and (c) line array source ............................................................... 13

# LIST OF TABLES

## ACKNOWLEDGEMENTS

I would like to sincerely thank Prof. Lissenden for his excellent guidance and supervision. Hearing me out when I was talking out of uninformed enthusiasm, encouraging me when I was stuck, pointing out the larger picture and patterns with my results. You have been a constant source of support and inspiration. I also want to convey my deepest gratitude to Dr. Nassar, Dr. Reutzel, and Cory Jamieson, for their invaluable insights into this project.

Credit is due to the members of the PennSUL group for maintaining a great spirit of cooperation and organization. Being a part of the PennSUL group has given me a great learning experience with overall growth. It's not just a research group but a family who care and encourage to excel.

I greatly appreciate my committee members, Dr. Kube, Dr. Jing, and Dr. Sparrow, for agreeing to serve on my Ph.D. thesis committee. Your expertise and insights at the crucial stages of the project helped me shape my research work.

Finally, I come to my wife, my parents, and my sister. You are my support system and my greatest strength. I will always be indebted to you.

Once again, a big shoutout and thanks to everyone!

This work is based upon the work supported by National Science Foundation (NSF) under award number: 1727292. This research was partially funded by the Government under Agreement No. W911W6-17-2-0003. The U.S. Government is authorized to reproduce and distribute reprints for Government purposes notwithstanding any copyright notation thereon.

# Chapter 1

# INTRODUCTION

## 1.1 Motivation

Additive manufacturing (AM) is a promising technology for manufacturing a wide range of structures and complex geometries directly from computer-aided design (CAD) files. The rapid on-demand fabrication of parts has attracted many high-value applications in the medical, aerospace, and defense sectors. AM process is well suited for producing parts with high variability and low volume as the process requires little or no tooling. It is also possible to fabricate parts with site-specific properties [1]. In addition, research has shown that AM can produce parts with comparable or even superior mechanical properties compared to conventional manufacturing processes [2]. However, the microstructure of the AM material is different than conventional materials and can vary locally due to process variability. The variations in the process parameters, power fluctuations, and powder quality have been linked to the generation of defects [3]. Inter- or intra-layer defects, high surface roughness, porosity, and lack of fusion are commonly observed in AM components [4,5]. Furthermore, the variations in the process parameters may lead to undesired microstructure resulting in subpar mechanical properties like yield strength and fracture toughness. The main causes for imperfect AM parts are lack of control and complex physical phenomenon like melting, repeated solidification cycles, heat and mass transfer, and vaporization [6]. Therefore, in-situ nondestructive evaluation (NDE) techniques to assess the structural integrity of the AM components are necessary for the future market expansion of additive manufacturing.

The lack of robust process monitoring techniques is impeding AM from attaining its full-potential and industry-wide acceptance [7]. The primary aim of process monitoring is the identification of flaws during, rather than after, manufacturing. Thus, if the defect is detected, the process can be stopped, curtailing the time and cost, or it may provide the opportunity to repair the defect. Presently, x-ray computed tomography (XCT) is being used extensively to detect defects in AM. However, XCT is not a viable in-process monitoring solution, and it is limited by high costs, radiation risks and limits part size [6,8]. Furthermore, the majority of the process monitoring techniques are vision-based. Thus, they are limited to monitoring only at the surface of the AM component and cannot provide information about the strength-related properties.

On the other hand, laser ultrasound is an attractive NDE technique that is considered a suitable candidate for in-process monitoring of AM as it is noncontact, which allows it to operate in harsh environments and perform rapid scanning. Thus, this research investigates the use of laser ultrasound generated Rayleigh waves for in-situ inspection of each AM layer (or a set of layers) immediately after they are deposited. One caveat for using laser ultrasound is its susceptibility to the high surface roughness of AM materials as it affects both the reception and Rayleigh wave propagation. Nevertheless, the linear and nonlinear features of ultrasonic waves can provide useful information about the material state, defects, density, elastic modulus, and strength. The proposed technique offers many benefits, including rapid in-situ quality assessment, the potential to enable repair or rejection of low-quality parts, and reduced post-process inspection costs.

## 1.2 Objective

The objective of this thesis is to develop a laser ultrasonic system integrated with the additive manufacturing system for in-situ component monitoring and to assess whether nonlinear Rayleigh waves can detect changes in the microstructure of AM materials within the processing environment. This objective is met by investigating the following research questions.

## 1.3 Research questions

The following research questions are answered in this work:

1. How are self-interacting and mutually-interacting Rayleigh waves affected by varying degrees of uniform (non-AM) surface roughness?
2. What effect does the surface roughness of DED-built Ti-6Al-4V specimens have on Rayleigh wave propagation and its nonlinearity?
3. Can narrowband laser generated Rayleigh waves be used to assess the material nonlinearity?
4. How can a laser ultrasonic system be integrated into the DED-AM chamber to detect the formation of realistic AM flaws during layer-by-layer processing?
5. Can nonlinear waveform distortion of broadband Rayleigh waves be used to detect changes in the AM process parameters using the integrated laser ultrasonic system?

## 1.4 Outline

The following section provides a brief overview of the upcoming chapters of this thesis.

- **Chapter 2:** This chapter first discusses the DED-AM system as a target system for this research, followed by a brief overview of the NDE methods for process monitoring of AM with a focus on laser ultrasound. Then, a description of laser ultrasonics as a niche NDE method is given, and the working principle of ultrasonic generation and reception using laser is discussed. Finally, the laser generation of narrowband and broadband Rayleigh waves is presented from the viewpoint of higher harmonic generation and waveform distortions.

- **Chapter 3**: This chapter addresses the first research question. This study uses three aluminum alloy blocks with different surface roughness to investigate the effects of surface roughness on the relative nonlinearity parameter for the second harmonic and mutually interacting Rayleigh waves. The single-frequency and dual-frequency Rayleigh waves are generated using angle beam transducers and received using a laser receptor. The results compare the measured and attenuation-corrected relative nonlinearity parameters to understand the roughness effects on the Rayleigh wave distortion.

- **Chapter 4:** This chapter addresses the second research question. Here, we show that Rayleigh wave distortion can provide useful information about DED-AM depositions having rough surfaces. We first demonstrate the differences in DED-AM and wrought microstructures for Ti-6Al-4V specimens, quantify the surface roughness, and discuss the differences in the (linear) wave speed and (nonlinear) distortion measurements for Rayleigh waves on wrought and DED-AM surfaces having different roughness values.

- **Chapter 5:** This chapter addresses the third research question. We investigate the feasibility of generating finite-amplitude Rayleigh waves using a pulsed laser to estimate material nonlinearity. Rayleigh wave amplitudes are compared for Q-switched Nd:YAG laser and piston-like piezoelectric transducer generation and laser interferometric reception on a reference aluminum sample. Furthermore, laser generated nonlinear Rayleigh waves are applied to 1) differentiate the nonlinearity of AISI 4130 steel plates with varying hardness levels, and 2) nonlinear measurements on the as-built DED-Ti-6Al-4V AM sample.

- **Chapter 6:** This chapter addresses the fourth research question. First, a detailed description of the integration of the laser ultrasound system into the DED-AM system is provided. Next, the capability of the integrated laser ultrasonic system to detect defects in-situ is demonstrated by three proof-of-concept studies, wherein artificial changes to the DED process are made to intentionally introduce changes to the Ti-6Al-4V builds. The in-situ laser ultrasound results provide indications of the flaws. Finally, the presence of flaws is confirmed by XCT and optical microscopy.

- **Chapter 7:** This chapter addresses the fifth research question. We aim to bring forth the applicability of nonlinear broadband Rayleigh waves using laser ultrasound for microstructural sensing and demonstrate their use in detecting subtle variations in DED process parameters in situ. Specifically, we demonstrate that the nonlinear evolution of Rayleigh waveforms for increasing propagation distances or generation laser output energy differs for DED-built Ti-6Al-4V and IN718 specimens processed with different process parameters.

### 1.5 References


1. Tammas-Williams, S.; Todd, I. Design for additive manufacturing with site-specific properties in metals and alloys. *Scr. Mater.* **2017**, *135*, 105–110, doi:10.1016/j.scriptamat.2016.10.030.
2. Rosenthal, I.; Stern, A.; Frage, N. Microstructure and Mechanical Properties of AlSi10Mg Parts Produced by the Laser Beam Additive Manufacturing (AM) Technology. *Metallogr. Microstruct. Anal.* **2014**, *3*, 448–453, doi:10.1007/s13632-014-0168-y.
3. Gong, H.; Rafi, K.; Gu, H.; Starr, T.; Stucker, B. Analysis of defect generation in Ti-6Al-4V parts made using powder bed fusion additive manufacturing processes. *Addit. Manuf.* **2014**, *1*, 87–98, doi:10.1016/j.addma.2014.08.002.
4. Bauereiß, A.; Scharowsky, T.; Körner, C. Defect generation and propagation mechanism during additive manufacturing by selective beam melting. *J. Mater. Process. Technol.* **2014**, *214*, 2522–2528, doi:10.1016/j.jmatprotec.2014.05.002.
5. Ahsan, M.N.; Bradley, R.; Pinkerton, A.J. Microcomputed tomography analysis of intralayer porosity generation in laser direct metal deposition and its causes. *J. Laser Appl.* **2011**, *23*, 022009, doi:10.2351/1.3582311.
6. Perraud, J.B.; Obaton, A.F.; Bou-Sleiman, J.; Recur, B.; Balacey, H.; Darracq, F.; Guillet, J.-P.; Mounaix, P. Terahertz imaging and tomography as efficient instruments for testing polymer additive manufacturing objects. *Appl. Opt.* **2016**, *55*, 3462–3467.

7. Everton, S.K.; Hirsch, M.; Stravroulakis, P.; Leach, R.K.; Clare, A.T. Review of in-situ process monitoring and in-situ metrology for metal additive manufacturing. *Mater. Des.* **2016**, *95*, 431–445, doi:10.1016/j.matdes.2016.01.099.

8. Heim, K.; Bernier, F.; Pelletier, R.; Lefebvre, L.-P. High resolution pore size analysis in metallic powders by X-ray tomography. *Case Stud. Nondestruct. Test. Eval.* **2016**, *6*, 45–52.

# Chapter 2

# BACKGROUND

## 2.1 The directed-energy-deposition additive manufacturing (DED-AM) system


Figure **2-1**. Photograph of the Optomec LENS MR-7 DED-AM system.

For this research, we chose the DED-AM system (Optomec, LENS® MR-7, Albuquerque, NM, USA) shown in Fig. 2-1, located at CIMP-3D at Penn State University for the integration of the laser ultrasonic (LU) system. This system has a relatively spacious AM chamber and feedback capabilities. In the DED-AM system, during deposition, the laser processing head remains stationary, and the substrate is moved in the X-Y plane by a translational stage. The metal powder is delivered by four radially symmetric nozzles and the powder is then fused by a 500 W, Ytterbium-doped fiber laser (IPG YLR-500-SM). After each layer is deposited the laser processing head is translated upwards (in the +Z direction) by a pre-defined layer increment. The DED-AM process produces AM components with very high surface roughness in the range of average asperity height, $R_a = 150\ \mu m\ to\ 200\ \mu m$ [1].

## 2.2 NDE techniques for process monitoring of AM

Traditional nondestructive evaluation (NDE) methods are inadequate for quality assurance testing of AM materials; these methods target flaws that occur on the surface or near the surface. However, due to the layer-wise AM deposition process, it is equally likely to have internal defects as surface defects [2]. Although x-ray computed tomography (XCT) is well suited for volumetric defect detection, it is not amenable for in-situ monitoring. In addition, it becomes less efficient as the size and complexity of parts increase [3,4]. Various approaches have been investigated for in-situ monitoring of AM builds as outlined in several review articles and surveys [5–9]. The typical strategies used for AM process monitoring include monitoring the melt pool metrics [10,11], part temperature [12,13], layer build height [14–16], laser/e-beam parameters [13], and optical emissions [17–21] during processing. Vision-based techniques such as high-speed camera, pyrometry, and infrared imaging are typically used in the commercial online monitoring modules for monitoring the melt pool. These techniques have shown promise; however, it is difficult to detect internal flaws in-situ due to the complex defect formation mechanism below the build surface [7]. Laser ultrasonics (LU) is being researched for process monitoring of AM because it is noncontact, which allows rapid scanning in harsh environments (such as AM in-situ NDE) and offers the advantages of ultrasonic testing [2].Furthermore, the laser generated Rayleigh waves are well suited for layer-wise monitoring the AM depositions. Since Rayleigh waves penetrate up to one wavelength in the material, the number of AM layers to be inspected can be controlled by controlling the frequency of the Rayleigh waves.

### 2.2.1 Current state of laser ultrasonic process monitoring techniques for AM

Currently, LU systems have not been integrated into AM chambers for in-situ defect detection. However, numerous researchers have proposed using LU towards online monitoring of AM. For in-situ applications, the main challenge is the laser reception of ultrasonic waves on AM samples due to the high surface roughness (even with the state-of-the-art laser receivers). Therefore, most of the studies are performed on polished AM specimens. Researchers from the University of Nottingham developed the spatially resolved acoustic spectroscopy technique that measures the changes in the surface wave speed to inspect surface defects and microstructural texture of PBF builds. Smith et al. [22] showed the capability of the system to detect defects with the size of 134 – 137 $\mu$m on polished PBF-produced Ti-6Al-4V specimens. The capability of the spatially resolved acoustic spectroscopy system to inspect rough AM parts for its application in in-situ monitoring is being investigated [23–26]. Piers et al. [27] used a laser induced phased array to detect artificially nested cylindrical holes with a diameter of 0.2 mm and depth of 26 mm in PBF-built AlSi10Mg specimens. Levesque et al. [28] also carried out off-line LU inspections combined with the synthetic aperture focusing technique from the underside of the baseplate of DED-AM samples. Ultrasonic B-scans were obtained for a titanium alloy (Ti-6Al-4V) and Inconel 718 specimens to image defects such as LoF and porosities. Cerniglia et al. [4] investigated using an LU system mounted on a laser powder deposition robot to obtain ultrasonic B-scan images for inline monitoring of AM process. Results obtained on Inconel reference samples show near-surface flaws with 100 $\mu$m diameter. Millon et al. [29] inspected DED-built 316L stainless steel samples that are polished using electrical discharge machining (EDM). The B-scan images were obtained to detect EDM notches of size 50 $\mu$m at a depth of 0.1 mm.

Davis et al. [30] carried out LU inspection on PBF-built sandblasted aluminum AlSi12 block using longitudinal waves in through-transmission configuration. Artificially seeded flat bottom holes of 1 mm diameter and depths ranging from 2 – 20 mm were successfully detected. Similar laser ultrasonic tests were conducted by Yu et al. [31], in which through-holes of varying diameters from 0.4 mm to 2 mm are inspected on sandblasted PBF built Ti-6Al-4V specimens. The results show successful detection of defects up to 800 $\mu$m diameter, and a linear relationship between the hole diameter and longitudinal wave attenuation was observed. Liu et al. [32] also used LU bulk waves to numerically and experimentally detect artificially seeded through-holes in AM nickel alloy and titanium alloy specimens, verified using XCT data. The authors claim that the proposed LU technique can detect defects as small as 300 $\mu$m.

Zou et al. [33] measured the elastic modulus of optically polished DED-built nickel alloy specimen using LU imaging. Using C-scan imaging, the authors mapped the elastic modulus and verified the results using micro-indentation tests. Zhan et al. [34,35] demonstrated the use of laser ultrasonics to determine the residual stress in polished DED Ti6Al-4V specimens. The authors studied the effect of scanning strategy and process parameters such as laser power, scan speed, and powder feed rate on residual stress of AM specimens.

Laser ultrasound has been used for (50 – 100 $\mu$m) defect detection on as-built PBF specimens, which have significantly lower surface roughness (20 – 50 $\mu$m) than as-built DED specimens (150 – 200 $\mu$m). Everton et al. [36,37] showed the capability of the LU system to detect artificially seeded powder-filled holes. The authors were also able to detect some porosity for as-built PBF Ti-6Al-4V specimens, produced with varying scan speed and hatch spacings. Recently, Zhang et al. [38] used LU C-scan imaging to detect and measure artificial notches of size 50 $\mu$m at a depth of 50 $\mu$m in an as-built PBF-produced specimen. Dai et al. [39] used LU testing to inspect artificially seeded near-surface defects at different depths in an as-built PBF 316L stainless steel specimen. The authors also compared the received waveforms for different locations of generation and detection lasers with respect to the near-surface defect. Near-surface defects within the depth of 0.5 mm were accurately detected using the LU C-scan imaging.

Xu et al. [40,41] addressed the low signal-to-noise ratio (SNR) problem of LU measurements due to the high surface roughness of AM using artificial neural networks and machine learning methods. The proposed multi-feature fusion and intelligent denoising algorithms significantly increased the resolution of LU imaging. The authors successfully detected 100 $\mu$m and 50 $\mu$m surface holes on as-built PBF 304L stainless steel specimens. Jiang et al. [42] used variational mode decomposition algorithm-based particle swarm optimization to denoise LU signals. Finite elements simulations were conducted to study the scattering of surface waves due to surface grooves and the effect of the generation laser beam spot size on defect accuracy. Furthermore, LU B-scans were performed to detect surface grooves on as-built PBF 316L stainless steel specimens.

Park et al. [43] proposed using an in-situ laser polishing operation to reduce the surface roughness prior to LU interrogation. The authors used femtosecond laser ultrasonic testing to estimate mechanical properties such as elastic modulus and Poisson's ratio of laser polished DED 316L stainless steel and verified the results with tensile testing. Zeng et al. [44,45] studied LU defect detection on as-built wire arc additive manufacturing specimens. The authors developed finite element models to simulate LU inspection on as-built specimens in ablative regime. Numerical studies were performed to investigate the effect of surface roughness and presence of different surface and near-surface anomalies such as cracks, flat-bottom holes, and through-holes on mode conversion of ultrasonic waves. The numerical studies provided guidance for experimental defect detection and optimization of LU inspection parameters. Volker et al. [46] improved the accuracy of defect imaging using the surface profiling method that uses the same data as the LU imaging. The authors demonstrated the proposed method using numerical simulations and experiments on as-built AM nickel-based alloy specimen with artificially seeded defects.

## 2.3 Laser ultrasonics

### 2.3.1 Laser generation of ultrasonic waves

A pulsed laser having a pulse duration of a few nanoseconds or lower is used for the generation of ultrasonic waves in metals. When a pulsed laser beam irradiates the surface of a material, the energy is absorbed into a very thin surface layer, causing rapid thermal expansion and contraction due to thermal stresses. This leads to the simultaneous generation of longitudinal, shear vertical, and Rayleigh ultrasonic waves [47]. This thesis will primarily focus on laser-generated Rayleigh waves.

Depending on the absorbed energy density, and the specific heat of fusion and evaporation of the material, the laser generation of ultrasonic waves can be distinguished mainly into two regimes: the thermoelastic regime and the ablative regime. The thermoelastic regime is predominantly used in this research as it is purely nondestructive. However, we also investigate the laser generation in the ablative regime as the damage caused by the vaporization is limited to a few microns, which is significantly lower than the DED layer thickness (~427 μm) and it is inconsequential due to the deposition of more AM layers. The radiation patterns, the efficiency of energy transfer from light to elastic waves, and the pulse shape of the Rayleigh waves are significantly different in the thermoelastic and the ablative regimes. Figures 2.2 (a) and (b) present the radiation patterns for the thermoelastic and the ablative regimes for a point source excitation, respectively. For the thermoelastic regime, the tangential forces resulting from the thermoelastic expansion act as the acoustic sources [48]. Whereas at high laser energies the strong normal force due to the ablation of the material work as the acoustic source.

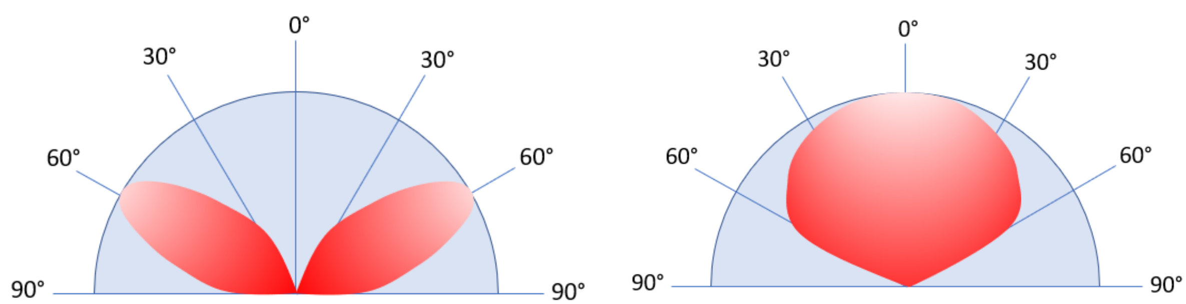


**(a)** **(b)**

Figure **2-2.** Radiation pattern for a point source for **(a)** thermoelastic regime, **(b)** and ablative regime [47].

### 2.3.2 Laser generation of narrowband Rayleigh waves

The Rayleigh waves generated by a laser pulse are inherently broadband in frequency. Interestingly, changing the illumination pattern of the laser beam incident on the surface makes it possible to control the Rayleigh wave propagation characteristics, refer to Fig. 2-3. For example, if the laser beam illuminating the surface is shaped into an array, we obtain a narrowband Rayleigh wave generation of the desired frequency with the array spacing dictating the wavelength and the number of lines determining the number of cycles in the Rayleigh wave signal. Furthermore, as the penetration depth of Rayleigh waves in the material is of the order of one wavelength, patterning the laser beam into an array helps control the interrogation region. Another reason for generating narrowband Rayleigh waves using laser is to study the nonlinear ultrasonic phenomenon of higher harmonic generation.

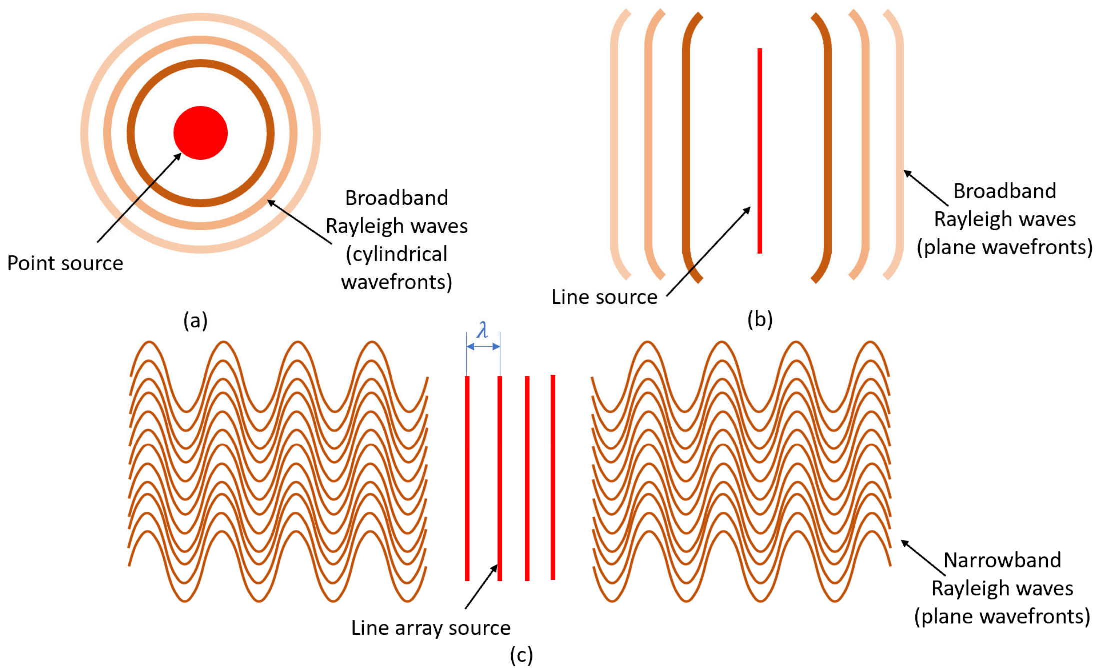


Figure **2-3**. Schematic showing the Rayleigh waves generated from (a) point source, (b) line source, and (c) line array source.

In recent years, a growing number of researchers have attempted to combine the advantages of laser ultrasonics and nonlinear ultrasonics. Laser-generated Rayleigh waves having a small amplitude (linear) are well researched for their use in flaw detection. However, the linear ultrasonic parameters have relatively small variations in response to changes in material microstructure. Therefore, laser generation of finite-amplitude (nonlinear) Rayleigh waves is sought as an advanced nondestructive evaluation technique to infer microstructural changes in AM parts.

Several different methods have been studied in the literature to pattern the laser beam into line arrays, such as microlens array [49], slit mask [50,51], and interference of two-laser beams [52].

Unfortunately, these methods also inevitably generate waves that coincide with the higher harmonic frequencies, complicating the nonlinear analysis [53]. In Chapter 5, we discuss the narrowband generation of nonlinear Rayleigh waves for slit mask and microlens array methods and attempt to cancel the contribution of the line array to the second harmonic amplitudes.

### 2.3.3 Nonlinear waveform distortion of laser generated broadband Rayleigh waves

Laser generation of broadband Rayleigh waves can be achieved by focusing the laser beam into a single line using a cylindrical lens. This method can effectively generate finite-amplitude Rayleigh waves, and more importantly, the problem with the inherent nonlinearity associated with the line array can be

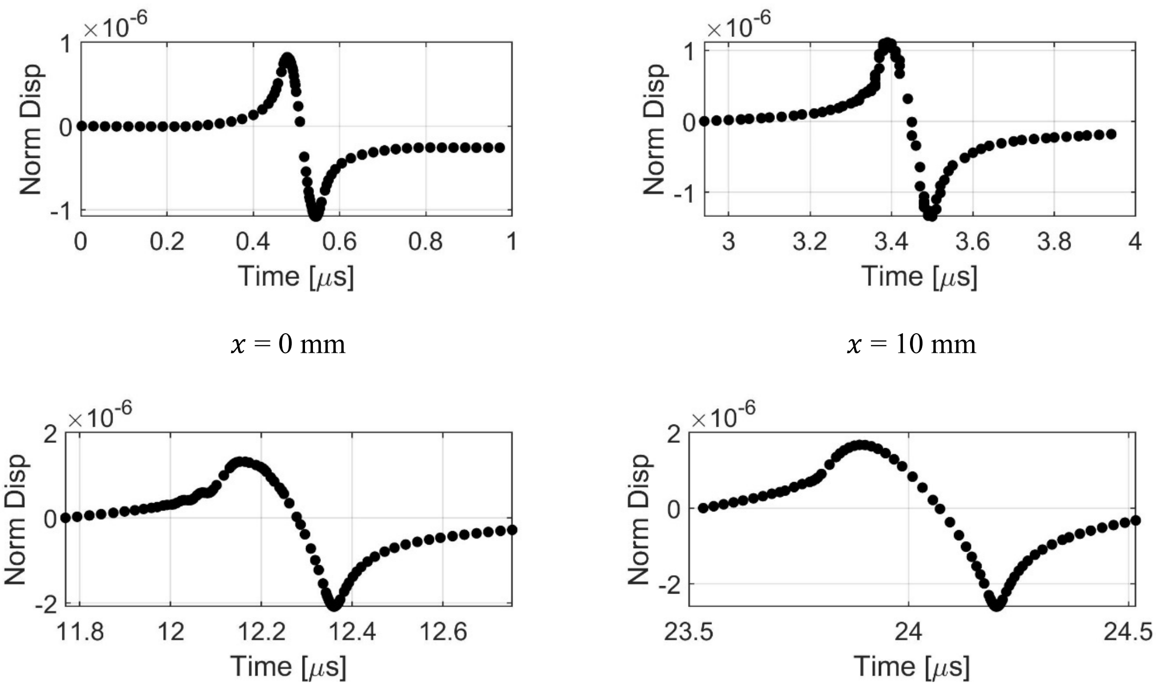


$x$ = 0 mm

$x$ = 10 mm

$x$ = 40 mm

$x$ = 80 mm

Figure **2-4**. Numerical simulation showing waveform evolution for nonlinear SAW with increasing propagation distance based on the data from [54].

avoided. The broadband nonlinear Rayleigh wave phenomenon has been studied in detail; however, the focus of these studies was mainly to develop a mathematical model to describe the temporal distortion of broadband Rayleigh waves in a nonlinear medium [55–58].

The time-domain waveforms for the nonlinear broadband Rayleigh waves are highly sensitive to the nonlinearity of the material. The finite-amplitude broadband Rayleigh waves, also termed nonlinear surface acoustic waves (SAW), evolve as they propagate in a nonlinear medium. Kolomenskii et al. [54] performed simulations to study the evolution of waveforms for increasing propagation distance in a nonlinear medium using a mathematical model. The authors presented their results in velocity fields. However, since we present our results in displacement fields, we have digitized their results and integrated them to obtain the displacement fields. We provide these results in Figure 2-4. When the propagation distance increases from 0 mm to 10 mm, a marginal distortion is evident in the positive peak. With a further increase in the propagation distance to 40 mm, the waveform appears to be significantly stretched, and the discontinuity in the positive peak becomes more evident. From 40 mm to 80 mm, a further stretching of the waveform is observed for the positive and negative parts of the waveform. Moreover, the initially line shaped central part of the waveform transforms into an arc shape.

For a constant propagation distance, the waveform evolution is dependent on the initial amplitudes of broadband nonlinear Rayleigh waves. Kolomenskii et al. [54] also studied the effect of varying initial amplitudes on waveform evolution in a nonlinear medium. Similar to the previous case, we have digitized the original results in velocity fields and converted them to displacement fields. Figure 2-5 presents the evolution of the waveforms for a fixed propagation distance of 40 mm. As the initial amplitude is increased from 8 m/s to 16 m/s, the positive peak and the whole pulse is broadened. When the initial amplitude is further increased to 24 m/s, the negative peak increases in amplitude compared to the positive peak. In addition, the positive peak becomes broader, and the negative peak becomes narrower compared to the waveform having initial amplitude of 8 m/s. A similar trend continues as the initial amplitude is increased to 32 m/s.

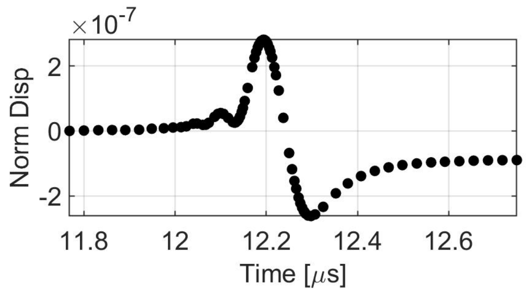


Initial amplitude = 8 m/s

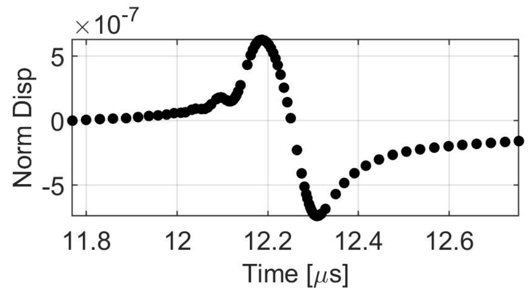


Initial amplitude = 16 m/s

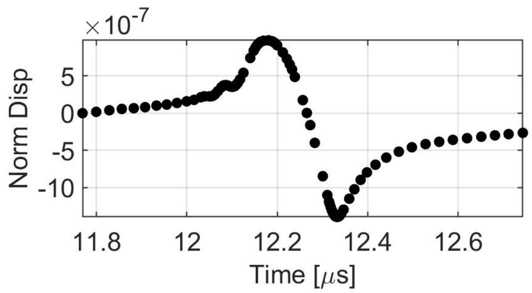


Initial amplitude = 24 m/s

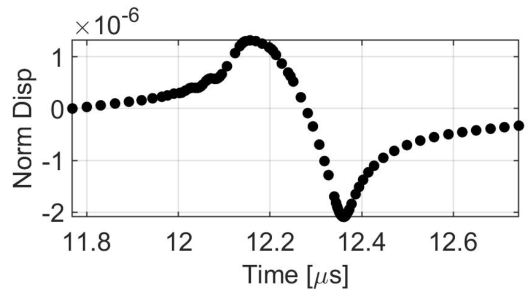


Initial amplitude = 32 m/s

Figure **2-5**. Numerical simulation showing waveform evolution for nonlinear SAW with increasing initial amplitude based on the data from [54].

Waveform distortion occurs due to differences in velocity of positive and negative parts of the waveform, manifested by the coefficient of nonlinearity of the medium. Suppose the coefficient of local nonlinearity is positive, the positive part of the waveform travels at a higher speed, and the negative part travels at a slower speed, leading to waveform compression. This effect is called waveform steepening [59], indicating a frequency-up conversion process (shifting of peak frequency to a higher value). In contrast, when the coefficient of local nonlinearity is negative, the positive and the negative parts of the waveform move away, causing a lengthening of the waveform, indicating a frequency-down conversion process (shifting of peak frequency to a lower frequency) [59]. The earlier mentioned examples have a negative coefficient of nonlinearity; thus, the lengthening of the waveform was observed. The waveform lengthening effect due to nonlinearity cannot be observed in the case of narrowband sinusoidal Rayleigh waves. Furthermore, in some cases, a simultaneous frequency-up and frequency-down conversion can occur, i.e., a part of the waveform can steepen, while another part can broaden simultaneously.

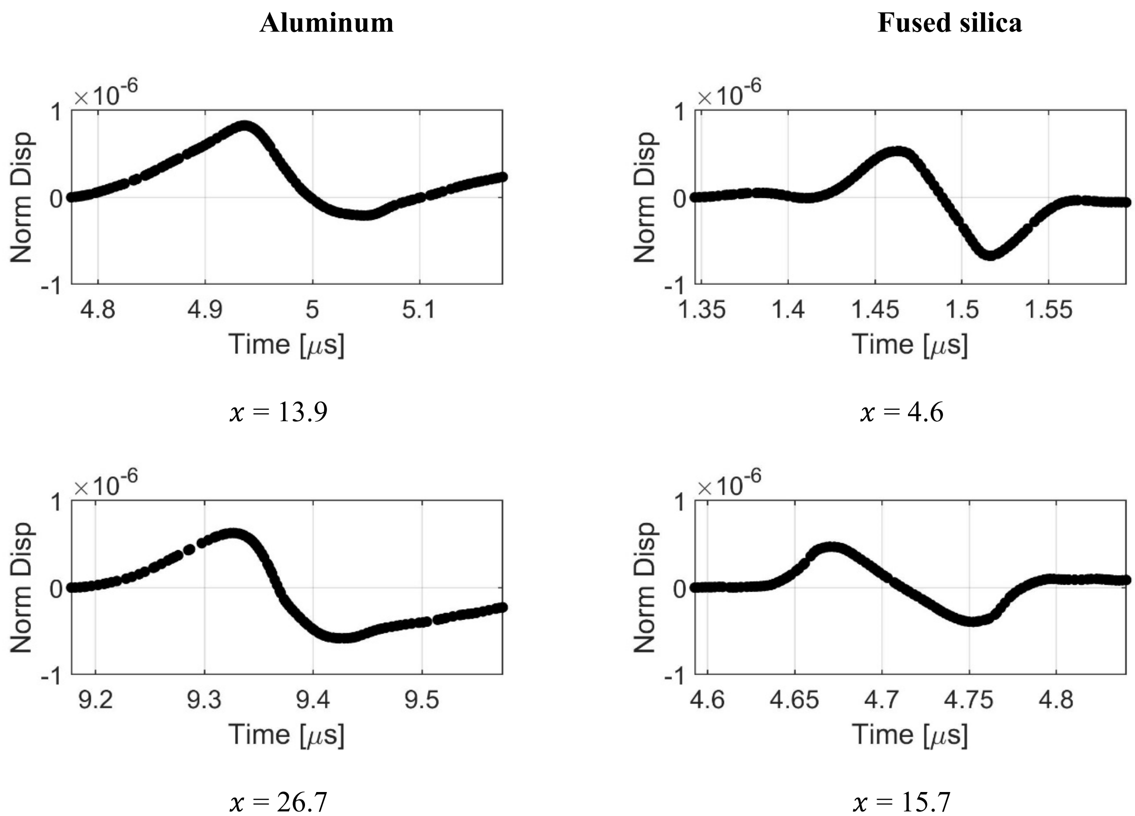


Figure **2-6**. Waveform evolution for nonlinear SAW showing compression in aluminum and stretching in fused silica based on the data from [60].

Kolomenskii and Schuessler [60] experimentally observed the waveform steepening effect in aluminum and the waveform lengthening effect in fused silica; both are isotropic materials. Figure 2-6 shows the waveforms obtained for aluminum and fused silica with increasing propagation distance. At the higher propagation distance, the waveform undergoes temporal compression in aluminum due to the positive coefficient of nonlinearity. In addition, the positive peak amplitude has a higher amplitude than the negative peak at the lower propagation distance. In comparison, the positive and negative peaks have comparable amplitudes at the higher propagation distance. Moreover, although the overall waveform is compressed, the positive peak broadens with increased propagation distance. Thus, simultaneous frequency-up and frequency-down effects are observed. In contrast, for the fused silica, a temporal stretching is observed with an increase in propagation distance due to the negative coefficient of nonlinearity.

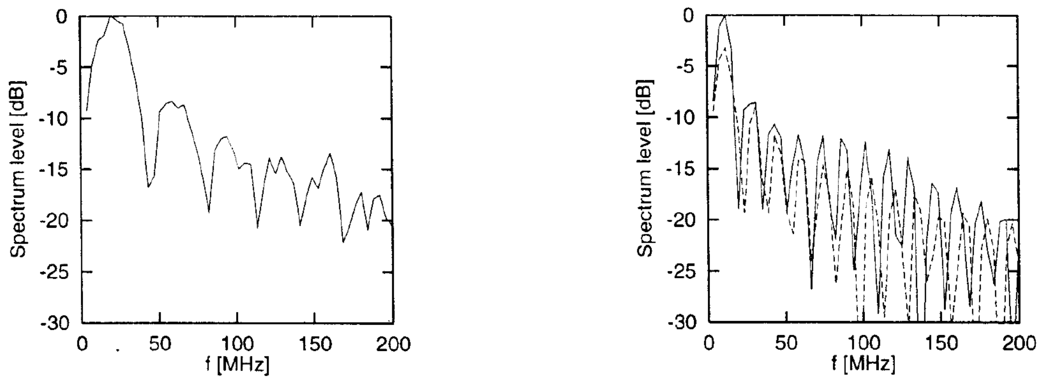


(a) (b)

Figure **2-7**. Frequency spectra for laser-excited broadband Rayleigh waves on fused silica at propagation distance (a) $x$ = 2.3 mm and (b) $x$ = 18.3 mm [61].

The evolution of the waveforms due to nonlinear distortions also has significant implications in the frequency domain. We provide the frequency spectra for laser-excited broadband Rayleigh waves obtained by Lomonosov et al. [61] at 2.3 mm and 18.3 mm propagation distances on a fused silica specimen. The results are shown in Figure 2-7. With the increase in the propagation distance, a shift in the peak frequency to a lower value (frequency-down conversion) is observed due to the nonlinear effect. In addition, the bandwidth of the main lobe is reduced, and the number of higher harmonic peaks in the frequency spectrum is increased.

**Shock formation in solids**

The formation of shocks in fluids is a well-known phenomenon [59,62]. Shock formation can also occur in solids due to nonlinear distortion of finite-amplitude broadband Rayleigh waveforms [61,63]. Interestingly, some features of distortion in solids are quite similar to features of shocks in fluids. For example, in fused silica, the in-plane velocity component distorts analogous to fluid with peak advancing and troughs receding. However, unlike fluid, a cusp forms in the in-plane velocity component while a peak forms in the out-of-plane velocity component. The cusping of the in-plane velocity component is attributed to the generation of higher harmonics leading to more energy of the wave to be concentrated near the surface (Recall that the energy of Rayleigh waves is concentrated within approximately one wavelength of the surface). Furthermore, it has been reported that the nonlinear broadband Rayleigh waves can either transform into compression shocks or rarefaction shocks in crystalline silicon, depending on the direction of propagation [58]. This phenomenon is not observed for narrowband Rayleigh waves. In some cases, the shock formation in solids may also lead to surface cracks as the high-frequency part of the pulse spectrum generates a stress-strain field that reaches the critical strength for nucleation cracks [64].

The generation of steep shock fronts is more easily observed for broadband Rayleigh waves than narrowband Rayleigh waves [65]. The generation of finite-amplitude broadband Rayleigh waves can be most easily achieved using a pulsed laser technique. Several authors have reported shock formation using the pulsed laser technique in isotropic solids [57,63,66] and crystalline media [58,63]. In addition, the theoretical descriptions of nonlinear broadband Rayleigh waves have been studied using two mathematical models: one model employs a Hamiltonian formalism [67], and the other model describes the surface velocities of broadband Rayleigh waves with an evolution equation [56].

### 2.3.4 Characteristic length scales

#### Characteristic diffraction length

Similar to nonlinearity, diffraction can also distort the shape of broadband Rayleigh waves. Diffraction mainly affects the lower frequency region (like a high-pass filter) of the broadband Rayleigh wave spectrum [68]. The characteristic diffraction length, $x_d$, which depends on the peak frequency, the Rayleigh wave speed, and the length of the laser line source (see equation 2-1), is a measure at which the diffraction effects become significant. In other words, the diffraction effects can be ignored for propagation distances much lower than $x_d$.

$$x_d = (f_{peak}/c_r)l^2 \tag{2-1}$$

Table **2-1.** Characteristic diffraction length for Ti-6Al-4V and IN-718 specimen.

| **Material** | **Rayleigh wave speed, $c_r$ (m/s)** | **Peak frequency, $f_{peak}$ (MHz)** | **Length of the laser line source, $l$ (mm)** | **Characteristic diffraction length, $x_d$ (mm)** |
|---|---|---|---|---|
| Ti-6Al-4V | 2920 | 1 | 20 | 137 |
| IN-718 | 2850 | 1 | 20 | 140 |

For example, we provide the diffraction length for broadband Rayleigh waves traveling on Ti-6Al-4V and IN-718 specimens in Table 2-1. The values used for the length of the laser line source and the peak frequency are based on the typical values observed in our experiments.

**Shock formation distance**

As the nonlinear waves in fluids transform into shocks, the broadband laser-excited Rayleigh waves can transform into shock type pulses. The generation of steep shock fronts is more easily observed for broadband Rayleigh waves than narrowband Rayleigh waves [65]. The shock formation can be characterized based on the shock formation distance, $x_s$, which is inversely related to the nonlinearity, the amplitude, and the frequency [58]. Equation 2-2 provides the expression for the shock formation distance.

$$x_s = \frac{1}{|\beta|\epsilon k} \tag{2-2}$$

where,

$\beta$ is the nonlinearity coefficient, which can be computed from the second and third-order elastic constants according to the expression provided in [69],

$\epsilon$ is the Mach number, which is the ratio of particle velocity and the Rayleigh wave speed, and $k$ is the wavenumber, which is equivalent to $\frac{2\pi f_{peak}}{c_r}$.

Table **2-2**. Second-order and third-order elastic constants for Ti alloy and Ni alloy [70].

| **Material** | $\boldsymbol{\lambda}$**, GPa** | $\boldsymbol{\mu}$**, GPa** | $\boldsymbol{\nu}$ | $\boldsymbol{l}$**, GPa** | $\boldsymbol{m}$**, GPa** | $\boldsymbol{n}$**, GPa** |
|---|---|---|---|---|---|---|
| Ti alloy | 76 | 44 | 0.3413 | -527 | -606 | -479 |
| Ni alloy | 121 | 80 | 0.2984 | -373 | -399 | -482 |

Table **2-3**. Estimates for the shock formation distance for Ti alloy and Ni alloy.

| **Material** | $\boldsymbol{\lvert\beta\rvert}$ | $\boldsymbol{\epsilon}$ | $\boldsymbol{k}$ | $\boldsymbol{x_s}$**, mm** |
|---|---|---|---|---|
| Ti alloy | 1.36 | 0.0082 | 2151.77 | 41.67 |
| Ni alloy | 1.23 | 0.0084 | 2204.63 | 43.90 |

The material properties for the titanium alloy and nickel alloy are given in Table 2-2. For example, we provide the estimates for the corresponding shock formation distances in Table 2-3. In this example, we have used the particle velocity as 24 m/s, and the peak frequency of 1 MHz as the representative values based on our experiments. Thus, the estimated shock formation distances for Ti alloy and Ni alloy specimens are 41.67 mm and 43.90 mm, which are much lower than the corresponding diffraction lengths (see Table 2-1). Since the in-situ laser ultrasonic measurements range from 20 mm to 40 mm, only the nonlinear distortion effects on the spatial evolution of broadband Rayleigh waves are considered in this research, and the diffraction effects are ignored.

We note that the spatial evolution of broadband Rayleigh waves can also be caused by attenuation and dispersion effects along with diffraction and nonlinear distortion effects described above. The attenuation effect is frequency-dependent and mainly affects the higher frequency region of the spectrum of broadband Rayleigh waves. Thus, it can be viewed as a low-pass filter [68]. Furthermore, for isotropic elastic halfspace, Rayleigh waves are non-dispersive. However, the presence of surface roughness can induce dispersion effects as well as the attenuation effects caused by the scattering of broadband Rayleigh waves [71–73].

### 2.3.5 Laser reception

A laser interferometer is used to receive the Rayleigh waves. The basic principle of laser interferometry is – when a laser beam is incident on the surface, the surface displacements cause phase change of the reflected laser beam. This phase change is detected by mixing the light with the reference beam, thereby providing the instantaneous surface displacements of the Rayleigh waves. There are numerous types of laser interferometers. The reflectivity and surface roughness are the primary issues that affect the performance of laser interferometers. However, improvements in laser interferometer technology in the last two decades have made them more robust and less susceptible to poor reflectivity and surface roughness issues [74]. This is of key importance for the in-situ inspection of AM components.

## 2.4 References

1. Gibson, I.; Rosen, D.; Stucker, B. Directed energy deposition processes. In *Additive Manufacturing Technologies*; Springer, 2015; pp. 245–268.

2. Honarvar, F.; Varvani-Farahani, A. A review of ultrasonic testing applications in additive manufacturing: Defect evaluation, material characterization, and process control. *Ultrasonics* **2020**, *108*, 106227, doi:10.1016/j.ultras.2020.106227.

3. Malekipour, E.; El-Mounayri, H. Common defects and contributing parameters in powder bed fusion AM process and their classification for online monitoring and control: a review. *Int. J. Adv. Manuf. Technol.* **2018**, *95*, 527–550, doi:10.1007/s00170-017-1172-6.

4. Cerniglia, D.; Scafidi, M.; Pantano, A.; Rudlin, J. Inspection of additive-manufactured layered components. *Ultrasonics* **2015**, *62*, 292–298, doi:10.1016/j.ultras.2015.06.001.

5. Reutzel, E.W.; Nassar, A.R. A survey of sensing and control systems for machine and process monitoring of directed-energy, metal-based additive manufacturing. *Rapid Prototyp. J.* **2015**, *21*, 159–167, doi:10.1108/RPJ-12-2014-0177.

6. Boddu, M.R.; Landers, R.G.; Liou, F.W. Control of laser cladding for rapid prototyping--A review. In Proceedings of the 2001 International Solid Freeform Fabrication Symposium; 2001.

7. Everton, S.K.; Hirsch, M.; Stravroulakis, P.; Leach, R.K.; Clare, A.T. Review of in-situ process monitoring and in-situ metrology for metal additive manufacturing. *Mater. Des.* **2016**, *95*, 431–445, doi:10.1016/j.matdes.2016.01.099.

8. Tapia, G.; Elwany, A. A Review on Process Monitoring and Control in Metal-Based Additive Manufacturing. *J. Manuf. Sci. Eng.* **2014**, *136*, doi:10.1115/1.4028540.

9. Foster, B.K.; Reutzel, E.W.; Nassar, A.R.; Dickman, C.J.; Hall, B.T. A brief survey of sensing for metal-based powder bed fusion additive manufacturing.; Harding, K.G., Yoshizawa, T., Eds.; 2015; p. 94890B.

10. Bi, G.; Schürmann, B.; Gasser, A.; Wissenbach, K.; Poprawe, R. Development and qualification of a novel laser-cladding head with integrated sensors. *Int. J. Mach. Tools Manuf.* **2007**, *47*, 555–561, doi:10.1016/j.ijmachtools.2006.05.010.

11. Hofman, J.T.; Pathiraj, B.; van Dijk, J.; de Lange, D.F.; Meijer, J. A camera based feedback control strategy for the laser cladding process. *J. Mater. Process. Technol.* **2012**, *212*, 2455–2462, doi:10.1016/j.jmatprotec.2012.06.027.

12. Bi, G.; Gasser, A.; Wissenbach, K.; Drenker, A.; Poprawe, R. Identification and qualification of temperature signal for monitoring and control in laser cladding. *Opt. Lasers Eng.* **2006**, *44*, 1348–1359, doi:10.1016/J.OPTLASENG.2006.01.009.

13. Song, L.; Mazumder, J. Feedback control of melt pool temperature during laser cladding process. *IEEE Trans. Control Syst. Technol.* **2011**, *19*, 1349–1356, doi:10.1109/TCST.2010.2093901.

14. Fathi, A.; Khajepour, A.; Toyserkani, E.; Durali, M. Clad height control in laser solid freeform fabrication using a feedforward PID controller. *Int. J. Adv. Manuf. Technol.* **2007**, *35*, 280–292, doi:10.1007/s00170-006-0721-1.

15. Zeinali, M.; Khajepour, A. Height Control in Laser Cladding Using Adaptive Sliding Mode Technique: Theory and Experiment. *J. Manuf. Sci. Eng.* **2010**, *132*, 041016, doi:10.1115/1.4002023.

16. Heralić, A.; Christiansson, A.-K.; Lennartson, B. Height control of laser metal-wire deposition based on iterative learning control and 3D scanning. *Opt. Lasers Eng.* **2012**, *50*, 1230–1241, doi:10.1016/j.optlaseng.2012.03.016.

17. Song, L.; Mazumder, J. Real time Cr measurement using optical emission spectroscopy during direct metal deposition process. *IEEE Sens. J.* **2012**, *12*, 958–964, doi:10.1109/JSEN.2011.2162316.

18. Stutzman, C.B.; Nassar, A.R.; Reutzel, E.W. Multi-sensor investigations of optical emissions and their relations to directed energy deposition processes and quality. *Addit. Manuf.* **2018**, *21*, 333–339, doi:10.1016/j.addma.2018.03.017.

19. Stutzman, C.B.; Mitchell, W.F.; Nassar, A.R. Optical emission sensing for laser-based additive manufacturing—What are we actually measuring? *J. Laser Appl.* **2021**, *33*, 012010, doi:10.2351/7.0000321.

20. Dunbar, A.J.; Nassar, A.R. Assessment of optical emission analysis for in-process monitoring of powder bed fusion additive manufacturing. *Virtual Phys. Prototyp.* **2018**, *13*, 14–19,

doi:10.1080/17452759.2017.1392683.

21. Montazeri, M.; Nassar, A.R.; Dunbar, A.J.; Rao, P. In-process monitoring of porosity in additive manufacturing using optical emission spectroscopy. *IISE Trans.* **2020**, *52*, 500–515, doi:10.1080/24725854.2019.1659525.

22. Smith, R.J.; Li, W.; Coulson, J.; Clark, M.; Somekh, M.G.; Sharples, S.D. Spatially resolved acoustic spectroscopy for rapid imaging of material microstructure and grain orientation. *Meas. Sci. Technol.* **2014**, *25*, 55902.

23. Patel, R.; Hirsch, M.; Dryburgh, P.; Pieris, D.; Achamfuo-Yeboah, S.; Smith, R.; Light, R.; Sharples, S.; Clare, A.; Clark, M. Imaging material texture of as-deposited selective laser melted parts using spatially resolved acoustic spectroscopy. *Appl. Sci.* **2018**, *8*, doi:10.3390/app8101991.

24. Pieris, D.; Patel, R.; Dryburgh, P.; Hirsch, M.; Li, W.; Sharples, S.D.; Smith, R.J.; Clare, A.T.; Clark, M. Spatially Resolved Acoustic Spectroscopy Towards Online Inspection of Additive Manufacturing. *Insight - Non-Destructive Test. Cond. Monit.* **2019**, *61*, 132–137, doi:10.1784/insi.2019.61.3.132.

25. Dryburgh, P.; Pieris, D.; Martina, F.; Patel, R.; Sharples, S.; Li, W.; Clare, A.T.; Williams, S.; Smith, R.J. Spatially resolved acoustic spectroscopy for integrity assessment in wire–arc additive manufacturing. *Addit. Manuf.* **2019**, *28*, 236–251, doi:10.1016/j.addma.2019.04.015.

26. Hirsch, M.; Catchpole-Smith, S.; Patel, R.; Marrow, P.; Li, W.; Tuck, C.; Sharples, S.D.; Clare, A.T. Meso-scale defect evaluation of selective laser melting using spatially resolved acoustic spectroscopy. *Proc. R. Soc. A Math. Phys. Eng. Sci.* **2017**, *473*, 20170194, doi:10.1098/rspa.2017.0194.

27. Pieris, D.; Stratoudaki, T.; Javadi, Y.; Lukacs, P.; Catchpole-Smith, S.; Wilcox, P.D.; Clare, A.;

Clark, M. Laser Induced Phased Arrays (LIPA) to detect nested features in additively manufactured components. *Mater. Des.* **2020**, *187*, 108412, doi:10.1016/j.matdes.2019.108412.

28. Lévesque, D.; Bescond, C.; Lord, M.; Cao, X.; Wanjara, P.; Monchalin, J.-P. Inspection of additive manufactured parts using laser ultrasonics. In Proceedings of the AIP Conference Proceedings; AIP Publishing LLC, 2016; Vol. 1706, p. 130003.

29. Millon, C.; Vanhoye, A.; Obaton, A.-F.; Penot, J.-D. Development of laser ultrasonics inspection for online monitoring of additive manufacturing. *Weld. World* **2018**, *62*, 653–661, doi:10.1007/s40194-018-0567-9.

30. Davis, G.; Nagarajah, R.; Palanisamy, S.; Rashid, R.A.R.; Rajagopal, P.; Balasubramaniam, K. Laser ultrasonic inspection of additive manufactured components. *Int. J. Adv. Manuf. Technol.* **2019**, *102*, 2571–2579, doi:10.1007/s00170-018-3046-y.

31. Yu, J.; Zhang, D.; Li, H.; Song, C.; Zhou, X.; Shen, S.; Zhang, G.; Yang, Y.; Wang, H. Detection of Internal Holes in Additive Manufactured Ti-6Al-4V Part Using Laser Ultrasonic Testing. *Appl. Sci.* **2020**, *10*, 365, doi:10.3390/app10010365.

32. Liu, S.; Jia, K.; Wan, H.; Ding, L.; Xu, X.; Cheng, L.; Zhang, S.; Yan, X.; Lu, M.; Ma, G.; et al. Inspection of the internal defects with different size in Ni and Ti additive manufactured components using laser ultrasonic technology. *Opt. Laser Technol.* **2022**, *146*, 107543, doi:10.1016/j.optlastec.2021.107543.

33. Zou, Y.; Chai, Y.; Wang, D.; Li, Y. Measurement of elastic modulus of laser cladding coatings by laser ultrasonic method. *Opt. Laser Technol.* **2022**, *146*, 107567, doi:10.1016/j.optlastec.2021.107567.

34. Zhan, Y.; Liu, C.; Zhang, J.; Mo, G.; Liu, C. Measurement of residual stress in laser additive

manufacturing TC4 titanium alloy with the laser ultrasonic technique. *Mater. Sci. Eng. A* **2019**, *762*, 138093, doi:10.1016/j.msea.2019.138093.

35. Zhan, Y.; Xu, H.; Du, W.; Liu, C. Study on the Effect of Scanning Strategy on Residual Stress in Laser Additive Manufacturing with the Laser Ultrasound Technique. *Exp. Mech.* **2021**, doi:10.1007/s11340-021-00795-6.

36. Everton, S.K.; Dickens, P.; Tuck, C.; Dutton, B. Identification of sub-surface defects in parts produced by additive manufacturing, using laser generated ultrasound. *Mater. Sci. Technol.* **2016**.

37. Everton, S.; Dickens, P.; Tuck, C.; Dutton, B. Using laser ultrasound to detect subsurface defects in metal laser powder bed fusion components. *Jom* **2018**, *70*, 378–383.

38. Zhang, J.; Wu, J.; Zhao, X.; Yuan, S.; Ma, G.; Li, J.; Dai, T.; Chen, H.; Yang, B.; Ding, H. Laser ultrasonic imaging for defect detection on metal additive manufacturing components with rough surfaces. *Appl. Opt.* **2020**, *59*, 10380, doi:10.1364/AO.405284.

39. Dai, T.; Jia, X.; Zhang, J.; Wu, J.; Sun, Y.; Yuan, S.; Ma, G.; Xiong, X.; Ding, H. Laser ultrasonic testing for near-surface defects inspection of 316L stainless steel fabricated by laser powder bed fusion. *China Foundry* **2021**, *18*, 360–368, doi:10.1007/s41230-021-1063-1.

40. Xu, W.; Li, X.; Zhang, J. Multi-feature fusion imaging via machine learning for laser ultrasonic based defect detection in selective laser melting part. *Opt. Laser Technol.* **2022**, *150*, 107918, doi:10.1016/j.optlastec.2022.107918.

41. Xu, W.; Zhang, J.; Li, X.; Yuan, S.; Ma, G.; Xue, Z.; Jing, X.; Cao, J. Intelligent denoise laser ultrasonic imaging for inspection of selective laser melting components with rough surface. *NDT E Int.* **2022**, *125*, 102548, doi:10.1016/j.ndteint.2021.102548.

42. Jiang, Y.; Wang, H.; Chen, S.; Zhang, Q.; Hu, P.; Li, X.; Zheng, K.; Wang, H. Quantitative

Imaging Detection of Additive Manufactured Parts Using Laser Ultrasonic Testing. *IEEE Access* **2020**, *8*, 186071–186079, doi:10.1109/ACCESS.2020.3030307.

43. Park, S.-H.; Liu, P.; Yi, K.; Choi, G.; Jhang, K.-Y.; Sohn, H. Mechanical properties estimation of additively manufactured metal components using femtosecond laser ultrasonics and laser polishing. *Int. J. Mach. Tools Manuf.* **2021**, *166*, 103745, doi:10.1016/j.ijmachtools.2021.103745.

44. Zeng, Y.; Wang, X.; Qin, X.; Hua, L.; Xu, M. Laser Ultrasonic inspection of a Wire + Arc Additive Manufactured (WAAM) sample with artificial defects. *Ultrasonics* **2021**, *110*, 106273, doi:10.1016/j.ultras.2020.106273.

45. Zeng, Y.; Wang, X.; Qin, X.; Hua, L.; Liu, G.; Guan, S. Laser ultrasonic inspection of defects in wire arc additive manufactured samples with different surface profiles. *Measurement* **2022**, *188*, 110597, doi:10.1016/j.measurement.2021.110597.

46. Volker, A. . & Klein, M. . & Bobbs, B. . & Wiedmann, M. . & Honarvar, M. Improved laser ultrasonic inspection for additive manufacturing by incorporating surface profiling. *Rev. Prog. Quant. Nondestruct. Eval.* **2019**.

47. Scruby, C.B.; Drain, L.E. *Laser ultrasonics techniques and applications*; CRC press, 1990; ISBN 0750300507.

48. Scruby, C.B.; Dewhurst, R.J.; Hutchins, D.A.; Palmer, S.B. Quantitative studies of thermally generated elastic waves in laser-irradiated metals. *J. Appl. Phys.* **1980**, *51*, 6210–6216.

49. McKie, A.D.W.; Wagner, J.W.; Spicer, J.B.; Penney, C.M. Laser generation of narrow-band and directed ultrasound. *Ultrasonics* **1989**, *27*, 323–330, doi:10.1016/0041-624X(89)90030-9.

50. Hasanian, M.; Choi, S.; Lissenden, C. Laser Ultrasonics for Remote Detection of Stress Corrosion Cracking in Harsh Environments. In Proceedings of the ASNT 27th Annual Research Symposium

Proceedings; ASNT, 2018; pp. 106–115.

51. Di Scalea, F.L.; Berndt, T.P.; Spicer, J.B.; Djordjevic, B.B. Remote laser generation of narrow-band surface waves through optical fibers. *IEEE Trans. Ultrason. Ferroelectr. Freq. Control* **1999**, *46*, 1551–1557, doi:10.1109/58.808880.

52. Hikata, A.; Elbaum, C. Generation of Ultrasonic Second and Third Harmonics Due to Dislocations. I. *Phys. Rev.* **1966**, *144*, 469–477, doi:10.1103/PhysRev.144.469.

53. Choi, S.; Nam, T.; Jhang, K.-Y.; Kim, C.S. Frequency response of narrowband surface waves generated by laser beams spatially modulated with a line-arrayed slit mask. *J. Korean Phys. Soc.* **2012**, *60*, 26–30, doi:10.3938/jkps.60.26.

54. Kolomenskii, A.A.; Lioubimov, V.A.; Jerebtsov, S.N.; Schuessler, H.A. Nonlinear surface acoustic wave pulses in solids: Laser excitation, propagation, interactions (invited). *Rev. Sci. Instrum.* **2003**, *74*, 448–452, doi:10.1063/1.1517188.

55. Gusev, V.E.; Lauriks, W.; Thoen, J. New evolution equations for the nonlinear surface acoustic waves on an elastic solid of general anisotropy. *J. Acoust. Soc. Am.* **1998**, *103*, 3203–3215, doi:10.1121/1.423036.

56. Gusev, V.E.; Lauriks, W.; Thoen, J. Theory for the time evolution of nonlinear Rayleigh waves in an isotropic solid. *Phys. Rev. B* **1997**, *55*, 9344–9347, doi:10.1103/PhysRevB.55.9344.

57. Kolomenskii, A.A.; Lomonosov, A.M.; Kuschnereit, R.; Hess, P.; Gusev, V.E. Laser generation and detection of strongly nonlinear elastic surface pulses. *Phys. Rev. Lett.* **1997**, *79*, 1325–1328, doi:10.1103/PhysRevLett.79.1325.

58. Lomonosov, A.M.; Hess, P.; Kumon, R.E.; Hamilton, M.F. Laser-generated nonlinear surface wave pulses in silicon crystals. *Phys. Rev. B - Condens. Matter Mater. Phys.* **2004**, *69*, 1–13,

doi:10.1103/PhysRevB.69.035314.

59. Ostrovsky, L.A. Nonlinear Acoustics. *J. Acoust. Soc. Am.* **1999**, *105*, 578–578, doi:10.1121/1.426968.

60. Kolomenskii, A.A.; Schuessler, H.A. Characterization of isotropic solids with nonlinear surface acoustic wave pulses. *Phys. Rev. B* **2001**, *63*, 085413, doi:10.1103/PhysRevB.63.085413.

61. Lomonosov, A.; Mikhalevich, V.G.; Hess, P.; Yu. Knight, E.; Hamilton, M.F.; Zabolotskaya, E.A. Laser-generated nonlinear Rayleigh waves with shocks. *J. Acoust. Soc. Am.* **1997**, *101*, 3080–3080, doi:10.1121/1.418785.

62. Gusev, V.E.; Karabutov, A.A. Laser optoacoustics. *NASA STI/Recon Tech. Rep. A* **1991**, *93*, 16842.

63. Lomonosov, A.; Hess, P. Laser Excitation and Propagation of Nonlinear Surface Acoustic Wave Pulses. In Proceedings of the Nonlinear Acoustics in Perspective Proc. 14th International Symposium on Nonlinear Acoustics; Wei, R.J., Ed.; Nanjing Univ. Press.: Nanjing, 1996; pp. 106–111.

64. Kozhushko, V. V.; Hess, P. Anisotropy of the strength of Si studied by a laser-based contact-free method. *Phys. Rev. B* **2007**, *76*, 144105, doi:10.1103/PhysRevB.76.144105.

65. Lomonosov, A.M.; Hess, P. Nonlinear surface acoustic waves: Realization of solitary pulses and fracture. *Ultrasonics* **2008**, *48*, 482–487, doi:10.1016/j.ultras.2008.06.002.

66. Lomonosov, A.; Mikhalevich, V.G.; Hess, P.; Knight, E.Y.; Hamilton, M.F.; Zabolotskaya, E.A. Laser-generated nonlinear Rayleigh waves with shocks. *J. Acoust. Soc. Am.* **1999**, *105*, 2093–2096, doi:10.1121/1.426814.

67. Zabolotskaya, E.A. Nonlinear propagation of plane and circular Rayleigh waves in isotropic solids. *J. Acoust. Soc. Am.* **1992**, *91*, 2569–2575, doi:10.1121/1.402993.

68. Lomonosov, A.; Mayer, A.P.; Hess, P. 3. Laser-based surface acoustic waves in materials science. In; 2001; pp. 65–134.

69. Hamilton, M.F.; Il'inskii, Y.A.; Zabolotskaya, E.A. Nonlinear surface acoustic waves in crystals. *J. Acoust. Soc. Am.* **1999**, *105*, 639–651, doi:10.1121/1.426255.

70. Rjelka, M.; Barth, M.; Reinert, S.; Koehler, B.; Bamberg, J.; Baron, H.-U. Third order elastic constants and Rayleigh wave dispersion of shot-peened aero-engine materials.; 2012; pp. 1430–1436.

71. Eguiluz, A.G.; Maradudin, A.A. Frequency shift and attenuation length of a Rayleigh wave due to surface roughness. *Phys. Rev. B* **1983**, *28*, 728–747, doi:10.1103/PhysRevB.28.728.

72. Krylov, V.; Smirnova, Z. Experimental study of the dispersion of a Rayleigh wave on a rough surface. *Sov. physics. Acoust.* **1990**, *36*, 583–585.

73. Kosachev, V. V.; Gandurin, Y.N. Dispersion and Attenuation of Rayleigh Waves at a One-Dimensional Random Roughness of the Free Surface of a Hexagonal Crystal. *Phys. Solid State* **2003**, *45*, 1808–1813, doi:10.1134/1.1611257.

74. Everton, S.; Dickens, P.; Tuck, C.; Dutton, B. Evaluation of laser ultrasonic testing for inspection of metal additive manufacturing. In Proceedings of the Laser 3d Manufacturing Ii; International Society for Optics and Photonics, 2015; Vol. 9353, p. 935316.

# Chapter 3

# SURFACE ROUGHNESS EFFECTS ON SELF-INTERACTING AND MUTUALLY INTERACTING RAYLEIGH WAVES[1]

Rayleigh waves are very useful for ultrasonic nondestructive evaluation of structural and mechanical components. Nonlinear Rayleigh waves have unique sensitivity to the early stages of material degradation because material nonlinearity causes distortion of the waveforms. The self-interaction of a sinusoidal waveform causes second harmonic generation, while the mutual interaction of waves creates disturbances at the sum and difference frequencies that can potentially be detected with minimal interaction with the nonlinearities in the sensing system. While the effect of surface roughness on attenuation and dispersion is well documented, its effects on the nonlinear aspects of Rayleigh wave propagation have not been investigated. Therefore, Rayleigh waves are sent along aluminum surfaces having small, but different, surface roughness values. The relative nonlinearity parameter increased significantly with surface roughness (average asperity heights 0.027–3.992 µm and Rayleigh wavelengths 0.29–1.9 mm). The relative nonlinearity parameter should be decreased by the presence of attenuation, but here it actually increased with roughness (which increases the attenuation). Thus, an attenuation-based correction was unsuccessful. Since the distortion from material nonlinearity and surface roughness occur over the same surface, it is necessary to make material nonlinearity measurements over surfaces having the same roughness or in the future develop a quantitative understanding of the roughness effect on wave distortion.

[1] This chapter is substantially based on:
Bakre, C.; Lissenden, C.J. Surface Roughness Effects on Self-Interacting and Mutually Interacting Rayleigh Waves. *Sensors* **2021**, *21*, 5495, doi:10.3390/s21165495.

## 3.1 Introduction

Many types of structures suffer damage due to rigorous operating and environmental conditions. Various degradation mechanisms such as fatigue, corrosion, and strength reduction can cause the failure of components, which may degrade structural performance or lead to catastrophic failure and life-threatening situations. Inspecting the structural integrity of mechanical components using nondestructive evaluation (NDE) techniques or structural health monitoring (SHM) techniques is crucial. Rayleigh waves, and surface acoustic waves (SAW) in general, are highly effective for surface inspections as their energy is concentrated near the surface [1]. The linear parameters of Rayleigh waves, such as the wave speed and the attenuation, have been effectively used to detect evolution of the material properties [2–5]. Rayleigh wave speed has a strong dependence on porosity [6], while attenuation depends on various factors, including absorption, diffraction, and scattering caused by voids, pores, inclusions, and grain boundaries [7,8].

Likewise, the nonlinearity of Rayleigh waves has been leveraged for detecting changes in the material or material microstructure that lead to macroscale damage [9]. The interaction of Rayleigh waves with the microstructure results in distortion of the waves and generation of higher harmonics. The relative nonlinearity parameter (to be defined subsequently) for Rayleigh waves depends on the spectral amplitudes at the primary and second harmonic frequencies. The relative nonlinearity parameter of Rayleigh waves is the following:

- effective in detecting fatigue cracking at an early stage [10,11];
- sensitive to plastic deformation, cold work, and residual stress [12];
- able to distinguish different aluminum alloys in pristine states based on their material nonlinearity due to lattice anharmonicity[13];
- sensitive to precipitate hardening due to heat treatments [14], thermal embrittlement [15,16], sensitization of stainless steel [17], and stress corrosion cracking [18].

Both linear and nonlinear Rayleigh wave measurements require sensors that send and receive the waves at ultrasonic frequencies. Recent studies of Rayleigh wave measurements include Ghafoor et al. [19], Li et al. [20], Song et al. [21], Li et al. [22], and Sarris et al. [23]. Many types of sensors can be used for this purpose including angle-beam, comb, interdigitated, and pulsed lasers. Understanding the sensor data, especially when using the relative nonlinearity parameter, is an important first step for NDE and SHM.

In the above-mentioned applications of Rayleigh waves, the researchers are careful to make measurements on smooth surfaces because roughness is known to affect the propagation characteristics of Rayleigh waves. Surface roughness in the Rayleigh wave transmission path causes scattering, which induces attenuation and dispersion [24–28]. Urazakov and Fal'kovskii [28] and Maradudin and Mills [25] first analytically studied the attenuation effects of surface roughness on Rayleigh wave propagation using Rayleigh's method and a Green's function method. The authors limit the amplitude of roughness to be sufficiently small compared to the Rayleigh wavelength in order to use perturbation theory. The surface irregularities act as scatterers causing mode conversion to bulk waves or other Rayleigh waves. Both approaches predict the Rayleigh wave attenuation to be primarily caused by mode conversion to bulk waves as opposed to Rayleigh waves in other directions. The studies also indicate that the attenuation is proportional to the fifth power of the frequency. Steg and Klemens [29] arrived at the same relationship between attenuation and frequency using the method of mass defects. De Billy et al.'s [30] attenuation measurements on duraluminum samples revealed the same fifth power dependence of attenuation on frequency, validating the theoretical predictions in [25] and [26].

De Billy et al. [30] also noticed a reduction in Rayleigh wave speed for one-dimensional surface roughness. Later, using Rayleigh's method, Eguiluz and Maradudin [27] obtained the dispersion relation for Rayleigh waves due to surface irregularities. Sinclair [31] used the method of mass loading on a smooth surface to obtain the frequency dependence of Rayleigh wave speed along rough surfaces. Krylov and Smirnova [24] also experimentally studied the dispersion effects of Rayleigh waves on rough surfaces and found that the surface roughness caused a reduction in the Rayleigh wave speed, and the decrease in speed increased with increasing frequency. The authors reported that the frequency dependence of the attenuation agrees with the theoretical models discussed by Eguiluz and Maradudin [27] and Huang and Maradudin [26]. A variation of 0.5–1.5% in the frequency-dependent velocity was observed for surface roughness with an RMS (root mean square) surface height deviation of 17 μm in the frequency range 1 to 4 MHz.

More recently, the adverse effect caused by surface roughness was studied relative to Rayleigh wave based residual stress measurement for a shot peening operation [32,33]. The dispersion caused by the surface roughness rendered a large deviation in the measurement of residual stress. In related research, Liu et al. [12] observed a decrease in the relative nonlinearity parameter from 81% to 44.5% when the rough shot-peened specimen was hand polished using emery paper (grit # 600, 800, 1200). However, very limited literature is available that accounts for the effect of surface roughness on the nonlinear characteristics of Rayleigh waves.

Detection of Rayleigh wave distortion associated with material nonlinearity can be a powerful tool for NDE and SHM, but since the wave distortion is typically small, it is necessary to well understand the other nonlinearities that creep into the measurement. The effect of attenuation on nonlinear Rayleigh waves has been accounted for by Cantrell [34], but it has not been applied to the surface roughness problem.

This chapter reports on Rayleigh wave propagation in a thick 7075 aluminum block. The objective of the chapter is to assess the effect that surface roughness has on the distortion of Rayleigh waves. Three specimens of the same material with different surface roughness are used to investigate the effects of surface roughness on the relative nonlinearity parameter for the second harmonic and mutually interacting Rayleigh waves. The single-frequency and dual-frequency Rayleigh waves are generated using angle beam transducers and received using a laser receptor. In this paper, the nonlinearity at various points in the sensing system are measured, viz. output from the amplifier, output from the transducer, and output from the wedge used for the angle beam transducer. Second, two different methods for the generation of dual-frequency Rayleigh waves are examined for their effectiveness in studying the mutual interaction, viz. using a single transducer attached to the wedge and using two adjacently placed wedge-transducers. Then, the attenuation coefficients are obtained for the three specimens with different surface roughness values. Finally, the measured and attenuation-corrected relative nonlinearity parameters are compared to understand the roughness effects on the Rayleigh wave distortion.

## 3.2 Methods

The experimental setup used to investigate the effect of surface roughness on nonlinear Rayleigh waves consists of an angle-beam transducer for the generation of Rayleigh waves on an aluminum alloy specimen and an adaptive interferometer for their reception. Toneburst excitations at single and dual frequencies enable the investigation of nonlinearity from self-interaction as well as from mutual interaction. We start characterizing the nonlinearity of the sensing system by receiving the vibratory response of the transducer itself by impinging the reception laser beam directly on the transducer surface, as shown in the block diagram and photograph in Figure 3-1.

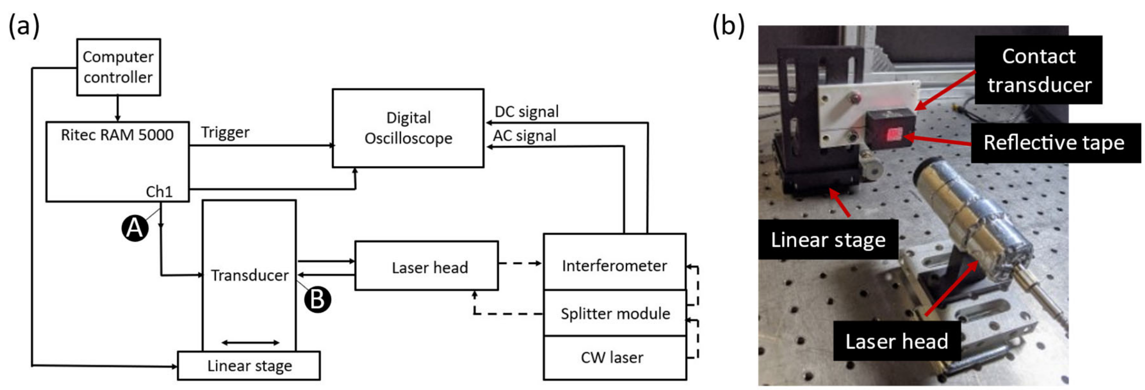


Figure **3-1:** Test setup for measurement of system nonlinearity: (a) Block diagram where solid and dashed lines represent electrical cables and optical fibers respectively, (b) Photograph of the laser head illuminating reflective tape on the transducer surface.

Contact transducers (Benchmark series 113-244-591, 113-863-600, or 113-232-591; Baker Hughes, Houston, TX, USA) are actuated by a gated amplifier (RAM-5000 SNAP, Ritec Inc., Warwick, RI, USA). These transducers have center frequencies of 2.25, 3.5, and 5.0 MHz, respectively. The transducer is mounted on a linear stage to enable focusing the laser interferometer on the surface of the transducer. Retroreflective tape is applied on the surface of the transducer to improve the reflectivity. An adaptive laser interferometer measures the out-of-plane displacement from the surface of the transducer. The received signals are observed using an oscilloscope and recorded for post-processing.

The laser interferometer (AIR-1550-TWM, Intelligent Optical Systems Inc., Torrance, CA, USA), used to measure the out-of-plane surface displacements, is comprised of four components: (1) a 1550 nm continuous wave (CW) laser with the maximum power capacity of 2 W, (2) a splitter module, (3) a laser head, (4) and an interferometer. The laser beam is delivered by an optical fiber. The splitter module divides the CW laser beam into a reference beam and a probe beam. An optical fiber delivers the probe beam to the laser head, which uses a collimating lens pair to focus it on the surface of the sample. The out-of-plane surface displacements distort the probe beam. The distorted probe beam reflected from the surface is re-captured by the laser head. The distorted probe beam and the reference beam are combined in a photorefractive material inside the interferometer. The photorefractive material generates a time-varying voltage that is proportional to the instantaneous surface displacements. The photorefractive material also inherently rejects slowly-varying changes (<10 kHz) typical of low-frequency background noise.

The laser interferometer provides two outputs, viz. an AC signal and a DC level, that are recorded on an oscilloscope (InfiniiVision MSOX3024T, Keysight, Santa Rosa, CA, USA). The AC signal contains the time-varying voltage proportional to the surface displacements, while the DC level provides a measure of the received light reflected from the surface. The amount of light received by the laser head depends mainly on the power of the incident probe beam, the reflectivity and roughness of the surface, and the position of the laser head relative to the surface. Thus, normalizing the AC signal by the DC level provides a means to compare the signals obtained from rough surfaces (that scatter the laser beam) with those obtained from smooth surfaces. In this research, the received AC signals are normalized by the corresponding DC level.

The test specimens are 7075 aluminum blocks 170 mm × 40 mm × 20 mm having different surface roughness values. Each block is made from the same material, for which the microstructure is shown in Figure 3-2. The length and width of the elongated grains in μm are (509 ± 16, 266 ± 10), (559 ± 16, 225 ± 9), (547 ± 15, 207 ± 10) for samples 1, 2, and 3, respectively. The hardness values are 111HV0.5, 112HV0.5, and 114HV5 for samples 1, 2, and 3, respectively. The moderate and rough surface samples are obtained by performing a three-pass and a single pass wire-cut EDM (M500S, Seibu Electric and Machinary, Koga, Japan) operation. The smooth surface is obtained by whetstone polishing.

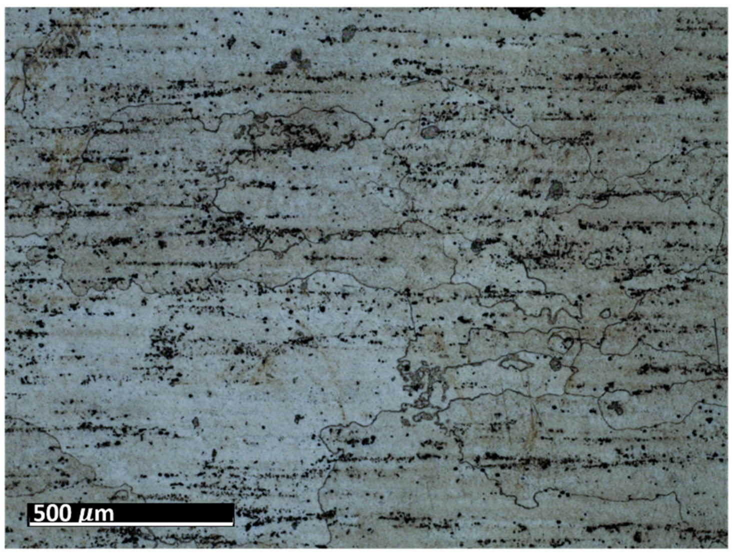


Figure **3-2**: Optical microscope (Zeiss SmartZoom) image of polished and etched (Kroll's reagent) aluminum block surface. Pancake-type grains and a distribution of fine precipitates are apparent.

The surface roughness is characterized using a white light interferometer (NexView 9000, Zygo, Middlefield, CT, USA) and quantified using Gwyddion, which is an open source software for Statistical Parametric Mapping (SPM) data analysis [35]. A 50× Mirau objective is used to achieve an optical resolution of 0.52 $\mu$m in the $x$ and $y$ directions based on the Sparrow criteria (Optical resolution = $0.5\lambda/\mathrm{NA}$, where $\lambda$ = 570 nm and NA = 0.55). The spatial sampling based on the camera pixel size is 0.17 $\mu$m and the area of the inspected region is 170 $\mu$m × 170 $\mu$m. Table 3-1 gives the 3D and 1D surface profiles for the three test blocks. While Deltombe et al. [36] describe a procedure to determine which surface roughness parameters are most relevant for a specific application, we simply provide the linear parameters (ISO 4287): $P_a$ (arithmetic average), $P_q$ (root mean square), and $P_t$ (peak-to-valley distance), and areal parameters (ISO 25178-2): $S_a$ (arithmetic mean height), $S_q$ (root mean square height), $S_z$ (maximum height), and $S_{dq}$ (root mean square gradient). The linear and areal surface roughness parameters for each sample are tabulated in Table 3-2. The mean values are calculated from 1022

Table **3-1**: 3D and 1D surface profiles for the three aluminum test blocks.

| **Sample** | **3D Surface Profile** | **1D Surface Profile** |
|---|---|---|
| 1<br>Smooth | 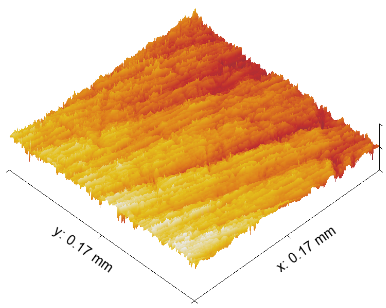 | 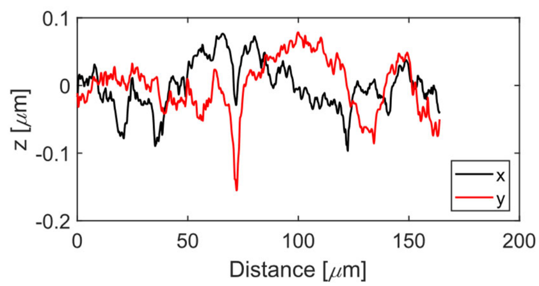 |
| 2<br>Moderate | 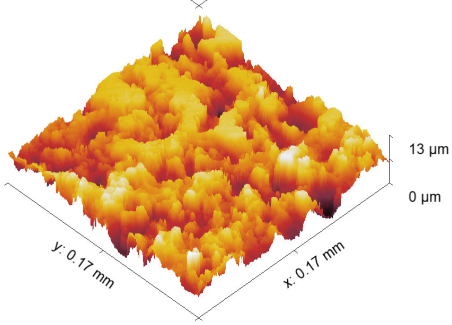 | 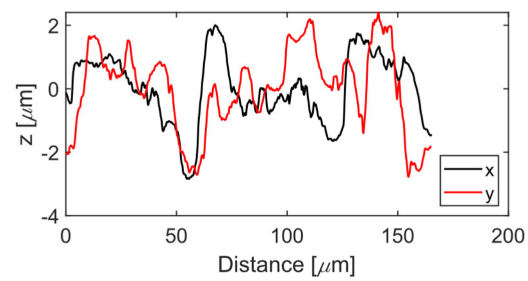 |
| 3<br>Rough | 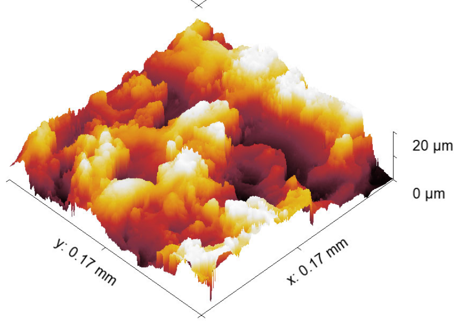 | 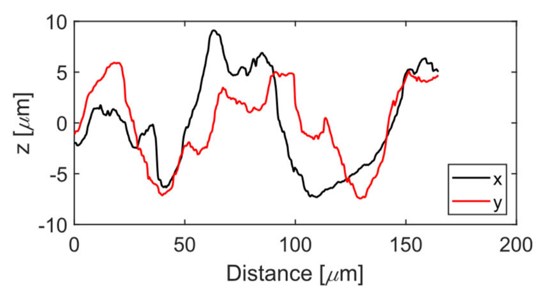 |

measurements. The surface roughness can affect the generation, wave propagation, as well as the reception of Rayleigh waves. However, this paper focuses on the effect of surface roughness on nonlinear Rayleigh wave propagation. This is much different than bulk waves reflecting from a rough surface as in Wang et al. [37]. Therefore, the specimen surface where the wedge is coupled is made smooth by sequential abrasion with emery paper (grit #400, 600, 800, 1000, 1500). This ensures that there is no influence of the surface roughness on the Rayleigh wave generation. In contrast, the surface where the Rayleigh waves are received is not polished. But as mentioned before, the laser interferometer used in this study is adaptive to the varying surface roughness and enables factoring out the effects of surface roughness on reception.

Table **3-2**: Surface roughness parameters for the three aluminum test blocks.

| **Sample** | **Linear Roughness Parameters (ISO 4287): x-Direction** | | |
|---|---|---|---|
| | $P_a$, $\mu$m | $P_q$, $\mu$m | $P_t$, $\mu$m |
| 1 (Smooth) | 0.027 | 0.034 | 0.173 |
| 2 (Moderate) | 0.872 | 1.081 | 4.849 |
| 3 (Rough) | 3.992 | 4.649 | 16.403 |

| **Sample** | **Linear Roughness Parameters (ISO 4287): y-Direction** | | |
|---|---|---|---|
| | $P_a$, $\mu$m | $P_q$, $\mu$m | $P_t$, $\mu$m |
| 1 (Smooth) | 0.033 | 0.040 | 0.234 |
| 2 (Moderate) | 1.034 | 1.304 | 5.178 |
| 3 (Rough) | 3.410 | 3.923 | 13.365 |

| **Sample** | **Areal Roughness Parameters (ISO 25178-2)** | | | |
|---|---|---|---|---|
| | $S_a$, $\mu$m | $S_q$, $\mu$m | $S_z$, $\mu$m | $S_{dq}$ |
| 1 (Smooth) | 0.0831 | 0.105 | 0.865 | 0.220 |
| 2 (Moderate) | 1.642 | 1.993 | 12.94 | 1.852 |
| 3 (Rough) | 4.349 | 5.118 | 20.450 | 2.832 |

The output level of the gated amplifier is varied from 20–80% in increments of 10% to increase the wave amplitude to determine the nonlinearity parameter. Finally, the Plexiglas wedge is coupled to the block with ultrasonic gel (Soundsafe, Sonotech, State College, PA, USA) and preloaded by a spring force.

### 3.2.1 Relative nonlinearity parameter

In this study the relative nonlinearity parameter is used as a relative measure to compare the effect of surface roughness on the self-interaction and mutual interaction of Rayleigh waves. The relative nonlinearity parameter for second harmonic generation (from self-interaction) is typically defined to be

$$\boldsymbol{\beta}' = \frac{\boldsymbol{A_2}}{\boldsymbol{A_1^2}} \tag{3-1}$$

where $A_1$ and $A_2$ are the spectral amplitudes at the primary and second harmonic frequencies respectively. The generalized definition of the relative nonlinearity parameter for mutual interaction of waves at the primary frequencies $f_a \leq f_b$ used herein is

$$\boldsymbol{\beta}' = \frac{\boldsymbol{A_{(f_b \pm f_a)}}}{\boldsymbol{A_{f_a} A_{f_b}}} \tag{3-2}$$

where the plus sign is associated with the sum frequency and the minus sign is associated with the difference frequency. If $f_a = f_b$ we have self-interaction instead of mutual interaction and Equation (3-2) gives the second harmonic in the case of the sum, and the quasi-static pulse at zero frequency in the case of the difference. To compute the relative nonlinearity parameter $\beta'$, $A_{(f_b \pm f_a)}$ is plotted as a function of $A_{f_a} A_{f_b}$ as the output level of the amplifier is increased. For the range of output levels where the graph is linear, $\beta'$ is obtained by linear regression.

### 3.2.2 Self-interaction of Rayleigh waves

When conducting nonlinear ultrasonic testing to assess the material nonlinearity, it is important to know what other nonlinearities are embedded in the measurements. In this work the nonlinearity of the sensing system is investigated by analyzing the signal in the sensing system at the points shown in Figure 3-3:

- Point A—amplifier output monitoring point
- Point B—surface of the transducer, measured by laser interferometer

- Point C—surface of the wedge, measured by laser interferometer
- Point D—surface of the specimen, measured by laser interferometer.

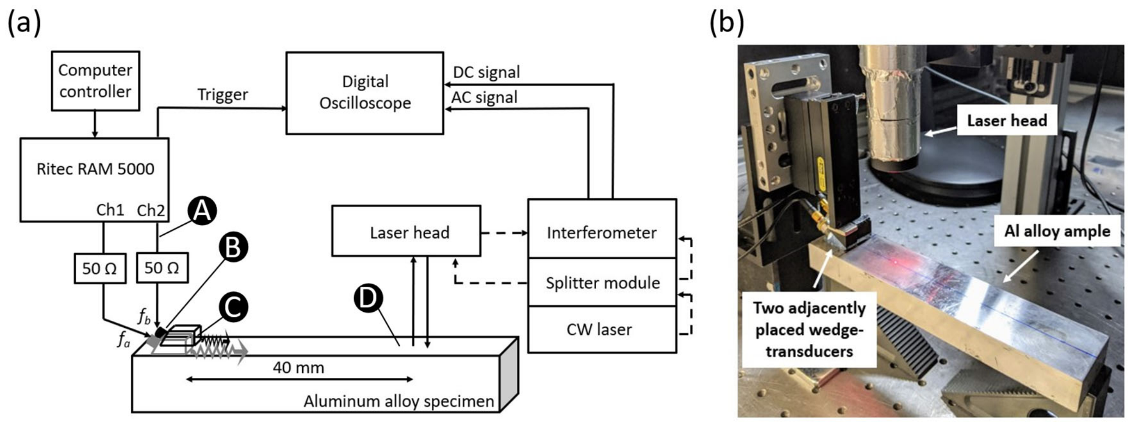


Figure **3-3**: Rayleigh wave test setup: (a) Block diagram where solid and dashed lines represent electrical cables and optical fibers respectively, (b) Adjacent angle-beam transducers actuate dual-frequency Rayleigh waves, which are received by the laser head.

The primary frequency used for system nonlinearity assessment is $f_0$ = 5 MHz, therefore the second harmonic occurs at 10 MHz.

The surface roughness effects on the self-interaction of Rayleigh waves are studied for the primary frequencies 2, 3.5, and 5 MHz, and the relative nonlinearity parameter are obtained on the three aluminum blocks with different surface roughness. The attenuation coefficients are obtained for the excitation frequencies and the respective second harmonic frequencies to check the veracity of the attenuation correction that accounts for the surface roughness effects on the relative nonlinearity parameter. The laser head is thus scanned from 30 mm to 130 mm from the angle beam transducer along the wave propagation direction, and the measurements are obtained in 5 mm increments.

### 3.2.3 Mutual interaction of Rayleigh waves

The mutual interaction of waves at primary frequencies $f_a$ = 3.2 MHz and $f_b$ = 3.84 MHz generated by a single transducer is studied. Note that the two frequencies are selected close to the nominal central frequency of the transducer. The peak amplitudes of the two tonebursts are equal, and their relative phase difference is zero. The second-order frequencies are: $f_b - f_a = 0.64$ MHz, $2f_a = 6.4$ MHz, $f_b + f_a = 7.04$ MHz, and $2f_b = 7.68$ MHz. When operated in the 'combine modulation' mode, the gated amplifier provides a dual-frequency toneburst signal on Channel 1. The signals are obtained at Point A and Point B, as shown in Figure 3-1.

For the adjacently placed wedge-transducers, the wave mixing occurs due to ultrasonic beam spreading. The use of two transducers allows for a wider selection of excitation frequencies. The signal being sent to the piezoelectric transducer is monitored, and Figure 3-4 shows the peak-to-peak voltages as a function of output level supplied to the transducers for 1.5 and 4.0 MHz toneburst signals. This method avoids the intermodulation distortion effect as each transducer is excited by a toneburst signal having a single central frequency. Although the system nonlinearity contributes higher harmonics, the mutual interaction between the waves, which at second order occurs at the sum and difference frequencies, is not convoluted by system nonlinearities.

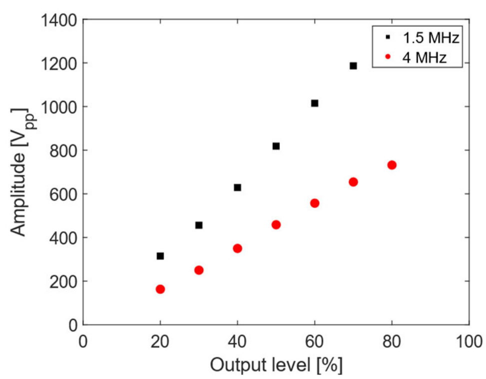


Figure **3-4**: Amplitude of toneburst signal sent to the transducer as a function of amplifier output level for center frequencies of 1.5 and 4.0 MHz.

### 3.2.4 Signal processing

1024 signals were synchronously averaged together and then recorded using the oscilloscope. The signals are normalized with respect to the DC level. Matlab algorithms are developed for further processing the recorded signals. A Hanning window is applied to the signal before computing the spectrum. The sampling frequency of the time record is 1.45 GHz. Zero-padding is used to improve the frequency resolution before the Fast Fourier Transform (FFT) function in Matlab is applied. The output of the Matlab FFT function is scaled by the time increment ($dt = 6.9 \times 10^{-10}$ s) to obtain the linear spectrum.

## 3.3 Results

### 3.3.1 Sensing system nonlinearity

As already mentioned, when conducting nonlinear ultrasonic testing to assess the material nonlinearity, it is crucial to know what other nonlinearities are embedded in the measurements. In this work, the nonlinearity of the sensing system is investigated by analyzing the signal at points A–D in the sensing system (Figure 3-3a). A sequence of A-scans and frequency spectra obtained at points A–D for a single frequency toneburst having central frequency $f_o$ = 5 MHz are shown in Figure 3-5. The frequency spectrum in Figure 3-5a indicates that in addition to the primary frequency, higher harmonics are sent from the gated amplifier to the transducer. The nonlinearity of the transducer output signal is determined by the transducer response characteristics such as its nonlinearity and bandwidth. Figure 3-5b shows the signal received on the surface of the transducer, in which we observe the suppression of the third harmonic (relative to Figure 3-5a). Ultrasonic gel couples the transducer to the Plexiglas wedge. The signal amplitude is reduced due to impedance mismatch and attenuation in the wedge. Nonlinearity of the wedge and possible contact nonlinearity between the transducer and the wedge increase the higher harmonic content of the signal in Figure 3-5c. The relative nonlinearity parameter measured using linear regression at Points A–C is shown in Figure 3-6. The nonlinearity at these points is entirely from the sensing system. We observe that although the signal amplitude reduces at each stage, the nonlinearity of the signal is increased by 2.17% at Point B and by 3.57% at Point C.

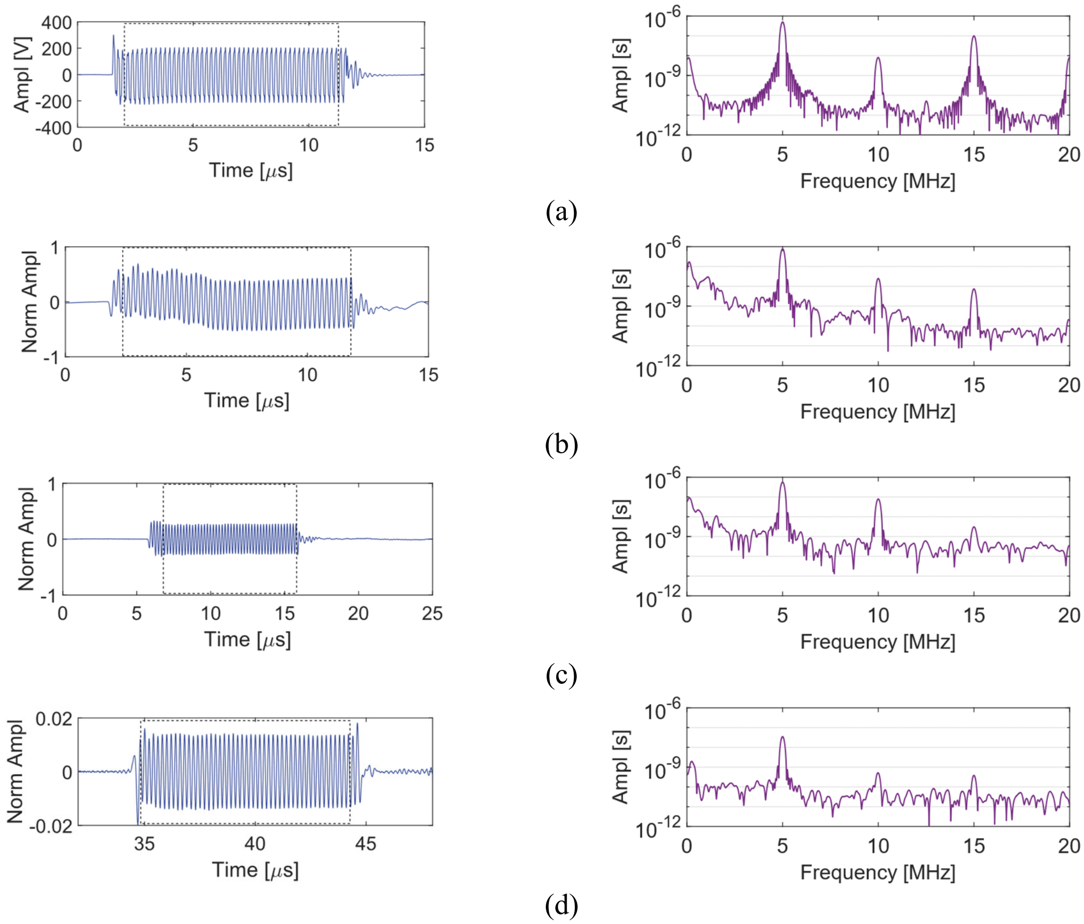


Figure **3-5**: A-scans and frequency spectra for 5 MHz toneburst excitation at the 75% output level: (a) Point A, (b) Point B, (c) Point C, and (d) Point D.

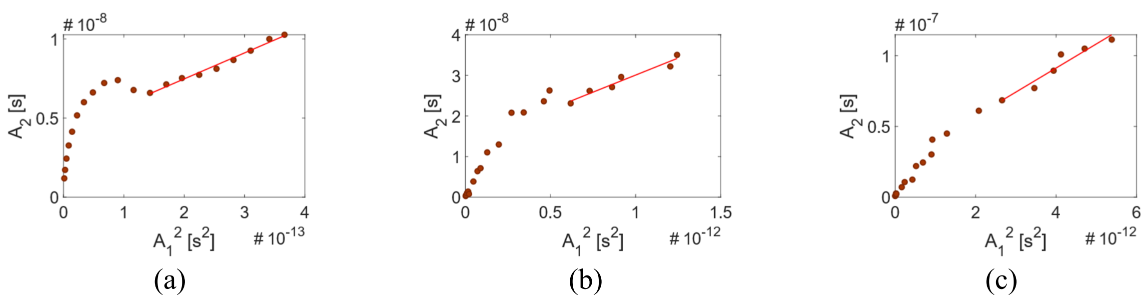


Figure **3-6**: Linear regression to determine the relative nonlinearity parameter for the sensing system given a 5 MHz signal: (a) $\beta'$ = 16433 at Point A, (b) $\beta'$ = 16790 at Point B, (c) $\beta'$ = 17019 at Point C.

The signal received at Point D is shown in Figure 3-5d. This signal contains all of the nonlinearities as the signal received at Point C as well as the nonlinearity associated with Rayleigh wave propagating 40 mm in the aluminum block. The nonlinearity associated with Rayleigh wave propagation is due to the material nonlinearity as well as the surface roughness. It may be possible to directly quantify the nonlinearity associated with Rayleigh wave propagation by subtracting the Point C spectrum from the Point D spectrum after they have been normalized with respect to the primary frequency. However, doing so presumes no interaction between the system nonlinearity, the material nonlinearity, and the surface roughness. We do not perform this subtraction in the remainder of this work because all measurements contain the same system nonlinearities. Therefore, we are interested in changes in the nonlinearity.

### 3.3.2 Nonlinear Rayleigh wave mixing methods

Two different methods for dual-frequency Rayleigh wave excitation for wave mixing are investigated from the viewpoint of the system nonlinearities. The first approach uses a single transducer excited by a dual-frequency toneburst. Figure 3-1 shows the test setup to study the response of the transducer as received by the laser interferometer. The mutual interaction of waves at primary frequencies $f_a$ = 3.2 MHz and $f_b$ = 3.84 MHz generated by a single transducer is studied. The second-order frequencies are: $\boldsymbol{f_b - f_a = 0.64}$ MHz, $\boldsymbol{2f_a = 6.4}$ MHz, $\boldsymbol{f_b + f_a = 7.04}$ MHz, and $\boldsymbol{2f_b = 7.68}$ MHz.

Figure 3-7 shows the A-scans and the frequency spectra for the signals received at Point A (output of amplifier) and Point B (surface of the transducer). The four packets observed in the A-scans indicate the presence of two excitation frequencies ($f_a$ and $f_b$). The two excitation frequencies, the corresponding second harmonics, and the sum and difference frequency peaks are marked in the frequency spectra. The frequency spectrum from Point A shows that the dual-frequency signal undergoes modulation before getting to the transducer. Thus, the basic premise for mixing waves is violated—i.e., there is energy present at the sum and difference frequencies that is not associated with the nonlinearity of the waveguide material. The higher harmonics generated due to the nonlinearity in the system complicate the measurement of the material nonlinearity. Several other high amplitude peaks can also be observed in the frequency spectrum. This is a typical phenomenon observed when two frequencies are mixed in a nonlinear device (amplifier) and is known as intermodulation distortion, wherein the higher harmonics of frequencies that are integral multiples of the two excitation frequencies are generated due to the electrical system nonlinearity. These harmonics can be represented as $|\boldsymbol{nf_a + mf_b}|$, where $\boldsymbol{n}$ and $\boldsymbol{m}$ are integers. The sum $|\boldsymbol{n}| + |\boldsymbol{m}|$ is referred to as the order of the distortion. Thus, additional peaks at other combinational frequencies such as $2f_a + f_b$, $2f_a - f_b$, $f_a + 2f_b$, $3f_a - 2f_b$ are also observed in the frequency spectrum.

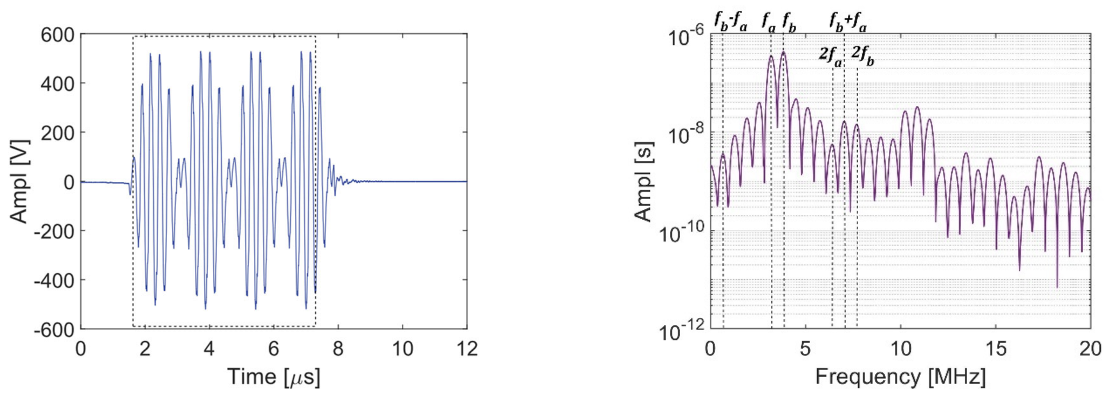


(a)

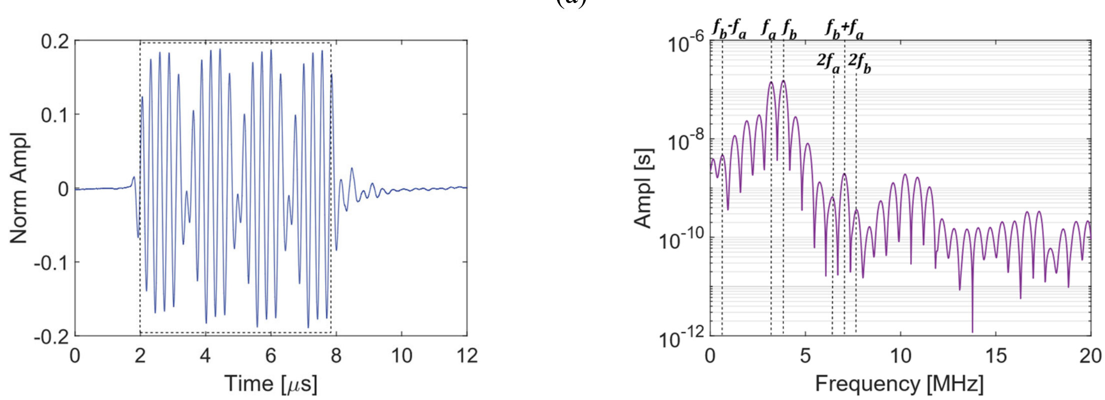


(b)

Figure **3-7**: A-scan and frequency spectrum given a dual-frequency excitation ($f_a$ = 3.2 MHz and $f_b$ = 3.8 MHz) excitation at the 75% output level: (a) Point A, (b) Point B.

The alternative to sending a dual-frequency signal to a single transducer is to send separate signals to two adjacent transducers. The 2.25 and 5 MHz transducers are placed on side-by-side wedges and the primary frequencies $f_a$ = 1.5 MHz and $f_b$ = 4.0 MHz are generated by the two gated amplifier channels. The second-order frequencies are: $\boldsymbol{f_b - f_a = 2.5}$ MHz, $\boldsymbol{2f_a = 3.0}$ MHz, $\boldsymbol{f_b + f_a = 5.5}$ MHz, and $\boldsymbol{2f_b = 8.0}$ MHz. The A-scans and frequency spectra for Points A-D are shown in Figure 3-8.

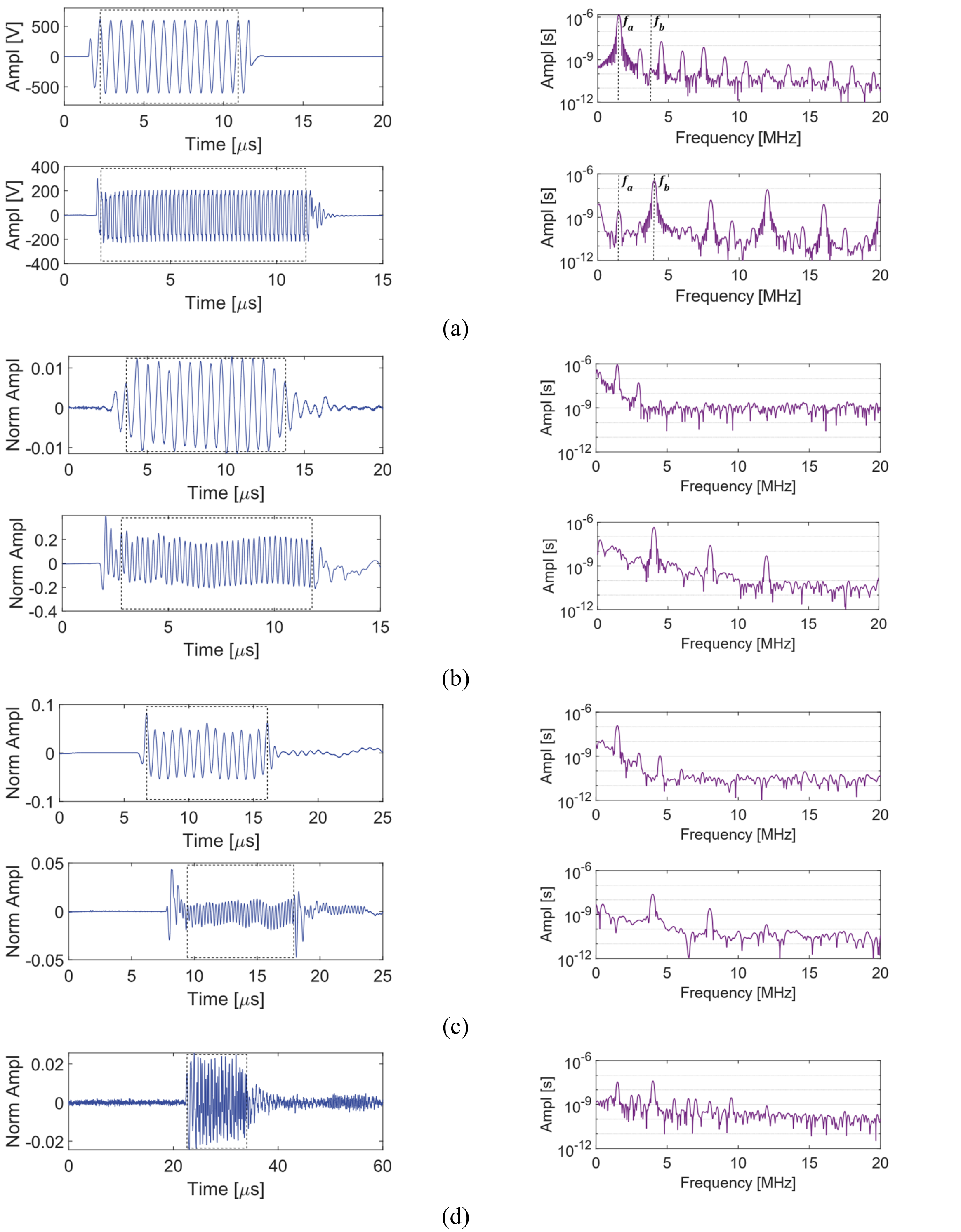


Figure **3-8**: A-scan and frequency spectrum given toneburst excitations to adjacent transducers at the 75% output level: (a) Point A, (b) Point B, (c) Point C, (d) Point D.

Figure 3-8a shows that amplifier Channel 1 outputs $f_a$ and its higher harmonics only, while Channel 2 outputs $f_b$ and its higher harmonics in addition to a small peak at $f_a$. However, the spurious peak at $f_a$ is not observed in the signal sent from the transducer in Figure 3-8b, perhaps due to limitations of the bandwidth of the transducer (although this was not investigated). Figure 3-8c presents the signals obtained on the wedges and their frequency spectra. Finally, the mixing Rayleigh waves are received at a point located 40 mm from the adjacent wedges and the signal is shown in Figure 3-8d. Unlike when a dual frequency signal was sent to a single transducer (Figure 3-7), where the frequency spectrum consists of many equal-width lobes, the frequency spectrum in Figure 3-8d consists of distinct peaks at the primary and second order frequencies

Finally, the mixing Rayleigh waves are received at a point located 40 mm from the adjacent wedges and the signal is shown in Figure 3-8d. Unlike when a dual frequency signal was sent to a single transducer (Figure 3-7), where the frequency spectrum consists of many equal-width lobes, the frequency spectrum in Figure 3-8d consists of distinct peaks at the primary and second order frequencies.

### 3.3.3 Surface roughness effects on Rayleigh wave interactions

On each sample the adjacent wedge transducers sent Rayleigh waves that were received by the laser interferometer. From the frequency spectrum the peaks at the primary and secondary frequencies were determined. Figure 3-9 plots the amplitude peak at the second harmonic frequency ($\boldsymbol{A_{2f_a}}$ or $\boldsymbol{A_{2f_b}}$) versus the square of the amplitude peak at the corresponding primary frequency ($\boldsymbol{A_{f_a}A_{f_a}}$ or $\boldsymbol{A_{f_b}A_{f_b}}$, respectively). Likewise, Figure 3-10 plots the amplitude peak at the combinational harmonic frequency ($\boldsymbol{A_{f_{b-a}}}$and $\boldsymbol{A_{f_{b+a}}}$) versus the product of the amplitude peaks at the corresponding primary frequencies ($\boldsymbol{A_{f_a}A_{f_b}}$). The relative nonlinearity parameters (Equation (3-2)) were regressed to the results shown in Figures 3-9 and 3-10 for self-interaction and mutual interaction, respectively. The relative nonlinearity parameters for each sample and secondary frequency are tabulated in Table 3-3. The relative nonlinearity parameter increases with surface roughness from Sample 1 to Sample 2 to Sample 3. The roughness magnification factors for Sample 2 relative to Sample 1 and for Sample 3 relative to Sample 1 were computed and are also given in Table 3-3. Magnification factors range from 1.10 to 2.44 for the moderate sample and from 2.79 to 16.0 for the rough sample, both taken relative to the smooth sample. The magnification factor is larger for self-interaction than mutual interaction, with the exception of Sample 2 at $f_{2a}$, which could be due to the larger system nonlinearity for the second harmonic relative to the sum and difference frequencies. The magnification factor is the smallest for $f_{b+a}$. Note that the largest average roughness value (3.992 $\mu$m) is two orders of magnitude smaller than the smallest wavelength (360 $\mu$m). The increase in relative nonlinearity parameter due to surface roughness is consistent with the results of Liu et al. [12].

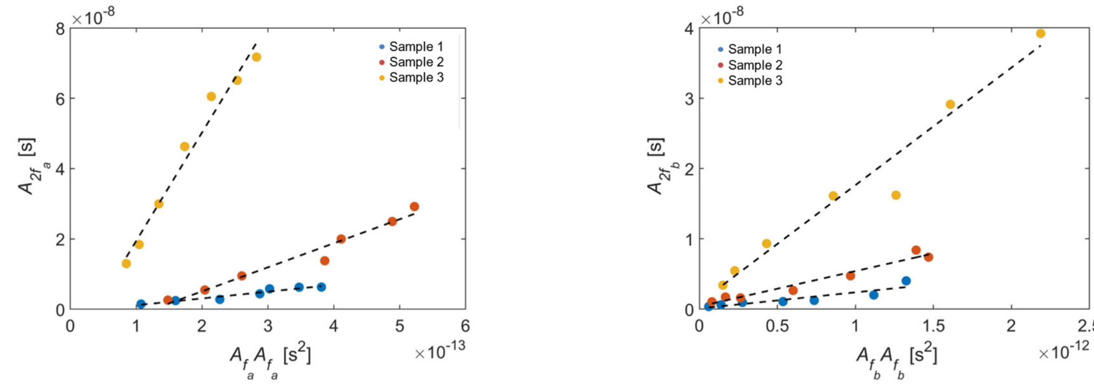


(a) (b)

Figure **3-9**: Second-order spectral amplitudes for self-interaction plotted as a function of the square of the primary frequency amplitudes for (a) $2f_a$ and (b) $2fb$. $f_a$ = 1.5 MHz and $f_b$ = 4.0 MHz.

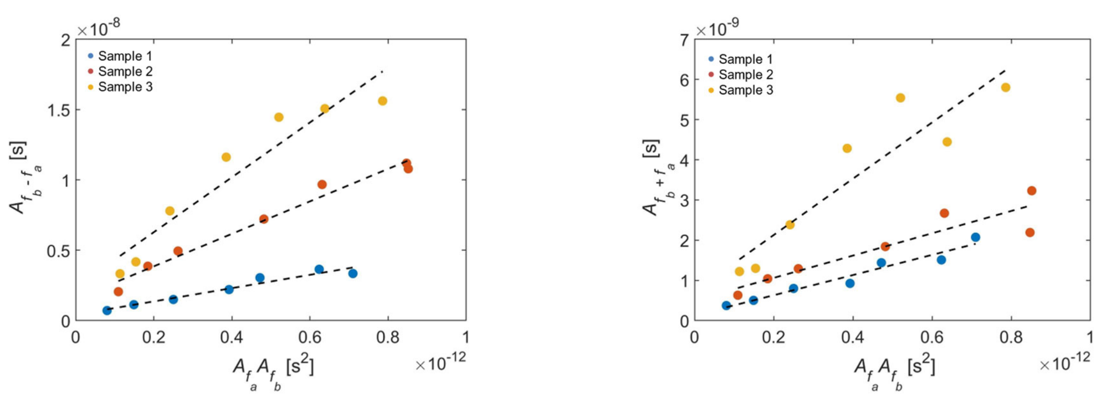


(a) (b)

Figure **3-10**: Second-order spectral amplitudes for mutual interaction plotted as a function of the product of the primary frequency amplitudes for (a) $f_{b\text{-}a}$ and (b) $f_{b+a}$. $f_a$ = 1.5 MHz and $f_b$ = 4.0 MHz.

Table **3-3**: Surface roughness parameters for the three aluminum test blocks.

| **Secondary Frequency (MHz)** | **Relative Nonlinearity Parameter** | | | **Roughness Magnification Factor** | |
|---|---|---|---|---|---|
| | **Sample 1 Smooth** | **Sample 2 Moderate** | **Sample 3 Rough** | **Sample 2/1** | **Sample 3/1** |
| $f_{b-a} = 2.5$ | 4725 | 11,545 | 19,514 | 2.44 | 4.13 |
| $f_{2a} = 3.0$ | 19,301 | 33,675 | 308,435 | 1.74 | 16.0 |
| $f_{b+a} = 5.5$ | 2509 | 2774 | 7003 | 1.10 | 2.79 |
| $f_{2b} = 8.0$ | 2298 | 5015 | 16,717 | 2.18 | 7.27 |

In the Introduction we noted that surface roughness causes scattering, which in turn causes attenuation. Other researchers have corrected the nonlinearity parameter for attenuation [38], which leads us to assess whether the variations in the relative nonlinearity parameter in Table 3-3 are due to the attenuation caused by surface roughness. Let us reconsider Equation (3-2) for the relative nonlinearity parameter for a material having attenuation that increases with frequency. In comparison with a lossless material, a lossy material will have a lower $\boldsymbol{\beta}'$ for the sum frequency, but a higher $\boldsymbol{\beta}'$ for the difference frequency (if the difference is less than $f_a$). Likewise, a lossy material will have a lower $\boldsymbol{\beta}'$ for second harmonics. Therefore, by increasing the attenuation and with all other material parameters remaining unchanged, $\boldsymbol{\beta}'$ should decrease. By this argument, the increasing $\boldsymbol{\beta}'$ with surface roughness observed in Table 3-3 is not associated with attenuation. We will go through the analysis to verify that the argument is indeed correct. Therefore, the attenuation of Rayleigh waves at different frequencies is characterized in the next section.

### 3.3.4 Effect of attenuation

Let the attenuation of the Rayleigh waves be given by

$$A_n = (A_n)_0 e^{-\alpha_n x} \tag{3-3}$$

where $A_n$ is the wave amplitude including attenuation, $(A_n)_0$ is the initial amplitude of the wave, $\alpha_n$ is the attenuation coefficient, $x$ is the propagation distance, $n = 1$ for the primary frequency and $n = 2$ for the second harmonic frequency. Attenuation coefficients are determined for the primary frequencies (2 MHz, 3.5 MHz, and 5 MHz) and the corresponding second harmonic frequencies (4 MHz, 7 MHz, and 10 MHz, respectively) by conducting a linear scan along the propagation path of the Rayleigh waves for the three samples. At each position in the scan the FFT is computed from the received A-scan in order to determine the amplitudes $A_1$ and $A_2$ corresponding to the primary frequency and the second harmonic frequency, respectively. Figure 3-11 shows example attenuation curves obtained for the Rayleigh waves with primary frequency $f_0$ = 2 MHz and second harmonic frequency $2f_0$ propagating on Sample 3 (the full set of attenuation curves are provided in the Supplementary Materials). Figure 3-12 shows the frequency-dependence of the attenuation coefficients for the three blocks is well-represented as 5th order. The regressed attenuation coefficients are seen to increase with increasing frequency and surface roughness in Table 3-4.

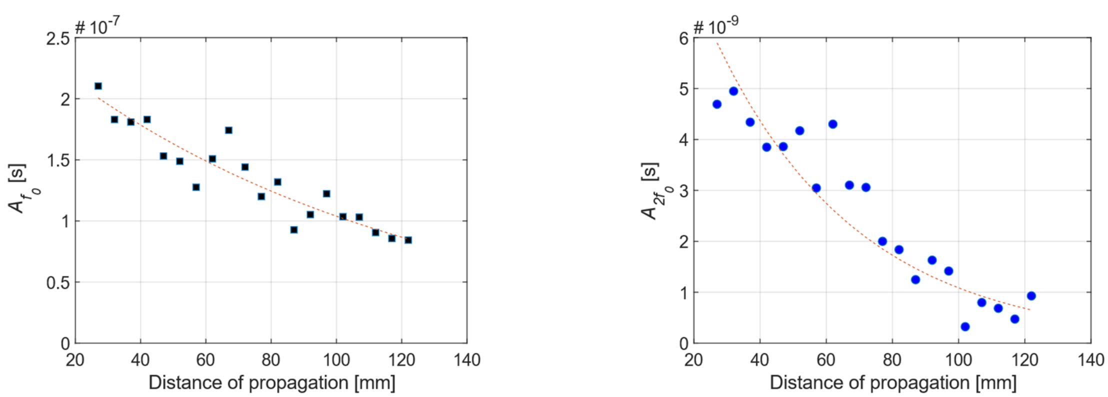


(a) (b)

Figure **3-11**: Sample attenuation curves for primary (2 MHz) and secondary (4 MHz) waves from Sample 3.

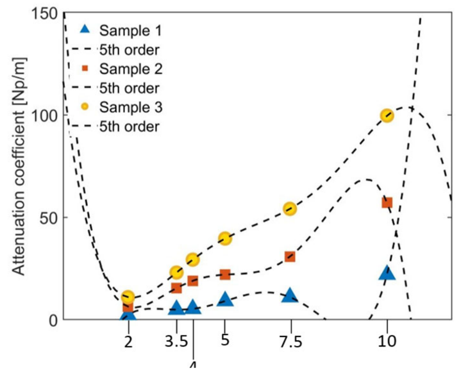


Figure **3-12**: Frequency dependence of the attenuation coefficients for Rayleigh waves on aluminum block.

Table **3-4**: Attenuation coefficient α in Np/m for primary and second harmonic Rayleigh waves.

| **Sample** | **Roughness** | | ***f*ₒ = 2.0 MHz** | ***f*ₒ = 3.5 MHz** | ***f*ₒ = 5.0 MHz** |
|---|---|---|---|---|---|
| 1 | Smooth | $f_o$ | 2.3 | 4.9 | 5.3 |
| | | $2f_o$ | 5.3 | 11.0 | 22.0 |
| 2 | Moderate | $f_o$ | 6.4 | 15.4 | 19.0 |
| | | $2f_o$ | 19.0 | 30.8 | 57.2 |
| 3 | Rough | $f_o$ | 11.0 | 23.0 | 29.3 |
| | | $2f_o$ | 29.3 | 54.1 | 99.6 |

On the other hand, the amplitude of the second harmonic is cumulative and increases linearly with propagation distance [39,40].

$$A_2 = \frac{1}{8}\beta A_1^2 k^2 x \tag{3-4}$$

Using Equations (3-3) and (3-4), the spatial change in the second harmonic wave amplitude due to distortion and attenuation can be expressed as

$$\frac{dA_2}{dx} = \frac{1}{8}\beta A_1^2 k^2 - \alpha_2 A_2 \tag{3-5}$$

which is a first order ordinary differential equation that can be solved by imposing the initial condition that $\boldsymbol{A_2 = 0}$ at $\boldsymbol{x = 0}$. Substituting Equation (3-3) in for $\boldsymbol{A_1}$, the solution (due to Hikata and Elbaum [41], see also Cantrell [34]) can be written as

$$\boldsymbol{A_2 = \frac{1}{8}\beta k^2 (A_1)_0^2 \left[\frac{\exp(-2\alpha_1 x) - \exp(-2\alpha_2 x)}{\alpha_2 - 2\alpha_1}\right]} \tag{3-6}$$

Let $\boldsymbol{\beta'_{meas}}$ be given by Equation (3-1) and use that to solve for the attenuation-corrected relative nonlinearity parameter

$$\boldsymbol{\beta'_{corrected} = \beta'_{meas} \frac{x(\alpha_2 - 2\alpha_1)}{1 - \exp[-x(\alpha_2 - 2\alpha_1)]}} \tag{3-7}$$

The relative nonlinearity parameters are obtained using the experimental method described in Section 2.4 for each sample and frequency. Figure 3-13 shows bar charts of the relative nonlinearity parameter for each excitation frequency. In Figure 3-13a, $\boldsymbol{\beta'_{meas}}$ is directly from the measurements, while in Figure 3-13b, $\boldsymbol{\beta'_{corrected}}$ is corrected for attenuation by using Equation (3-7).

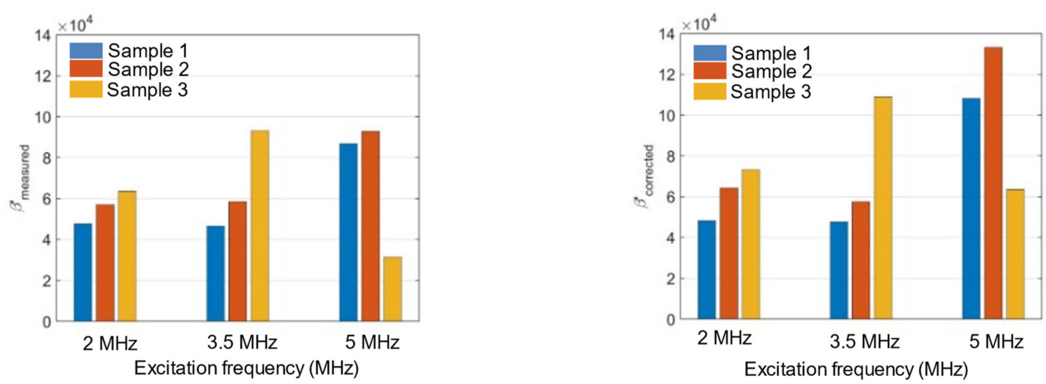


(a) (b)

Figure **3-13**: Relative nonlinearity parameter for each excitation frequency: (a) measured, (b) corrected.

In Figure 3-13a, we observe that for the 2 MHz and 3.5 MHz excitation frequencies, the $\boldsymbol{\beta'_{meas}}$ increases with the increase in the surface roughness. This observation is consistent with the effect observed for the mutual interaction study described in the previous section. For the 5 MHz excitation frequency, the relative nonlinearity parameter increases from Sample 1 to 2 but decreases for Sample 3. We attribute the reduction in the relative nonlinearity parameter for Sample 3 to the dominance of the attenuation effects over the harmonic generation, since the attenuation effects are more pronounced at higher frequency and surface roughness. $\boldsymbol{\beta'}_{\boldsymbol{meas}}$ generally increases with frequency until attenuation overwhelms the nonlinearity.

Table 3-5 provides the correction factors (fraction on right-hand side of Equation (3-7)) computed for each excitation frequency and surface roughness. The correction factors range from 0.9841 to 2.0347. We note that the correction factors are generally higher for both higher frequency and larger surface roughness, except for a slight decrease observed for 3.5 MHz excitation on Sample 2. If the attenuation correction worked as intended, the $\boldsymbol{\beta'}_{\boldsymbol{corrected}}$ for a prescribed frequency would have been the same for all three samples. Clearly, it is not. Moreover, attenuation should make $\boldsymbol{\beta'}_{\boldsymbol{corrected}} < \boldsymbol{\beta'}_{\boldsymbol{meas}}$, and the correction factor less than one. Clearly, it is not. These results suggest that the surface roughness effects on the relative nonlinearity parameter cannot be corrected by attenuation. In general, we infer that the surface roughness influences the relative nonlinearity parameter and its effect depends on the average asperity height and the wavelength of the Rayleigh waves.

Table **3-5**: Relative nonlinearity parameter correction factor (Equation 3-7).

| **Sample** | **Roughness** | $f_o$ **= 2.0 MHz** | $f_o$ **= 3.5 MHz** | $f_o$ **= 5.0 MHz** |
|---|---|---|---|---|
| 1 | Smooth | 1.0141 | 1.0242 | 1.2453 |
| 2 | Moderate | 1.1290 | 0.9841 | 1.4327 |
| 3 | Rough | 1.1531 | 1.1707 | 2.0347 |

## 3.4 Discussions

Our experimental results in Table 3-3 and Figure 3-13 show that the variation of average asperity height ($P_a$) from 0.027–3.992 μm along an aluminum surface has a substantial effect on the distortion of Rayleigh waves for excitation frequencies between 1.5 and 5 MHz. These asperities are small compared to the wavelengths. The largest Rayleigh wavelength is 1.9 mm at 1.5 MHz, while the smallest wavelength is 0.29 mm for the second harmonic at 10 MHz. Here, we quantify wave distortion through the relative nonlinearity parameter given in Equation (3-2). While surface roughness increases the attenuation of Rayleigh waves relative to a smooth surface, increased attenuation actually decreases the wave distortion. In contrast, Table 3-5 indicates that the roughness-induced attenuation actually increases the nonlinearity parameter.

Rayleigh wave distortion (nonlinearity) is useful for nondestructively assessing structural integrity and material degradation. However, these results strongly suggest that in order to use Rayleigh waves to assess material nonlinearity, we need to have a good understanding of the nonlinearities associated with surface roughness in addition to those associated with the sensing system. The interaction between the material nonlinearity and the surface roughness is entirely different from its interaction with the sensing system because material and surface nonlinearities occur in parallel, while material and sensing system nonlinearities occur in series.

These experiments were conducted due to our interest in using Rayleigh waves to monitor the additive manufacturing process. However, the roughness of metal surfaces during powder bed fusion and directed energy deposition processes is significantly larger than it was here. Current research is investigating this challenging problem. A future research direction is to explore the physics underlying the Rayleigh wave distortion associated with small surface asperities.

## 3.5 Conclusions

Nonlinear Rayleigh wave measurements aimed at correlating with nonlinear material response are complicated by sensing system nonlinearities and surface roughness. The sensing system nonlinearities are quantified by obtaining signals at four generation stages: the output of the amplifier, the surface of the transducer, on the acrylic wedge, and the surface of the specimen. Wave mixing experiments enable material nonlinearities to be received at frequencies free from sensing system nonlinearities only if separate transducers are used to generate the waves that mix only in the waveguide.

The effects of surface roughness on the nonlinearity (distortion) of Rayleigh waves that are self-interacting or mutually interacting were investigated. The experimentally determined relative nonlinearity parameter exhibits a frequency-dependent relationship with the surface roughness. The variation in the relative nonlinearity parameter for different surface roughness is not correctable through attenuation and needs to be investigated further to understand the physics associated with roughness increasing the wave distortion.

### 3.6 References

1. Staszewski, W.J. Structural Health Monitoring Using Guided Ultrasonic Waves. In *Advances in smart technologies in structural engineering*; Springer, 2004; pp. 117–162.

2. Hirsekorn, S. The scattering of ultrasonic waves by polycrystals. *J. Acoust. Soc. Am.* **1982**, *72*, 1021–1031, doi:10.1121/1.388233.

3. Badidi Bouda, A. Grain size influence on ultrasonic velocities and attenuation. *NDT E Int.* **2003**, *36*, 1–5, doi:10.1016/S0963-8695(02)00043-9.

4. Papadakis, E.P. Rayleigh and Stochastic Scattering of Ultrasonic Waves in Steel. *J. Appl. Phys.* **1963**, *34*, 265–269, doi:10.1063/1.1702596.

5. Moghanizadeh, A.; Farzi, A. Effect of heat treatment on an AISI 304 austenitic stainless steel evaluated by the ultrasonic attenuation coefficient. *Mater. Test.* **2016**, *58*, 448–452, doi:10.3139/120.110878.

6. Laux, D.; Cros, B.; Despaux, G.; Baron, D. Ultrasonic study of UO2: effects of porosity and grain size on ultrasonic attenuation and velocities. *J. Nucl. Mater.* **2002**, *300*, 192–197, doi:https://doi.org/10.1016/S0022-3115(01)00747-4.

7. Tardy, F.; Nadal, M.H.; Gondard, C.; Paradis, L.; Guy, P.; Baboux, J.C. Microstructural Characterization of Materials by a Rayleigh Wave Analysis. In *Review of Progress in Quantitative*

*Nondestructive Evaluation*; Springer US: Boston, MA, 1997; pp. 1399–1405.

8. Wang, M.; Bu, Y.; Dai, Z.; Zeng, S. Characterization of Grain Size in 316L Stainless Steel Using the Attenuation of Rayleigh Wave Measured by Air-Coupled Transducer. *Materials (Basel).* **2021**, *14*, 1901, doi:10.3390/ma14081901.

9. Chakrapani, S.K.; Bond, L.J. Rayleigh Wave Nondestructive Evaluation for Defect Detection and Materials Characterization. In *Nondestructive Evaluation of Materials*; ASM International, 2018; Vol. 17, pp. 266–282.

10. Nagy, P.B. Fatigue damage assessment by nonlinear ultrasonic materials characterization. *Ultrasonics* **1998**, *36*, 375–381.

11. Walker, S. V.; Kim, J.Y.; Qu, J.; Jacobs, L.J. Fatigue damage evaluation in A36 steel using nonlinear Rayleigh surface waves. *NDT E Int.* **2012**, *48*, 10–15, doi:10.1016/j.ndteint.2012.02.002.

12. Liu, M.; Kim, J.Y.; Jacobs, L.; Qu, J. Experimental study of nonlinear Rayleigh wave propagation in shot-peened aluminum platesFeasibility of measuring residual stress. *NDT E Int.* **2011**, *44*, 67–74, doi:10.1016/j.ndteint.2010.09.008.

13. Thiele, S.; Kim, J.-Y.; Qu, J.; Jacobs, L.J. Air-coupled detection of nonlinear Rayleigh surface waves to assess material nonlinearity. *Ultrasonics* **2014**, *54*, 1470–1475, doi:10.1016/j.ultras.2014.04.020.

14. Matlack, K.H.; Bradley, H.A.; Thiele, S.; Kim, J.-Y.; Wall, J.J.; Jung, H.J.; Qu, J.; Jacobs, L.J. Nonlinear ultrasonic characterization of precipitation in 17-4PH stainless steel. *NDT E Int.* **2015**, *71*, 8–15, doi:10.1016/j.ndteint.2014.11.001.

15. Gutiérrez-Vargas, G.; Ruiz, A.; Kim, J.-Y.; Jacobs, L.J. Characterization of thermal embrittlement in 2507 super duplex stainless steel using nonlinear acoustic effects. *NDT E Int.* **2018**, *94*, 101–108, doi:10.1016/j.ndteint.2017.12.004.

16. Jun, J.; Seo, H.; Jhang, K.Y. Nondestructive evaluation of thermal aging in Al6061 alloy by measuring acoustic nonlinearity of laser-generated surface acoustic waves. *Metals (Basel).* **2020**, *10*, 38, doi:10.3390/met10010038.

17. Doerr, C.; Kim, J.Y.; Singh, P.; Wall, J.J.; Jacobs, L.J. Evaluation of sensitization in stainless steel 304 and 304L using nonlinear Rayleigh waves. *NDT E Int.* **2017**, *88*, 17–23, doi:10.1016/j.ndteint.2017.02.007.

18. Zeitvogel, D.T.; Matlack, K.H.; Kim, J.-Y.; Jacobs, L.J.; Singh, P.M.; Qu, J. Characterization of stress corrosion cracking in carbon steel using nonlinear Rayleigh surface waves. *NDT E Int.* **2014**, *62*, 144–152, doi:10.1016/j.ndteint.2013.12.005.

19. Ghafoor, I.; Tse, P.W.; Rostami, J.; Ng, K.-M. Non-Contact Inspection of Railhead via Laser-Generated Rayleigh Waves and an Enhanced Matching Pursuit to Assist Detection of Surface and Subsurface Defects. *Sensors* **2021**, *21*, 2994, doi:10.3390/s21092994.

20. Li, K.; Jing, S.; Yu, J.; Zhang, B. Complex Rayleigh Waves in Nonhomogeneous Magneto-Electro-Elastic Half-Spaces. *Materials (Basel).* **2021**, *14*, 1011, doi:10.3390/ma14041011.

21. Song, H.; Hong, J.; Choi, H.; Min, J. Concrete Delamination Depth Estimation Using a Noncontact MEMS Ultrasonic Sensor Array and an Optimization Approach. *Appl. Sci.* **2021**, *11*, 592, doi:10.3390/app11020592.

22. Li, H.; Pan, Q.; Zhang, X.; An, Z. An Approach to Size Sub-Wavelength Surface Crack Measurements Using Rayleigh Waves Based on Laser Ultrasounds. *Sensors* **2020**, *20*, 5077, doi:10.3390/s20185077.

23. Sarris, G.; Haslinger, S.G.; Huthwaite, P.; Nagy, P.B.; Lowe, M.J.S. Attenuation of Rayleigh waves due to surface roughness. *J. Acoust. Soc. Am.* **2021**, *149*, 4298–4308, doi:10.1121/10.0005271.

24. Krylov, V.; Smirnova, Z. Experimental study of the dispersion of a Rayleigh wave on a rough

surface. *Sov. physics. Acoust.* **1990**, *36*, 583–585.

25. Maradudin, A.A.; Mills, D.L. The attenuation of Rayleigh surface waves by surface roughness. *Ann. Phys. (N. Y).* **1976**, *100*, 262–309.

26. Huang, X.; Maradudin, A.A. Propagation of surface acoustic waves across random gratings. *Phys. Rev. B* **1987**, *36*, 7827–7839, doi:10.1103/PhysRevB.36.7827.

27. Eguiluz, A.G.; Maradudin, A.A. Frequency shift and attenuation length of a Rayleigh wave due to surface roughness. *Phys. Rev. B* **1983**, *28*, 728–747, doi:10.1103/PhysRevB.28.728.

28. Urazakov, E.I.; Fal'kovskii, L.A. Propagation of a Rayleigh wave along a rough surface. *Jetp* **1973**, *36*, 1214–1216.

29. Steg, R.G.; Klemens, P.G. Scattering of Rayleigh waves by surface defects. *J. Appl. Phys.* **1974**, *45*, 23–29, doi:10.1063/1.1662964.

30. De Billy, M.; Quentin, G.; Baron, E. Attenuation measurements of an ultrasonic Rayleigh wave propagating along rough surfaces. *J. Appl. Phys.* **1987**, *61*, 2140–2145, doi:10.1063/1.337972.

31. Sinclair, R. Velocity Dispersion of Rayleigh Waves Propagating along Rough Surfaces. *J. Acoust. Soc. Am.* **1971**, *50*, 841–845, doi:10.1121/1.1912708.

32. Ruiz, A.; Nagy, P.B. Laser-ultrasonic surface wave dispersion measurements on surface-treated metals. *Ultrasonics* **2004**, *42*, 665–669, doi:10.1016/j.ultras.2004.01.045.

33. Ruiz, A.; Nagy, P.B. SAW dispersion measurements for ultrasonic characterization of surface-treated metals. *Instr. Meas. Metrol. 3* **2003**, *59*.

34. Cantrell, J. Fundamentals and Applications of Nonlinear Ultrasonic Nondestructive Evaluation. In *Ultrasonic Nondestructive Evaluation*; CRC Press, 2003.

35. Nečas, D.; Klapetek, P. Gwyddion: an open-source software for SPM data analysis. *Open Phys.* **2012**, *10*, doi:10.2478/s11534-011-0096-2.

36. Deltombe, R.; Kubiak, K.J.; Bigerelle, M. How to select the most relevant 3D roughness parameters of a surface. *Scanning* **2014**, *36*, 150–160, doi:10.1002/sca.21113.

37. Wang, Z.; Cui, X.; Ma, H.; Kang, Y.; Deng, Z. Effect of Surface Roughness on Ultrasonic Testing of Back-Surface Micro-Cracks. *Appl. Sci.* **2018**, *8*, 1233, doi:10.3390/app8081233.

38. Torello, D.; Thiele, S.; Matlack, K.H.; Kim, J.-Y.; Qu, J.; Jacobs, L.J. Diffraction, attenuation, and source corrections for nonlinear Rayleigh wave ultrasonic measurements. *Ultrasonics* **2015**, *56*, 417–426, doi:10.1016/j.ultras.2014.09.008.

39. Jhang, K.-Y.; Lissenden, C.J.; Solodov, I.; Ohara, Y.; Gusev, V. *Measurement of Nonlinear Ultrasonic Characteristics*; Springer Series in Measurement Science and Technology; Springer Singapore: Singapore, 2020; ISBN 978-981-15-1460-9.

40. Kundu, T. *Ultrasonic Nondestructive Evaluation*; CRC Press, 2003; ISBN 9780203501962.

41. Hikata, A.; Elbaum, C. Generation of Ultrasonic Second and Third Harmonics Due to Dislocations. I. *Phys. Rev.* **1966**, *144*, 469–477, doi:10.1103/PhysRev.144.469.

**Chapter 4**

# ULTRASONIC RAYLEIGH WAVE INTERROGATION OF DED Ti-6Al-4V HAVING A ROUGH SURFACE[1]

In-situ monitoring techniques for additive manufacturing are in high demand to help produce reliable parts. The structural integrity of these parts depends on both the presence of flaws and their microstructure. Ultrasonic Rayleigh waves have the potential to identify flaws and assess the local microstructure during directed energy deposition (DED) additive manufacturing processes, but the scattering associated with the surface roughness degrades the ultrasonic signal and must be understood to extract useful information. Herein, the microstructures and surface profiles of DED and wrought Ti-6Al-4V are compared to provide context for measured Rayleigh wave speeds and second harmonic generation. The Rayleigh wave speed and second harmonic generation for DED and wrought Ti-6Al-4V materials having comparable surface roughness are significantly different. The wave speed measured in DED material is 3% slower than in wrought material, and the relative nonlinearity parameter, commonly used to characterize second harmonic generation, is 3.5-6.0 times higher for polished surfaces. Wave speed and second harmonic generation measurements are also made along the hatch and across the hatch for both as-built and glazed DED surfaces. Based on our results, we conclude that in-situ Rayleigh wave linear and nonlinear measurements are possible; although we acknowledge that in-situ angle-beam transducer generation would be challenging, and thus we will investigate pulsed laser generation in future work.

[1] This chapter is largely based on the manuscript:
C. Bakre, A.R. Nassar, E.W. Reutzel, C. Lissenden, Ultrasonic Rayleigh wave interrogation of DED Ti-6Al-4V having a rough surface, J. Nondestruct. Eval. Diagnostics Progn. Eng. Syst. (2022) 1–31. https://doi.org/10.1115/1.4054539.

## 4.1 Introduction

Additive manufacturing (AM) has emerged as a transformative technology [1]. However, the adoption of AM to produce critical, load-bearing components is limited due to concerns about the repeatability of qualified parts [2,3]. Common flaws (i.e., material discontinuities) observed in directed energy deposition (DED) AM and powder-bed fusion (PBF) AM include gas porosity and lack-of-fusion [4,5]. Entrapment of gas during the melting process, melt pool instabilities, the presence of trapped gas in the powder particles are the leading causes of gas porosity, resulting in spherical discontinuities within the solidified material [6,7]. In contrast, irregularly-shaped lack-of-fusion flaws result from suboptimal process parameters, such as hatch spacing, speed, and power [8–10], interactions with spatter [11], or localized instabilities [12]. In either case, these flaws can be detrimental for the AM parts as they can act as crack initiation sites or reduce the load-bearing capacity [13,14]. Along with gas porosity and lack-of-fusion flaws, the microstructure plays a role in determining strength and fracture properties [15]. Many variables, such as suboptimal process parameter selection, fluctuations in the energy source, and variations in the feedstock material, can lead to an undesired or nonuniform microstructure of the AM part [16].

Traditional post-build inspection techniques, like X-ray computed tomography, can be used to identify flaws, but are time-consuming and limited by the scale of production [17]. Metallographic techniques can be used to assess microstructure, but they are destructive in nature. Also, the AM process is attractive for low-volume production and high product variants, rendering conventional statistical quality control methods inapplicable. In contrast, if in-situ process monitoring of AM can identify flaws and assess microstructure during the process, there is the potential to reduce variability and increase repeatability of AM parts by providing the opportunity to abort the build or perform inter-layer repair to produce a high quality part. Thus, in-situ process monitoring is essential for AM to attain its full potential.

A primary aim of in-process monitoring is the identification of flaws during, rather than after, manufacturing. Many researchers have reviewed in-process monitoring techniques for AM [18–21]. The typical strategies used for monitoring AM include monitoring the melt pool metrics [22,23], part temperature [24,25], layer build height [26–28], laser/e-beam parameters [25], and optical emissions [29] during processing. Vision-based techniques that rely on a high-speed camera, pyrometer, and infrared imaging for monitoring melt pools, can be inefficient in detecting interlayer defects [20]. Recently, in-situ ultrasonic testing techniques have emerged as a promising means to detect flaws and estimate mechanical properties [30].

The complex geometry and heterogeneous microstructure of AM parts can make the signal analysis of ultrasonic waves challenging [31]. Since AM parts are made in a layer-by-layer process, the use of Rayleigh waves to monitor the material as it is processed could prove beneficial. In particular, laser-based ultrasonics may offer a viable alternative for in-situ layer-wise ultrasonic testing of AM due to its non-contact nature. Here, we aim to explore the use of Rayleigh waves to interrogate surface and near-surface material during the DED build.

Nonlinear Rayleigh wave techniques could be highly effective for the process monitoring of AM. The sensitivity of nonlinear Rayleigh waves to variations in microstructural features such as dislocation density [32,33], presence of precipitates [34], and grain structure [35] has been well established in the literature. When a finite-amplitude Rayleigh wave propagates through a material, it undergoes distortion due to its interaction with the microstructural features, leading to the generation of higher order harmonic waves [36]. The nonlinear analysis of Rayleigh waves relies upon measuring the frequency-domain amplitudes of these waves at the primary and second harmonic frequencies in order to compute the relative nonlinearity parameter. However, surface roughness effects can complicate the implementation of nonlinear Rayleigh wave techniques for in-process monitoring of AM.

AM specimens are characterized by the presence of complex microstructure and high surface roughness. The complex microstructure is due to the excessively high solidification rates and the repeated heating and cooling cycles. The roughness in AM builds is mainly due to the hatch pattern, powder size, and the presence of partially melted powder on the surface. The surface roughness levels typically range from 50 – 100 μm for PBF builds and 150 – 200 μm for DED builds. Most of the proposed techniques in the literature for ultrasonic testing of AM use polished AM specimens [37–41]. Thus, for the in-situ laser ultrasonic testing of AM using Rayleigh waves, it is important to understand the effect of the complex microstructure and the high surface roughness of AM deposits on Rayleigh wave propagation.

The objective of this chapter is to show that Rayleigh wave distortion can provide useful information about DED-AM depositions having rough surfaces. This objective will be obtained through a sequence of experiments on Ti-6Al-4V specimens that:

- document differences in DED-AM and wrought microstructures;
- quantify surface roughness;
- demonstrate that wave speed and distortion measurements are possible on DED-AM surfaces having different roughness values;
- demonstrate that DED-AM material has slower Rayleigh wave speeds and causes more Rayleigh wave distortion than wrought material for comparable roughness values.

The materials and methods used for Ti-6Al-4V deposition and material characterization are described in the next section, which is followed by surface profilometry and metallography results. Next, the instrumentation and methods used for ultrasonic Rayleigh wave testing are described, followed by the linear (wave speed) and nonlinear (relative nonlinearity parameter) results. Context for the linear and nonlinear results are provided in the discussion section, which is followed by conclusions regarding the capability of ultrasonic Rayleigh waves to monitor Ti-6Al-4V DED-AM builds.

## 4.2 Materials and methods – Deposition and characterization

### 4.2.1 DED Ti-6Al-4V

The additively manufactured Ti-6Al-4V specimens are processed using the LENS MR-7 DED system (Optomec, Albuquerque, NM, USA). Spherical, ASTM Grade 23 Eli Ti-6Al-4V powder (Phelly

Materials Inc., Upper Saddle River, NJ, USA) is used for the deposition process with powder size ranging from 44 – 149 μm (-100/+325 mesh). The DED-AM system utilizes a laser-based energy source (IPG YLR-500-SM) to melt the powder delivered by four radially-symmetric nozzles. The deposition process is carried out in an Argon-filled chamber. The deposition head deposits Ti-6Al-4V material atop a Ti-6Al-4V baseplate that is clamped to the build platform mounted on a 3-axis stage. After each layer is deposited, the deposition head translates upwards by a fixed increment equivalent to the layer height (nominally 127 $\mu$m). Ten layers of material are deposited with a raster scan strategy in the 76 mm × 102 mm region on two baseplates having dimensions 102 mm × 152 mm × 6.4 mm. The DED process parameters used for the deposition are provided in Table 4-1. The hatch spacing between individual depositions is known to have a marked effect of the surface roughness [42–44].

Table **4-1**. Ti-6Al-4V DED-AM process parameters

| **Parameters** | **Values** |
|---|---|
| Scan speed | 10.58 mm/s |
| Laser power | 450 W |
| Hatch spacing | 0.9 mm |

A laser surface modification process, termed here as ‘glazing’, is applied to the top layer of one of the Ti-6Al-4V as-built specimens to improve Rayleigh wave reception. The process involves repeating the scan pattern on the uppermost surface using the same laser power but without powder. The laser beam follows the same tracks and remelts loose or partially melted powder particles on the surface. In the literature, the glazing process is also referred to as ‘surface remelting’ or ‘skin scanning’ and is a common practice to improve the surface finish [45–48]. Figure 4-1 shows the three Ti-6Al-4V specimens used in this investigation: as-built deposition, glazed deposition, and baseplate.

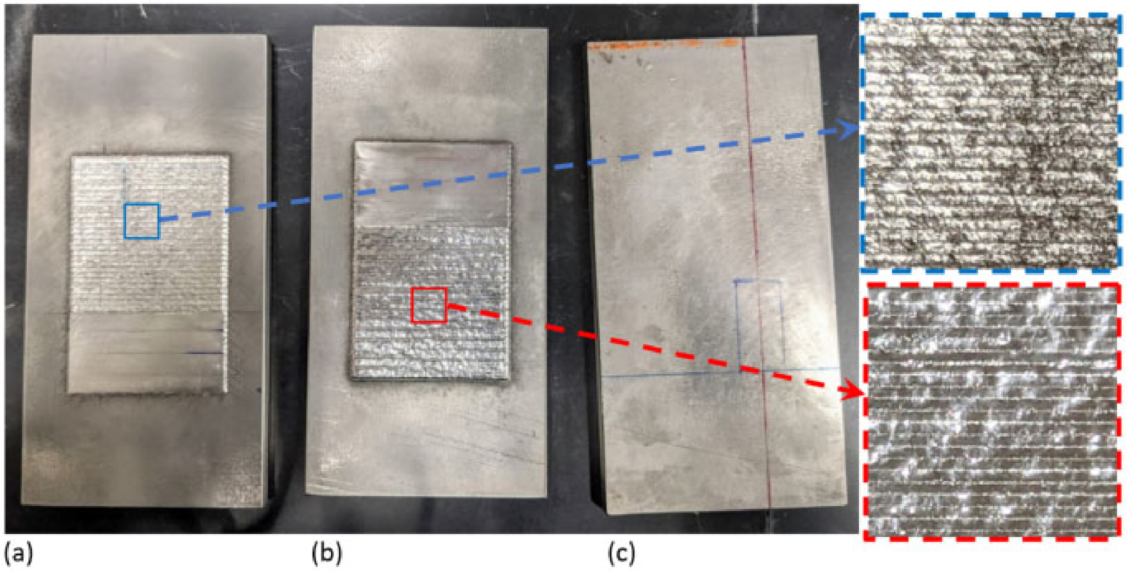


Figure **4-1:** Test setup for measurement of system nonlinearity: (a) Block diagram where solid and dashed lines represent electrical cables and optical fibers respectively, (b) Photograph of the laser head illuminating reflective tape on the transducer surface.

### 4.2.2 Surface characterization

A 76 mm × 38 mm region on the as-built and glazed depositions is end milled and then wet abraded using emery paper (grit # 320, 600, 800). We will refer to these regions as 'polished as-built' and 'polished glazed', respectively. The baseplate surface is also sequentially wet abraded using emery paper (grit # 320, 600, 800). The surface profiles for the polished baseplate, the as-built specimen, and the glazed specimen are obtained using optical profilometry (Nexview NX2, Zygo, Middlefield, CT, USA) and quantified using Gwyddion, which is an open-source software for statistical parametric mapping data analysis [49]. The specifications for the surface roughness measurements of the polished baseplate and the AM deposited surfaces are provided in Table 4-2.

Table **4-2:** Ti-6Al-4V surface roughness measurement specifications

| **Specimen** | **Objective** | **Optical resolution ($\mu$m)** | **Spatial sampling ($\mu$m)** | **Inspection region** |
|---|---|---|---|---|
| **Polished baseplate** | 10X (Mirau) | 0.95 | 0.82 | 0.82 $\mu$m × 0.82 $\mu$m |
| **As-built and Glazed AM** | 2.75X (Michelson) | 3.56 | 2.93 | 3 mm × 3 mm |

### 4.2.3 Metallography

After the ultrasonic testing is performed, the specimens are sectioned along and across the hatch directions in the region where the ultrasonic interrogation is carried out. The top face and the two side faces are ground and polished using standard metallographic techniques. The polished faces were etched using Kroll's reagent and imaged using an optical microscope (Nikon Epiphot 200, Nikon USA, Melville, NY, USA). This microstructure is characterized to aid in interpreting the ultrasonic results.

## 4.3 Results – Deposition and characterization

Figure 4-2 shows the 3D and 1D surface profiles for the three specimens. We provide the linear parameters (ISO 4287): $P_a$ (arithmetic average), $P_q$ (root mean square), and $P_t$ (peak-to-valley distance) in Table 4-3. For the DED-AM deposited surfaces, the 1D surface parameters are provided both across the hatch (i.e., normal to path of the deposition laser head) and along the hatch directions.

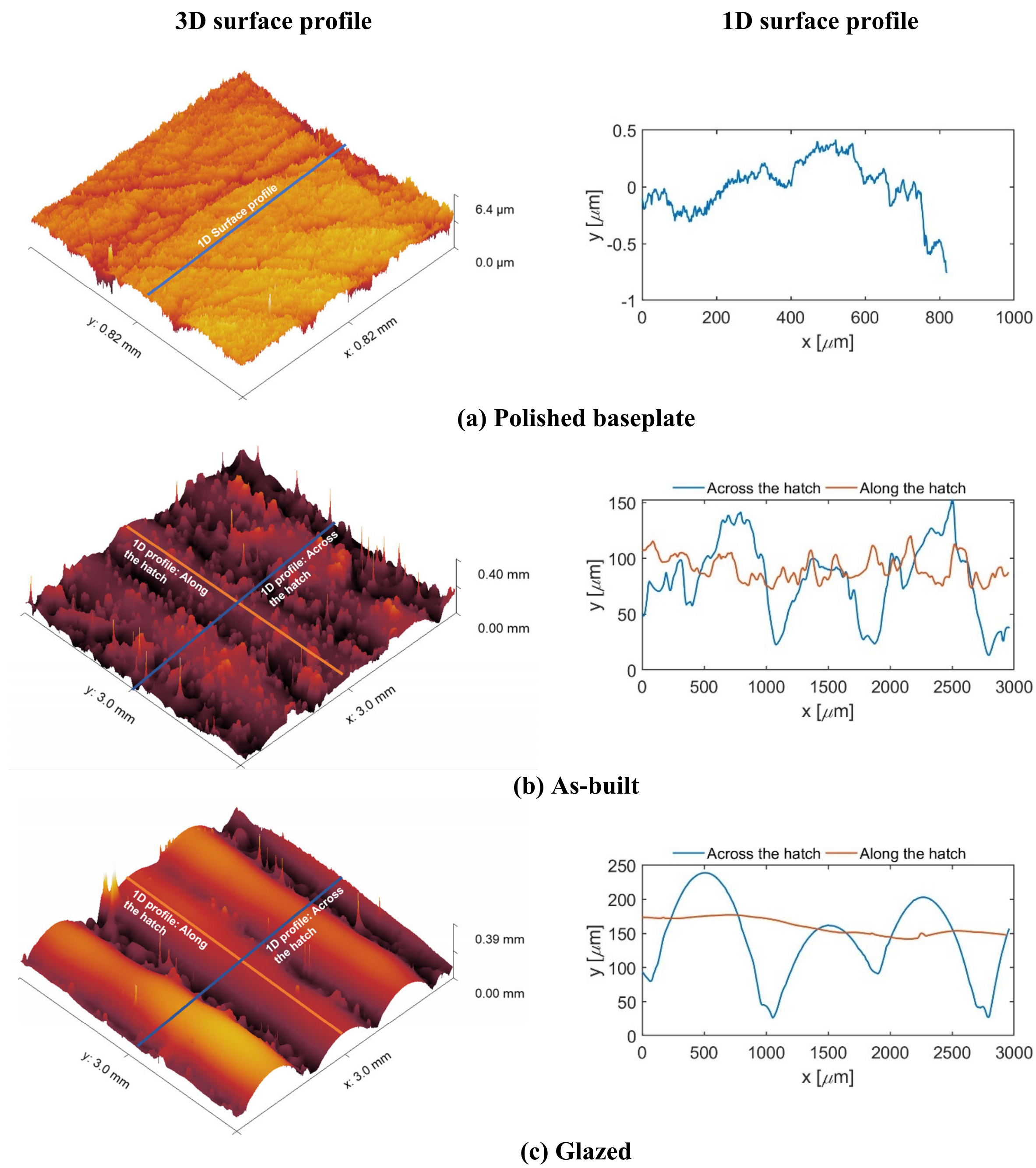


Figure **4-2:** 3D and 1D surface profiles for Ti-6Al-4V (a) polished baseplate, (b) as-built specimen, and (c) glazed specimen. Note that the y-axis scales vary.

Table **4-3:** Ti-6Al-4V surface roughness parameters (in μm)

| Specimen | $P_a$ | $P_q$ | $P_t$ |
|---|---|---|---|
| **Polished Baseplate** | 0.18 | 0.23 | 1.16 |
| **Glazed DED-AM Along the Hatch** | 10.97 | 11.82 | 35.50 |
| **As-Built DED-AM Along the Hatch** | 9.46 | 11.09 | 47.61 |
| **Glazed DED-AM Across the Hatch** | 47.43 | 57.30 | 212.00 |
| **As-Built DED-AM Across the Hatch** | 27.87 | 34.01 | 139.36 |

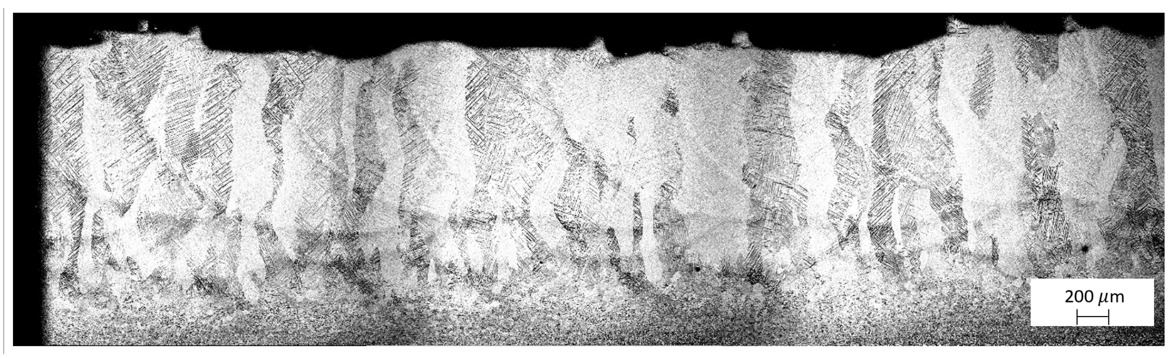


Figure **4-3:** Ti-6Al-4V optical micrograph (stitched): side view of the as-built specimen showing columnar grain structure consisting of large prior beta grains in the build direction and the surface roughness.

We note that the surface roughness parameters across the hatch are significantly higher than along the hatch for the as-built and glazed DED-AM specimens. Thus, Rayleigh waves traveling in the two orthogonal directions experience different surface-induced attenuation effects. Furthermore, it should be noted that while the glazing process reduces the high frequency surface roughness associated with the unmelted or partially melted powder on the surface resulting in lower roughness values, it does not reduce the low frequency waviness caused by the hatch pattern.

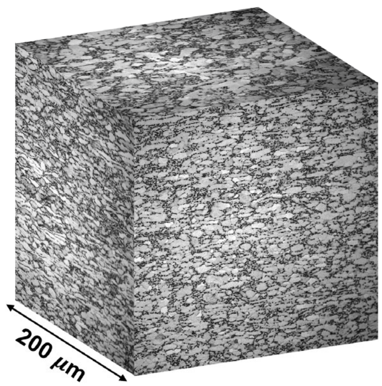


(a) Baseplate

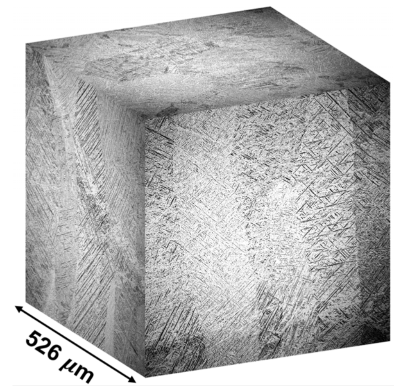


(b) As-built DED-AM

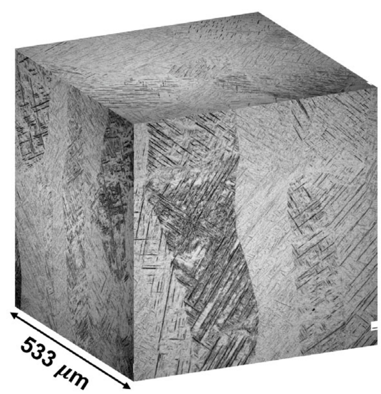


(c) Glazed DED-AM

Figure **4-4:** Pseudo 3D optical micrographs: (a) baseplate, (b) as-built DED-AM, and (c) glazed DED-AM specimens.

Figure 4-3 shows the polished and etched section across the hatch and Figure 4-4 shows pseudo-3D representations of the micrographs of the baseplate and the DED-AM specimens. The baseplate consists of a slightly elongated alpha+beta microstructure that is typical of a rolled Ti-6Al-4V plate. In contrast, the microstructure of DED-AM Ti-6Al-4V is characterized by large, columnar prior-beta grains, oriented along the build direction. Within these prior-beta grains lie fine Widmanstätten, or possible martensitic alpha microstructure containing narrow alpha platelets with inter-granular beta.

## 4.4 Instrumentation and methods – Ultrasonics Rayleigh waves

### 4.4.1 Angle beam transducer generation

A contact transducer (Benchmark series 113-232-591; Baker Hughes, Houston, TX, USA) having a central frequency of 5 MHz is coupled to a 70 degree Plexiglas wedge and actuated by a gated amplifier (RAM-5000 SNAP, Ritec Inc., Warwick, RI, USA) to generate Rayleigh waves. A toneburst with a 5 MHz central frequency and 10 $\mu s$ pulse width is applied. Figure 4-5 shows the experimental setup through a block diagram and a photograph. The Plexiglas wedge is coupled to the transducer and specimen with ultrasonic gel (Soundsafe, Sonotech, State College, PA, USA) and preloaded by a spring force. This angle-beam transducer is used to provide a wave packet having a high signal-to-noise ratio (SNR). A laser interferometer (AIR-1550-TWM, Intelligent Optical Systems Inc., Torrance, CA, USA) that is adaptive to the varying surface roughness and reflectivity, is used to measure the out-of-plane displacement from the specimen's surface. The laser interferometer provides two outputs, viz. an AC signal and a DC level. The AC signal contains the time-varying voltage proportional to the surface displacements, while the DC level provides a measure of the received light reflected from the surface. Thus, normalizing the AC signal by the DC level provides a means to compare the signals obtained from surfaces with different reflectivities. A detailed description of the operation of the laser interferometer can be found in [50]. The received signals are observed using an oscilloscope and recorded for post-processing.

Wave speed measurements are carried out by scanning the receiving laser along the specimen on the centerline of the wedge in the Rayleigh wave propagation direction. The measurements are obtained in the range of 10 mm to 28 mm from the wedge with 0.9 mm increments (i.e., at the hatch spacing). The individual tracks on the surface of the AM specimen give a waviness to the surface texture, as seen in Figures 4-2b and 4-2c. This waviness can reflect the beam away from the receiver, resulting in decreased light collection and the loss of signal information. Therefore, the incremental distance is chosen to be equal to the hatch spacing such that the reception laser beam is always focused approximately on the top of each track, thereby maximizing reflection back to the receiver and minimizing the loss of signal information.

For the wave speed calculations, pairs of measurement points from the linear scan are chosen such that the distance between them is 9 mm, and the difference in their time-of-flight is determined. Thus, the wave speed is calculated by dividing the propagation distance (9 mm) by the time-of-flight difference. Finally, the nonlinear measurements are performed by varying the output level of the gated amplifier from 75-95% in increments of 2% to increase the wave amplitude to determine the relative nonlinearity parameter. The propagation distance is fixed at 10 mm from the wedge for the nonlinear measurements.

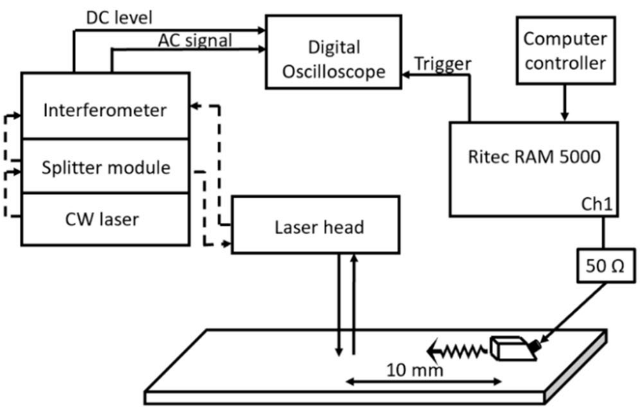


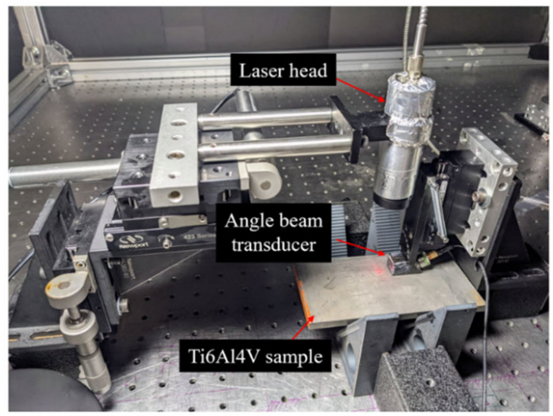


(a) (b)

Figure **4-5**: Rayleigh wave test setup: (a) Block diagram where solid and dashed lines represent electrical cables and optical fibers respectively, (b) Angle-beam transducer actuates Rayleigh waves, which are received by the laser head.

### 4.4.2 Pulsed laser generation

Narrowband Rayleigh waves are generated using a Q-switched Nd:YAG pulsed laser (Inlite III-10, Continuum, Milpitas, CA, USA) and a microlens array (Part # 86-843, Edmond Optics Inc., Barrington, NJ, USA) by obtaining a line-arrayed illumination pattern. The objective of using this alternative Rayleigh wave generating technique is to achieve a secondary confirmation for the wave speed measurements using a different strategy that could be less susceptible to the surface waviness because it is not based on time-of-flight measurement. Moreover, the noncontact nature of pulsed laser Rayleigh wave generation is more suitable for making in-situ measurements, as we intend to show in future publication.

The laser receiver is focused along the centerline at a distance of 10 mm from the closest edge of the microlens array to receive the Rayleigh waves. Figure 4-6 provides a block diagram and a photograph of the test setup. The 7 mm diameter generation laser beam is expanded using a 3X beam expander (Part # 35-099, Edmond Optics Inc., Barrington, NJ, USA) and then reflected using a mirror (Part #38-900, Edmond Optics Inc., Barrington, NJ, USA) onto the microlens array. The pitch of the microlens array is 500 $\mu$m. The laser generates incident energy of 270 mJ per pulse. We note that the laser generation caused subtle discoloration of the surface due to surface ablation. The Rayleigh wave signals are obtained for the baseplate and the as-built specimen with waves propagating across the hatch direction. The peak primary frequencies for the two specimens are compared from the frequency spectrum of the received signals.

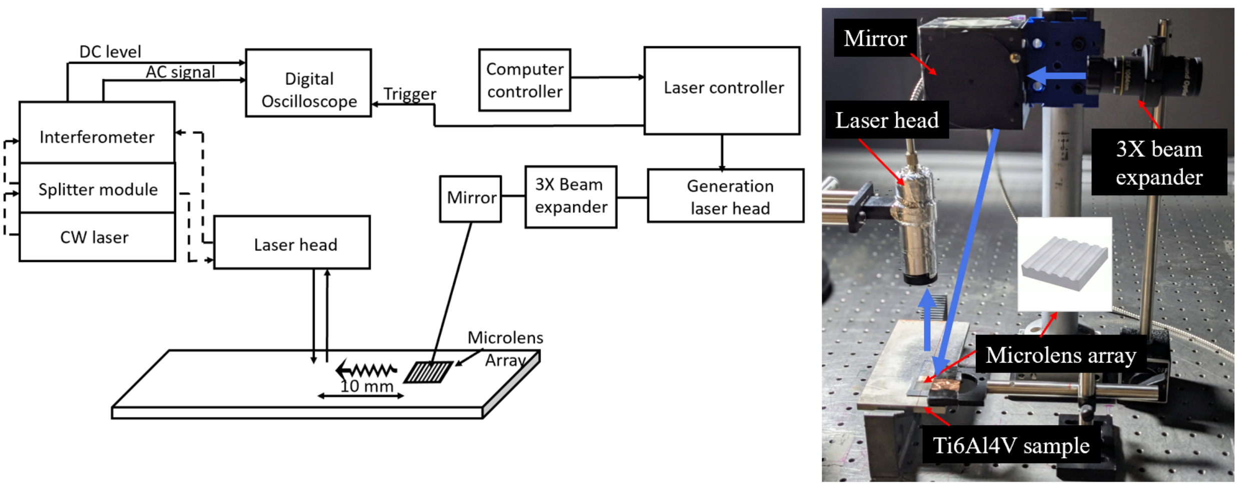


(a) (b)

Figure **4-6**: Laser ultrasonic test setup to generate and receive narrowband Rayleigh waves using a microlens array: (a) block diagram (b) photograph.

### 4.4.3 Signal processing

We synchronously averaged 1024 signals from the laser interferometer and then recorded them using an oscilloscope (InfiniiVision MSOX3024T, Keysight, Santa Rosa, CA, USA). The AC signals are normalized with respect to the DC level. A Hanning window is applied to the signal before computing the spectrum. The sampling frequency of the time record is 308 MHz. Zero-padding is used to improve the frequency resolution, and a discrete Fourier transform is achieved using the Fast Fourier Transform (FFT) function in Matlab [51]. The output of the Matlab FFT function is scaled by the time increment ($3.25 \times 10^{-9}$ s) to obtain the linear spectrum.

## 4.5 Results – Ultrasonics Rayleigh waves

### 4.5.1 Wave speed measurements

Linear ultrasonics results are given in Figure 4-7, which shows the Rayleigh wave speeds obtained from different points along the linear scan, and in Figure 4-8, which shows a bar chart of the mean wave speeds and error bars representing the standard error. Since it is known that surface roughness affects Rayleigh wave speed [52–55], we start by comparing the results from polished surfaces in order to remove roughness effects from the comparison. The mean wave speed for the polished as-built and polished glazed specimens is 2.8-3.1% lower than for the baseplate, as shown in Figure 4-8. A plausible explanation for the wave speed reduction in the DED-AM specimens is the increased dislocation density associated with the DED-AM process, which is addressed in the Discussion section.

The surface roughness of as-built and glazed specimens leads to more variability in the wave speed results, as evident in Figures 4-7b, 4-7c, 4-7e, and 4-7f as well as the increased standard errors in Figure 4-8. The reduced surface roughness associated with the glazing process has no perceivable effect on the wave speed variability, implying that the waviness associated with the hatch pattern is a more important factor than is the roughness associated with partially melted powder. This explanation is supported, albeit somewhat weakly, by the mean wave speeds along the hatch being closer to the polished surface results than the mean waves speeds across the hatch. In this analysis we presume the material to be isotropic, but there could be some anisotropy, and this should be assessed in future work.

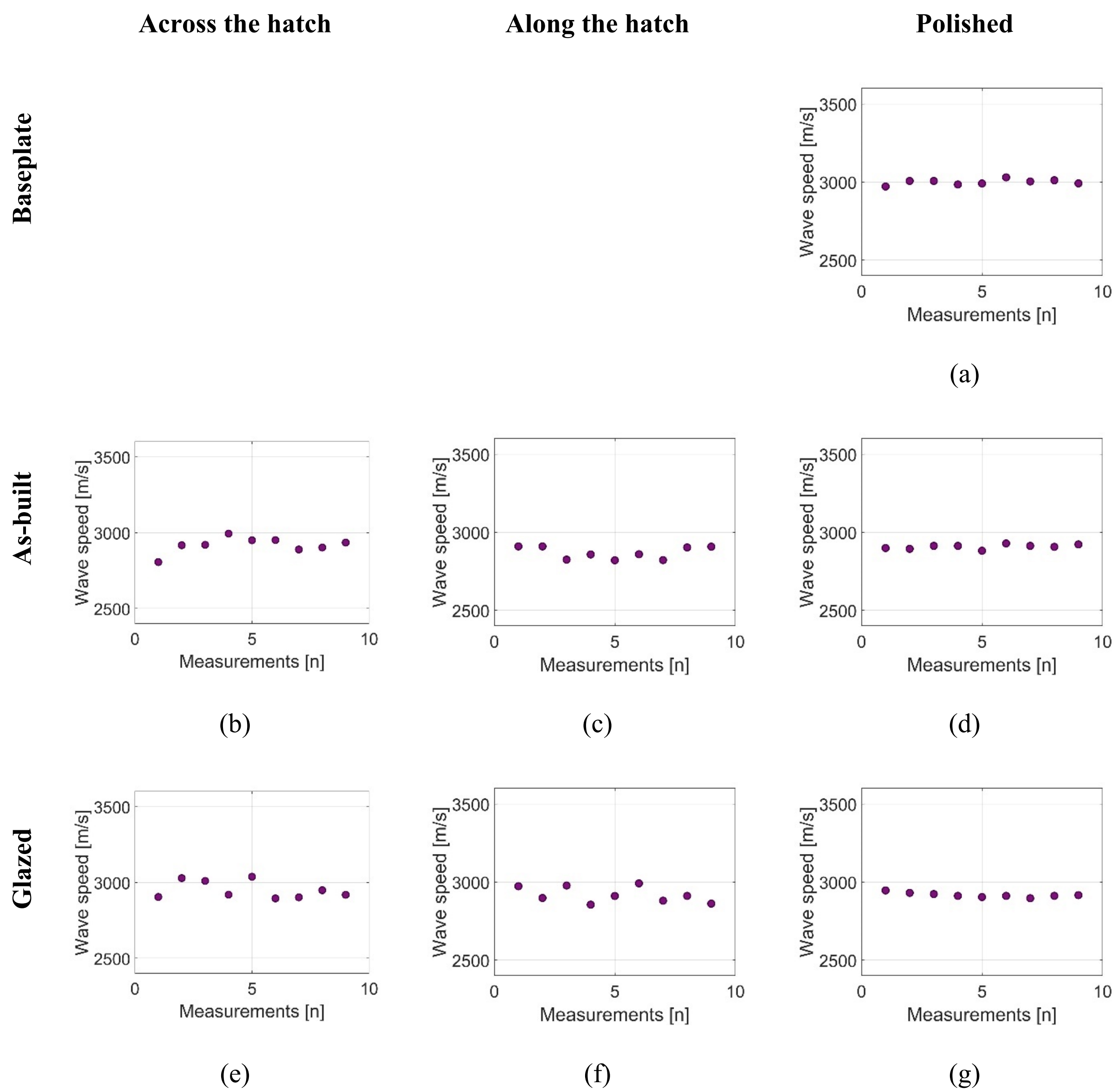


Figure **4-7:** Rayleigh wave velocity measurements from the linear scan: (a) polished baseplate, (b) as-built sample with waves traveling across the hatch, (c) as-built sample with waves traveling along the hatch, (d) polished region on the as-built sample with waves traveling along the hatch, (e) glazed sample with waves traveling across the hatch, (f) glazed sample with waves traveling along the hatch, and (g) polished region on the glazed sample with waves traveling along the hatch.

The difference in the mean speed of Rayleigh waves propagating across and along the hatch directions is small for the as-built and glazed AM specimens, as seen in Figure 4-8. This slight change in the speed could be due to anisotropy of the material as it is well known that the mechanical properties of AM Ti-6Al-4V depend on the build direction [56,57]. Finally, the error bars for the unpolished as-built and the unpolished glazed specimens are higher than the polished specimens (see Figure 4-8). Thus, we surmise that the surface roughness increases the scatter in the speed measurements.

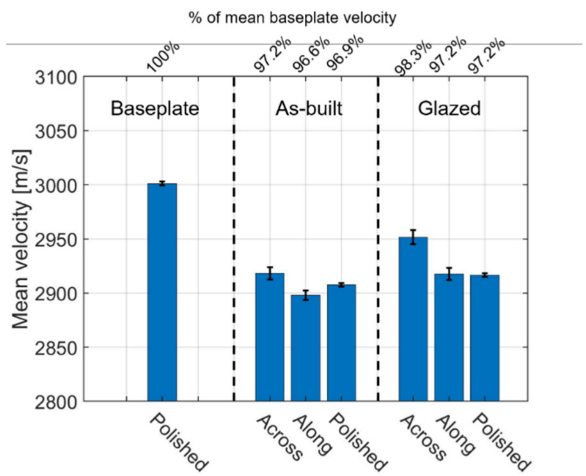


Figure **4-8**: Ti-6Al-4V Rayleigh wave speed mean and standard error from angle-beam transducer generation.

The wave speeds in Figures 4-7 and 4-8 are group velocities. If these are indeed Rayleigh waves, then they are nondispersive (surface roughness can cause dispersion) and the group velocity and phase velocity are the same. We can use the microlens array and pulsed laser generation to compute the phase velocity from

$$\boldsymbol{c = \lambda f} \tag{4-1}$$

where $c$ is the phase velocity, $\lambda$ is the wavelength, and $f$ is the frequency of the Rayleigh waves. Here, the wavelength of 509 $\mu$m is dictated by the pitch of microlens array and the oblique incidence of the laser beam. The frequency will be determined from the FFT of the received signal.

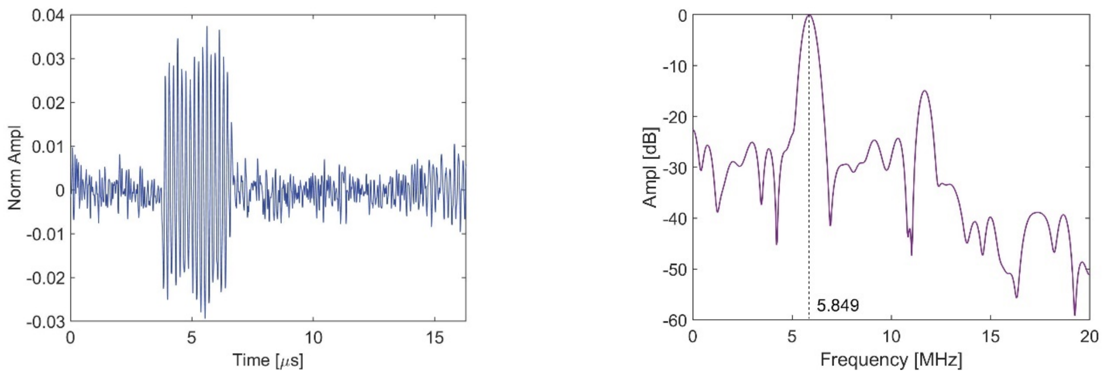


(a)

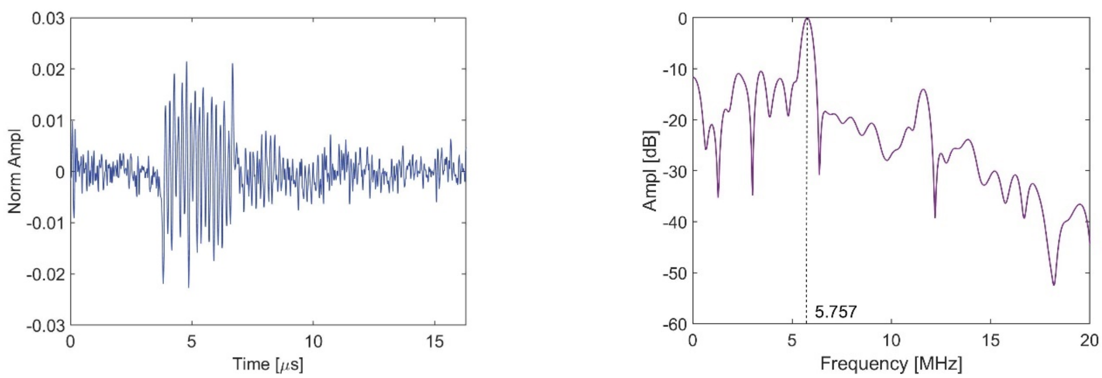


(b)

Figure **4-9**. Laser generated Rayleigh waves; A-scans (left) and frequency spectra (right): (a) polished baseplate (SNR = 8.06), (b) as-built specimen with waves travelling across the hatch (SNR = 6.86).

Figure 4-9 shows the A-scans and associated frequency spectra for narrowband laser-generated Rayleigh waves using the microlens array on the baseplate and the as-built specimen (with Rayleigh waves propagating across the hatch). The primary spectra peaks are marked in Figure 4-9. As per Equation 4-1, the phase wave speeds are 2977 and 2930 m/s for the baseplate and the as-built specimen (across the hatch) respectively. Whereas the group speeds obtained from the linear scans (Figure 4-8) are $3001 \pm 17$ and $2918 \pm 52$ m/s for the baseplate and the as-built specimen respectively. The differences in phase and group wave speeds for baseplate and as-built specimen are just 24 and 12 m/s respectively. Thus, the wave speed measurements for a fixed wavelength confirm there is a significant wave speed difference between the baseplate and as-built specimens.

### 4.5.2 Wave distortion

Material nonlinearity causes elastic waves to distort, thus making it possible for nonlinear waves to indicate the presence of microstructural features such as dislocation structures and precipitation [32–36]. Sample A-scans and frequency spectra for Rayleigh waves obtained on polished baseplate, as-built and glazed Ti-6Al-4V specimens with waves propagating along and across the hatch directions, and the polished regions of the as-built and glazed DED-AM specimens are shown in Figure 4-10 for angle-beam transducer generation. As described in the signal processing section, the received AC signal from the laser interferometer is normalized with respect to the DC signal in order to remove the effect of laser light scattering from the surface, which depends on the roughness. The wave packets received on polished specimens, both baseplate and DED-AM, are much more uniform than the wave packets received from unpolished surfaces. The same Hanning window size was used for each FFT, and the window size was selected such that the transient portions at the beginning and end of the wave packet could be excluded. The second harmonic peaks at 10 MHz are significantly higher for the DED-AM specimens than the baseplate indicating that Rayleigh waves experience much higher distortion for the DED-AM build than the wrought Ti-6Al-4V. It is likely that this effect can be attributed to the increased dislocation density in the DED-AM specimens, which is expected to be high. The high sensitivity of nonlinear Rayleigh waves to the variations in the dislocation density is well established both analytically and experimentally in the literature and will be addressed in the Discussion section.

The relative nonlinearity parameter defined by

$$\boldsymbol{\beta}' = \frac{\boldsymbol{A_2}}{\boldsymbol{A_1^2}} \tag{4-2}$$

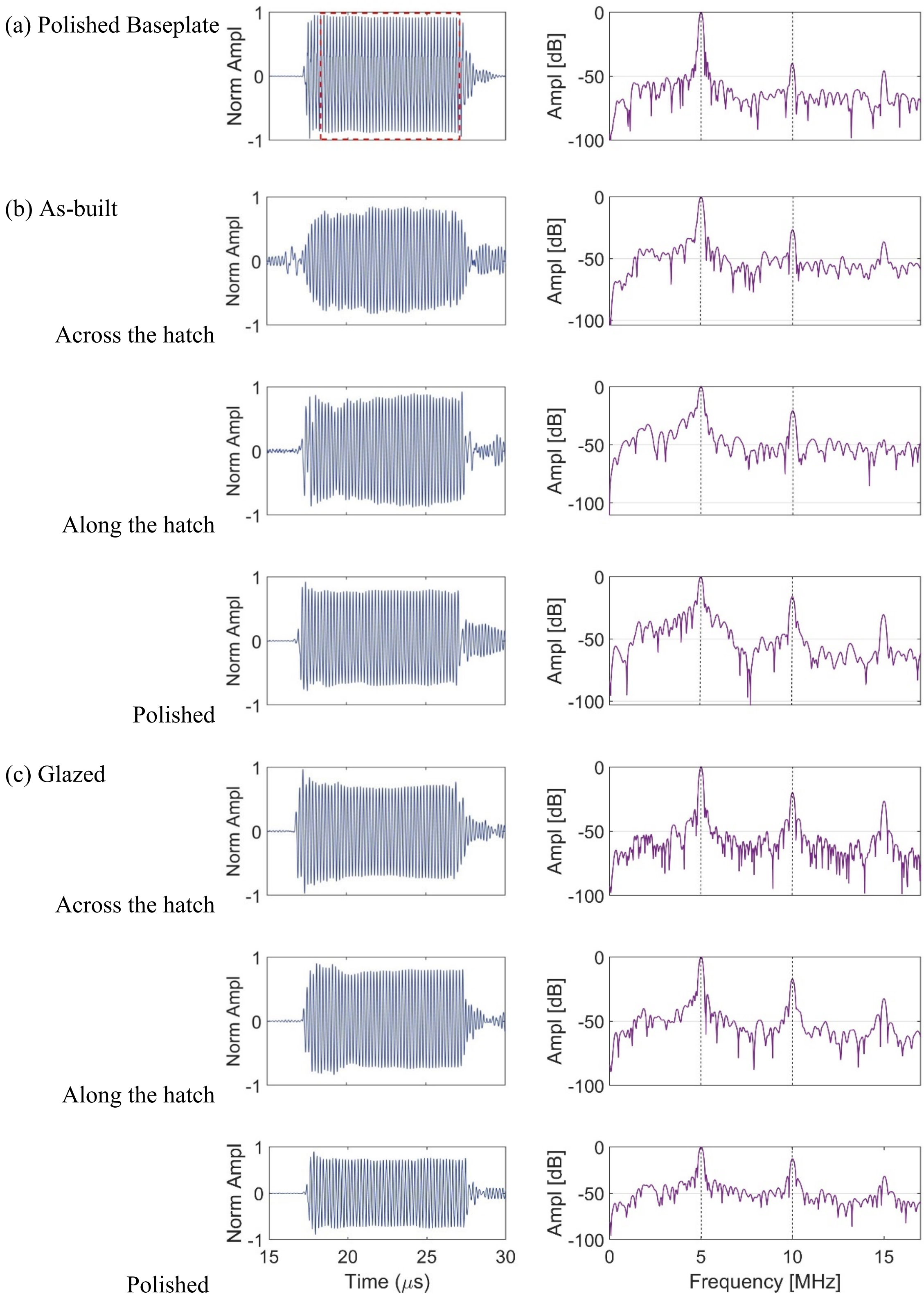


Figure **4-10**: A-scans (left) and spectra (right) for Rayleigh waves from angle-beam transducer generation at 90% output level: (a) polished baseplate, (b) as-built DED-AM specimen, (c) glazed.

is computed to characterize the distortion of Rayleigh waves for each case, where $\boldsymbol{A_1}$ and $\boldsymbol{A_2}$ are the spectral amplitudes at the primary and second harmonic frequencies respectively. Rather than compute $\boldsymbol{\beta'}$ from one output level of the gated amplifier (as could be done from Figure 4-10), a range of outputs (75-95%) is used and then $\boldsymbol{\beta'}$ is regressed to the data. Results from two trials are provided in Table 4-4. After Trial 1 data were acquired, the Plexiglas wedge was removed from the specimen, the couplant was replaced, and then the wedge was re-seated in nominally the same location on the specimen in order to acquire Trial 2 data. The measured $\boldsymbol{\beta'}$ values are tabulated in Table 4-4 for all the specimens and grouped by surface finish as polished, as-built, and glazed. The $\boldsymbol{R^2}$ values for the measured $\boldsymbol{\beta'}$ values range between 0.79-0.93 for polished surfaces and between 0.69-0.90 for unpolished surfaces.

Table **4-4:** Relative nonlinearity parameters and correction factors

| | **Specimen** | $\boldsymbol{\alpha_1}$ **[Np/m]** | $\boldsymbol{\alpha_2}$ **[Np/m]** | **Correction factor** | **Measured** $\boldsymbol{\beta'}$ **[Hz]** | $\boldsymbol{R^2}$ **for** $\boldsymbol{\beta'}$ | **Corrected** $\boldsymbol{\beta'}$ **[Hz]** |
|---|---|---|---|---|---|---|---|
| | | | | Polished | | | |
| | Baseplate | 16.2 | 30.6 | 0.99 | 38938 | 0.86 | 38589 |
| | | | | | 29650 | 0.84 | 29384 |
| | As-built | 27.7 | 58.1 | 1.01 | 139540 | 0.86 | 141432 |
| | | | | | 118746 | 0.79 | 120356 |
| | Glazed | 35.4 | 61.2 | 0.95 | 206743 | 0.93 | 196979 |
| | | | | | 190525 | 0.88 | 181527 |
| | | | | Unpolished | | | |
| As-built | Across the hatch | 43.8 | 162.2 | 1.42 | 65026 | 0.72 | 922567 |
| | | | | | 79520 | 0.73 | 112835 |
| | Along the hatch | 60.3 | 105.8 | 0.93 | 97899 | 0.86 | 90834 |
| | | | | | 95162 | 0.79 | 88294 |
| Glazed | Across the hatch | 56.8 | 193.7 | 1.45 | 89463 | 0.70 | 130026 |
| | | | | | 112054 | 0.69 | 162859 |
| | Along the hatch | 62.2 | 128.9 | 1.02 | 121258 | 0.88 | 124007 |
| | | | | | 152551 | 0.90 | 156009 |

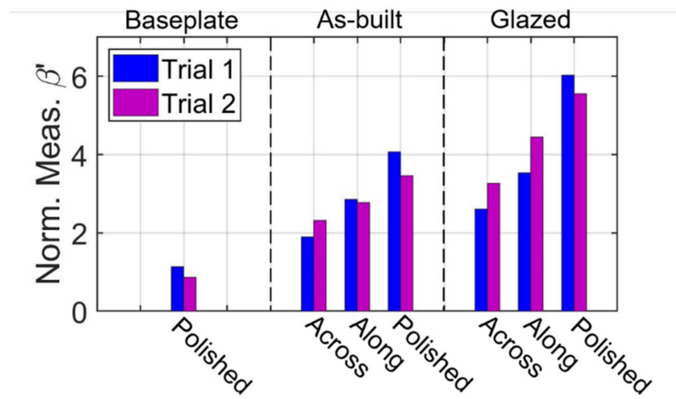


(a)

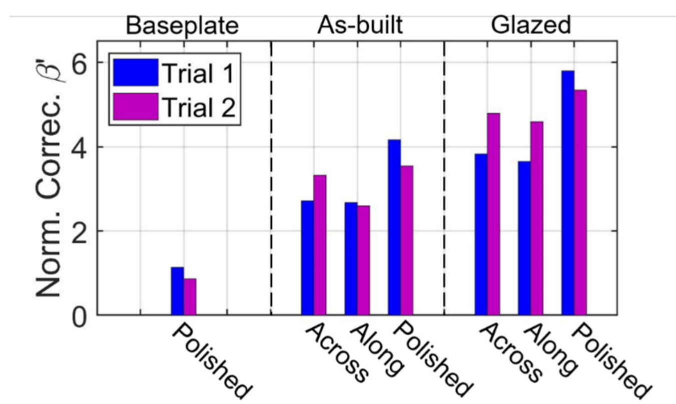


(b)

Figure **4-11:** Normalized relative nonlinearity parameters for baseplate, as-built, and glazed specimens for angle-beam transducer generation: (a) Measured, (b) Attenuation-corrected.

The regressed $\boldsymbol{\beta'}$ values normalized with respect to the average of the two trials on the baseplate are shown in Figure 4-11a. First and foremost we compare the measured $\boldsymbol{\beta'}$ values for the polished surfaces. For the polished as-built specimens the values are 3.5 and 4.0 times larger than the baseplate and for the polished glazed specimens the values are 5.6 and 6.0 times larger than the baseplate. Thus, given the same surface finish the relative nonlinearity parameter is 3.5-6.0 times larger for DED-AM specimens than for the baseplate. The reason for the difference between $\boldsymbol{\beta'}$ values for polished as-built and glazed specimens is more likely to be due to specimen-to-specimen variation than the glazing process because we would expect that the surface effects of glazing would have been end-milled off during the surface polishing operation. Even with the variation between as-built and glazed specimens the difference between DED-AM specimens and the baseplate is substantial.

The Rayleigh waves propagating ‘across the hatch’ experience much more roughness/waviness than do waves propagating ‘along the hatch’ (see Figure 4-2). The $\boldsymbol{\beta'}$ values in Figure 4-11a increase from ‘across the hatch’ to ‘along the hatch’ to ‘polished’, which corresponds to decreasing surface roughness. Knowing that surface roughness increases attenuation and that attenuation masks second harmonic generation [50], we apply a correction to account for attenuation in the measured $\boldsymbol{\beta'}$,

$$\boldsymbol{\beta'}_{corrected} = \boldsymbol{\beta'}_{meas} \frac{\boldsymbol{x(\alpha_2 - 2\alpha_1)}}{\mathbf{1 - exp}[-\boldsymbol{x(\alpha_2 - 2\alpha_1)}]} \tag{4-3}$$

where $\boldsymbol{\beta'}_{corrected}$ is the attenuation-corrected relative nonlinearity parameter, $\boldsymbol{\beta'}_{meas}$ is the measured relative nonlinearity parameter, $\boldsymbol{\alpha_1}$ and $\boldsymbol{\alpha_2}$ are the attenuation coefficients at the primary frequency and second harmonic frequency respectively, and $\boldsymbol{x}$ is the wave propagation distance. This correction has been used by Hikata and Elbaum [58], Cantrell [59], Matlack [34], and Bakre and Lissenden [50].

The attenuation coefficients for each specimen are obtained from the linear scan described earlier. At each measurement point of the linear scan, spectral amplitudes at the primary and second harmonic frequencies are measured, and an exponential equation is fit to the propagation distance to estimate the attenuation coefficients $\boldsymbol{\alpha_1}$ and $\boldsymbol{\alpha_2}$, which are listed in Table 4-4. The $\boldsymbol{\beta'}_{meas}$ multiplier in Equation 4-3 is a correction factor and is also tabulated in Table 4-4. Since we expect $\boldsymbol{\alpha_2 > \alpha_1}$ due to the frequency dependence of attenuation, the correction factor should be greater than one. Only the correction factors for ‘across the hatch’ are significantly greater than one. Moreover, the correction factors for polished samples are ~1, indicating that attenuation along the polished surface is not an issue for the wave propagation distances considered. The attenuation corrected $\boldsymbol{\beta'}$ values are evaluated using Equation 4-3 for each specimen. The corrected $\boldsymbol{\beta'}$ values are listed in Table 4-4 and plotted in Figure 4-11b. The corrected $\boldsymbol{\beta'}$ values for 'across the hatch' are in much better agreement with 'along the hatch' values than the measured $\boldsymbol{\beta'}$ values. Recent results obtained from aluminum surfaces having variable roughness also exhibited different corrected $\boldsymbol{\beta'}$ values [50]. Thus, it appears that attenuation is not the only surface roughness related cause for variation in the relative nonlinearity parameter. However, it is clear from Figure 4-11b that the nonlinearity of the DED-AM specimens is considerably larger than the nonlinearity of the baseplate regardless of the surface condition. It seems reasonable to conclude that nonlinear ultrasonic Rayleigh wave measurements can provide useful comparative information about the DED-AM material from in-situ testing provided the surface roughnesses are comparable.

In summary, comparing Figures 4-8 and 4-11 indicates that the relative nonlinearity parameter is more sensitive to the material differences between wrought baseplate and DED-AM than is Rayleigh wave speed, but that there is also more scatter. Surface roughness effects increase the scatter in the wave speed measurements and $\boldsymbol{\beta'}$ is susceptible to surface roughness effects and requires the additional step of calculating the attenuation correction factor.

## 4.6 Discussions

### 4.6.1 Wave speed

According to [15,60,61], the high solidification rates of the Ti-6Al-4V DED-AM process result in nonequilibrium microstructures with high dislocation densities. Prasad and Kumar showed for steel that ultrasonic wave speeds decrease with increasing dislocation density [62]. Conversely, Vasudevan et al. reported an increase in the ultrasonic wave speed during annealing of cold-worked austenitic steel and attributed it to the decreased dislocation density [63]. Moreover, while elastic wave speeds are primarily dependent upon the material's composition through the chemical bonds, there is evidence that the microstructural features can affect the wave speed enough to be measureable [64–67].

Bulk ultrasonic wave speed is dictated by the elastic modulus, density, poisson's ratio of the material; in fact the wave speed increases as density decreases. Thus, if the DED-AM material has some porosity, then the wave speed would be higher than the wrought material. Therefore, the DED-AM material's lower wave speed should not be attributed to the porosity. Papadakis et al. reported this effect on SAE 4150 [66]. Karthik et al. also observed a decrease in the ultrasonic wave speed with increasing density for 17-P PH stainless steel PBF-AM specimens [68]. The ultrasonic wave speed is influenced by the microstructure through changes in the elastic modulus of the individual grains, the orientation of the grains by texture, and the secondary phases. A substructure (like the columnar prior beta grains) that strains the lattice or interrupts the continuity of the matrix reduces the elastic modulus and the speed of ultrasonic waves [67].

### 4.6.2 Wave distortion

As observed relative to Figure 4-10, the high sensitivity of nonlinear Rayleigh waves to the variations in the dislocation density is well established both analytically and experimentally in the literature. We cite two examples. Hikata et al. [69] presented a theoretical model and experimental evidence to show the increase in the second harmonic generation due to increasing dislocation density. Kim et al. [70] demonstrated early-stage evaluation of fatigue damage using the distortion of ultrasonic waves caused by increasing dislocation density.

Additionally, the DED-AM Ti-6Al-4V contains columnar prior-$\beta$-grains with lengths of several millimeters, spanning multiple DED layers along the build direction, evident in the micrograph shown in Figure 4-3. The large prior-$\beta$-grains have crystalline spacing that differ from that of the matrix, which results in a lattice mismatch and lattice distortions. The lattice mismatch creates local strain field in the matrix and distorts the propagating Rayleigh waves leading to the generation of higher harmonics [71]. Hence, higher second harmonic amplitudes are observed for the DED-AM specimens as seen in Figures 4-10b-e and 4-11.

## 4.7 Conclusions

Ti-6Al-4V processed by directed energy deposition (DED-AM) has a much different microstructure than wrought material. Although dislocation structures were not imaged herein, DED-AM is believed to have significantly higher dislocation density than wrought. The ultrasonic Rayleigh wave results presented herein show that the relative nonlinearity parameter is markedly higher (i.e., 3.5-6.0 times) for DED-AM Ti-6Al-4V than for wrought Ti-6Al-4V and the wave speed is measurably less (i.e., ~3%). Thus, linear and nonlinear Rayleigh wave measurements have potential to provide beneficial information about DED-AM Ti-6Al-4V via process monitoring. However, the above-mentioned results are for polished surfaces, while in-situ DED-AM surfaces have substantial roughness that affects the Rayleigh wave propagation. The comparable results on rough surfaces display more scatter, but still provide useful information about the material nonlinearity for as-built and glazed surfaces both 'across the hatch' and 'along the hatch'. Attenuation from 'across the hatch' results was reasonably well corrected by a standard equation. These results were obtained using an angle-beam transducer, which is probably not a viable option for process monitoring inside the DED chamber. Thus, ongoing research is investigating narrowband Rayleigh wave generation with a pulsed laser and a line-arrayed beam pattern provided by a slit mask or a microlens array.

## 4.8 References


1. Brandt, M. *Laser Additive Manufacturing*; Elsevier, 2017; ISBN 9780081004333.
2. Tofail, S.A.M.; Koumoulos, E.P.; Bandyopadhyay, A.; Bose, S.; O'Donoghue, L.; Charitidis, C. Additive manufacturing: scientific and technological challenges, market uptake and opportunities. *Mater. Today* **2018**, *21*, 22–37, doi:10.1016/j.mattod.2017.07.001.
3. Kim, H.; Lin, Y.; Tseng, T.-L.B. A review on quality control in additive manufacturing. *Rapid Prototyp. J.* **2018**, *24*, 645–669, doi:10.1108/RPJ-03-2017-0048.
4. Brennan, M.C.; Keist, J.S.; Palmer, T.A. Defects in Metal Additive Manufacturing Processes. *J.*

*Mater. Eng. Perform.* **2021**, *30*, 4808–4818, doi:10.1007/s11665-021-05919-6.

5. Snow, Z.; Nassar, A.R.; Reutzel, E.W. Invited Review Article: Review of the formation and impact of flaws in powder bed fusion additive manufacturing. *Addit. Manuf.* **2020**, *36*, 101457, doi:10.1016/j.addma.2020.101457.

6. Sames, W.J.; List, F.A.; Pannala, S.; Dehoff, R.R.; Babu, S.S. The metallurgy and processing science of metal additive manufacturing. *Int. Mater. Rev.* **2016**, *61*, 315–360, doi:10.1080/09506608.2015.1116649.

7. TREVISAN, R.E.; SCHWEMMER, D.D.; OLSON, D.L. The Fundamentals of Weld Metal Pore Formation. In; 1990; pp. 79–115.

8. Khanzadeh, M.; Chowdhury, S.; Tschopp, M.A.; Doude, H.R.; Marufuzzaman, M.; Bian, L. In-situ monitoring of melt pool images for porosity prediction in directed energy deposition processes. *IISE Trans.* **2019**, *51*, 437–455, doi:10.1080/24725854.2017.1417656.

9. Vilaro, T.; Colin, C.; Bartout, J.D. As-Fabricated and Heat-Treated Microstructures of the Ti-6Al-4V Alloy Processed by Selective Laser Melting. *Metall. Mater. Trans. A* **2011**, *42*, 3190–3199, doi:10.1007/s11661-011-0731-y.

10. Kim, F.H.; Moylan, S.P. *Literature review of metal additive manufacturing defects*; Gaithersburg, MD, 2018;

11. Zekovic, S.; Dwivedi, R.; Kovacevic, R. Numerical simulation and experimental investigation of gas–powder flow from radially symmetrical nozzles in laser-based direct metal deposition. *Int. J. Mach. Tools Manuf.* **2007**, *47*, 112–123, doi:10.1016/j.ijmachtools.2006.02.004.

12. Stutzman, C.B.; Nassar, A.R.; Reutzel, E.W. Multi-sensor investigations of optical emissions and their relations to directed energy deposition processes and quality. *Addit. Manuf.* **2018**, *21*, 333–339, doi:10.1016/j.addma.2018.03.017.

13. DebRoy, T.; Wei, H.L.; Zuback, J.S.; Mukherjee, T.; Elmer, J.W.; Milewski, J.O.; Beese, A.M.; Wilson-Heid, A.; De, A.; Zhang, W. Additive manufacturing of metallic components – Process, structure and properties. *Prog. Mater. Sci.* **2018**, *92*, 112–224, doi:10.1016/j.pmatsci.2017.10.001.

14. Gorelik, M. Additive manufacturing in the context of structural integrity. *Int. J. Fatigue* **2017**, *94*, 168–177, doi:10.1016/j.ijfatigue.2016.07.005.

15. Galindo-Fernández, M.A.; Mumtaz, K.; Rivera-Díaz-del-Castillo, P.E.J.; Galindo-Nava, E.I.; Ghadbeigi, H. A microstructure sensitive model for deformation of Ti-6Al-4V describing Cast-and-Wrought and Additive Manufacturing morphologies. *Mater. Des.* **2018**, *160*, 350–362, doi:10.1016/j.matdes.2018.09.028.

16. Gong, H.; Rafi, K.; Gu, H.; Starr, T.; Stucker, B. Analysis of defect generation in Ti-6Al-4V parts made using powder bed fusion additive manufacturing processes. *Addit. Manuf.* **2014**, *1*, 87–98, doi:10.1016/j.addma.2014.08.002.

17. Malekipour, E.; El-Mounayri, H. Common defects and contributing parameters in powder bed fusion AM process and their classification for online monitoring and control: a review. *Int. J. Adv. Manuf. Technol.* **2018**, *95*, 527–550, doi:10.1007/s00170-017-1172-6.

18. Reutzel, E.W.; Nassar, A.R. A survey of sensing and control systems for machine and process monitoring of directed-energy, metal-based additive manufacturing. *Rapid Prototyp. J.* **2015**, *21*, 159–167, doi:10.1108/RPJ-12-2014-0177.

19. Boddu, M.R.; Landers, R.G.; Liou, F.W. Control of laser cladding for rapid prototyping--A review. In Proceedings of the 2001 International Solid Freeform Fabrication Symposium; 2001.

20. Everton, S.K.; Hirsch, M.; Stravroulakis, P.; Leach, R.K.; Clare, A.T. Review of in-situ process monitoring and in-situ metrology for metal additive manufacturing. *Mater. Des.* **2016**, *95*, 431–445, doi:10.1016/j.matdes.2016.01.099.

21. Tapia, G.; Elwany, A. A Review on Process Monitoring and Control in Metal-Based Additive

Manufacturing. *J. Manuf. Sci. Eng.* **2014**, *136*, doi:10.1115/1.4028540.

22. Bi, G.; Schürmann, B.; Gasser, A.; Wissenbach, K.; Poprawe, R. Development and qualification of a novel laser-cladding head with integrated sensors. *Int. J. Mach. Tools Manuf.* **2007**, *47*, 555–561, doi:10.1016/j.ijmachtools.2006.05.010.

23. Hofman, J.T.; Pathiraj, B.; van Dijk, J.; de Lange, D.F.; Meijer, J. A camera based feedback control strategy for the laser cladding process. *J. Mater. Process. Technol.* **2012**, *212*, 2455–2462, doi:10.1016/j.jmatprotec.2012.06.027.

24. Bi, G.; Gasser, A.; Wissenbach, K.; Drenker, A.; Poprawe, R. Identification and qualification of temperature signal for monitoring and control in laser cladding. *Opt. Lasers Eng.* **2006**, *44*, 1348–1359, doi:10.1016/J.OPTLASENG.2006.01.009.

25. Song, L.; Mazumder, J. Feedback control of melt pool temperature during laser cladding process. *IEEE Trans. Control Syst. Technol.* **2011**, *19*, 1349–1356, doi:10.1109/TCST.2010.2093901.

26. Fathi, A.; Khajepour, A.; Toyserkani, E.; Durali, M. Clad height control in laser solid freeform fabrication using a feedforward PID controller. *Int. J. Adv. Manuf. Technol.* **2007**, *35*, 280–292, doi:10.1007/s00170-006-0721-1.

27. Zeinali, M.; Khajepour, A. Height Control in Laser Cladding Using Adaptive Sliding Mode Technique: Theory and Experiment. *J. Manuf. Sci. Eng.* **2010**, *132*, doi:10.1115/1.4002023.

28. Heralić, A.; Christiansson, A.-K.; Lennartson, B. Height control of laser metal-wire deposition based on iterative learning control and 3D scanning. *Opt. Lasers Eng.* **2012**, *50*, 1230–1241, doi:10.1016/j.optlaseng.2012.03.016.

29. Song, L.; Mazumder, J. Real time Cr measurement using optical emission spectroscopy during direct metal deposition process. *IEEE Sens. J.* **2012**, *12*, 958–964, doi:10.1109/JSEN.2011.2162316.

30. Honarvar, F.; Varvani-Farahani, A. A review of ultrasonic testing applications in additive manufacturing: Defect evaluation, material characterization, and process control. *Ultrasonics* **2020**, *108*, 106227, doi:10.1016/j.ultras.2020.106227.

31. Rieder, H.; Spies, M.; Bamberg, J.; Henkel, B. On-and offline ultrasonic characterization of components built by SLM additive manufacturing. In Proceedings of the AIP Conference Proceedings; AIP Publishing LLC, 2016; Vol. 1706, p. 130002.

32. Nagy, P.B. Fatigue damage assessment by nonlinear ultrasonic materials characterization. *Ultrasonics* **1998**, *36*, 375–381.

33. Walker, S. V.; Kim, J.Y.; Qu, J.; Jacobs, L.J. Fatigue damage evaluation in A36 steel using nonlinear Rayleigh surface waves. *NDT E Int.* **2012**, *48*, 10–15, doi:10.1016/j.ndteint.2012.02.002.

34. Matlack, K.H.; Bradley, H.A.; Thiele, S.; Kim, J.-Y.; Wall, J.J.; Jung, H.J.; Qu, J.; Jacobs, L.J. Nonlinear ultrasonic characterization of precipitation in 17-4PH stainless steel. *NDT E Int.* **2015**, *71*, 8–15, doi:10.1016/j.ndteint.2014.11.001.

35. Doerr, C.; Kim, J.Y.; Singh, P.; Wall, J.J.; Jacobs, L.J. Evaluation of sensitization in stainless steel 304 and 304L using nonlinear Rayleigh waves. *NDT E Int.* **2017**, *88*, 17–23, doi:10.1016/j.ndteint.2017.02.007.

36. Jhang, K.-Y.; Lissenden, C.J.; Solodov, I.; Ohara, Y.; Gusev, V. *Measurement of Nonlinear Ultrasonic Characteristics*; Springer Series in Measurement Science and Technology; Springer Singapore: Singapore, 2020; ISBN 978-981-15-1460-9.

37. Millon, C.; Vanhoye, A.; Obaton, A.-F.; Penot, J.-D. Development of laser ultrasonics inspection for online monitoring of additive manufacturing. *Weld. World* **2018**, *62*, 653–661, doi:10.1007/s40194-018-0567-9.

38. Cerniglia, D.; Scafidi, M.; Pantano, A.; Rudlin, J. Inspection of additive-manufactured layered components. *Ultrasonics* **2015**, *62*, 292–298, doi:10.1016/j.ultras.2015.06.001.

39. Pieris, D.; Stratoudaki, T.; Javadi, Y.; Lukacs, P.; Catchpole-Smith, S.; Wilcox, P.D.; Clare, A.; Clark, M. Laser Induced Phased Arrays (LIPA) to detect nested features in Additively Manufactured Components. *Mater. Des.* **2019**, 108412, doi:10.1016/j.matdes.2019.108412.

40. Davis, G.; Nagarajah, R.; Palanisamy, S.; Rashid, R.A.R.; Rajagopal, P.; Balasubramaniam, K. Laser ultrasonic inspection of additive manufactured components. *Int. J. Adv. Manuf. Technol.* **2019**, *102*, 2571–2579, doi:10.1007/s00170-018-3046-y.

41. Smith, R.J.; Hirsch, M.; Patel, R.; Li, W.; Clare, A.T.; Sharples, S.D. Spatially resolved acoustic spectroscopy for selective laser melting. *J. Mater. Process. Technol.* **2016**, *236*, 93–102.

42. Dong, Z.; Liu, Y.; Wen, W.; Ge, J.; Liang, J. Effect of Hatch Spacing on Melt Pool and As-built Quality During Selective Laser Melting of Stainless Steel: Modeling and Experimental Approaches. *Materials (Basel).* **2018**, *12*, 50, doi:10.3390/ma12010050.

43. Maamoun, A.H.; Xue, Y.F.; Elbestawi, M.A.; Veldhuis, S.C. Effect of Selective Laser Melting Process Parameters on the Quality of Al Alloy Parts: Powder Characterization, Density, Surface Roughness, and Dimensional Accuracy. *Mater.* 2018, *11*.

44. Foster, S.; Carver, K.; Dinwiddie, R.; List, F.; Unocic, K.; Chaudhary, A.; Babu, S. Process-Defect-Structure-Property Correlations During Laser Powder Bed Fusion of Alloy 718: Role of In Situ and Ex Situ Characterizations. *Metall. Mater. Trans. A* **2018**, *49*, doi:10.1007/s11661-018-4870-2.

45. Yasa, E.; Kruth, J.-P. Application of laser re-melting on selective laser melting parts. *Adv. Prod. Eng. Manag.* **2011**, *6*, 259–270.

46. Alrbaey, K.; Wimpenny, D.; Tosi, R.; Manning, W.; Moroz, A. On Optimization of Surface Roughness of Selective Laser Melted Stainless Steel Parts: A Statistical Study. *J. Mater. Eng. Perform.* **2014**, *23*, 2139–2148, doi:10.1007/s11665-014-0993-9.

47. Rombouts, M.; Maes, G.; Hendrix, W.; Delarbre, E.; Motmans, F. Surface Finish after Laser Metal

Deposition. *Phys. Procedia* **2013**, *41*, 810–814, doi:10.1016/j.phpro.2013.03.152.

48. Alfieri, V.; Argenio, P.; Caiazzo, F.; Sergi, V. Reduction of Surface Roughness by Means of Laser Processing over Additive Manufacturing Metal Parts. *Materials (Basel).* **2016**, *10*, 30, doi:10.3390/ma10010030.

49. Nečas, D.; Klapetek, P. Gwyddion: an open-source software for SPM data analysis. *Open Phys.* **2012**, *10*, doi:10.2478/s11534-011-0096-2.

50. Bakre, C.; Lissenden, C.J. Surface Roughness Effects on Self-Interacting and Mutually Interacting Rayleigh Waves. *Sensors* **2021**, *21*, 5495, doi:10.3390/s21165495.

51. Frigo, M.; Johnson, S.G. FFTW: an adaptive software architecture for the FFT. In Proceedings of the Proceedings of the 1998 IEEE International Conference on Acoustics, Speech and Signal Processing, ICASSP ’98 (Cat. No.98CH36181); IEEE; Vol. 3, pp. 1381–1384.

52. Krylov, V.; Smirnova, Z. Experimental study of the dispersion of a Rayleigh wave on a rough surface. *Sov. physics. Acoust.* **1990**, *36*, 583–585.

53. Eguiluz, A.G.; Maradudin, A.A. Frequency shift and attenuation length of a Rayleigh wave due to surface roughness. *Phys. Rev. B* **1983**, *28*, 728–747, doi:10.1103/PhysRevB.28.728.

54. De Billy, M.; Quentin, G.; Baron, E. Attenuation measurements of an ultrasonic Rayleigh wave propagating along rough surfaces. *J. Appl. Phys.* **1987**, *61*, 2140–2145, doi:10.1063/1.337972.

55. Sinclair, R. Velocity Dispersion of Rayleigh Waves Propagating along Rough Surfaces. *J. Acoust. Soc. Am.* **1971**, *50*, 841–845, doi:10.1121/1.1912708.

56. Akhtar, A.; Teghtsoonian, E. Prismatic slip in α-titanium single crystals. *Metall. Trans. A* **1975**, *6*, 2201, doi:10.1007/BF02818644.

57. Justinger, H.; Hirt, G. Estimation of grain size and grain orientation influence in microforming processes by Taylor factor considerations. *J. Mater. Process. Technol.* **2009**, *209*, 2111–2121,

doi:10.1016/j.jmatprotec.2008.05.008.

58. Hikata, A.; Elbaum, C. Generation of Ultrasonic Second and Third Harmonics Due to Dislocations. I. *Phys. Rev.* **1966**, *144*, 469–477, doi:10.1103/PhysRev.144.469.

59. Cantrell, J. Fundamentals and Applications of Nonlinear Ultrasonic Nondestructive Evaluation. In *Ultrasonic Nondestructive Evaluation*; CRC Press, 2003.

60. Gorsse, S.; Hutchinson, C.; Gouné, M.; Banerjee, R. Additive manufacturing of metals: a brief review of the characteristic microstructures and properties of steels, Ti-6Al-4V and high-entropy alloys. *Sci. Technol. Adv. Mater.* **2017**, *18*, 584–610, doi:10.1080/14686996.2017.1361305.

61. Krakhmalev, P.; Fredriksson, G.; Yadroitsava, I.; Kazantseva, N.; Plessis, A. du; Yadroitsev, I. Deformation Behavior and Microstructure of Ti6Al4V Manufactured by SLM. *Phys. Procedia* **2016**, *83*, 778–788, doi:10.1016/j.phpro.2016.08.080.

62. Prasad, R.; Kumar, S. Study of the influence of deformation and thermal treatment on the ultrasonic behaviour of steel. *J. Mater. Process. Technol.* **1994**, *42*, 51–59, doi:10.1016/0924-0136(94)90074-4.

63. Vasudevan, M.; Palanichamy, P.; Venkadesan, S. A novel technique for characterizing annealing behaviour. *Scr. Metall. Mater.* **1994**, *30*, 1479–1483, doi:10.1016/0956-716X(94)90249-6.

64. Palanichamy, P.; Joseph, A.; Jayakumar, T.; Raj, B. Ultrasonic velocity measurements for estimation of grain size in austenitic stainless steel. *NDT E Int.* **1995**, *28*, 179–185, doi:10.1016/0963-8695(95)00011-L.

65. Papadakis, E.P. Ultrasonic attenuation and velocity in SAE 52100 steel quenched from various temperatures. *Metall. Trans.* **1970**, *1*, 1053–1057, doi:10.1007/BF02811803.

66. Papadakis, E.P. Ultrasonic Attenuation and Velocity in Three Transformation Products in Steel. *J. Appl. Phys.* **1964**, *35*, 1474–1482, doi:10.1063/1.1713652.

67. Gür, C.H.; Tuncer, B.O. Characterization of microstructural phases of steels by sound velocity measurement. *Mater. Charact.* **2005**, *55*, 160–166, doi:https://doi.org/10.1016/j.matchar.2005.05.002.

68. Karthik, N.; Gu, H.; Pal, D.; Starr, T.; Stucker, B. High Frequency Ultrasonic Non Destructive Evaluation of Additively Manufactured Components.; 2013.

69. Hikata, A.; Chick, B.B.; Elbaum, C. Dislocation Contribution to the Second Harmonic Generation of Ultrasonic Waves. *J. Appl. Phys.* **1965**, *36*, 229–236, doi:10.1063/1.1713881.

70. Kim, J.-Y.; Jacobs, L.J.; Qu, J.; Littles, J.W. Experimental characterization of fatigue damage in a nickel-base superalloy using nonlinear ultrasonic waves. *J. Acoust. Soc. Am.* **2006**, *120*, 1266–1273, doi:10.1121/1.2221557.

71. Kim, C.; Hyun, C.; Park, I.; Jhang, K. Ultrasonic characterization for directional coarsening in a nickel-based superalloy during creep exposure. *J. Nucl. Sci. Technol.* **2012**, *49*, 366–372, doi:10.1080/00223131.2012.669238.

## Chapter 5

# FEASIBILITY ANALYSIS OF MATERIAL NONLINEARITY MEASUREMENT USING LASER-GENERATED NARROWBAND RAYLEIGH WAVES[1]

## 5.1 Introduction

Nonlinear ultrasonic techniques are well accepted to be sensitive to the changes in the material microstructure. Key microstructural features of metallic materials such as lattice anharmonicity [1], dislocations density [2], residual stress, and plastic deformation [3] are responsible for varying degrees of nonlinear elastic behavior. Due to the nonlinear material behavior, the finite-amplitude ultrasonic waves distort, leading to the generation of higher harmonics [4]. Thus, the nonlinear ultrasonic evaluation methods provide a means to correlate ultrasonic features with microstructural features. Since microstructure is connected with the various macroscale mechanical properties such as tensile strength and fracture toughness, it is possible to infer such properties from nonlinear ultrasonic testing. One high-value application of current interest is additively manufactured (AM) structural components. Due to the complex physics associated with additive manufacturing, subtle changes in the process parameters can result in changes in the microstructure locally within the part or from one part to the next [5].

Of particular interest for the additive manufacturing application is developing an in-situ component monitoring technique. The primary aim of in-situ monitoring is the identification of flaws and undesired microstructure during, rather than after, manufacturing. For this purpose, laser ultrasonics is viewed as a suitable technique due its noncontact operation and rapid scanning capabilities. In the past decade, several laser ultrasonic investigations have been carried out to detect defects in additively

[1] This chapter is largely based on the manuscript:
C. Bakre *et. al*, "Feasibility analysis of material nonlinearity measurement using laser-generated narrowband waves", in preparation.

manufactured parts with a possibility for in-situ implementation [6–8]. While few studies have investigated the use of laser generated bulk ultrasonic waves [9–11], the majority of studies use laser generated Rayleigh waves as they are better suited for in-situ inspection of layer-wise deposition process [12–17].

Laser generated Rayleigh waves having a small amplitude (linear) are well researched for their use in flaw detection. However, the linear ultrasonic parameters have relatively small variations in response to changes in material microstructure. Therefore, laser generation of finite-amplitude (nonlinear) Rayleigh waves is sought as an advanced nondestructive evaluation technique to infer microstructural changes in AM parts. In general, laser ultrasound is regarded as a weaker source in the thermoelastic regime and has a broad frequency bandwidth. Since, typically, narrowband ultrasonic waves are favored for nonlinear ultrasonic techniques, several methods are used in literature to pattern the laser beam to create a line array source to achieve narrowband Rayleigh wave generation. McKie et al. [18] were the first to demonstrate narrowband Rayleigh wave generation using a pulsed laser. They used a microlens array to create the line array source, which can be used to analyze the resulting ultrasonic wave. Other techniques for laser generation of narrowband Rayleigh waves include slit mask [19,20] and interference of two-laser beams [21]. Unfortunately, these methods also inevitably generate waves that coincide with the higher harmonic frequencies, complicating the nonlinear analysis [22]. Thus, it is crucial to account for the system nonlinearity produced due to the line-array generation of Rayleigh waves.

A few authors have used laser-generated nonlinear Rayleigh waves to detect early-stage damage detection by estimating the material nonlinearity. A new technique that emits laser line array pattern called Sagnac interferometer-based optical system (SIOS) is proposed in [23,24] and demonstrated to evaluate the material nonlinearity of rail material based on second harmonic generation. Jun et al. [25] used a slit mask to generate a line arrayed source and evaluated the thermal aging in Al 6061 alloy by measuring the acoustic nonlinearity parameter. The same method has also been applied to determine the progression of bending fatigue damage in Al 6061 alloy and evaluate acoustic nonlinearity in plastically deformed aluminum alloy specimens [26,27]. However, these studies fails to acknowledge the contribution of system nonlinearity due to the line array source. Therefore, a feasibility analysis to assess the use of laser-generated narrowband Rayleigh waves to measure material nonlinearity and a comparison with the conventional method of measuring material nonlinearity are needed. Thus, the objectives of this research are as follows:

- To investigate the actuation of finite-amplitude Rayleigh waves for material nonlinearity estimation using noncontact laser generation. Rayleigh wave amplitudes are compared for Q-switched Nd:YAG laser and the conventional piston-like piezoelectric transducer generation and laser interferometric reception on a reference aluminum sample to assess the nonlinearity. In addition, the contribution of the system nonlinearity associated with the line array source to the relative nonlinearity parameter is studied.
- To show that laser-generated Rayleigh waves can have sufficiently high amplitude to measure the relative nonlinearity parameter for AISI 4130 steel plates with varying hardness levels.
- Finally, the application of nonlinear laser ultrasonic technique is demonstrated on an as-built DED-AM Ti-6Al-4V sample.

## 5.2 Methods

### 5.2.1 Laser generation and angle beam transducer generation of finite-amplitude Rayleigh waves

An experimental setup is designed to compare the nonlinear measurements from laser-generated and the conventional angle beam piezoceramic transducer generated Rayleigh waves. Figure 5-1 presents the block diagram and the experimental setup. A Q-switched Nd:YAG pulsed laser (Inlite III-10, Continuum, Milpitas, CA, USA) and a microlens array (Part # 86-843, Edmond Optics Inc., Barrington, NJ, USA), having 10 mm by 10 mm dimensions, pitch of 500 $\mu$m, and 20 lens elements in the array, is used to generate narrowband Rayleigh waves at one end of the aluminum alloy 7075 block. The aluminum block has dimensions 170 mm × 40 mm × 20 mm, and the top surface is mirror-polished.

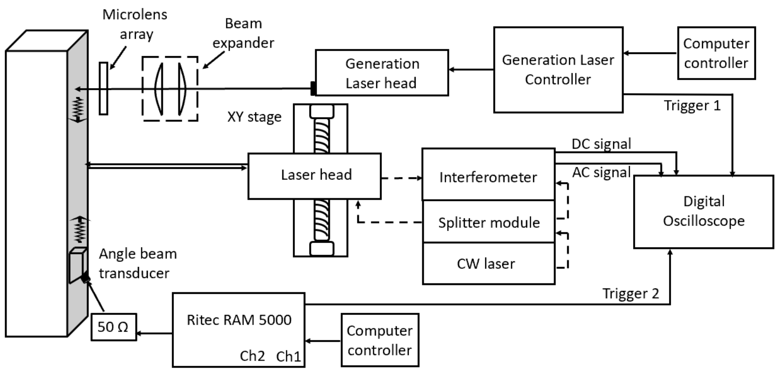


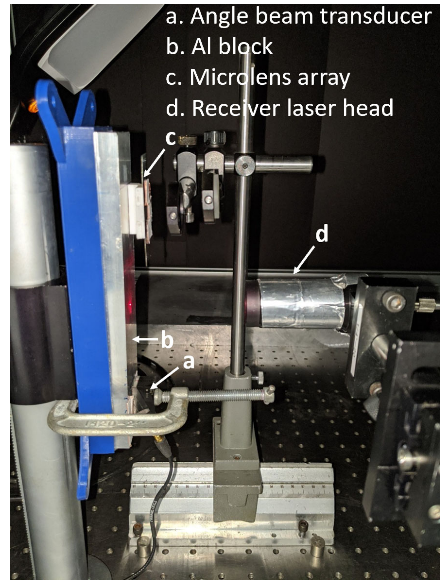


(a) (b)

Figure **5-1:** Test setup for measurement of system nonlinearity: (a) Block diagram where solid and dashed lines represent electrical cables and optical fibers respectively, (b) Photograph of the laser head illuminating reflective tape on the transducer surface.

The laser beam is expanded using a pair of plano-concave and plano-convex lenses prior to irradiating the microlens array. The lift-off distance between the specimen surface and the microlens array is approximately equal to its focal length (11.1 mm). A burn mark is obtained on lens alignment paper (Part # ZAP-IT-G, Kentek, Pittsfield, NH, USA) to characterize the line-array illumination source using ImageJ software. The laser generates incident energy of 180 mJ per pulse with a pulse repetition rate of 5 Hz.

For the angle beam generation, a contact transducer (Benchmark series 113-232-591; Baker Hughes, Houston, TX, USA) having a center frequency of 5 MHz is coupled to a 70-degree Plexiglas wedge and actuated by a high power gated amplifier (RAM-5000 SNAP, Ritec Inc., Warwick, RI, USA) with a pulse repetition rate of 5 Hz. A C-clamp is used to clamp the angle beam transducer at the other end of the aluminum block with ultrasonic gel couplant (Soundsafe, Sonotech, State College, PA, USA). The centerline from the two-generation methods is collinear. The frequency and the signal amplitude is obtained such that it is identical to the laser-generated narrowband Rayleigh wave measured at an equidistant point.

A laser interferometer (AIR-1550-TWM, Intelligent Optical Systems Inc., Torrance, CA, USA) is used to measure Rayleigh waves on the specimen's surface along the centerline. The laser receiver head is mounted on a translational stage to scan vertically and obtain Rayleigh waves at different propagation distances. The scan is conducted in the far-field for both the generation methods over a 45-90 mm range in 5 mm increments. A detailed information about the operation of the laser receiver can be found in [28]. 1024 Rayleigh wave signals are synchronously averaged and recorded using an oscilloscope (InfiniiVision MSOX3024T, Keysight, Santa Rosa, CA, USA). The signal acquisition rate is 0.38 GHz. Matlab algorithms are developed for further processing the recorded signals. A Hanning window is applied to the signal before computing the spectrum. Zero-padding is used to improve the frequency resolution before the Fast Fourier Transform (FFT) function in Matlab is applied.

### 5.2.2 Relative nonlinearity parameter measurement of AISI 4130 steel plates using laser ultrasound

This section describes the experimental procedure to measure the relative nonlinearity of AISI 4130 steel plates tempered to have varied hardness levels using all noncontact laser ultrasonic method.

Mechanical components subjected to elevated temperatures in nuclear, aerospace and chemical industries undergo thermal modifications of material properties that affect their performance over time. Moreover, alloying metals are often heat-treated, and it is desired to nondestructively evaluate if the optimal quality is reached during the heat treatment process. Many researchers have demonstrated the use of contact nonlinear ultrasonic techniques to correlate mechanical properties with the ultrasonic nonlinearity for metals subjected to different heat treatments [25,29–33]. However, laser ultrasonic technique can be highly advantageous as it could potentially monitor the microstructural evolution of the part during the heat treatment process.

Investigations are carried out on three quenched and tempered AISI 4130 steel plates labeled with their Rockwell C hardness values as HRC 22, HRC 32, and HRC 52. These plates are called Plate 22, Plate 32 and Plate 52 in the rest of the chapter. Each plate is first heated to a temperature of 857 °C and held for 45 minutes, followed by oil quenching for approximately 20 minutes. The plates are then tempered at 662.8 °C, 560.0 °C, and 176.7 °C temperatures for 2 hours. AISI 4130 is low-alloy steel or Cr-Mo steel with composition in wt%: 0.28-0.33 C, 0.80-1.10 Cr, 0.15-0.25 Mo, 0.40-0.60 Mn, 0.035 max P, 0.040 max S, 0.15-0.35 Si, and remainder is Fe. The plate dimensions are 254 mm × 152 mm × 10 mm. The inspection region is polished using a sequence of emery paper grit sizes 400/600/800/1000.

Figure 5-2 shows the noncontact setup for nonlinear Rayleigh wave inspections. The 7 mm diameter generation laser beam is expanded using a 3X beam expander (Part # 35-099, Edmond Optics Inc., Barrington, NJ, USA) and then reflected using a mirror (Part #38900, Edmond Optics Inc., Barrington, NJ, USA) onto the slit mask having 13 slits, pitch of 1 mm, slit width of 0.45 mm, and length of 15 mm. The generation beam is reflected at an oblique angle of 5 degrees to reduce the distance

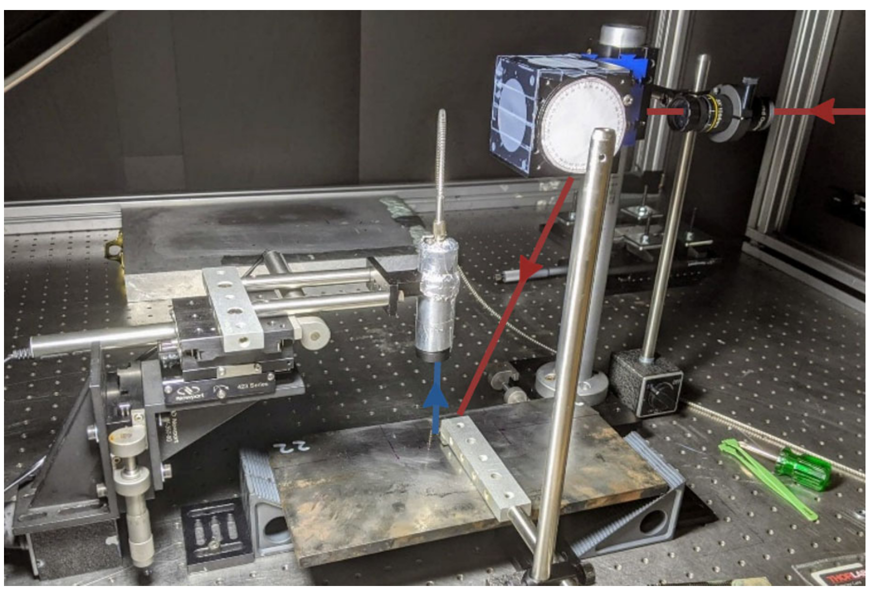

Figure **5-2**. Nd:YAG pulsed laser and laser interferometer setup for AISI 4130 steel plates.

Between the generation and reception beams. The distance of propagation for the Rayleigh waves is fixed at 15 mm. A burn mark is obtained from the slit mask illumination for source characterization on lens alignment paper. The laser pulse energy varies from 180 to 270 mJ with 10 mJ increments.

Rayleigh waves are received using the laser interferometer at each energy level. 1024 Rayleigh wave signals are synchronously averaged and recorded using an oscilloscope (InfiniiVision MSOX3024T, Keysight, Santa Rosa, CA, USA). The signal acquisition rate is 0.258 GHz for the contact and 1.23 GHz for the noncontact measurements. Matlab algorithms are developed for further processing the recorded signals. A Hanning window is applied to the signal before computing the spectrum. Zero-padding is used to improve the frequency resolution before the Fast Fourier Transform (FFT) function in Matlab is applied. Lastly, the velocity of each plate is measured by scanning the laser receptor in the wave propagation direction. The averaged velocity is obtained from the time of flight (TOF) measurements for 18 reception points separated by 1 mm along the scan.

### 5.2.3 DED-Ti64 – Relative Nonlinearity parameter (β') estimation using laser ultrasound

As shown in Chapter 4, the unique microstructure of AM material leads to the distortion of Rayleigh waves. The AM microstructure is characterized by significantly higher dislocation density than the wrought material due to high solidification rates, large dendritic grains along the build direction with sharp interfaces, and residual stresses that can lead to distortion of Rayleigh waves [34–36]. Furthermore, variations in the process parameters such as scan speed, hatch spacing, and laser power affect the material microstructure. In addition, nonlinear ultrasonic techniques are well accepted to be sensitive to the changes in the material microstructure. Therefore, our goal is to investigate the use of laser ultrasound to infer the microstructural changes in AM parts in-situ, by leveraging the nonlinear distortion of Rayleigh waves. Here, we provide what is believed to be the first determination of the relative nonlinearity parameter on as-built AM samples using laser ultrasound.

Figure 5-3 provides the laser ultrasonic experimental setup and the as-built DED-AM Ti-6Al-4V specimen with the inspection region marked. The process parameters used for the deposition of interest are shown in Table 5-1. In general, the laser ultrasonic measurements are similar to the previous section.

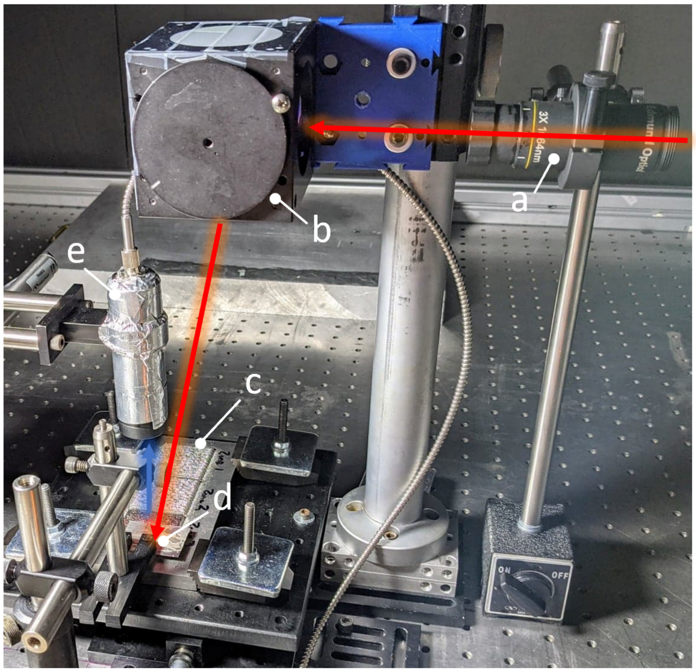


(a)

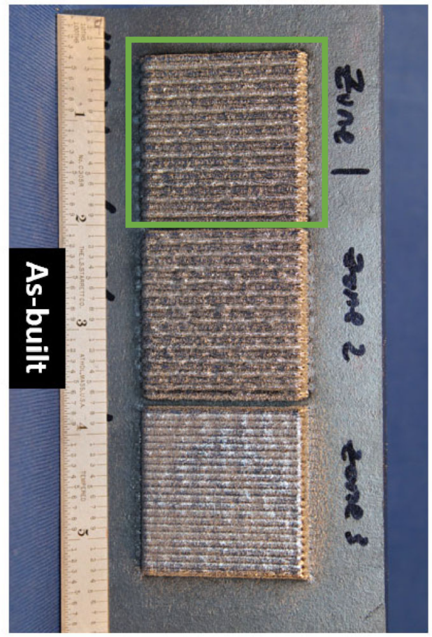


(b)

Figure **5-3**. (a) Laser ultrasonic test setup (a: beam expander, b: mirror, c: as-built DED-Ti-6Al-4V specimen, d: slit mask, and e: laser receiver head) and (b) as-built DED-Ti64 specimen.

Table **5-1:** Processing parameters for DED-AM Ti-6Al-4V

| **Parameters** | **Values** |
|---|---|
| Laser power | 450 W |
| Scan speed | 10.6 in/min |
| Powder flow rate | 2.8 g/min |
| Hatch spacing | 0.81 mm |

The relative nonlinearity parameter is estimated by measuring the primary and second harmonic spectra amplitudes for two methods: 1) varying propagation distance from 10.5 mm to 11.1 mm with 0.1 mm increments with fixed laser energy at 200 mJ, and 2) varying the pulsed laser energy from 180 mJ -270 mJ in 10 mJ increments with fixed propagation distance of 10 mm. However, the key challenge for laser ultrasonic inspection of as-built AM sample is the low SNR and the occasional loss of the signal due to the high surface roughness. Thus, the following two strategies are used to overcome challenges in laser reception.

- Lower distance of propagation: The laser generation beam is reflected onto the AM sample at an oblique incidence of 8 degrees from the vertical axis to reduce the propagation distance and minimize the attenuation effects.
- Normalization: The laser receiver used in this study provides two output signals – the A.C. signal that contains the Rayleigh wave signal information and the D.C. level that provides a measure of the reflected light received from the surface of the specimen. Thus, the A.C. signals are normalized by the D.C. level so that the signals received at different measurement points can be compared.

## 5.3 Results

### 5.3.1 Laser generation and angle beam transducer generation of finite-amplitude Rayleigh waves on smooth aluminum block

Our results show that although the relative nonlinearity parameter ($\beta'$), defined in Equation 3-1, obtained for the laser generation is an order of magnitude higher than the angle beam transducer generation, a similar monotonically increasing trend is observed for the increasing propagation distance, indicative of the cumulative nonlinear effect. The cause for the higher $\beta'$ obtained for the laser generation can be attributed to the system nonlinearity associated with the line array source, which is shown to be compensated at the lowest propagation distance, making the $\beta'$ comparable to that obtained using angle transducer generation.

The feasibility of laser-generated Rayleigh waves to measure the material nonlinearity is tested by comparing with the conventional angle beam transducer method on the aluminum 7075 block. The input parameters are adjusted such that the Rayleigh waves received by the laser interferometer have identical excitation frequency and signal amplitude measured at an equidistant point from the two sources. Figures 5-4a and 5-4b present the A-scans for the angle beam transducer and the pulsed laser sources measured at a distance of 45 mm, respectively. Figures 5-4c and 5-4d show the corresponding frequency spectra. The primary frequency of excitation for both the sources is 5.8 MHz. The broadband spectrum in Fig. 5-4d shown by the dashed red line represents the Rayleigh wave generation due to a single line in the line array generated using the microlens array.

We investigate the narrowband laser generation of Rayleigh waves by characterizing the line array source created by microlens array from the burn mark shown in Figure 5-5a. The narrowband Rayleigh wave is generated due to the modulation from the sixteen lines (N = 16) in the array producing an equal number of cycles [18]. The width of each line is 0.14 mm, and the pitch of the array, $d$ = 0.5 mm. Thus, knowing the Rayleigh waves speed in the Aluminum 7075 specimen ($c$ = 2920 m/s), the frequency can be calculated as the ratio of wave speed and wavelength (equivalent to the pitch). Thus, the excitation frequency is estimated to be 5.84 MHz, which matches the frequency spectrum shown in Figure 5-4d. Figure 5-5b presents the 1D intensity profiles for the line array source. The variation in the peak intensities for each line is due to the non-uniformity of the laser beam irradiating the microlens array. As a result, nonuniform amplitudes for each cycle are observed in Figure 5-4b. Furthermore, a Gaussian shaped intensity profile is obtained for each line in the array pattern for the microlens array, as seen in Fig. 5-5d.

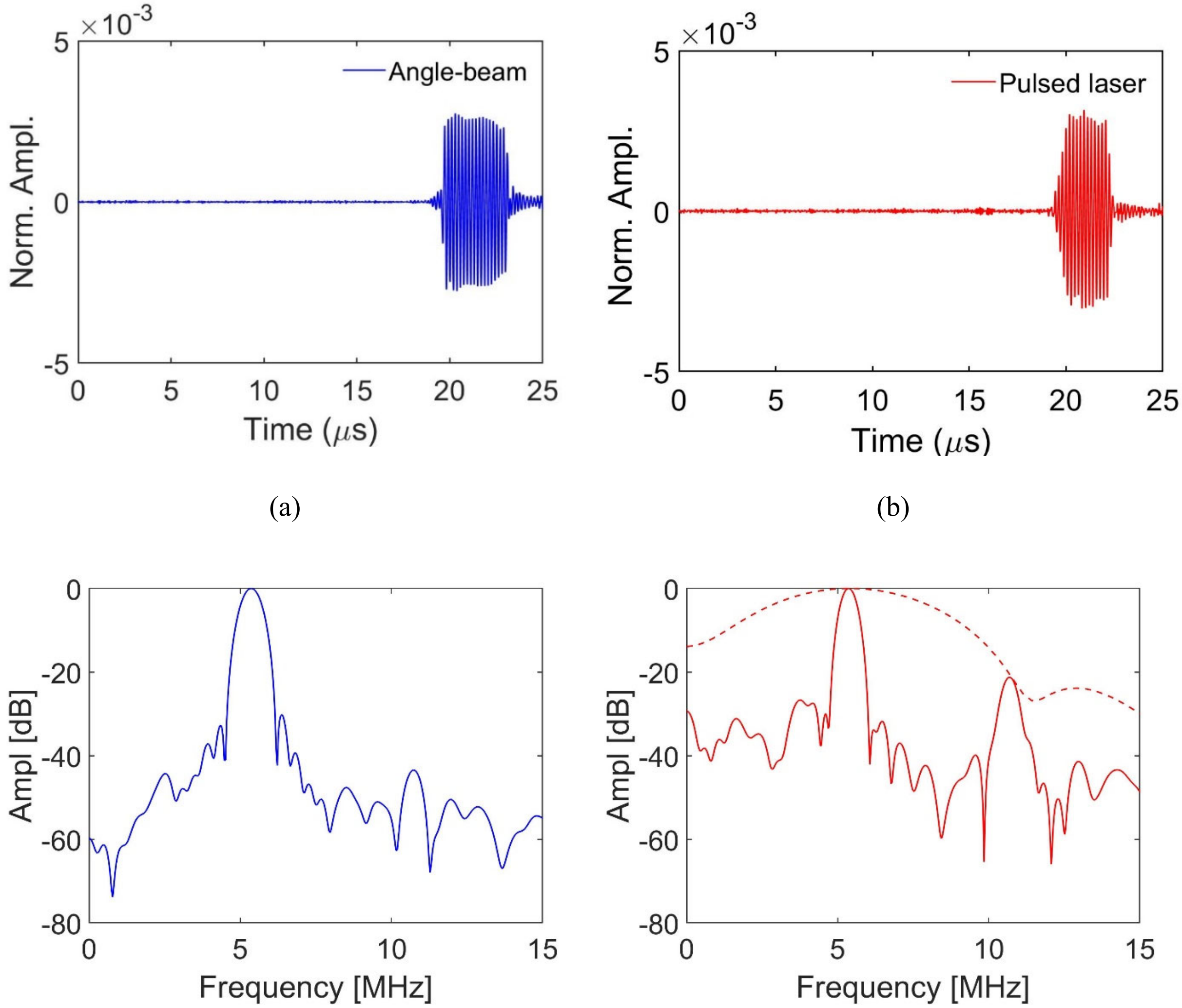


(a) (b)

(c) (d)

Figure **5-4**. A-scans and frequency spectrum for angle-beam transducer and laser generation.

The significantly higher second harmonic amplitudes for laser generation, as seen in Figure 5-4d, is an outcome of the line arrayed source as reported previously in the literature [22]. Figure 5-6 provides the plot for the relative nonlinearity parameter ($\beta'$) versus the propagation distance for the pulsed laser and the angle beam transducer generation. The dotted line represents the linear regression and the relative nonlinearity parameter measured from the slope of the dotted line. The measured slopes for the angle beam transducer generation is $6\times10^{-4}$ (arb. units) and for laser generation is $5.1\times10^{-3}$ (arb. units). We note that the slopes are much different for the two generation methods.

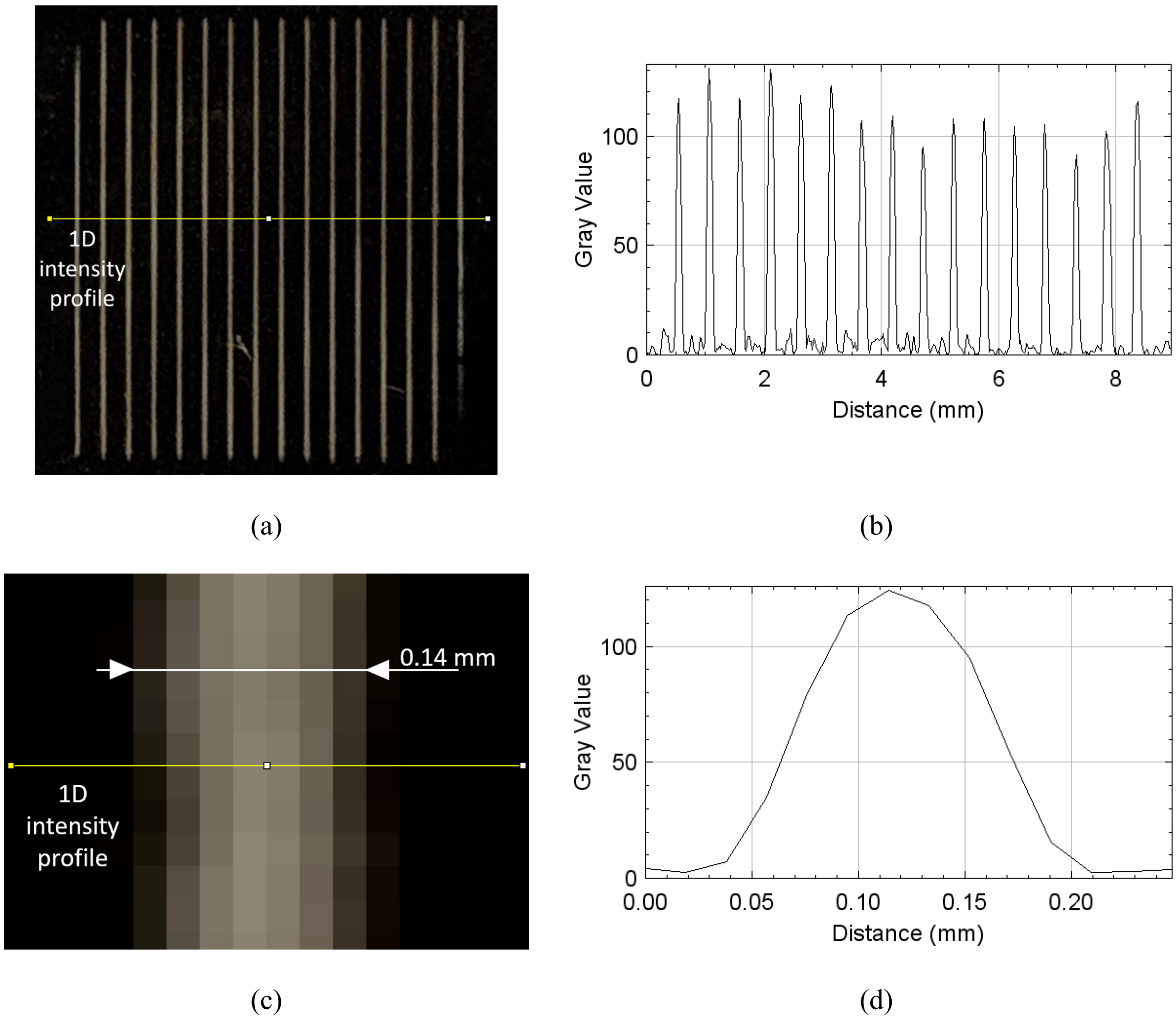


Figure **5-5**. (a) Burn mark from the microlens array enable source characterization. (b) Intensity pattern along the horizontal line in (a), (c) Zoomed image of the single line in the line array, and (d) Intensity pattern along the horizontal line in (c) shows a gaussian-shaped energy distribution.

Despite the difference in the measured slopes, a cumulative growth of the relative nonlinearity parameter with propagation distance is observed. Furthermore, the $\beta'$ values approach a maximum at approximately 85 mm for the angle beam generation and 80 mm for the laser generation and then reduces with a further increase in the propagation distance. This distance is termed the maximum cumulative propagation distance (MCPD). The reduction in $\beta'$ after MCPD is due to the attenuation effects that dominate the nonlinear effects. The diffraction effects are considered to be negligible as the range of propagation distances for this study are much lower than the characteristic diffraction length ($x_d$ = 201 mm) calculated based on the expression given in Eqn 2-1.

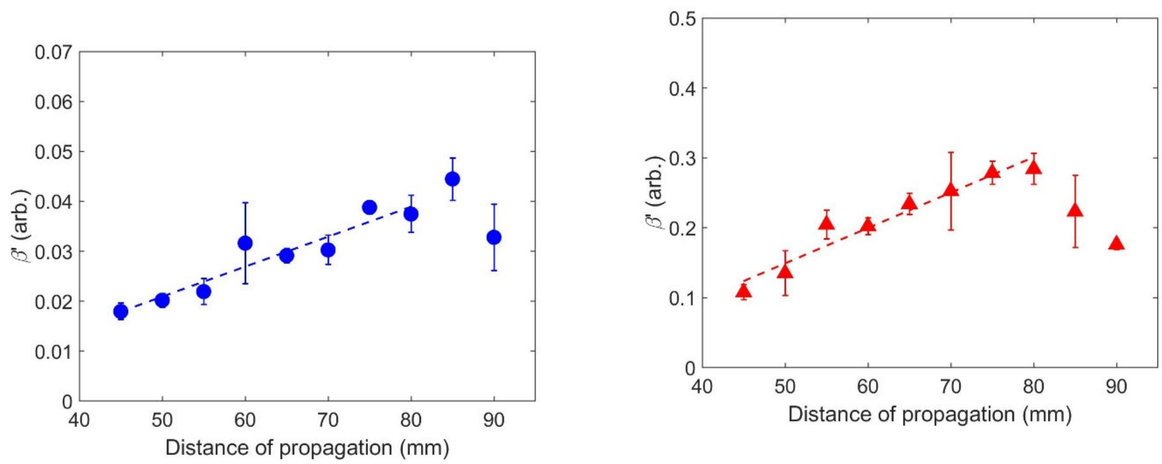


(a) (b)

Figure **5-6**. Plots show the relative nonlinearity parameter for increasing propagation distances for (a) angle beam generation and (b) laser generation.

We conclude our analysis by subtracting the inherent nonlinearity of the line array source from the relative nonlinearity parameter for the laser generation measured at 45 mm propagation distance. We estimate the system nonlinearity of the line array source by using a similar method provided in [22]; the difference is that our analysis uses experimental data. The $S(f)$ shown in Figure 5-7 is computed according to the Eqn 5-1. $H(f)$ is the experimentally determined broadband spectrum of Rayleigh waves generated by exciting a single line of the line array source, and $G(f)$ is the frequency domain multiplication of the $S(f)$ and $H(f)$ amplitudes, according to Eqn. 5-2. We can see that the resulted spectrum $G(f)$ contains peaks at primary and second harmonic frequencies in Fig. 5-7.

$$S(f) = \frac{\sin(\pi N f \Delta t)}{\sin(\pi f \Delta t)} \tag{5-1}$$

$$G(f) = H(f)S(f) \tag{5-2}$$

where $S(f)$ is the array function, $H(f)$ is the frequency spectrum of the signal obtained by illumination of a single line in the array, $\Delta t$ is the ratio of pitch of a line in the array and the Rayleigh wave speed, and N is the number of lines in the array.

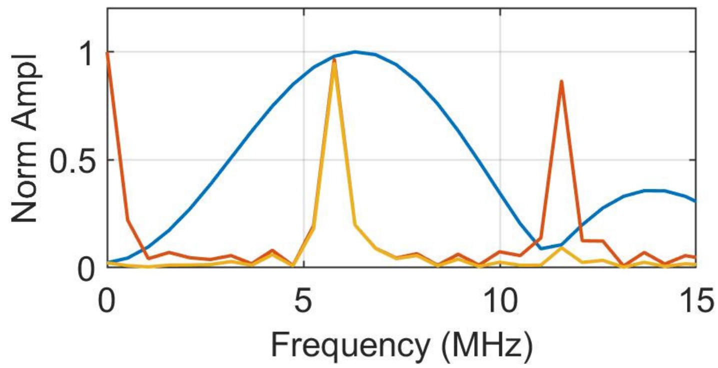


Figure **5-7**. Plots show the $S(f)$ (orange), $H(f)$ (blue), and $G(f)$ (yellow) for the line array source generated using the microlens array.

Table **5-2**. Spectral amplitudes and relative nonlinearity parameters at 45 mm propagation distance for angle beam generation, laser generation, and laser generation compensated for the system nonlinearity effect

| | $A_1$ | $A_2$ | $\beta' = \frac{A_2}{A_1^2}$ |
|---|---|---|---|
| **Angle beam generation** | 1.233 | 0.027 | 0.018 |
| **Laser generation** | 1.187 | 0.152 | 0.108 |
| **Laser generation compensated for the system nonlinearity** | 1.187 | 0.036 | 0.025 |

We measure the peak spectral amplitudes at the primary and second harmonic frequencies, $A_1$ and $A_2$, respectively to quantify the system nonlinearity. The measured values are: $A_1$ = 0.95 and $A_2$ = 0.09. That is, the $A_2$ is 9.75% of $A_1$. Thus, the $A_2$ generated due to the system nonlinearity at 45 mm propagation distance is 9.75% of $A_1$ (at 45 mm propagation distance), or 0.116. The $A_2$ obtained after subtracting the contribution from inherent nonlinearity is 0.036. As seen in Table 5-2, the $\beta'$ values obtained for the angle beam generation and laser generation after compensating the system nonlinearity effect are comparable. The minimal differences could be due to the system nonlinearity in the angle beam generation.

### 5.3.2 Relative nonlinearity parameter measurement of AISI 4130 steel plates using noncontact methods

Our results show a minimal variation in the Rayleigh wave speeds and, contrastingly, a substantial increase in the relative nonlinearity parameter for the three AISI 4130 steel plates with increasing hardness levels, which is consistent with the literature.

We begin our analysis by comparing the average Rayleigh wave speeds for the AISI 4130 steel plates. The average Rayleigh wave speeds for Plate 22, 32, and 52 are 2994 m/s, 2993 m/s, and 2960 m/s, respectively, as shown in the bar chart in Fig 5-8. The error bars represent the standard error of 18 tests. The different hardness levels for the first two plates have no significant effect on the wave speeds. However, we note that the plate with the highest hardness level has a noticeably lower wave speed. This result matches closely with the results obtained on the identical test specimens by Williams et al. [37]. The results confirm the literature that a minimal variation in the wave speeds is observed for plates with varying hardness levels and provides the motivation to conduct the nonlinear ultrasonic tests [38].

Nonlinear measurements for the three AISI 4130 steel plates having different hardness are carried out using the all-optical laser ultrasonic setup. The relative nonlinearity parameter is obtained by measuring the second harmonic amplitudes at various primary frequency amplitudes with fixed propagation distance. Figure 5-9 provides a sample A-scan and its frequency spectrum. We note the high amplitude at the second harmonic frequency due to the system nonlinearity effects caused by laser line array excitation. However, since the same slit mask is used to generate Rayleigh waves for each plate, we do not subtract the system nonlinearity contribution of the slit mask in this study. Furthermore, the frequency spectrum from the single slit excitation is plotted with a dotted line in Fig. 5-9b.

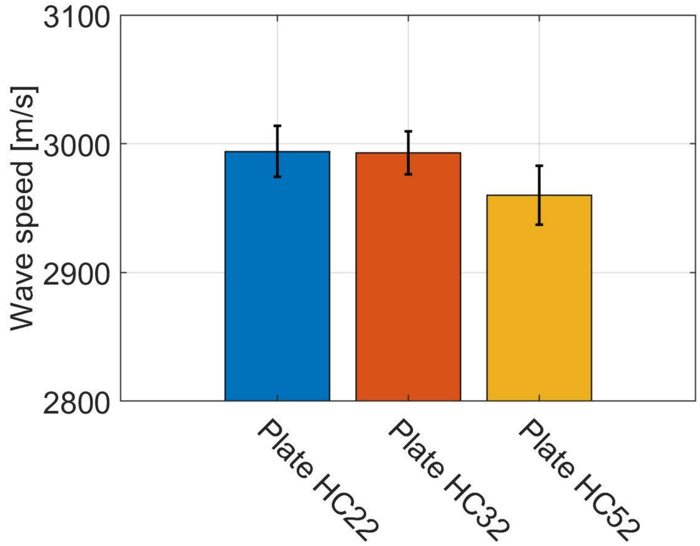


Figure **5-8**. Bar chart showing the average Rayleigh wave speeds for the three AISI 4130 plates.

Similar to the previous study, we characterize the laser ultrasonic source using the burn mark of the line-array pattern from the slit mask, shown in Fig 5-10a. Figure 5-10b delineates the 1D variation of intensity across the slit mask. The narrowband Rayleigh wave is generated due to the modulation from the thirteen lines (N = 13) in the array producing an equal number of cycles. The width of each line is 0.45 mm, the pitch of the array, $d$ = 1 mm, and the length of each line is 15 mm. The variation in the intensity profile is caused by the non-uniformity of the laser beam irradiating the slit mask, which results in the variation of peak amplitudes in the Rayleigh wave signal. Figure 5-10c shows the zoomed view of a single line in the array. In contrast to the microlens array, the 1D intensity profile for a single slit of a slit mask has a uniform shape; refer to Figures 5-5d and 5-10d.

The relative nonlinearity parameters are measured from the slope of the line regression for the $A_2$ and the $A_1^2$ plots shown in Figure 5-11. The relative nonlinearity parameter obtained for each plate is provided in Table 5-3. The relative nonlinearity parameters ($\beta'$) are normalized with respect to Plate 22 and shown in the bar chart in Figure 5-12. The increase in $\beta'$ for the second plate is 35.7 % and for the third plate is 63.8 %. Thus, we note that the $\beta'$ increases with the hardness level, which is consistent with the literature. Hurley et al. [38] reported a monotonic increase in $\beta'$ with the increase in the % carbon content (0.1 – 0.4 % mass C) or hardness levels (39.0 – 57.5 HRC) due to tempering of 9310, 4320, 4340 steel specimens. Metya et al. [31] also found a similar dependency of $\beta'$ and the hardness level of 9Cr-1Mo steel samples. The $\beta'$ and the hardness of the specimens increased to a maximum with increasing tempering temperatures followed their reduction upon further increase in the tempering temperatures.

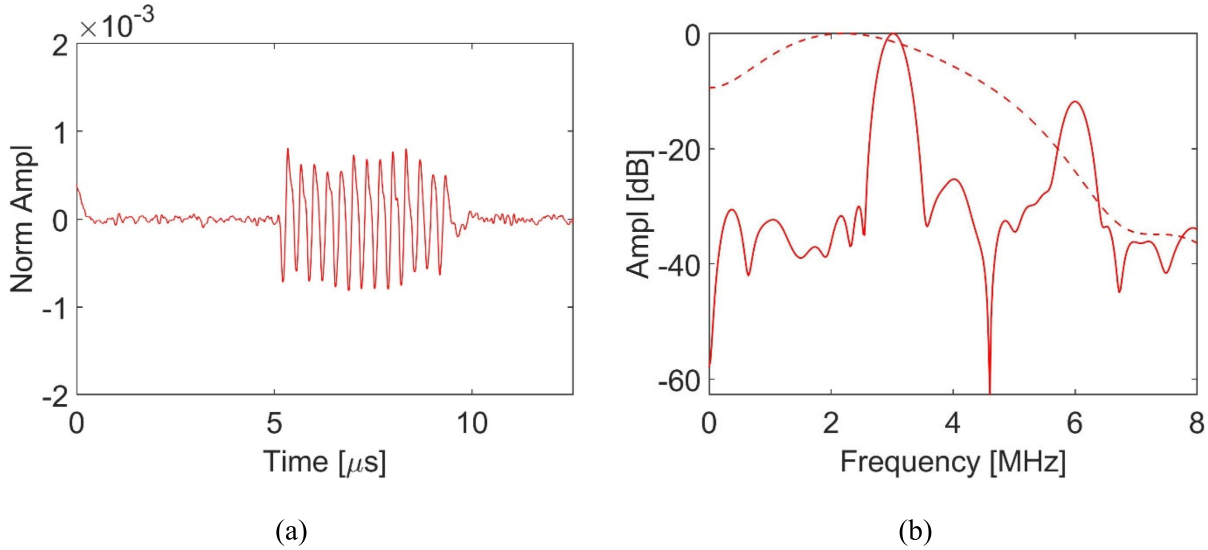


Figure **5-9**. (a) Example A-scan and (b) frequency spectrum for AISI 4130 plate (dotted line represents the broadband frequency spectrum obtained for single line source excitation).

Many other authors have also observed a similar relation between the hardness level and the $\beta'$ due to different heat treatment methods [29,32,33,39–41]. Cantrell et al. [42] established a relationship between the effect of tempering times on $\beta'$ and hardness for aluminum alloy 2024 using a theoretical model and experiments. The authors claim that the initial increase in the hardness level followed by their reduction with increasing tempering times can be used to assess the optimal tempering times for the material nondestructively. Thus, the result obtained in Fig. 5-12 is the first step toward online monitoring of tempering effects on the material properties using laser ultrasound within the furnace. Further investigations toward online monitoring require consideration of the temperature effects on the laser generation and Rayleigh wave propagation.

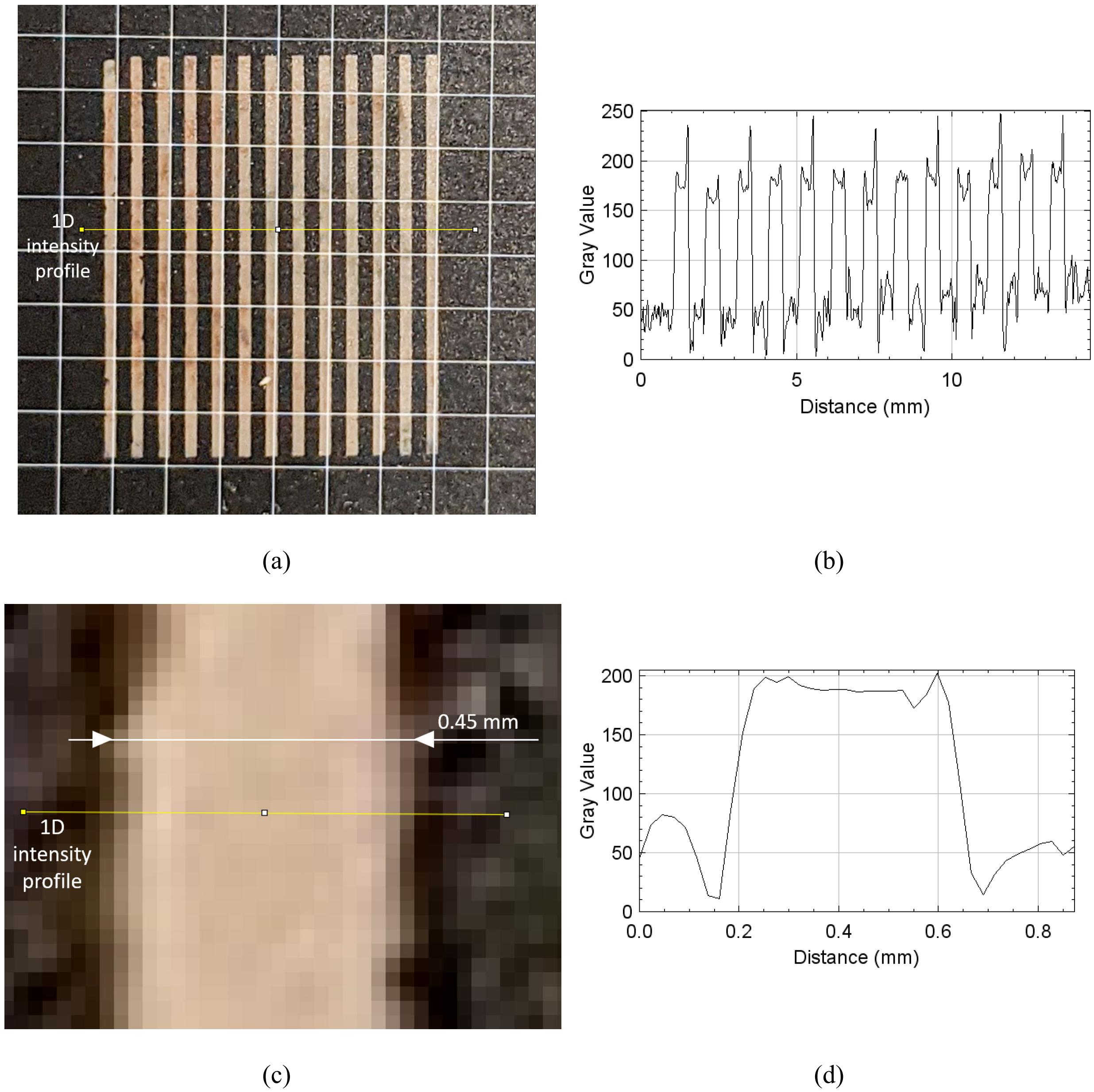


Figure **5-10**. (a) Burn mark from the slit mask array enable source characterization. (b) Intensity pattern along the horizontal line in (a), (c) Zoomed image of a single line in the line array, and (d) Intensity pattern along the horizontal line in (c) shows a top-hat shaped energy distribution.

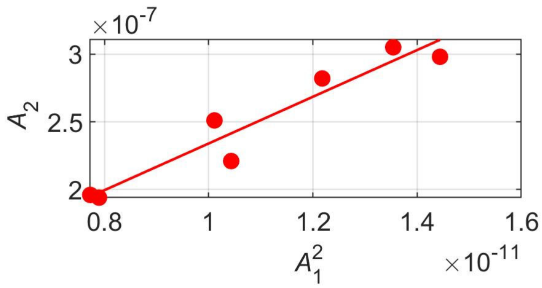


Plate 22

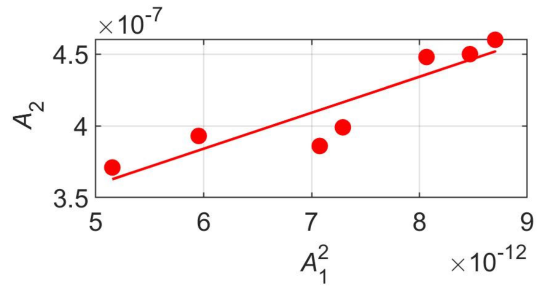


Plate 32

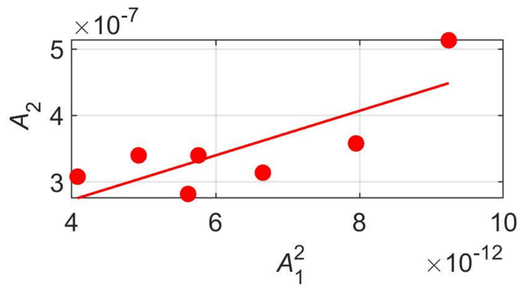


Plate 52

Figure **5-11**. Linear regression of the $A_2$ and the $A_1^2$ plots for Plate 22, Plate 32, and Plate 52.

Table **5-3**. Relative nonlinearity parameters at 45 mm propagation distance for laser generation.

| **Plate** | **Relative nonlinearity parameter ($\boldsymbol{\beta'}$), Hz** |
|---|---|
| **Plate HC22** | $7.72 \times 10^7$ |
| **Plate HC32** | $1.05 \times 10^8$ |
| **Plate HC52** | $1.26 \times 10^8$ |

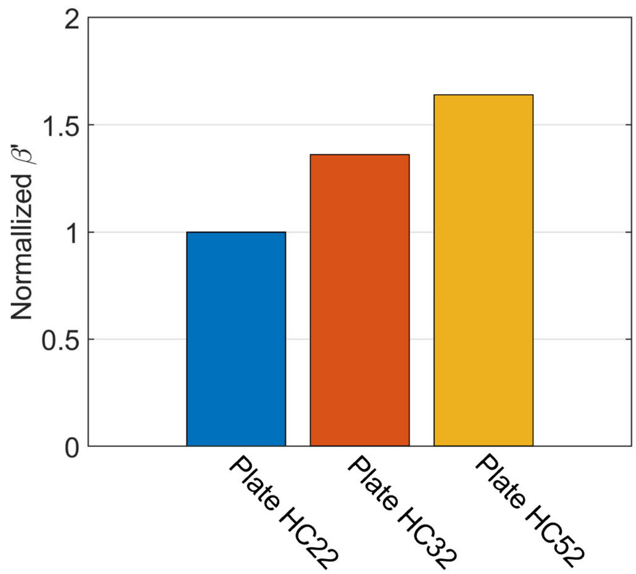


Figure **5-12**. Relative nonlinearity parameters normalized with respect to the Plate HC22.

### 5.3.3 DED-Ti64 – Relative Nonlinearity parameter (β') estimation using laser ultrasound

This section investigates the prospect of estimating the relative nonlinearity parameter ($\beta'$) on as-built AM material using narrowband laser-generated Rayleigh waves. A sample A-scan and frequency spectrum is shown in Figure 5-13. Figures 5-14a & 5-14b show the spectral amplitudes of Rayleigh waves at primary and secondary frequencies ($A_1$and $A_2$), respectively, for increasing propagation distances. The distance of propagation for this study is low (10.5 mm to 11.1 mm) as it is challenging to measure the material nonlinearity for higher propagation distances due to the high roughness of AM samples (average asperity height: $S_a$ = 33.04 $\mu$m). In Fig 5-14a and 5-14b, we note an exponential reduction in $A_1$ and an increase in $A_2$ with propagation distance. While the reduction in $A_1$ is mainly due to the attenuation effects, the increase in the $A_2$ can be explained by the cumulative nonlinear effect that distorts the Rayleigh waves as they propagate. Figure 5-14c shows the linear regression for the $\beta'$ values calculated from the ratio of $A_2$ and square of $A_1$ at different propagation distances. It is well known that $\beta'$ varies linearly with propagation distance and the slope of the linear regression is proportional to the material nonlinearity [4]. The measured slope is $6.9 \times 10^7$ [Hz] and $R^2 = 0.93$ for the linear fit. Here, we do not attempt to subtract the system nonlinearity of the line array source directly from the measured

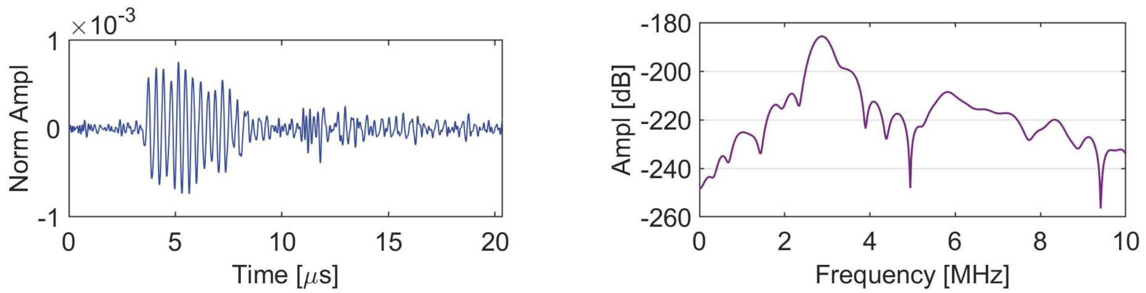


(a) (b)

Figure **5-13**. Sample A-scan and frequency spectrum at 200 mJ pulse energy.

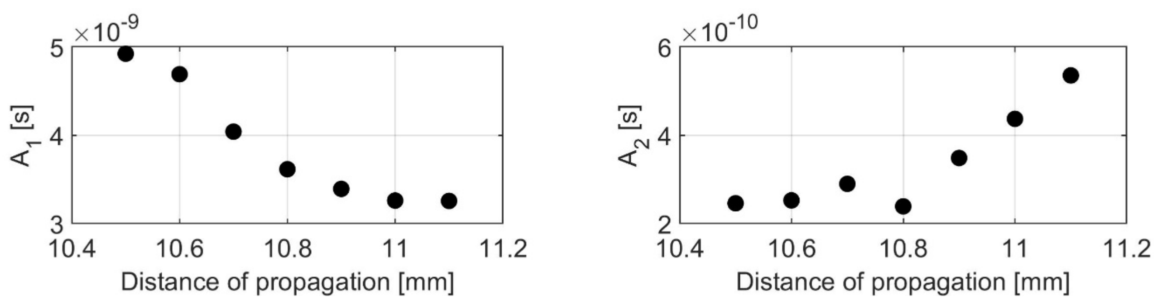


(a) (b)

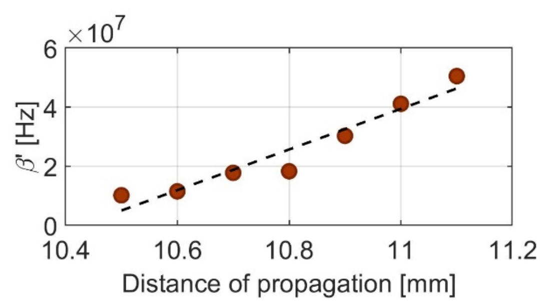


(c)

Figure **5-14**. Linear scan results (a) $A_1$, (b) $A_2$, and (c) $\beta'$ vs. $x$.

values. This is because, due to the high surface roughness effects of AM samples, the primary and second harmonic amplitudes decrease with increasing propagation distance. Thus, a model needs to be developed in the future to account for surface roughness effects on $A_1$ and $A_2$ and then use the method of subtraction of system nonlinearity contribution to evaluate the material nonlinearity.

We also report the relative nonlinearity parameter obtained by measuring the second harmonic amplitudes at varying primary amplitudes at a fixed propagation distance. Figure 5-15a presents the spectral amplitude, $A_1$, for the increasing laser energy. Figure 5-15b presents the $A_2$ vs. $A_1^2$ plot and its linear regression. The $\beta'$ is obtained from the slope of the linear regression as 8.8 × $10^7$ [Hz] and the $R^2$ = 0.83 for the linear fit.. Further investigation is required to find which amongst the above two methods is better suited for material nonlinearity measurement on AM specimens.

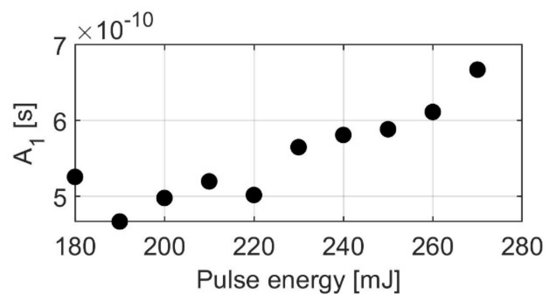


(a)

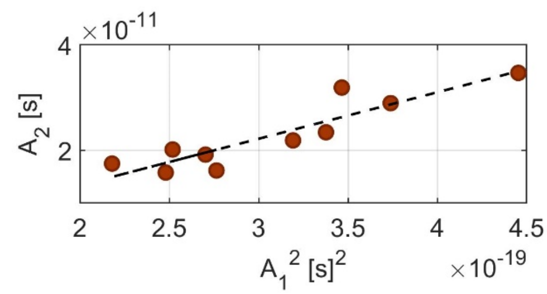


(b)

Figure **5-15**. (a) Variation of peak amplitude at the primary frequency (b) Linear regression to determine the relative nonlinearity parameter of Rayleigh waves propagation on the DED-Ti64 sample.

### 5.4 Conclusions

This chapter investigates whether laser ultrasound can generate narrowband Rayleigh waves with high enough amplitudes to assess the material nonlinearity. The experimental results show that the $\beta'$ obtained for the laser generation using microlens array and angle beam transducer generation have a similar linearly increasing trend for increasing propagation distance. The linearly increasing trend with the propagation distance is indicative of the cumulative effect of the material nonlinearity. However, the slopes of the $\beta'$ vs. propagation distance are found to be an order of magnitude higher for the laser generation due to the system nonlinearity caused by the line array source. The characterization of the line array source is carried out to measure the contribution of the system nonlinearity to the measured $\beta'$, and after subtraction, it is shown to be comparable to the $\beta'$ for angle beam generation at the lowest propagation distance.

The second part of the chapter investigates the application of narrowband laser generation using a slit mask to assess the nonlinearity of the AISI 4130 steel plates having varying hardness levels. The $\beta'$ measured by increasing the laser energy and fixed propagation distance shows a monotonically increasing trend of $\beta'$ with increasing hardness, which is in agreement with the literature. Finally, the laser ultrasonic interrogation carried out for the as-built DED Ti-6Al-4V specimen present what is believed to be the first report on laser ultrasonic nonlinearity measurement on an as-built AM specimen.

## 5.5 References


1. Lissenden, C.J. Nonlinear ultrasonic guided waves—Principles for nondestructive evaluation. *J. Appl. Phys.* **2021**, *129*, 021101, doi:10.1063/5.0038340.

2. Nagy, P.B. Fatigue damage assessment by nonlinear ultrasonic materials characterization. *Ultrasonics* **1998**, *36*, 375–381.

3. Liu, M.; Kim, J.Y.; Jacobs, L.; Qu, J. Experimental study of nonlinear Rayleigh wave propagation in shot-peened aluminum platesFeasibility of measuring residual stress. *NDT E Int.* **2011**, *44*, 67–74, doi:10.1016/j.ndteint.2010.09.008.

4. Jhang, K.-Y.; Lissenden, C.J.; Solodov, I.; Ohara, Y.; Gusev, V. *Measurement of Nonlinear Ultrasonic Characteristics*; Springer Series in Measurement Science and Technology; Springer Singapore: Singapore, 2020; ISBN 978-981-15-1460-9.

5. Gong, H.; Rafi, K.; Gu, H.; Starr, T.; Stucker, B. Analysis of defect generation in Ti-6Al-4V parts made using powder bed fusion additive manufacturing processes. *Addit. Manuf.* **2014**, *1*, 87–98,

doi:10.1016/j.addma.2014.08.002.

6. Honarvar, F.; Varvani-Farahani, A. A review of ultrasonic testing applications in additive manufacturing: Defect evaluation, material characterization, and process control. *Ultrasonics* **2020**, *108*, 106227, doi:10.1016/j.ultras.2020.106227.

7. Everton, S.K.; Hirsch, M.; Stravroulakis, P.; Leach, R.K.; Clare, A.T. Review of in-situ process monitoring and in-situ metrology for metal additive manufacturing. *Mater. Des.* **2016**, *95*, 431–445, doi:10.1016/j.matdes.2016.01.099.

8. Tapia, G.; Elwany, A. A Review on Process Monitoring and Control in Metal-Based Additive Manufacturing. *J. Manuf. Sci. Eng.* **2014**, *136*, doi:10.1115/1.4028540.

9. Davis, G.; Nagarajah, R.; Palanisamy, S.; Rashid, R.A.R.; Rajagopal, P.; Balasubramaniam, K. Laser ultrasonic inspection of additive manufactured components. *Int. J. Adv. Manuf. Technol.* **2019**, *102*, 2571–2579, doi:10.1007/s00170-018-3046-y.

10. Yu, J.; Zhang, D.; Li, H.; Song, C.; Zhou, X.; Shen, S.; Zhang, G.; Yang, Y.; Wang, H. Detection of Internal Holes in Additive Manufactured Ti-6Al-4V Part Using Laser Ultrasonic Testing. *Appl. Sci.* **2020**, *10*, 365, doi:10.3390/app10010365.

11. Liu, S.; Jia, K.; Wan, H.; Ding, L.; Xu, X.; Cheng, L.; Zhang, S.; Yan, X.; Lu, M.; Ma, G.; et al. Inspection of the internal defects with different size in Ni and Ti additive manufactured components using laser ultrasonic technology. *Opt. Laser Technol.* **2022**, *146*, 107543, doi:10.1016/j.optlastec.2021.107543.

12. Zou, Y.; Chai, Y.; Wang, D.; Li, Y. Measurement of elastic modulus of laser cladding coatings by laser ultrasonic method. *Opt. Laser Technol.* **2022**, *146*, 107567, doi:10.1016/j.optlastec.2021.107567.

13. Zhan, Y.; Liu, C.; Zhang, J.; Mo, G.; Liu, C. Measurement of residual stress in laser additive manufacturing TC4 titanium alloy with the laser ultrasonic technique. *Mater. Sci. Eng. A* **2019**, *762*, 138093, doi:10.1016/j.msea.2019.138093.

14. Everton, S.K.; Dickens, P.; Tuck, C.; Dutton, B. Identification of sub-surface defects in parts produced by additive manufacturing, using laser generated ultrasound. *Mater. Sci. Technol.* **2016**.

15. Zhang, J.; Wu, J.; Zhao, X.; Yuan, S.; Ma, G.; Li, J.; Dai, T.; Chen, H.; Yang, B.; Ding, H. Laser ultrasonic imaging for defect detection on metal additive manufacturing components with rough surfaces. *Appl. Opt.* **2020**, *59*, 10380, doi:10.1364/AO.405284.

16. Pieris, D.; Stratoudaki, T.; Javadi, Y.; Lukacs, P.; Catchpole-Smith, S.; Wilcox, P.D.; Clare, A.; Clark, M. Laser Induced Phased Arrays (LIPA) to detect nested features in Additively Manufactured Components. *Mater. Des.* **2019**, 108412, doi:10.1016/j.matdes.2019.108412.

17. Smith, R.J.; Hirsch, M.; Patel, R.; Li, W.; Clare, A.T.; Sharples, S.D. Spatially resolved acoustic spectroscopy for selective laser melting. *J. Mater. Process. Technol.* **2016**, *236*, 93–102.

18. McKie, A.D.W.; Wagner, J.W.; Spicer, J.B.; Penney, C.M. Laser generation of narrowband and directed ultrasound. *Ultrasonics* **1989**, *27*, 323–330, doi:10.1016/0041-624X(89)90030-9.

19. Hasanian, M.; Choi, S.; Lissenden, C. Laser Ultrasonics for Remote Detection of Stress Corrosion Cracking in Harsh Environments. In Proceedings of the ASNT 27th Annual Research Symposium Proceedings; ASNT, 2018; pp. 106–115.

20. Di Scalea, F.L.; Berndt, T.P.; Spicer, J.B.; Djordjevic, B.B. Remote laser generation of narrowband surface waves through optical fibers. *IEEE Trans. Ultrason. Ferroelectr. Freq. Control* **1999**, *46*, 1551–1557, doi:10.1109/58.808880.

21. Hikata, A.; Elbaum, C. Generation of Ultrasonic Second and Third Harmonics Due to

Dislocations. I. *Phys. Rev.* **1966**, *144*, 469–477, doi:10.1103/PhysRev.144.469.

22. Choi, S.; Nam, T.; Jhang, K.-Y.; Kim, C.S. Frequency response of narrowband surface waves generated by laser beams spatially modulated with a line-arrayed slit mask. *J. Korean Phys. Soc.* **2012**, *60*, 26–30, doi:10.3938/jkps.60.26.

23. Masurkar, F.; Ming Ng, K.; Tse, P.W.; Yelve, N.P. Interrogating the health condition of rails using the narrowband Rayleigh waves emitted by an innovative design of non-contact laser transduction system. *Struct. Heal. Monit.* **2020**, 147592172096760, doi:10.1177/1475921720967600.

24. Ng, K.M.; Masurkar, F.; Tse, P.W.; Yelve, N.P. Design of a new optical system to generate narrowband guided waves with an application for evaluating the health status of rail material. *Opt. Lett.* **2019**, *44*, 5695, doi:10.1364/OL.44.005695.

25. Jun, J.; Seo, H.; Jhang, K.Y. Nondestructive evaluation of thermal aging in Al6061 alloy by measuring acoustic nonlinearity of laser-generated surface acoustic waves. *Metals (Basel).* **2020**, *10*, 38, doi:10.3390/met10010038.

26. Choi, S.; Seo, H.; Jhang, K.-Y. Noncontact Evaluation of Acoustic Nonlinearity of a Laser-Generated Surface Wave in a Plastically Deformed Aluminum Alloy. *Res. Nondestruct. Eval.* **2015**, *26*, 13–22, doi:10.1080/09349847.2014.934496.

27. Nam, T.; Choi, S.; Lee, T.; Jhang, K.Y.; Kim, C.S. Acoustic nonlinearity of narrowband laser-generated surface waves in the bending fatigue of Al6061 alloy. *J. Korean Phys. Soc.* **2010**, *57*, 1212–1217, doi:10.3938/jkps.57.1212.

28. Bakre, C.; Lissenden, C.J. Surface Roughness Effects on Self-Interacting and Mutually Interacting Rayleigh Waves. *Sensors* **2021**, *21*, 5495, doi:10.3390/s21165495.

29. Zhang, S.; Li, X.; Chen, C.; Jeong, H.; Xu, G. Characterization of Aging Treated 6061 Aluminum

Alloy Using Nonlinear Rayleigh Wave. *J. Nondestruct. Eval.* **2019**, *38*, 1–9, doi:10.1007/s10921-019-0630-5.

30. Moghanizadeh, A.; Farzi, A. Effect of heat treatment on an AISI 304 austenitic stainless steel evaluated by the ultrasonic attenuation coefficient. *Mater. Test.* **2016**, *58*, 448–452, doi:10.3139/120.110878.

31. Metya, A.K.; Ghosh, M.; Parida, N.; Balasubramaniam, K. Effect of tempering temperatures on nonlinear Lamb wave signal of modified 9Cr–1Mo steel. *Mater. Charact.* **2015**, *107*, 14–22, doi:10.1016/j.matchar.2015.06.036.

32. Mini, R.S.; Balasubramaniam, K.; Ravindran, P. An Experimental Investigation on the Influence of Annealed Microstructure on Wave Propagation. *Exp. Mech.* **2015**, *55*, 1023–1030, doi:10.1007/s11340-015-0003-7.

33. Abraham, S.T.; Albert, S.K.; Das, C.R.; Parvathavarthini, N.; Venkatraman, B.; Mini, R.S.; Balasubramaniam, K. Assessment of sensitization in AISI 304 stainless steel by nonlinear ultrasonic method. *Acta Metall. Sin. (English Lett.* **2013**, *26*, 545–552, doi:10.1007/s40195-013-0168-y.

34. Galindo-Fernández, M.A.; Mumtaz, K.; Rivera-Díaz-del-Castillo, P.E.J.; Galindo-Nava, E.I.; Ghadbeigi, H. A microstructure sensitive model for deformation of Ti-6Al-4V describing Cast-and-Wrought and Additive Manufacturing morphologies. *Mater. Des.* **2018**, *160*, 350–362, doi:10.1016/j.matdes.2018.09.028.

35. Gorsse, S.; Hutchinson, C.; Gouné, M.; Banerjee, R. Additive manufacturing of metals: a brief review of the characteristic microstructures and properties of steels, Ti-6Al-4V and high-entropy alloys. *Sci. Technol. Adv. Mater.* **2017**, *18*, 584–610, doi:10.1080/14686996.2017.1361305.

36. Krakhmalev, P.; Fredriksson, G.; Yadroitsava, I.; Kazantseva, N.; Plessis, A. du; Yadroitsev, I. Deformation Behavior and Microstructure of Ti6Al4V Manufactured by SLM. *Phys. Procedia* **2016**, *83*, 778–788, doi:10.1016/j.phpro.2016.08.080.

37. Williams, C.; Borigo, C.; Rivière, J.; Lissenden, C.J.; Shokouhi, P. Nondestructive Evaluation of Fracture Toughness in 4130 Steel Using Nonlinear Ultrasonic Testing. *J. Nondestruct. Eval.* **2022**, *41*, 13, doi:10.1007/s10921-022-00846-5.

38. Hurley, D.C.; Balzar, D.; Purtscher, P.T.; Hollman, K.W. Nonlinear ultrasonic parameter in quenched martensitic steels. *J. Appl. Phys.* **1998**, *83*, 4584–4588, doi:10.1063/1.367241.

39. Sahu, M.K.; Swaminathan, J.; Bandhoypadhyay, N.R.; Sagar, S.P. Rayleigh Surface wave based non linear ultrasound to assess effect of precipitation hardening during tempering in P92 steel. *Mater. Sci. Eng. A* **2017**, *703*, 76–84, doi:10.1016/j.msea.2017.07.014.

40. Thiele, S.; Matlack, K.H.; Kim, J.-Y.; Qu, J.; Wall, J.J.; Jacobs, L.J. Assessment of precipitation in alloy steel using nonlinear Rayleigh surface waves.; 2014; pp. 682–689.

41. Matlack, K.H.; Bradley, H.A.; Thiele, S.; Kim, J.-Y.; Wall, J.J.; Jung, H.J.; Qu, J.; Jacobs, L.J. Nonlinear ultrasonic characterization of precipitation in 17-4PH stainless steel. *NDT E Int.* **2015**, *71*, 8–15, doi:10.1016/j.ndteint.2014.11.001.

42. Cantrell, J.H.; Yost, W.T. Effect of precipitate coherency strains on acoustic harmonic generation. *J. Appl. Phys.* **1997**, *81*, 2957–2962, doi:10.1063/1.364327.

**Chapter 6**

# IN-SITU LASER ULTRASOUND-BASED RAYLEIGH WAVE PROCESS MONITORING OF DED-AM METALS[1]

## 6.1 Introduction

The additive manufacturing (AM) of metals is revolutionizing materials processing and component fabrication by using digitally-controlled layered deposition [1,2]. The two main processing routes for metal additive manufacturing are directed energy deposition (DED) and powder bed fusion (PBF). As AM technology matures, it is gaining increasing popularity in industries like aerospace, medical, and defense, where there are strict requirements for part quality [3]. However, the microstructure of AM material is different from conventional materials and can vary locally due to process variability. In some cases, flaws are formed, while in others, the elasticity, strength, fatigue, and fracture properties are affected [4–6]. The instability of the heat source, variations in feedstock material, and random factors during processing are some of the leading causes for the formation of flaws such as lack-of-fusion (LoF), voids, cracks, and undesired microstructure [7]. Thus, there is a high demand for a robust nondestructive technique, particularly an in-situ monitoring technique that can detect processing flaws, thus providing an opportunity to stop a build or repair the defect and thereby increasing the affordability and reliability of AM parts [8,9].

Traditional nondestructive evaluation (NDE) methods are inadequate for quality assurance testing of AM materials; these methods target flaws that occur on the surface or near the surface. However, due to the layer-wise AM deposition process, it is equally likely to have internal defects as surface defects

---

[1] This chapter is largely based on the manuscript:
C. Bakre *et. al*, "In-situ laser ultrasound-based Rayleigh wave process monitoring of DED-AM metals", *Research in Nondestructive Evaluation*, submitted.

[10]. Although x-ray computed tomography (XCT) is well suited for volumetric defect detection, it is not amenable for in-situ monitoring. In addition, it becomes less efficient as the size and complexity of parts increase [11,12]. Various approaches have been investigated for in-situ monitoring of AM builds as outlined in several review articles and surveys [13–17]. The typical strategies used for AM process monitoring include monitoring the melt pool metrics [22,23], part temperature [18,19], layer build height [20–22], laser/e-beam parameters [19], and optical emissions [23–27] during processing. Vision-based techniques such as high-speed camera, pyrometry, and infrared imaging are typically used in the commercial online monitoring modules for monitoring the melt pool. These techniques have shown promise; however, it is difficult to detect internal flaws in-situ due to the complex defect formation mechanism below the build surface [15]. Laser ultrasonics (LU) is being researched for process monitoring of AM because it is noncontact, which allows rapid scanning and offers the advantages of ultrasonic testing [10]. As discussed in Section 2.2.1, currently, LU systems have not been integrated into AM chambers for in-situ process monitoring of AM. However, numerous researchers have carried out ex-situ studies using laser ultrasonics for inspecting AM specimens with a final goal of in-situ process monitoring.

Here, we report on the integration of a laser ultrasonic (LU) system into a DED chamber for in-situ monitoring of defects and microstructure. Although DED-AM is chosen for this research, the developed methods can be extended to PBF. The integrated LU system utilizes linear features, such as scattering and wave speed measurements, to detect material discontinuities and nonlinear features, such as distortion and harmonic generation, to infer microstructural differences. A novelty of the integrated LU system is that it is designed to leverage nonlinear ultrasonic wave propagation features to obtain information about the material microstructure. Interactions between nonlinear material and laser-generated Rayleigh waves cause a trackable distortion of waveform shapes. Therefore, the nonlinear laser-generated Rayleigh waveform evolution can be used to infer microstructural changes during the AM process, caused by variation in the process parameters and conditions. The broadband Rayleigh wave distortion due to nonlinearity is a well-known phenomenon [28–31]. However, to the author's knowledge it has yet to be applied for nondestructive evaluation.

The main objective of this chapter is to demonstrate in-situ monitoring for defects and material non-uniformity in DED Ti-6Al-4V specimens using an integrated laser ultrasound system. First, a detailed description of the integration of the LU system into the DED-AM system is provided and challenges are discussed. Next, the capability of the integrated laser ultrasonic system to detect defects in-situ is demonstrated by three proof-of-concept studies, wherein artificial changes to the DED process are made to intentionally introduce anomalies into the Ti-6Al-4V builds. The in-situ LU results provide indications of the flaws. Finally, the presence of flaws is confirmed by XCT and optical microscopy.

## 6.2 Methods

### 6.2.1 Integration of laser ultrasonic (LU) system in the DED-AM chamber

The integration of the LU system into the DED chamber is the first step towards in-situ defect detection. The AM chamber is a complex environment. The main integration challenges include the limited space inside the DED chamber, positioning the laser generation and reception hardware, protecting the laser optics from airborne metal powder particles, and minimizing system vibration effects. The DED-AM system is described in Section 2.1. This section is divided into three parts, the laser ultrasonic (LU) system, and the integration of the LU system with the DED system.

#### 6.2.1.1 Laser ultrasonic (LU) system

Rayleigh waves are generated using a Q-switched Nd:YAG pulsed laser (Inlite III-10, Continuum, Milpitas, CA, USA). The pulse duration was 6 ns and pulse energies of 45 mJ was used. The 7 mm diameter laser beam is first expanded using a 3X beam expander (Part # 35-099, Edmond Optics Inc., Barrington, NJ, USA), and then reflected using a mirror (Part #38-900, Edmond Optics Inc., Barrington, NJ, USA) onto the beam patterning optics at an oblique incidence of 8 degrees from the vertical. Next, the beam patterning optics create a single line illumination using a cylindrical lens (LJ1703RM-B, Thorlabs Inc., Newton, NJ, USA) or a line-arrayed illumination pattern using a slit mask. The slit mask consists of 13 slits with pitch of 1 mm, and slit lengths of 10 mm. The pitch of the slit mask dictates the wavelength of the Rayleigh waves. Thus, a broadband pulse or a narrowband burst generated the Rayleigh waves on the specimen surface. The lift-off distance from the specimen surface for the cylindrical lens is nominally its focal length (FL = 75 mm), and the lift-off distance for the slit mask was fixed at 1 mm.

A laser interferometer (AIR-1550-TWM, Intelligent Optical Systems Inc., Torrance, CA, USA) is used to measure the out-of-plane displacement of the Rayleigh waves. The laser receiver head is mounted on an XY stage to allow linear scanning along the centerline of the generation laser source. The reception of Rayleigh waves from the AM surface using a laser interferometer poses a significant challenge due to the high surface roughness, which are addressed using the following strategies.

- The laser interferometer used in this study plays a crucial role in obtaining reliable measurements as it is adaptive to varying surface roughness and reflectivity. The laser interferometer provides two outputs: an AC signal and a DC level. The AC signal contains the time-varying voltage proportional to the surface displacements, while the DC level provides a measure of the received light reflected from the surface. Thus, normalizing the AC signal by the DC level provides a means to compare the signals obtained from surfaces with varying surface roughness and reflectivity.
- The surface roughness of AM builds is mainly due to the hatch pattern, powder size, and partially melted powder on the surface. The individual tracks on the surface of the AM specimen give a waviness to the surface texture. This waviness scatters the incident laser beam resulting in decreased light collection and the loss of signal information. Therefore, the incremental distance for the linear scan is chosen to be a multiple of the hatch spacing such that the reception laser beam is always focused approximately on the top of each track, thereby minimizing the loss of signal information.

- The Rayleigh wave propagation distance is kept small to minimize the attenuation caused by surface roughness and diffraction, which enables the SNR to be maintained. The oblique incidence of the generation laser beam on the surface helps to minimize the wave propagation distance.

However, despite these strategies, it is worth mentioning that it is occasionally impossible to receive Rayleigh waves at a particular monitoring point. In such cases, the position of the monitoring point is adjusted to receive a good signal.

#### 6.2.1.2 System Integration

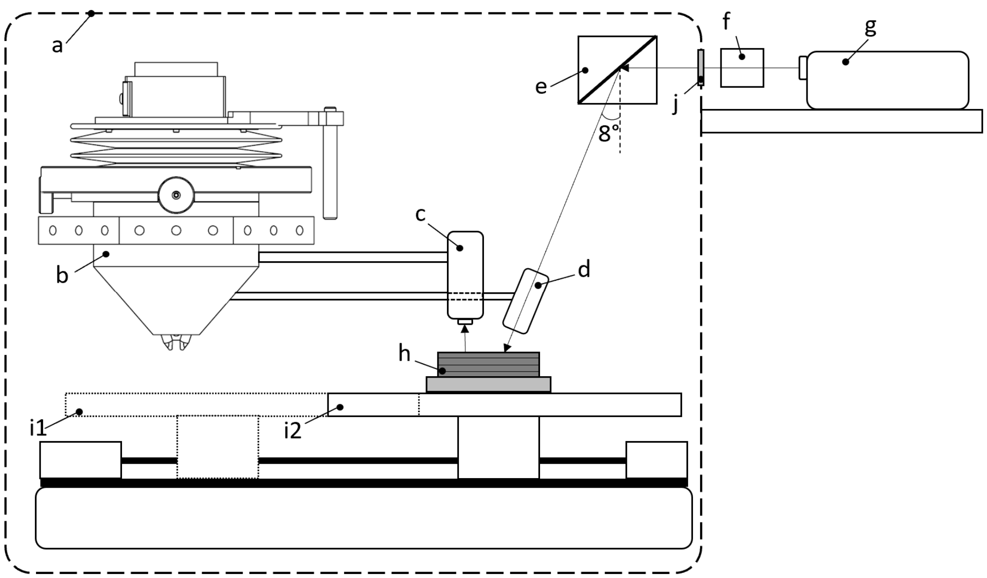


Figure **6-1**. Schematic of the integrated system: a – the DED chamber, b – deposition head, c – reception laser head mounted on an XY stage (not shown), d – beam patterning optics holder, e – mirror, f – beam expander, g – generation laser head, h – AM specimen, i1 – DED stage at the deposition position, i2 – DED stage at LU testing position, j – glass window.

The laser ultrasonic system is fully integrated into the DED system to enable inspection between deposition layers. Figure 6-1 provides a schematic of the setup and Figure 6-2 shows the actual system. The reception laser beam is fiber-delivered into the DED chamber while its control unit is mounted on a rack outside the chamber. Similarly, the generation laser head emits a 1064 nm beam into the DED chamber via a window located on the top right of the DED chamber while its control unit is on the rack. A PC on the rack platform controls the generation laser and the XY stage. An oscilloscope (InfiniiVision MSOX3024T, Keysight, Santa Rosa, 269 CA, USA) is used for signal observation and acquisition..

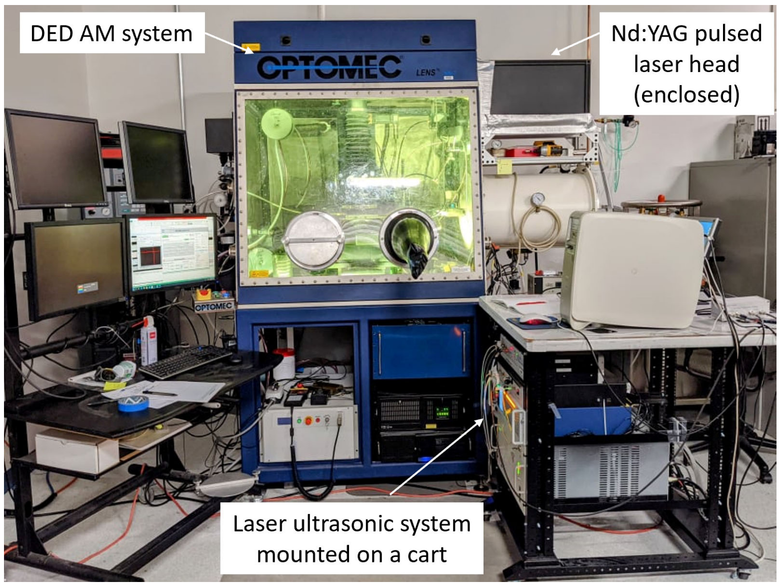


Figure **6-2**. Overview of the integrated system.

With this integrated system material layers are deposited and then the build platform is translated into a position where the LU interrogation is performed, after which the build platform is translated back into position for further deposition. This mode of operation is expected to be too slow for industrial production, thus a system re-design is envisioned whereby the laser heads for interrogation are built into the deposition head to enable interrogation without interrupting deposition.

An aluminum frame is attached to the top of the right-hand side of the DED chamber to provide a platform for the Nd:YAG pulsed laser head and beam expander. The pulsed laser beam is first expanded using the 3X beam expander and then enters horizontally into the DED chamber through an air-tight glass window. Inside the DED chamber, the pulsed laser beam is reflected obliquely towards the specimen using a turning mirror. The oblique incidence enables the reception laser head to be positioned closer to the beam patterning optics. An alternative design could incorporate both beam patterning optics and reception laser head into one fixture. The mirror is mounted inside an enclosure attached to the top of the DED chamber using rails. This arrangement allows the horizontal movement of the mirror. Furthermore, to protect the mirror from the metal powder, an argon purge line is connected to the mirror enclosure to create a positive pressure. The obliquely-incident, pulsed laser beam is then patterned using either a cylindrical lens or a slit mask, held inside a beam patterning optics holder (lens tube) to create a single line or a line-array illumination on the specimen surface. The lens tube is vertically adjusted to achieve an appropriate lift-off distance from the specimen surface. Figure 6-3a shows the experimental setup inside the DED chamber including the coupling of the XY stage, laser receiver head, and beam patterning optics with the DED deposition head. Two Argon purge lines are used to create a gas curtain to protect the reception laser head and the beam patterning optics. Figure 6-3b provides a close-up of the beam patterning optics holder, laser receiver head, and the AM specimen under inspection. The generation and the reception laser beams are marked by red and blue arrows, respectively.

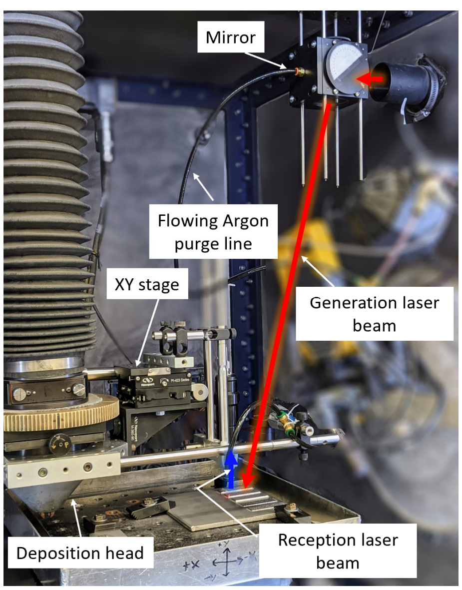


(a)

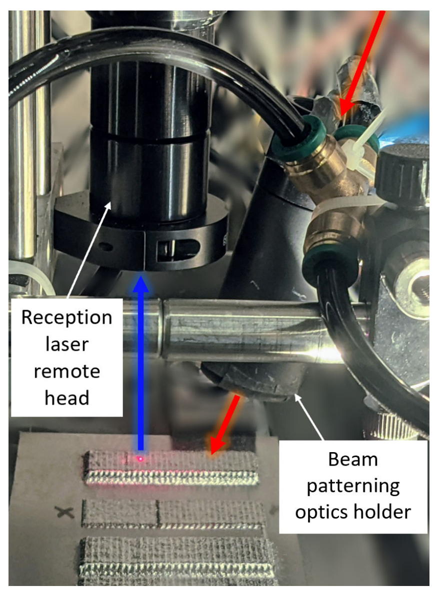


(b)

Figure **6-3**. Photographs of showing the laser integration setup inside the DED chamber.

Table **6-1**. Nominal processing parameters for DED-AM Ti-6Al-4V.

| **Parameters** | **Values** |
| --- | --- |
| Laser power | 450 W |
| Scan speed | 10.6 mm/s |
| Powder flow rate | 2.8 g/min |
| Hatch spacing | 0.81 mm |

Finally, the height of the build increases as the AM layers are deposited. However, it is crucial to maintain the lift-off distance of the laser receiver head and the beam patterning optics (cylindrical lens or slit mask) from the surface of the AM build for laser ultrasonic inspection. Therefore, they are both coupled to the DED deposition head, which moves up by a fixed increment after depositing each layer, thereby maintaining the lift-off distance from the specimen surface.

### 6.2.2 In-situ tests

Based on the experience of some of the co-investigators, we attempted to artificially induce quasi-realistic flaws during processing.

In-situ LU tests are performed after deposition of select layers. After deposition of a pre-determined number of layers using the nominal process parameters given in Table 6-1, the DED stage translates the substrate from a location below the laser deposition head to below the LU generation and reception lasers (the i2 position illustrated in Figure 6-1). Following inspection, the DED stage translates the substrate back below the deposition head (the i1 position illustrated in Figure 6-1) and the DED process is resumed. Three types of defects are artificially seeded by locally changing the deposition process (see Table 6-2):

**Test A** – Skipped hatches: Four Ti-6Al-4V layers are deposited on the baseplate with nominal process parameters. Then a notch-like flaw is induced by skipping two consecutive hatches in two layers.

Finally, two more nominal layers are deposited, during which the metal fills in the gap from the skipped hatches and results in a depressed surface.

Table **6-2**. Build plans for Tests A, B, and C

| | | | |
|---|---|---|---|
| | Two nominal layers | Two nominal layers | One nominal layer |
| | Two layers with two consecutive skipped hatches | Two layers with three consecutive hatches with 1.2 mm hatch spacing | Al powder impurity spread over 15 mm by 25 mm on top surface |
| | Four nominal layers | Four nominal layers | Four nominal layers |
| | Ti-6Al-4V Baseplate | Ti-6Al-4V Baseplate | Ti-6Al-4V Baseplate |
| **Deposition direction** | **Test A – Skipped Hatches** | **Test B – Varied Hatches** | **Test C – Added Impurity** |

**Test B** – Varied hatches: Four nominal Ti-6Al-4V layers are deposited on the baseplate. Then two 'defect layers' are deposited by locally changing the hatch spacing from 0.8 mm (nominal) to 1.2 mm for three consecutive hatches. Finally, two more nominal layers are deposited. The result is that LoF defects are created that extend through the specimen's width.

Note: Each layer of the two defect layers consisted of three steps: (1) Deposit 23 hatches with 0.8 mm hatch spacing, (2) deposit 3 hatches with 1.2 mm hatch spacing, and (3) deposit 56 hatches with the 0.8 mm hatch spacing hatch spacing. However, after completing (1), we failed to increment the sample where the next layer was supposed to be deposited. Therefore, the first hatch of (2) overlapped the last hatch of (1). Similarly, the third hatch of (2) overlapped on the first hatch of (3). This led to a rather complicated flaw geometry depicting two mountains with one hatch in the middle that are separated by two valleys.

**Test C** – Added impurity: Four nominal Ti-6Al-4V layers are deposited on the baseplate. Al powder is spread as an impurity on the surface. The Al powder was held in place by cyanoacrylate. Finally, one nominal layer is deposited on top. The result is that defects such as spherical voids, interface cracks, and surface non-uniformities are observed, along with discoloration of the defect region in the top layer.

### 6.2.3 Rayleigh wave data acquisition and processing

The XY stage scans the laser receiver head along the centerline of the generation laser's illumination pattern. The AC and DC ports of the laser interferometer are connected to the oscilloscope to observe and record the Rayleigh wave signals. To increase the signal-to-noise ratio (SNR), 128 signals are synchronously averaged together. The AC signals are normalized by the DC level. Matlab [32] algorithms are used for further processing the recorded signals.

A Butterworth filter (0.5 MHz – 8 MHz) is applied to the narrowband signals generated from the line-arrayed source, followed by a Hanning window. On the other hand, the broadband signals generated using the cylindrical lens are first filtered using Butterworth filter (0.1 – 20 MHz), but no windowing operation is performed. Furthermore, zero-padding is used to improve the frequency resolution of the Fast Fourier Transform (FFT). The output of Matlab's FFT function is scaled by the time increment to obtain the linear spectrum.

### 6.2.4 X-ray computed tomography and optical microscopy

After deposition, the defect regions of the builds from the three tests are sectioned across the width and then along the length (marked as I and II in Figure 6-4). The sectioned builds are analyzed with X-ray Computed Tomography (XCT). Image stacks (slices) are extracted from the XCT data using the myVGL viewer app (VolumeGraphics.com) along the top and the two side planes. Material discontinuities are labeled and quantified.

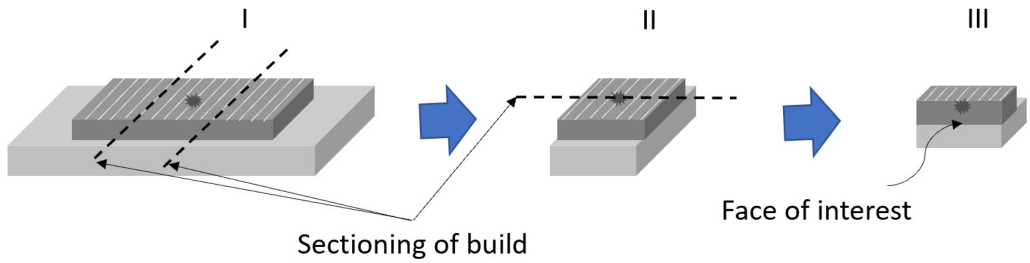


Figure **6-4**. Procedure of sectioning of the builds for XCT and optical microscopy.

A metallographic analysis is then performed by further sectioning the builds along the length through the centerline (marked as III). Next, the exposed face of interest (labeled) is ground and polished using standard metallographic techniques. Finally, the polished faces were etched using Kroll's reagent and imaged using an optical microscope (Nikon Epiphot 200, Nikon USA, Melville, NY, USA).

## 6.3 Results

The results of the three tests (A-C), where LU testing is performed in-situ followed by ex-situ imaging, are discussed in this section. However, here we characterize the flaws first and then provide the ultrasonic results that show the successful detection of flaws. In all cases, Rayleigh wave propagation is along the length of the test specimen and normal to the hatches. The broadband Rayleigh waves have a frequency bandwidth of up to 5 MHz. Thus, the Rayleigh wavelengths vary from approximately 0.6 – 2.9 mm.

### 6.3.1 Test A: Skipped hatches

Skipped hatches create a notch-like flaw that is detected by both broadband pulse and narrowband toneburst Rayleigh wave transmission reduction, as well as pulse reflection. After normal deposition resumed, the buried notch morphs into a more subtle depression in the surface that continues to reduce transmission relative to the nominal condition.

The skipped hatches leave a notch-shaped flaw nominally 0.86 mm deep × 1.8 mm wide × 25 mm long in the defect layers. The test specimen, a sample surface profile, and micrograph are shown in Figure 6-5. The surface profile reveals the valley-like depression feature (maximum depth of approximately 0.26 mm) that resulted from the skipped hatches below the surface, and the micrograph shows that the skipped hatches affected the thermal patterns associated with the melt pool. It is conceivable that the disrupted temperature field could affect the local strength properties. The XCT and optical microscopy conducted after processing revealed no internal discontinuities.

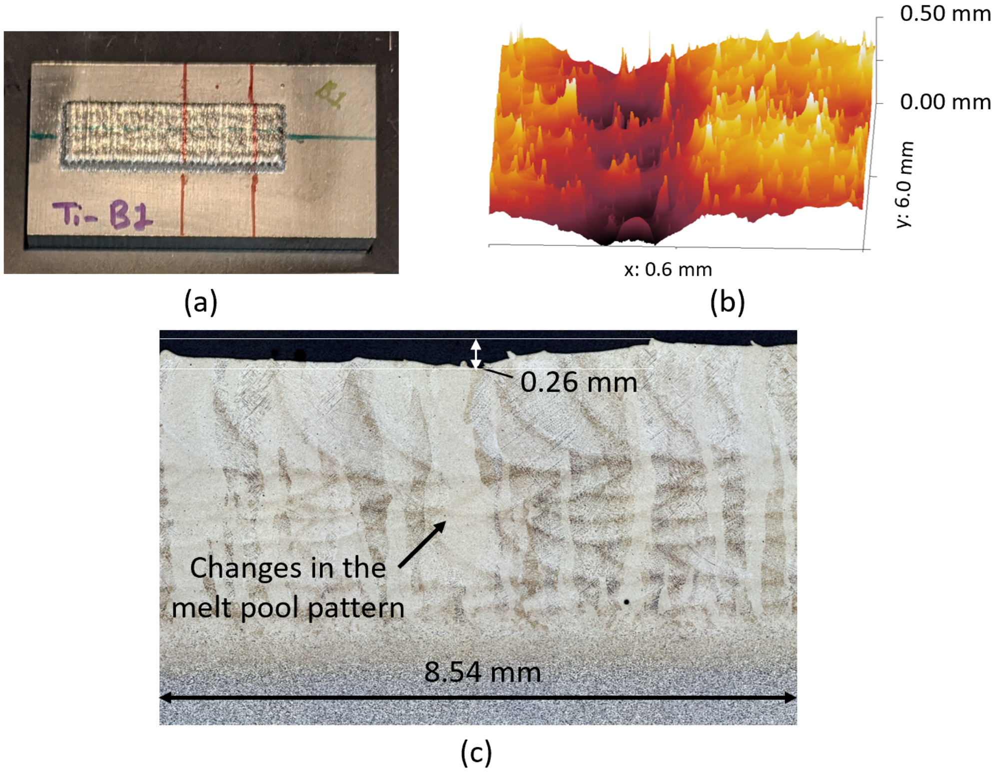


Figure **6-5**. (a) Ti-6Al-4V specimen for Test A, (b) Optical profilometric surface profiles for Test A specimen in the region of flaw, and (c) Optical micrograph showing the surface depression and the changes in the melt pool pattern in the flaw region.

Laser ultrasonic signals are analyzed based on the reduction in the signal amplitude, reflections due to the flaw, and area under the linear spectrum. However, first signal repeatability is addressed by comparing the received signals at Point 1 for Steps 1-3 (Figure 6-6). The pulse generated by the cylindrical lens contains a negative peak followed by a smaller positive peak. The normalized peak-to-peak amplitudes of these pulses and the time period between the peaks are tabulated in Table 6-3.

As described previously, the laser interferometer AC signal is always normalized with respect to the DC signal to account for variable light scattering from the rough surface. Based on Table 6-3, the maximum deviation from the mean values for peak-to-peak amplitudes is 5.03 %, and for the time difference between peaks is 17.72 %. Thus, we note that the signals obtained at similar distances are fairly repeatable. We also observe that the maximum deviation for the time difference between peaks is marginally higher, which is most likely due to the variations in the shape of the positive and negative peaks. In addition, the minimal variations observed in Table 6-3 can also be due to the slight differences in the lift-off distance of the cylindrical lens and the surface of the specimen.

During the longitudinal scan Rayleigh waves were received at points on either side of the flawed region, the signals received at these points are shown in Figure 6-6. The peak-to-peak amplitude ratio (Point 2/Point 1) was 0.95 for Step 1 prior to the skipped hatches, but decreased to 0.47 for Step 2 after the skipped hatches, before recovering to 0.72 after the flaw was buried. The amplitude ratio for Step 1 being less than unity can be explained by attenuation due to the rough surface as well as the evolution of the pulse shape with propagation distance. The much larger reduction in amplitude ratio for Step 2 suggests that the flaw reflects a portion of the Rayleigh wave, which is confirmed in Figure 6-6c, where the elapsed time between the incident pulse and the echo (marked by *) decreases as the reception point (1 -> 2 -> 3) approaches the flaw. The measurement points marked as 1, 2, and 3 are at 2 mm, 1.5 mm, and 1.3 mm distances from the flaw. The time difference between the direct arriving Rayleigh wave pulse and the reflected Rayleigh wave pulse reduces - point 1: 1.36 $\mu$s, point 2: 1.06 $\mu$s, and point 3: 0.927 $\mu$s. The predicted arrival times based on the Rayleigh wave speed closely match the measured time of arrival of the reflected Rayleigh wave pulses. Thus, it is possible to detect the flaw even at lower propagation distances.

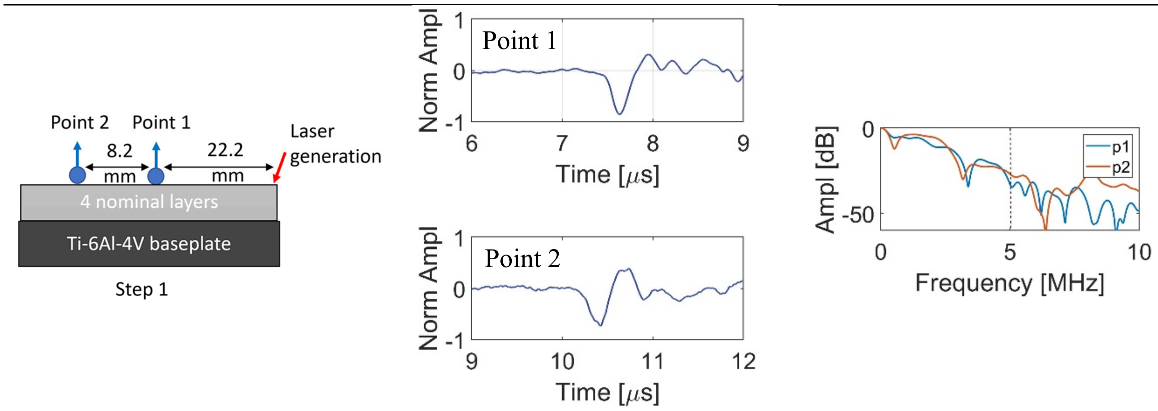

Point 2
Point 1
8.2 mm
22.2 mm
Laser generation
4 nominal layers
Ti-6Al-4V baseplate
Step 1
Point 1
Norm Ampl
Time [$\mu$s]
Point 2
Norm Ampl
Time [$\mu$s]
Ampl [dB]
p1
p2
Frequency [MHz]


(a)

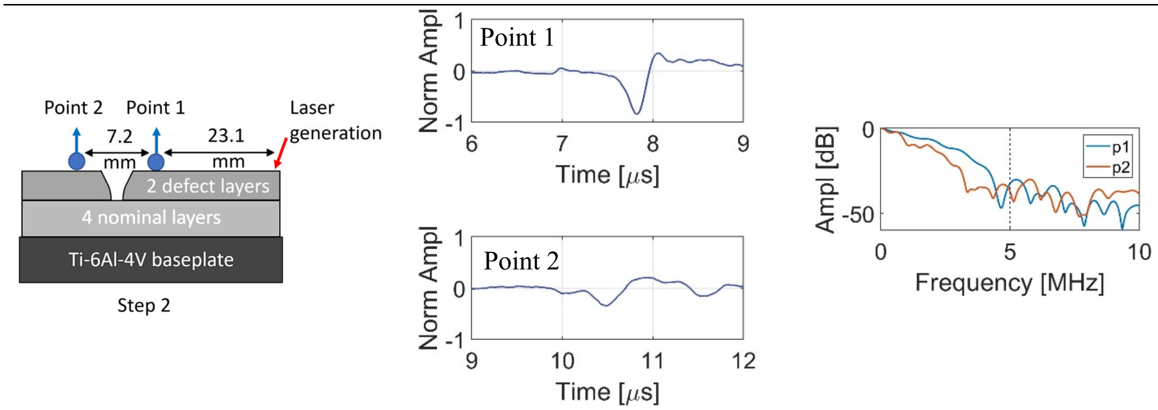

Point 2
Point 1
7.2 mm
23.1 mm
Laser generation
2 defect layers
4 nominal layers
Ti-6Al-4V baseplate
Step 2
Point 1
Norm Ampl
Time [$\mu$s]
Point 2
Norm Ampl
Time [$\mu$s]
Ampl [dB]
p1
p2
Frequency [MHz]


(b)

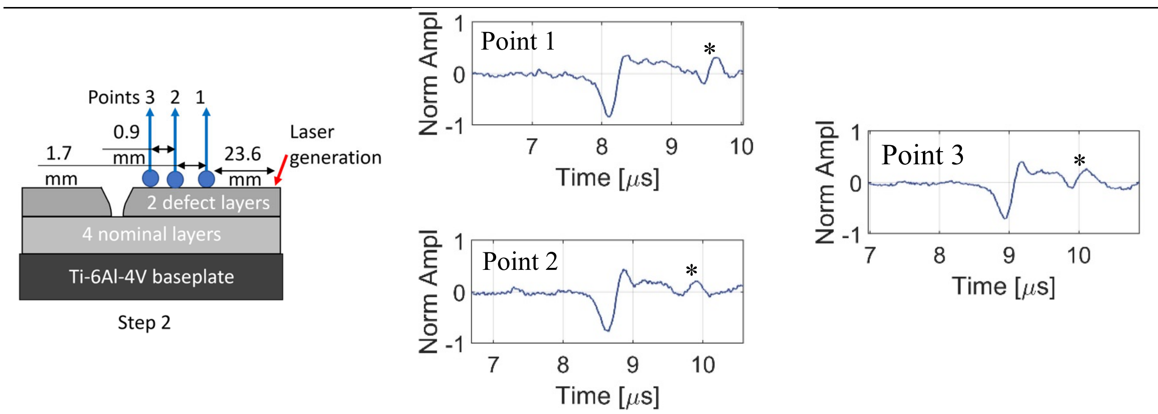

Points 3 2 1
0.9 mm
1.7 mm
23.6 mm
Laser generation
2 defect layers
4 nominal layers
Ti-6Al-4V baseplate
Step 2
Point 1
Norm Ampl
Time [$\mu$s]
Point 2
Norm Ampl
Time [$\mu$s]
Point 3
Norm Ampl
Time [$\mu$s]


(c)

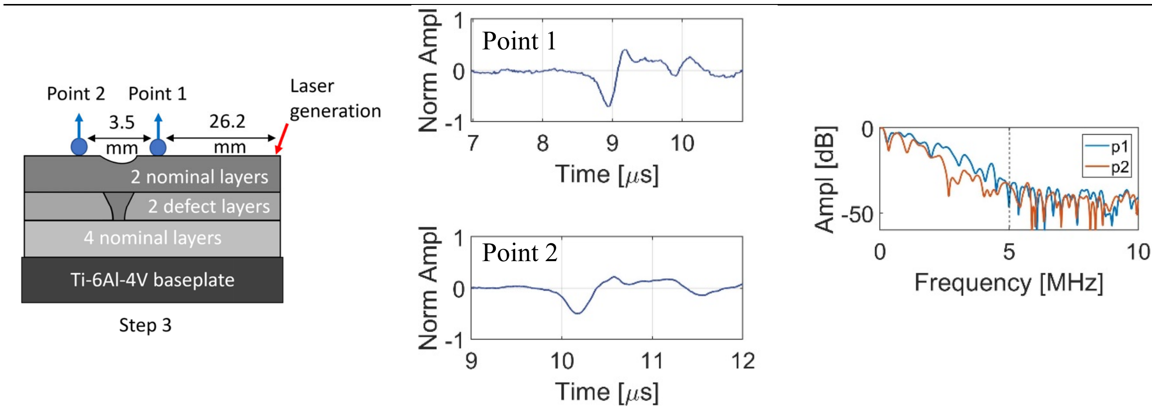


(d)

Figure **6-6**. A-scans and frequency spectra from broadband source for Test A having skipped hatches.

Table **6-3.** The normalized peak-to-peak amplitudes and the time period between the peaks for the pulses shown in Figure 6-6.

| **Shown in** | **Point** | **Propagation Distance (mm)** | **Peak-to-peak** | **Time between peaks (µs)** |
|---|---|---|---|---|
| Fig 6a | 1 | 22.2 | 1.168 | 0.31 |
| Fig 6b | 1 | 23.1 | 1.170 | 0.24 |
| Fig 6d | 1 | 26.2 | 1.225 | 0.26 |
| Fig 6c | 1 | 23.6 | 1.208 | 0.28 |
| Fig 6c | 2 | 25.3 | 1.217 | 0.23 |
| Fig 6c | 3 | 26.2 | 1.126 | 0.26 |

Although the linear spectra are plotted on a dB scale in Figure 6-6, the area under the curve up to 5 MHz is computed based on a linear scale and shown in Table 6-4. Note that these areas can only be compared for each step individually due to the different sampling rates used for different steps.

Table **6-4.** Area under the frequency spectrum (linear scale) up to 5 MHz

| | **Peak-to-peak amplitude ratio** | **Area under frequency spectrum up to 5 MHz (in Hz)** | |
|---|---|---|---|
| **Step** | **Point 2/Point 1** | **Point 1** | **Point 2** |
| 1 | 0.95 | 0.129 | 0.126 |
| 2 | 0.47 | 0.131 | 0.050 |
| 3 | 0.72 | 1.127 | 0.814 |

Passing the pulsed laser beam through the slit mask creates a line-arrayed source that generates a narrowband toneburst Rayleigh wave packet having the wavelength of the slit mask pitch (1 mm). Most of the Rayleigh wave energy is within one wavelength of the surface, therefore for Rayleigh waves having fixed wavelength the material depth being interrogated is known. Given the nominal layer thickness of 429 $\mu$m, the Rayleigh waves penetrate through the top two layers. We demonstrate the capability of the integrated laser ultrasonic system to generate narrowband Rayleigh waves for flaw detection. The key advantage of using narrowband Rayleigh waves is to set a lower limit on the size of the flaw and control the depth at which the flaw needs to be detected. Here, we generated a Rayleigh wave having using a slit mask with a primary frequency of 3 MHz. The inspection strategy used for signal acquisition is shown in the schematic in Fig. 6-6, with the two monitoring points located on either side of the flaw at a distance of 19 mm and 27 mm from the source. Figure 6-7 shows the A-scans and the corresponding spectra for the three steps. For Step 1, when there is no flaw in the propagation path of Rayleigh waves, the reduction in the signal peak-to-peak amplitude from 0.18 to 0.13 is mainly due to the attenuation caused by surface roughness and the beam spreading. The shape of the signal remains largely unaffected. For Step 2, the highest drop in the signal amplitude is observed as the flaw is on the surface. The reduction in the peak-to-peak amplitude is from 0.18 to 0.06, and the shape of the wave packet at Point 2 is moderately altered than the shape at Point1. Finally, for Step 3, the signal amplitude appears to have recovered as the peak-to-peak amplitude reduction is less, 0.17 to 0.10. This observation is consistent with the broadband Rayleigh wave inspections. Furthermore, due to the reverberation of Rayleigh waves from the edges of the surface depression caused by multiple reflections, we observe an increase in the signal length in Fig. 6-7h, and the signal amplitudes appear to be reducing along the tail.

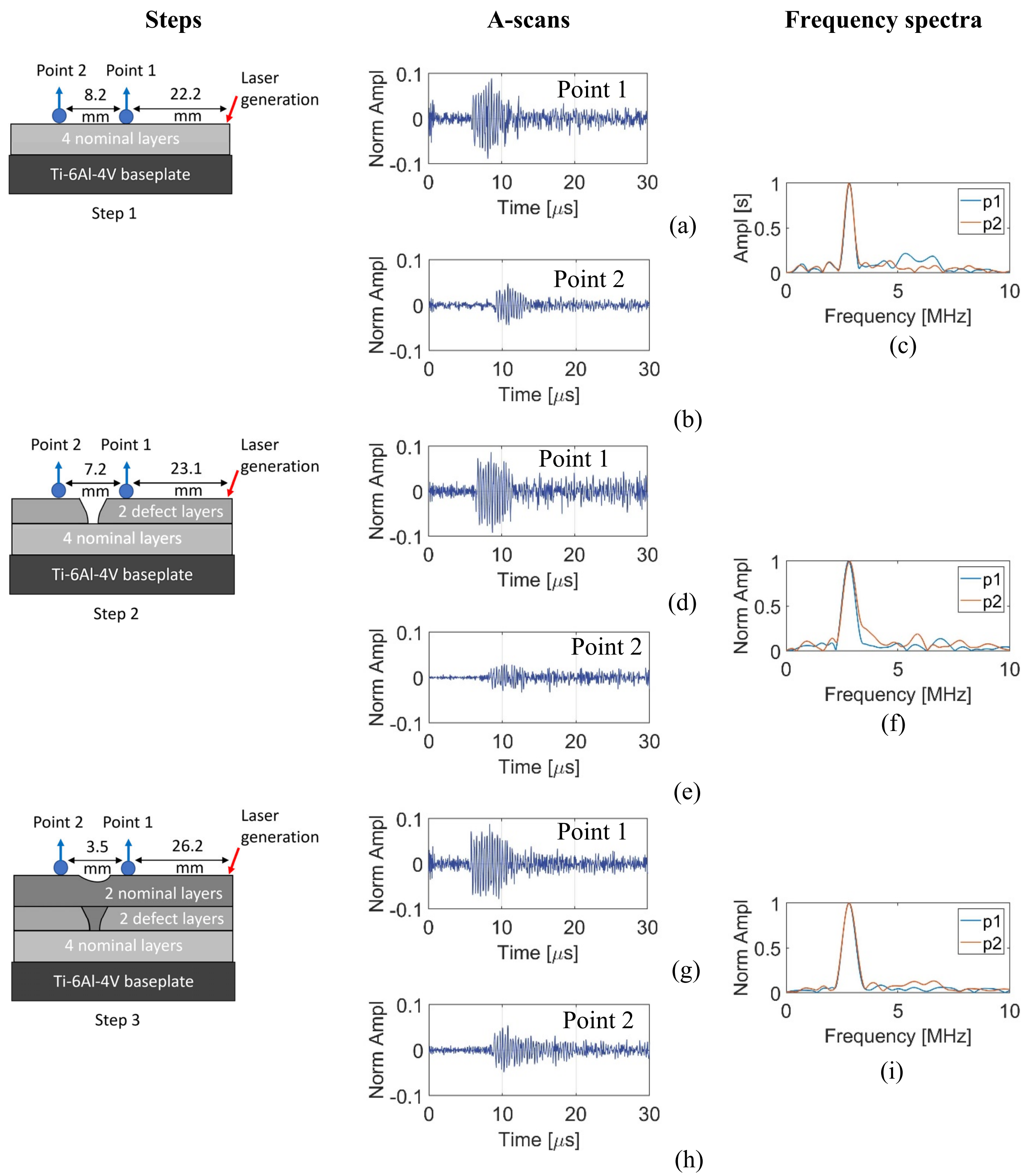


Figure **6-7**. A-scans and frequency spectra from narrowband source for Test A having missing hatches.

### 6.3.2 Test B: Varied hatches

The results of Test B will show that the laser ultrasonic system can detect surface flaws as well as near-surface lack-of-fusion (LoF) flaws using broadband and narrowband Rayleigh waves in-situ. The flaw detection capability is demonstrated based on the reduction in the Rayleigh wave amplitudes and their reflection from the underlying flaw.

The local variation in the hatch spacing from 0.8 mm (nominal) to 1.2 mm for three consecutive hatches and two layers creates a complicated surface geometry. Figure 6-8a shows the specimen for Test B. After depositing the two defect layers, the surface flaw is expected to have two notches separated by a hatch, with each notch having a maximum depth of 0.8 mm, a width of 0.4 mm, and a length of 15 mm. After depositing two more nominal layers atop the two defect layers, the lack-of-fusion (LoF) flaw extending across the AM deposition width is created, as seen in the XCT images shown in Fig. 6-8b. Figure 6-8c shows the optical micrograph of the specimen with various distances and the local change in the melt pool pattern marked.

Figure 6-9 provides the schematics of the four steps of the in-situ LU tests performed at different deposition stages and the results for broadband Rayleigh waves as well as A-scans and the frequency spectra for each step. As described in section 2.3.4, the attenuation mainly affects the higher frequency region of the broadband Rayleigh wave spectrum. This effect can be clearly observed from the A-scans for Step 1 & 2. Firstly, the peak-to-peak amplitude is reduced from 0.28 for Step 1 to 0.25 for Step 2. Secondly, a V-shaped signal is obtained for the baseplate and an inverted-N shaped waveform is obtained for the nominal AM deposition [33]. The changes in the pulse shape can be attributed to the attenuation of higher frequency content due to the significantly higher surface roughness of the AM deposition. In addition, we also observe the reduction of energy in the high frequency region and the contraction of the bandwidth in the frequency spectrum for Step 2 in comparison with Step 1. The peak-to-peak amplitude received on the defect layer in Step 3 decreased from 0.25 to 0.15. In addition, an expansion in the signal pulse is observed due to the surface flaw. Lastly, the peak-to-peak amplitude of signal received after

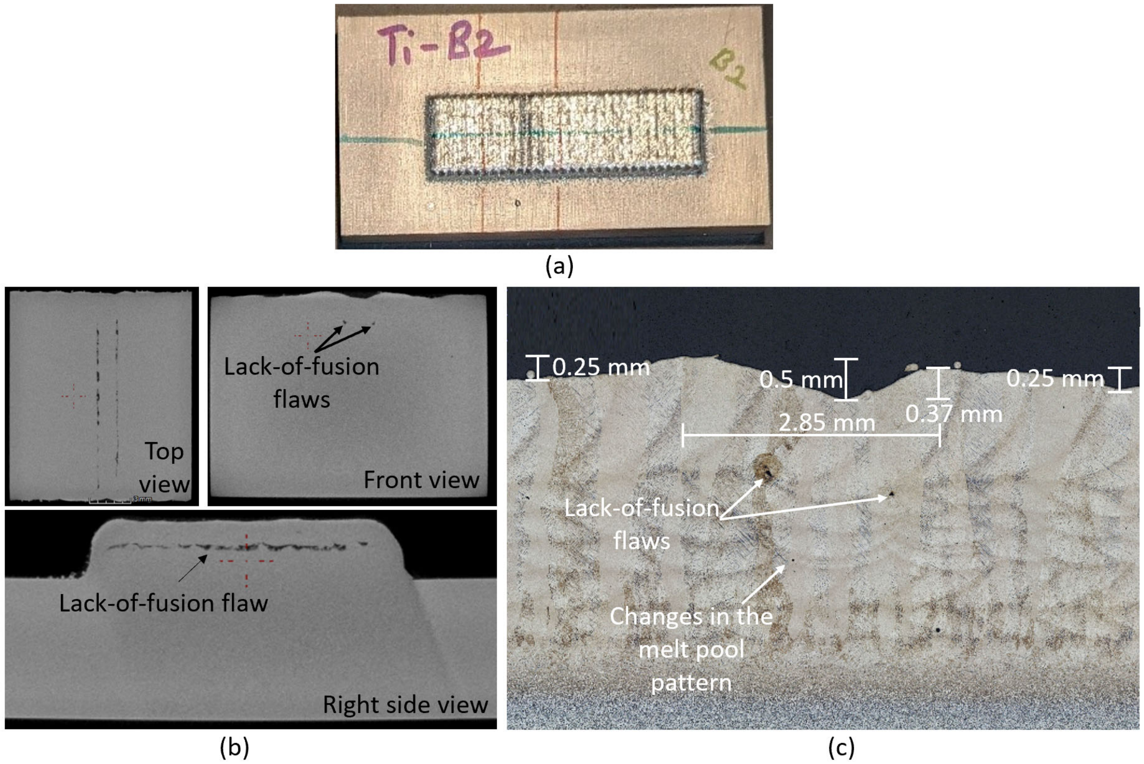


Figure **6-8**. (a) Test specimen for Test B, (b) XCT images showing the lack-of-fusion (LoF) flaw, and (c) Optical micrograph of Front View showing the surface depression and the changes in the melt pool pattern in the flaw region.

deposition two nominal layers in Step 4 partially restores from 0.15 to 0.18. However, the A-scan contains multiple peaks, which could be due to the reflections of the Rayleigh wave due to the buried material discontinuity. A similar phenomenon was observed by Dai et al. [45], where the near-surface defects were inspected using laser-generated Rayleigh waves.

Narrowband Rayleigh waves generated using a slit mask have a primary frequency of 3 MHz. The results are illustrated in Fig. 6-10. For Step 1, high signal amplitude with a low noise floor is observed. Due to the high surface roughness of AM sample, the A-scans obtained for Step 2 have a reduced amplitude and a higher noise floor. Referring to the frequency spectrum for Step 2, we not that the second harmonic is completely attenuated due to the surface roughness effects. A steep reduction in the signal amplitude and an extension in the signal length is observed for Step 3. This effect can be attributed to the attenuation and the reflections of Rayleigh waves caused by the surface anomaly.

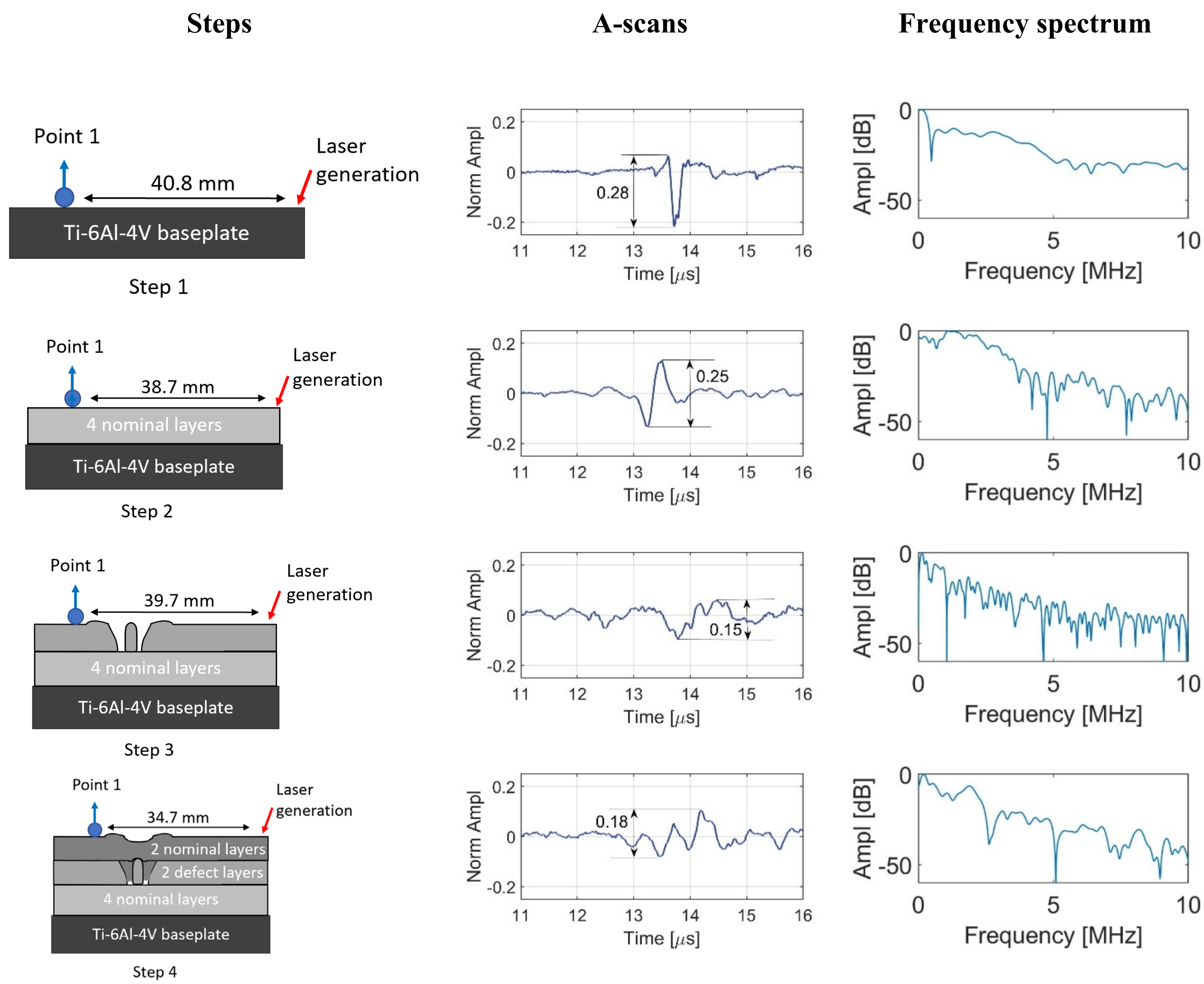


Figure **6-9**. A-scans and frequency spectra from broadband source for Test B having varied hatches.

We also note the high frequency part at the beginning of the wave packet. As a consequence, a second peak has appeared at approx. 6 MHz frequency. The possible cause for it is the mode conversion effect due to the interaction of Rayleigh wave and the surface flaw. However, future work is required to investigate the cause of the high frequency peak seen in the frequency spectrum of Step 3. Lastly, for Step 4, the signal amplitude is higher than Step 3; however, the higher pulse length is still observed. The most likely cause for this is the reflections and mode conversions from the buried material discontinuity. The generation of many higher frequency wave modes is evident from the peaks observed in the frequency spectrum.

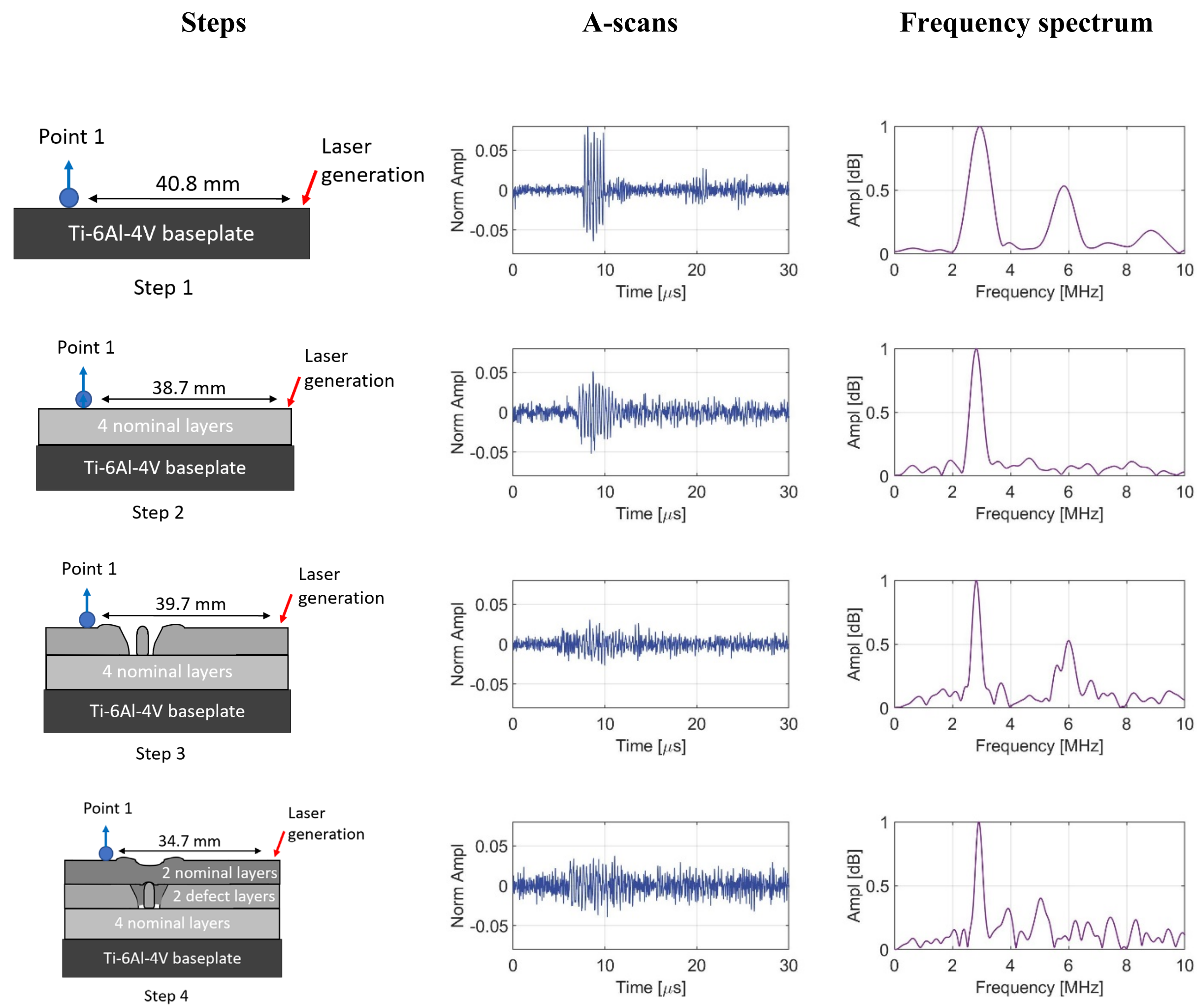


Figure **6-10**. A-scans and frequency spectra from narrowband source for Test B having varied hatches.

### 6.3.3 Test C: Added Impurity

The results from Test C will demonstrate the detection of flaws consisting of localized spherical pores, inclusions, cracks at melt pool boundaries, and surface lumps, using the integrated laser ultrasonic system. The surface non-uniformity created by melting of the added impurity (aluminum powder) can be observed on the test specimen shown in Fig. 6-11. The XCT images in Fig. 6-11 show that the surface lumps contain spherical porosities. The maximum height and the width of the surface lump are 4.86 mm and 7.05 mm as marked. Optical micrographs are shown in Figure 6-12. The discoloration of the region of the layer where the Al powder is infused can be observed in Fig. 6-12aa. The most likely cause of the discoloration is the formation of titanium aluminide intermetallic. Furthermore, the sudden increase in aluminum would lead to a perturbation in vapor pressure in the laser-interaction zone, which may have led to a pore-trapping instability. We note that the grain growth of the columnar prior-beta grains is disrupted at the flaw region of the top layer. This effect can be attributed to the alpha stabilizing property of the aluminum in titanium alloys. In addition, cracks and pores are observed at the melt pool boundaries in the flaw region, as seen in Fig. 6-12b. The adhesive used in the process may have led to the carbide formation that causes cracking. The maximum pore size is 0.08 mm.

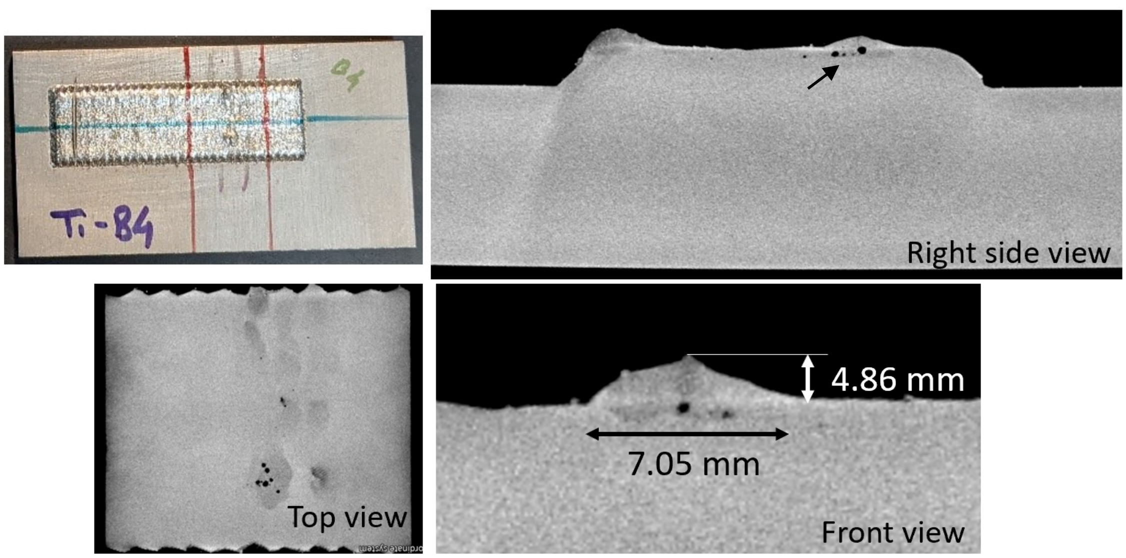


Figure **6-11**. Test specimen for Test C and XCT scan images showing formation of voids from different views.

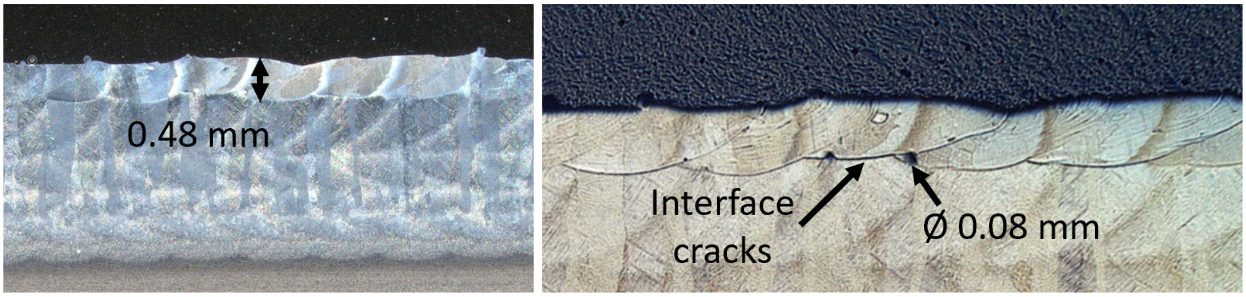


(a) (b)

Figure **6-12**. Optical micrographs showing the (a) microstructural change (discoloration) and (b) formation of voids.

In-situ laser ultrasonic testing is carried out and the results at two monitoring points located at 24 mm and 29 mm from the laser source are presented. Figure 6-13 presents the schematic of the two steps of interrupted in-situ laser ultrasonic testing. The A-scans and the frequency spectra observed at monitoring points 1 for Steps 1 & 2 have a similar form and peak-to-peak amplitudes (0.36 and 0.31, respectively). The spectral distribution of the energy is also relatively similar, as expected, since flaw is not in the propagation path of Rayleigh waves. The signal received at monitoring point 2 for Step 1 has a slightly different pulse shape and a lower peak-to-peak amplitude of 0.23, primarily caused by the attenuation of the signal due to surface roughness. However, for monitoring point 2, the waveform shape and the signal amplitude are drastically different (0.087 peak-to-peak) for Step 2. The time of arrival of the signal is also noticeably larger. Implying that, aluminum impurity changes the elastic coefficients in the flaw region of the top layer and affects the Rayleigh wave speed. The substantially reduced amplitude of the time domain signal and the emergence of new peaks in the lower frequency region of the frequency spectrum indicate the in-situ detection of the flaw.

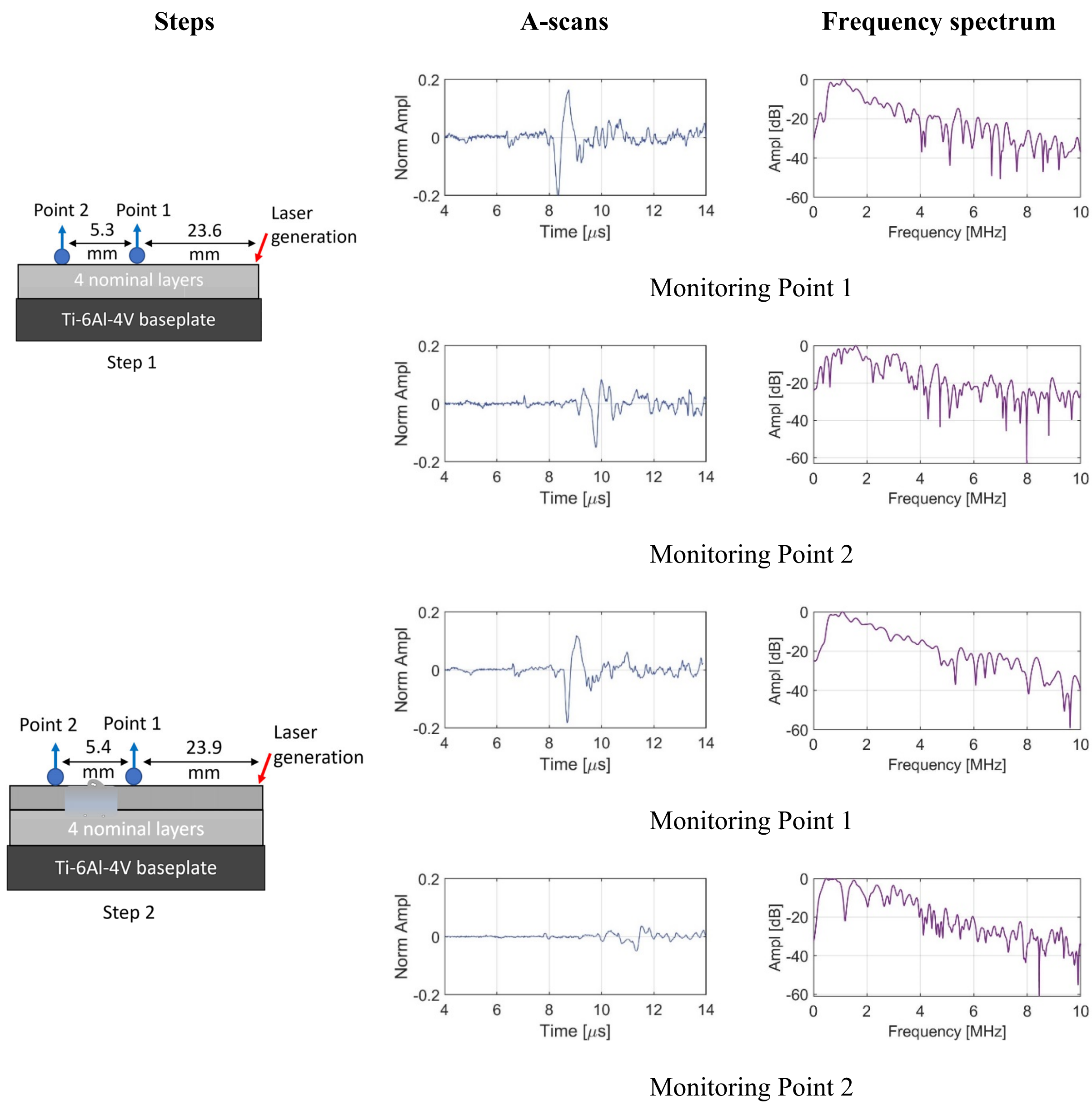


Figure **6-13.** A-scans and frequency spectra from broadband source for Test C having an added impurity.

## 6.4 Conclusions

The proposed laser ultrasonic system integration into the DED chamber is carried out successfully to enable in-situ detection of AM depositions. Three defect detection studies are conducted in which realistic AM defects are introduced by locally altering the AM process. These include skipping hatches, locally changing the hatch spacing, and added impurity, resulting in a surface flaw, near-surface lack-of-fusion flaw, and intermetallic and surface lumps formation. Laser ultrasonic results are provided at different stages of the deposition process (viz, defect-free nominal deposition, deposition with the introduced anomaly, and deposition of nominal layers on top of the defected layers), indicate successful detection using the integrated system. In addition, the capability of the laser ultrasonic system to use both narrowband and broadband Rayleigh waves for part interrogation is shown.

## 6.5 References


1. Wong, K. V; Hernandez, A. A Review of Additive Manufacturing. *ISRN Mech. Eng.* **2012**, *2012*, 1–10, doi:10.5402/2012/208760.
2. Brandt, M. *Laser Additive Manufacturing*; Elsevier, 2017; ISBN 9780081004333.
3. Kim, H.; Lin, Y.; Tseng, T.-L.B. A review on quality control in additive manufacturing. *Rapid Prototyp. J.* **2018**, *24*, 645–669, doi:10.1108/RPJ-03-2017-0048.
4. Galindo-Fernández, M.A.; Mumtaz, K.; Rivera-Díaz-del-Castillo, P.E.J.; Galindo-Nava, E.I.; Ghadbeigi, H. A microstructure sensitive model for deformation of Ti-6Al-4V describing Cast-and-Wrought and Additive Manufacturing morphologies. *Mater. Des.* **2018**, *160*, 350–362, doi:10.1016/j.matdes.2018.09.028.
5. Brennan, M.C.; Keist, J.S.; Palmer, T.A. Defects in Metal Additive Manufacturing Processes. *J. Mater. Eng. Perform.* **2021**, *30*, 4808–4818, doi:10.1007/s11665-021-05919-6.
6. Snow, Z.; Nassar, A.R.; Reutzel, E.W. Invited Review Article: Review of the formation and impact of flaws in powder bed fusion additive manufacturing. *Addit. Manuf.* **2020**, *36*, 101457, doi:10.1016/j.addma.2020.101457.
7. Gong, H.; Rafi, K.; Gu, H.; Starr, T.; Stucker, B. Analysis of defect generation in Ti-6Al-4V parts made using powder bed fusion additive manufacturing processes. *Addit. Manuf.* **2014**, *1*, 87–98, doi:10.1016/j.addma.2014.08.002.
8. Mazumder, J. Design for Metallic Additive Manufacturing Machine with Capability for "Certify

as You Build." *Procedia CIRP* **2015**, *36*, 187–192, doi:10.1016/j.procir.2015.01.009.

9. Chua, Z.Y.; Ahn, I.H.; Moon, S.K. Process monitoring and inspection systems in metal additive manufacturing: Status and applications. *Int. J. Precis. Eng. Manuf. Technol.* **2017**, *4*, 235–245, doi:10.1007/s40684-017-0029-7.
10. Honarvar, F.; Varvani-Farahani, A. A review of ultrasonic testing applications in additive manufacturing: Defect evaluation, material characterization, and process control. *Ultrasonics* **2020**, *108*, 106227, doi:10.1016/j.ultras.2020.106227.
11. Malekipour, E.; El-Mounayri, H. Common defects and contributing parameters in powder bed fusion AM process and their classification for online monitoring and control: a review. *Int. J. Adv. Manuf. Technol.* **2018**, *95*, 527–550, doi:10.1007/s00170-017-1172-6.
12. Cerniglia, D.; Scafidi, M.; Pantano, A.; Rudlin, J. Inspection of additive-manufactured layered components. *Ultrasonics* **2015**, *62*, 292–298, doi:10.1016/j.ultras.2015.06.001.
13. Reutzel, E.W.; Nassar, A.R. A survey of sensing and control systems for machine and process monitoring of directed-energy, metal-based additive manufacturing. *Rapid Prototyp. J.* **2015**, *21*, 159–167, doi:10.1108/RPJ-12-2014-0177.
14. Boddu, M.R.; Landers, R.G.; Liou, F.W. Control of laser cladding for rapid prototyping--A review. In Proceedings of the 2001 International Solid Freeform Fabrication Symposium; 2001.
15. Everton, S.K.; Hirsch, M.; Stravroulakis, P.; Leach, R.K.; Clare, A.T. Review of in-situ process monitoring and in-situ metrology for metal additive manufacturing. *Mater. Des.* **2016**, *95*, 431–445, doi:10.1016/j.matdes.2016.01.099.
16. Tapia, G.; Elwany, A. A Review on Process Monitoring and Control in Metal-Based Additive Manufacturing. *J. Manuf. Sci. Eng.* **2014**, *136*, doi:10.1115/1.4028540.
17. Foster, B.K.; Reutzel, E.W.; Nassar, A.R.; Dickman, C.J.; Hall, B.T. A brief survey of sensing for metal-based powder bed fusion additive manufacturing.; Harding, K.G., Yoshizawa, T., Eds.; 2015; p. 94890B.
18. Bi, G.; Gasser, A.; Wissenbach, K.; Drenker, A.; Poprawe, R. Identification and qualification of

temperature signal for monitoring and control in laser cladding. *Opt. Lasers Eng.* **2006**, *44*, 1348–1359, doi:10.1016/J.OPTLASENG.2006.01.009.

19. Song, L.; Mazumder, J. Feedback control of melt pool temperature during laser cladding process. *IEEE Trans. Control Syst. Technol.* **2011**, *19*, 1349–1356, doi:10.1109/TCST.2010.2093901.
20. Fathi, A.; Khajepour, A.; Toyserkani, E.; Durali, M. Clad height control in laser solid freeform fabrication using a feedforward PID controller. *Int. J. Adv. Manuf. Technol.* **2007**, *35*, 280–292, doi:10.1007/s00170-006-0721-1.
21. Zeinali, M.; Khajepour, A. Height Control in Laser Cladding Using Adaptive Sliding Mode Technique: Theory and Experiment. *J. Manuf. Sci. Eng.* **2010**, *132*, doi:10.1115/1.4002023.
22. Heralić, A.; Christiansson, A.-K.; Lennartson, B. Height control of laser metal-wire deposition based on iterative learning control and 3D scanning. *Opt. Lasers Eng.* **2012**, *50*, 1230–1241, doi:10.1016/j.optlaseng.2012.03.016.
23. Song, L.; Mazumder, J. Real time Cr measurement using optical emission spectroscopy during direct metal deposition process. *IEEE Sens. J.* **2012**, *12*, 958–964, doi:10.1109/JSEN.2011.2162316.
24. Stutzman, C.B.; Nassar, A.R.; Reutzel, E.W. Multi-sensor investigations of optical emissions and their relations to directed energy deposition processes and quality. *Addit. Manuf.* **2018**, *21*, 333–339, doi:10.1016/j.addma.2018.03.017.
25. Stutzman, C.B.; Mitchell, W.F.; Nassar, A.R. Optical emission sensing for laser-based additive manufacturing—What are we actually measuring? *J. Laser Appl.* **2021**, *33*, 012010, doi:10.2351/7.0000321.
26. Dunbar, A.J.; Nassar, A.R. Assessment of optical emission analysis for in-process monitoring of powder bed fusion additive manufacturing. *Virtual Phys. Prototyp.* **2018**, *13*, 14–19, doi:10.1080/17452759.2017.1392683.
27. Montazeri, M.; Nassar, A.R.; Dunbar, A.J.; Rao, P. In-process monitoring of porosity in additive manufacturing using optical emission spectroscopy. *IISE Trans.* **2020**, *52*, 500–515,

doi:10.1080/24725854.2019.1659525.

28. Hamilton, M.F.; Il'inskii, Y.A.; Zabolotskaya, E.A. Nonlinear surface acoustic waves in crystals. *J. Acoust. Soc. Am.* **1999**, *105*, 639–651, doi:10.1121/1.426255.

29. Kolomenskii, A.A.; Lioubimov, V.A.; Jerebtsov, S.N.; Schuessler, H.A. Nonlinear surface acoustic wave pulses in solids: Laser excitation, propagation, interactions (invited). *Rev. Sci. Instrum.* **2003**, *74*, 448–452, doi:10.1063/1.1517188.

30. Gusev, V.E.; Lauriks, W.; Thoen, J. New evolution equations for the nonlinear surface acoustic waves on an elastic solid of general anisotropy. *J. Acoust. Soc. Am.* **1998**, *103*, 3203–3215, doi:10.1121/1.423036.

31. Gusev, V.E.; Lauriks, W.; Thoen, J. Theory for the time evolution of nonlinear Rayleigh waves in an isotropic solid. *Phys. Rev. B* **1997**, *55*, 9344–9347, doi:10.1103/PhysRevB.55.9344.

32. Frigo, M.; Johnson, S.G. FFTW: an adaptive software architecture for the FFT. In Proceedings of the Proceedings of the 1998 IEEE International Conference on Acoustics, Speech and Signal Processing, ICASSP '98 (Cat. No.98CH36181); IEEE; Vol. 3, pp. 1381–1384.

33. Lomonosov, A.; Mayer, A.P.; Hess, P. 3. Laser-based surface acoustic waves in materials science. In; 2001; pp. 65–134.

# Chapter 7

# LASER-BASED SURFACE WAVE DISTORTION TECHNIQUE FOR IN-SITU MICROSTRUCTURAL SENSING OF ADDITIVE MANUFACTURING[1]

## 7.1 Introduction

Additive manufacturing (AM) is a promising technology for manufacturing a wide range of structures and complex geometries directly from computer-aided design (CAD) files. The rapid on-demand fabrication of parts has attracted many high-value applications in the medical, aerospace, and defense sectors. However, the AM technology is still maturing, and the complex physical and metallurgical processes during deposition may lead to undesired microstructure in the final part. The phase transitions, thermal behavior, and melt pool behavior during the AM process strongly depend on the process parameters such as hatch spacing, processing speed, laser power and are difficult to observe in real-time [1]. Subtle changes in the process parameters can lead to undesired microstructure in a part or variability from one part to another [2]. Thus, an in-situ monitoring technique capable of sensing the changes in the microstructure of the part is highly demanded.

Numerous in-situ monitoring strategies have been explored for additive manufacturing; laser ultrasonics is considered one of the promising candidates. Several review articles have been published on in-situ monitoring of AM [3–5]. Monitoring the electron or laser beam characteristics, process characteristics, and motion characteristics are the typical strategies used for in-situ AM monitoring [6,7]. Another common strategy is the study of melt pool dynamics, as it is critical in determining the quality of the AM deposition. These studies typically use vision-based techniques to monitor and control melt pool

[1] This chapter is based largely on the manuscript:
C. Bakre *et. al*, "Laser-based surface wave distortion technique for in-situ microstructural sensing of additive manufacturing", *Scientific Reports*, in preparation.

parameters. The ultrasonic techniques for in-situ monitoring of AM are of particular interest due to their ability to detect internal defects and high sensitivity. Honarvar and Farahani [8] conducted an in-depth review of the ultrasonic techniques for nondestructive testing of AM. While most traditional techniques are impractical for in-situ monitoring of AM, laser ultrasound is identified as one of the suitable candidates as it is noncontact [9,10]. Thus, a tremendous amount of research is currently underway on laser ultrasonic in-situ monitoring of AM [11–17].

Here, we present the first integrated laser ultrasonic system capable of detecting changes in the microstructure of AM depositions instilled by subtle variations in the process parameters. A detailed description of the integration of the laser ultrasonic system in the DED chamber and defect detection studies are discussed in Chapter 6. This chapter covers the capability of the integrated laser ultrasonic system to detect the changes in the microstructure of AM part, in-situ, using nonlinear broadband Rayleigh waves. The integrated laser ultrasonic system generates and receives high-amplitude broadband Rayleigh waves on DED specimens. While linear (small-amplitude) ultrasonic methods can detect material discontinuities having sizes comparable to their wavelength, they are less sensitive to microstructural changes in the material. On the other hand, nonlinear (finite-amplitude) ultrasonic methods are known to be highly sensitive to the changes in the microstructure of the material [18]. Nonlinear ultrasonic methods have been applied to characterize damage progression and microstructural changes for various applications such as early-stage fatigue damage [19,20], precipitate hardening [21], and plastic deformation [22].

The main novelty of this research is investigating the use of broadband Rayleigh waves for nonlinear ultrasonic characterization. The majority of the studies concerning nonlinear ultrasonics, theoretical and experimental, only treat narrowband ultrasonic waves [23,24]. The broadband nonlinear Rayleigh wave phenomenon has also been studied in detail; however, the focus of these studies was mainly to develop a mathematical model to describe the temporal distortion of broadband Rayleigh waves in a nonlinear medium [25–28]. To the author’s best knowledge, the nonlinear broadband Rayleigh wave phenomenon has not been applied to detect the changes in the microstructure or to inspect the material degradation in general. So, this research aims to bring forth the applicability of nonlinear broadband Rayleigh waves using laser ultrasound for microstructural sensing and demonstrate their use in detecting subtle variations in DED process parameters, in-situ. Specifically, we aim to demonstrate that the nonlinear evolution of Rayleigh waveforms with increasing propagation distance or laser energy differs for DED-built titanium alloy and nickel alloy specimens processed with different process parameters due to their microstructures.

The organization of the chapter is as follows: (i) The laser ultrasonic setup integrated into the DED chamber is described. (iii) The in-situ laser ultrasonic testing conducted on DED-built titanium and nickel specimen having varying process parameters is described. (iii) Finally, the evolution of a broadband pulse is studied from the physics of wave propagation perspective. The presented test results successfully differentiate AM depositions having different process parameters.

## 7.2 Methods

The systems used to accomplish the objectives of this chapter are the same as described in Chapter 6. The only differences are in the deposition of the Ti-6Al-4V and IN-718 builds and the experimental procedures of the laser ultrasonic tests, which are described in the following section.

### 7.2.1 DED deposition and in-situ laser ultrasonic tests

#### 7.2.1.1 DED Ti-6Al-4V depositions with identical process parameters

First, we demonstrate the repeatability of the waveform evolution for Ti-6Al-4V specimens deposited using identical process parameters. In-situ linear scanning tests are performed on three Ti-6Al-4V specimens deposited using process parameters provided in Table 7.1. Here we refer to the deposition made by these process parameters as nominal depositions for Ti-6Al-4V. Each deposition consists of four layers deposited atop the Ti-6Al-4V baseplate. The energy of the generation laser is 60 mJ with an 8 Hz repetition rate. The results are shown for two monitoring points at 23 mm and 35 mm propagation distances.

#### 7.2.1.2 DED Ti-6Al-4V and IN-718 specimen with varying process parameters

The DED builds are created such that the subtle changes in the process parameters will affect the part microstructure, but no material discontinuities would be created. The variations in the process parameters are decided based on the previous research carried out on the same additive manufacturing system and the experience of collaborators at Penn State's CIMP-3D.

**DED Ti-6Al-4V**

The in-situ laser ultrasonic tests are performed for DED Ti-6Al-4V specimens with varied deposition power and hatch spacing. Two separate builds, Build 1 and Build 2, are created for the varied deposition power and hatch spacing, respectively. The build plans and the laser ultrasonic testing for the two builds are shown in Figure 7-1. Build 1 contains eight AM layers deposited atop Ti-6Al-4V baseplate – the bottom four layers are deposited with the nominal process parameters provided in Table 7-1, and the top four layers are deposited with 15% lower deposition power (from 450 W (nominal) to 380 W (varied)); other parameters remain unchanged. Build 2 also has eight AM layers deposited atop Ti-6Al-4V baseplate – the bottom four layers are deposited with nominal process parameters, and the top four layers are deposited with 0.1 mm higher hatch spacing (from 0.8 mm (nominal) to 0.9 mm (varied)); other parameters unchanged). We provide in-situ laser ultrasonic results for

- Ti-6Al-4V baseplate,
- Four AM layers deposited using nominal process parameters,
- Four AM layers with varied power (other parameters unchanged),
- Four AM layers depositions with varied hatch spacing (other parameters unchanged).

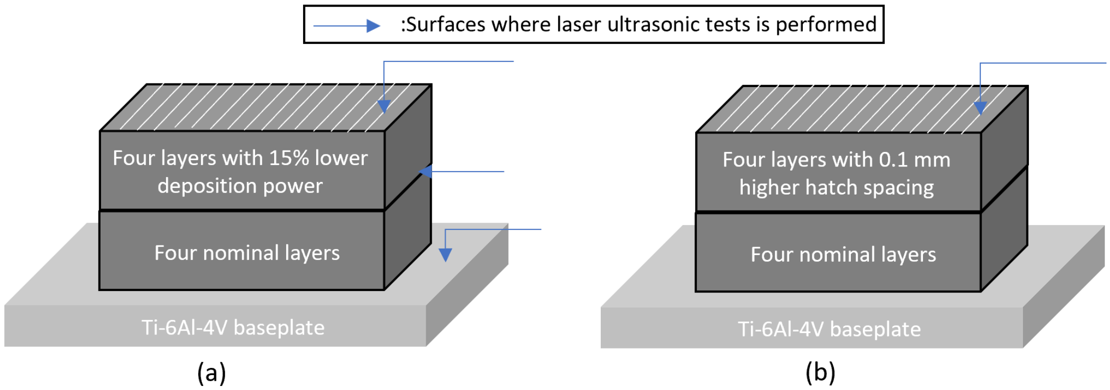


Figure **7-1**. Schematic showing the build plan and laser ultrasonic testing for DED Ti-6Al-4V specimens (a) Build 1 – deposition power varied and (b) Build 2 – hatch spacing varied.

Table **7-1**. Nominal processing parameters of DED-AM Ti-6Al-4V

| **Parameters** | **Values** |
|---|---|
| Laser power | 450 W |
| Scan speed | 10.6 mm/s |
| Powder flow rate | 2.8 g/min |
| Hatch spacing | 0.8 mm |

**DED IN-718**

The in-situ tests are performed on three DED IN-718 builds with varied process parameters. The nominal process parameters for IN-718 builds are provided in Table 7-2. The build plan and laser ultrasonic testing for the three builds – Builds 3-5, are shown in Figure 7-2.

Build 3 – Pulsed-wave deposition: Build 3 consists of 8 layers deposited atop an IN-718 baseplate. First, four layers are deposited with nominal process parameters, which uses a continuous laser beam. The top four layers are deposited using a pulsed laser beam. The other process parameters for the top four layers are enlisted in Table 7-2.

Build 4 – Processing speed varied: Build 4 consists of 12 layers deposited atop an IN-718 baseplate. The bottom four layers are deposited with nominal process parameters (10.6 mm/s). Next, four more layers are deposited with 9.3 mm/s processing speed (other parameters unchanged). Finally, four more layers are deposited with 11.8 mm/s processing speed (other parameters unchanged).

Build 5 – Hatch spacing varied: Build 5 also consists of 12 layers deposited atop an IN-718 baseplate. The first four layers are deposited with nominal process parameters (0.6 mm hatch spacing. The next four more layers are deposited with 0.75 mm hatch spacing (other parameters unchanged). Lastly, top four layers are deposited with 0.85 mm hatch spacing (other parameters unchanged).

Two types of in-situ laser ultrasonic tests are performed for the Ti-6Al-4V and IN-718 builds: (1) PROPAGATION DISTANCE VARIATION TEST: with fixed generation laser energy of 60 mJ and increasing propagation distance, and (2) INITIAL AMPLITUDE VARIATION TEST: with fixed propagation distance of 23 mm and increasing generation laser energy (initial amplitudes). For the first case, we provide results obtained at 23 mm and 39 mm propagation distances, and for the second case, we provide results at 30 mJ (thermoelastic regime) and 120 mJ (ablative regime).

Table **7-2**. Processing parameters for nominal and pulsed wave DED-AM IN718 depositions

| **Parameters** | **Nominal deposition** | **Pulsed wave (PW) deposition** |
|---|---|---|
| Laser power | 400 W | 400 W |
| Scan speed | 10.6 mm/s | 5.3 mm/s |
| Powder flow rate | 5.9 g/min | 3 g/min |
| Hatch spacing | 0.6 mm | 0.6 mm |

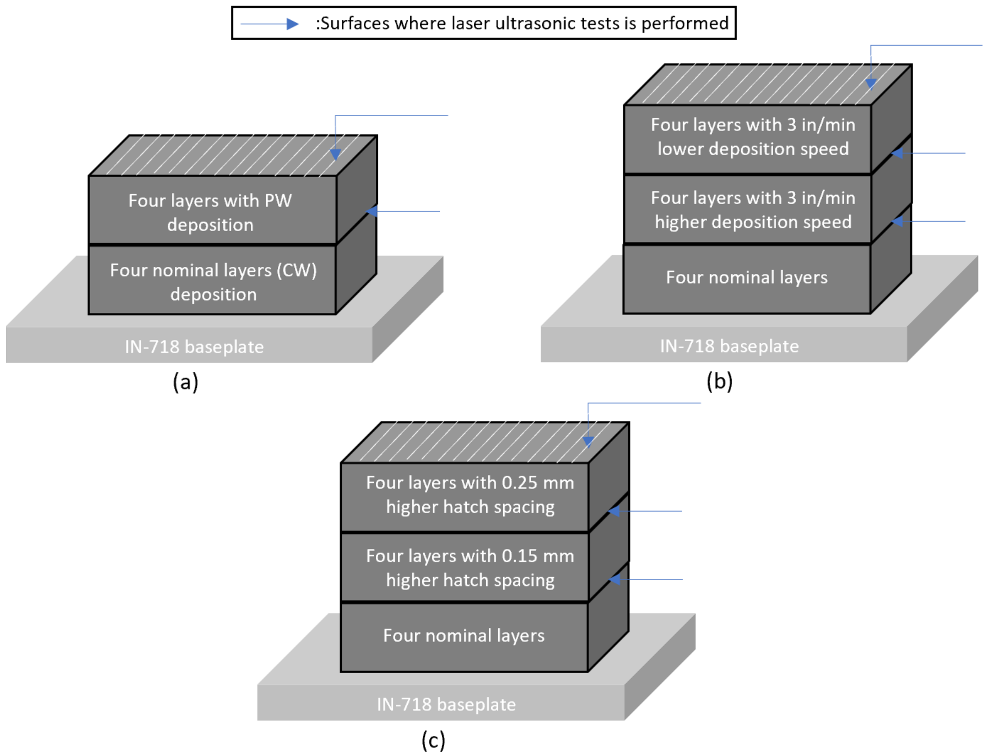


Figure **7-2**. Schematic showing the build plan and laser ultrasonic testing for DED IN-718 specimens (a) Build 3 – pulsed wave deposition, (b) Build 4 – Deposition speed varied, and (c) Build 5 – Hatch spacing varied.

### 7.2.2 Effects of varying the process parameters

Effects of varying the hatch spacing on the microstructure, surface quality, and mechanical properties have been studied in the literature. The hatch spacing determines the overlap rate of the subsequent tracks. If the overlap is too low, lack-of-fusion defects are created due to insufficient melting between neighboring tracks. In contrast, local over-sintering between the neighboring tracks occurs if the overlap is too high. In addition, the increase in the hatch spacing reduces the relative density of the AM builds. Hatch spacing also has the highest impact on the surface roughness characteristics [29]. However, in this study, the hatch spacing is marginally increased, leading to minimal differences in the surface roughness. The surface profiles for builds processed by different parameters are obtained using optical profilometry (Nexview NX2, Zygo, Middlefield, CT, USA) and quantified using Gwyddion, open-source software for statistical parametric mapping data analysis [30]. The surface roughness measurements for the Ti-6Al-4V and IN-718 builds are provided in Tables 7-3 and 7-4. For Ti-6Al-4V, the average surface roughness changes from 33.04 $\mu$m to 30.63 $\mu$m due to increasing the hatch spacing by 0.1 mm. For IN-718, the average surface roughness reduces from 16.05 $\mu$m to 13.89 $\mu$m with an increase in the hatch spacing by 0.15 mm and then increases to 25.60 $\mu$m with a further increase in the hatch spacing by 0.25 mm.

Table **7-3**. Surface roughness parameters for Ti-6Al-4V builds.

| **Sample** | $S_a$ **(**$\mu$**m)** | $S_q$ **(**$\mu$**m)** |
|---|---|---|
| Ti-6Al-4V baseplate | 1.14 | 1.42 |
| Nominal deposition | 33.04 | 41.39 |
| Processing power lowered by 15% | 33.09 | 42.26 |
| Hatch spacing increased by 0.1 mm | 30.63 | 38.84 |

Table **7-4**. Surface roughness parameters for IN-718 builds.

| **Sample** | $S_a$ **(**$\mu$**m)** | $S_q$ **(**$\mu$**m)** |
|---|---|---|
| Nominal deposition | 19.59 | 25.23 |
| Pulsed wave deposition | 16.05 | 21.23 |
| Hatch spacing 0.75 mm | 13.89 | 18.16 |
| Hatch spacing 0.85 mm | 25.60 | 31.82 |
| Deposition speed 22 in/min | 18.27 | 22.65 |
| Deposition speed 28 in/min | 17.52 | 21.76 |

Increasing the processing speed or reducing the deposition power and vice versa has a similar effect in terms of the amount of energy transferred to the melt pool and, in turn, the microstructure and mechanical properties of the AM part [2]. For instance, reducing the processing speed or increasing the deposition power allows more energy to be transferred to the melt pool, increasing its size and affecting the fusion zone morphology. Corbin et al. [31] and Kistler et al. [32,33] studied the effect of varying the processing speed on the microstructure and morphology of DED IN-718 depositions using the same system as this research. The processing speed effects are studied for 8.5 mm/s, 10.6 mm/s, 12.7 mm/s, and 16.9 mm/s, and the deposition power effects are studied for 250 W, 300 W, 350 W, and 400 W. The authors found that the processing speed is the primary influencer for all geometries, significantly influencing the bead width and the height. The variation of processing speed and deposition power have a minimal impact on the average surface roughness, as seen in Tables 7-3 and 7-4.

We refer to the literature [34] , which establishes the differences in the microstructure for the continuous and pulsed laser AM depositions. The pulsed laser deposition causes rapid cooling, a greater degree of melt pool stirring, and reduced thermal aging, leading to refined microstructure and more uniform microstructural and mechanical properties. The variation of average surface roughness for the continuous wave and pulsed wave depositions is relatively low (19.59 $\mu$m for continuous wave and 16.05 $\mu$m for pulsed wave).

After deposition, the laser ultrasonic inspection regions of all the builds are sectioned and examined with X-ray Computed Tomography (XCT) for the presence of material discontinuities. Image stacks (slices), extracted from the XCT data using the myVGL commercial software, showed no material discontinuities for all the builds, as intended. Therefore, we do not show the XCT results in this chapter.

## 7.3 Results

### 7.3.1 Repeatability analysis of Rayleigh wave distortion

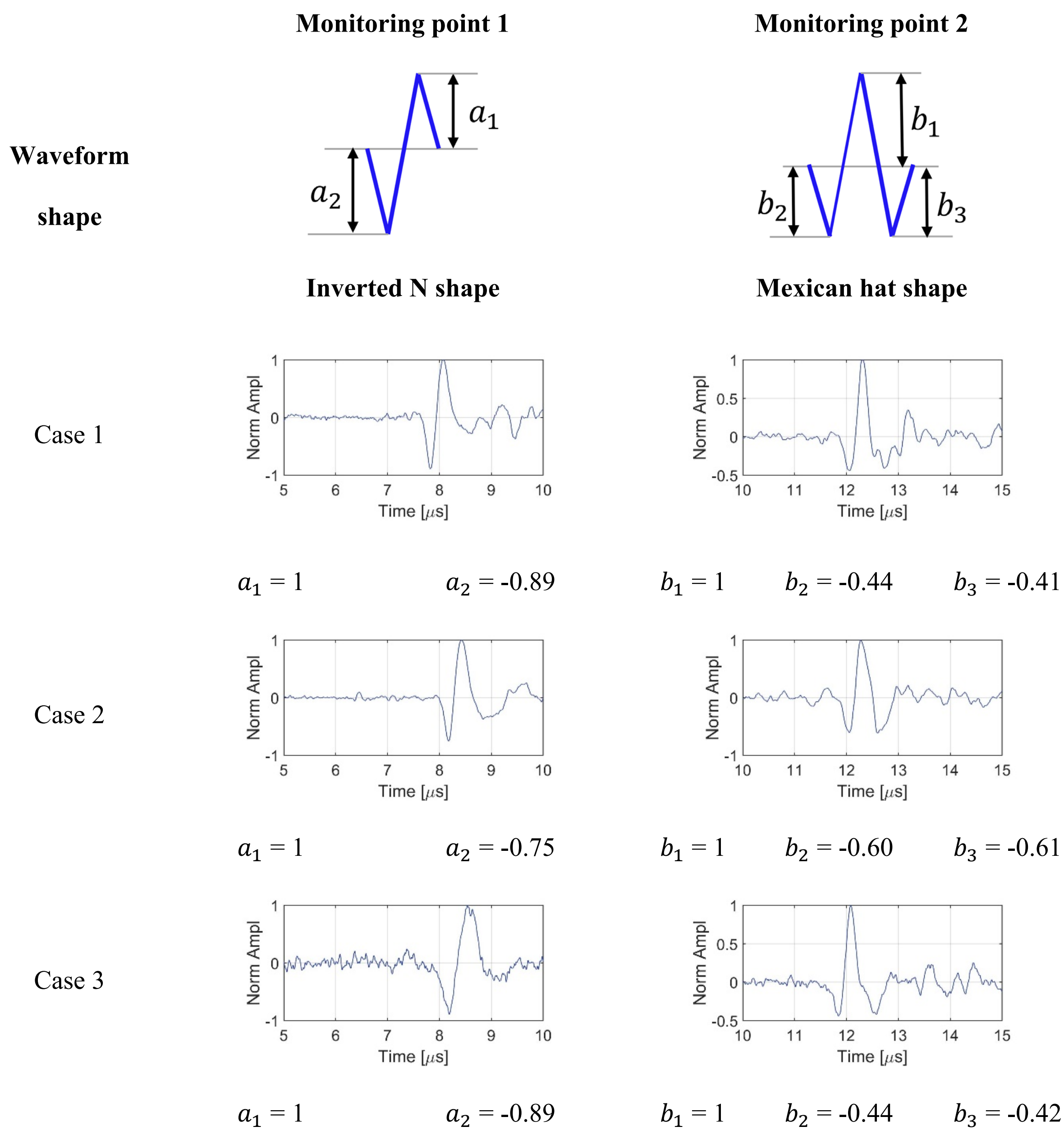


Figure **7-3**. Plots show the waveforms and their peak amplitudes obtained at two consecutive locations along the longitudinal scan for 3 cases of nominal AM depositions. The two locations are 23 mm and 35 mm from the source.

We observe a similar trend in the nonlinear evolution of waveforms for three DED Ti-6Al-4V depositions processed using identical process parameters. Figure 7-3 presents the waveforms and the corresponding peak amplitudes obtained at 23 mm and 35 mm for the three Ti-6Al-4V depositions processed using the nominal processing parameters provided in Table 7-1. For each case, an inverted N-shaped bipolar pulse observed at 23 mm propagation distance evolves into a Mexican hat shaped waveform at 35 mm propagation distance. As described in section 2.3.3, the nonlinear broadband Rayleigh waves evolve as they propagate depending on the nonlinearity of the media. Therefore, this analysis shows that reasonable repeatability exists in the material microstructure and the waveform evolution when the processing parameters are unchanged. Furthermore, although the waveforms evolve into similar shapes for the three cases, the peak amplitudes are noticeably different for case 2. The differences in the received signals can be attributed to the process variability and the variability in the footprint of the laser irradiation.

### 7.3.2 DED Ti-6Al-4V depositions with varied power and hatch spacing

#### PROPAGATION DISTANCE VARIATION TEST

We begin our analysis by comparing the waveforms obtained for the baseplate and the AM depositions. Figures 7-4 (a)-(h) provide Rayleigh wave signals obtained at 23 mm and 39 mm propagation distances for the Ti-6Al-4V baseplate, Ti-6Al-4V deposited with nominal process parameters, Ti-6Al-4V deposited with 15% lower power, and Ti-6Al-4V deposited with 0.1 mm higher hatch spacing. Although the comparison with the baseplate and AM depositions is not the main objective, the disparity seen in the waveform shapes at 23 mm for the baseplate (monopolar V-shaped) and three AM depositions (bipolar inverted N-shaped) is an interesting result. This disparity mainly exists due to the drastically different microstructures and surface roughness for the baseplate and the AM depositions. This effect is discussed in detail in Chapter 4. We note that the surface roughness-induced attenuation dissipates the energy as the Rayleigh wave propagates, which increases the shock formation distance (provided the nonlinear effects are more dominant than the attenuation effects) and the higher nonlinearity of the AM material reduces the shock formation distance (see Eqn. 2-2). At 39 mm propagation distance, a shock or a discontinuity in the waveform, is observed for the baseplate. On the other hand, the initially inverted N-shaped bipolar pulse evolves into a Mexican hat-shaped waveform for the nominal AM deposition.

The differences in the waveform evolution are also evident from the corresponding frequency spectra. In Figure 7-5, (a) & (d) present the frequency spectra for Ti-6Al-4V baseplate, (b) & (e) for Ti-6Al-4V deposited with varied power, and (c) & (f) Ti-6Al-4V deposited with varied hatch spacing at 23 mm and 39 mm propagation distances, respectively, with the corresponding spectra for Ti-6Al-4V deposited with nominal process parameters overlapped for comparison. When the propagation distance increases, a reduction in bandwidth is observed for all the cases, but most strikingly for the baseplate. This effect is similar to the frequency spectra discussed in Fig. 2-7 in chapter 2. The shift in the peak frequency is one key parameter to differentiate the nonlinear distortion effects in the frequency domain. Table 7-5 provides the peak frequencies for all the spectra and their percent shift. The peak frequencies are significantly different for the baseplate and the AM depositions. Moreover, the peak frequencies increase with the propagation distance for the baseplate and the nominal AM deposition, indicating a positive coefficient of nonlinearity [35]. The increase in the peak frequency is much higher (31 %) for the baseplate than the nominal AM deposition (14 %). Although the AM material has a significantly higher nonlinearity than the baseplate, the drastically high surface roughness dissipates the energy, thereby increasing the shock formation distance.

The notable differences in the waveform evolutions for the three AM depositions indicate the capability of nonlinear broadband waves to detect subtle variations in the AM process parameters. Note that the generation laser energy and propagation distance are the same, and the differences in the surface roughness for the AM depositions are insignificant. For the AM deposition with varied power, the waveform trough contracts with the reduction of the right-side peak amplitude, and the waveform approaches a V-shape. For the AM deposition with varied hatch spacing, the waveform retains its shape with a slight reduction in the right peak amplitude.

In contrast with nominal deposition, the peak frequency shifts to a lower value with increased propagation distance for the depositions with varied deposition power and hatch spacing. A reduction in the peak amplitude by 14 % and 59 % is observed for the AM depositions with varied deposition power and hatch spacing, respectively, indicating a negative coefficient of nonlinearity in the inspection region. Lastly, we note that the spectral amplitudes in the high-frequency region (> 5 MHz) are higher for the AM depositions with varied deposition power and hatch spacing than the nominal deposition owing to the nonlinear effects. Refer to Figures 7-5 (b) & (e) and Figures 7-5 (c) & (f).

**Baseplate** | **Nominal deposition** | **Power varied** | **Hatch spacing varied**

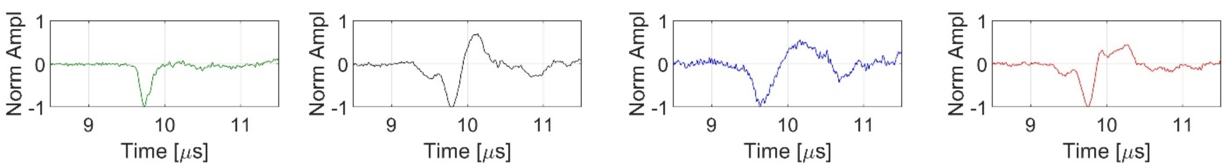


(a) (b) (c) (d)

At 23 mm

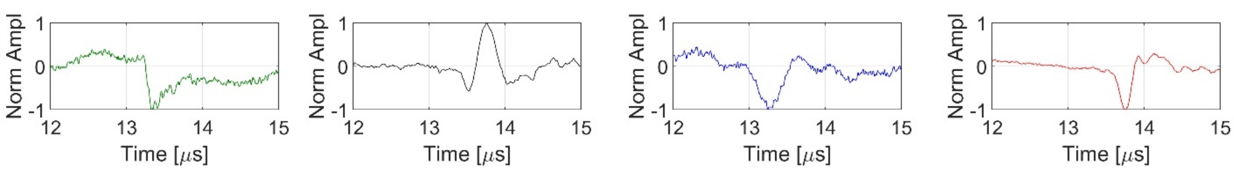


(e) (f) (g) (h)

At 39 mm

Figure **7-4**. Plots show A-scans at two consecutive locations along the longitudinal scan for baseplate (green): (a) & (e), nominal Ti-6Al-4V depositions (black): (b) & (f), Ti-6Al-4V deposition with 15% lower depositions power (blue): (c) & (g), and Ti-6Al-4V deposition with 0.1 mm increased hatch spacing (red): (d) & (h).

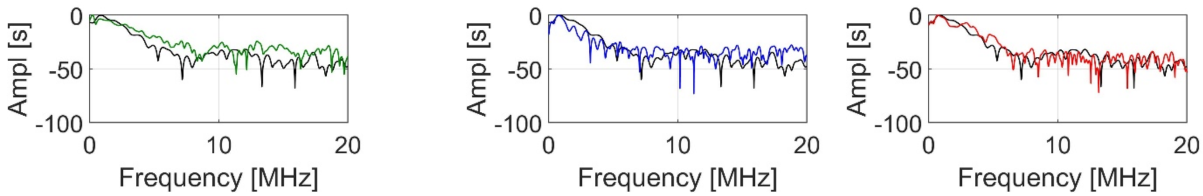


(a) (b) (c)

At 23 mm

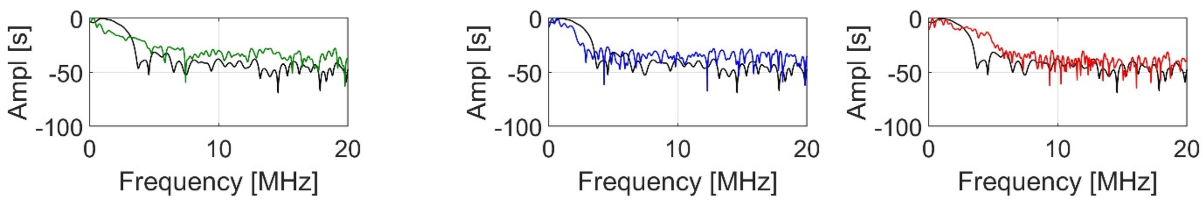


(d) (e) (f)

At 39 mm

Figure **7-5**. Plots show the frequency spectra for the A-scans shown in Fig 11: Baseplate (green): (a) & (d), Ti-6Al-4V deposited with 15% lower depositions power (blue): (b) & (e), and Ti-6Al-4V deposited with 0.1 mm increased hatch spacing (red): (c) & (f), with the corresponding spectra for Ti-6Al-4V deposited with nominal process parameters overlapped for comparison (black).

Table **7-5**. Peak frequencies and percent shift from the frequency spectra shown in Figure 7-5.

| | **Frequency (MHz)** | | | |
|---|---|---|---|---|
| **Propagation Distance (mm)** | **Baseplate** | **Nominal deposition** | **Power varied** | **Hatch spacing varied** |
| 23 | 0.211 | 0.8613 | 0.7539 | 0.7109 |
| 39 | 0.277 | 0.9844 | 0.65 | 0.2941 |
| **% Shift** | (+) 31 % | (+) 14 % | (-) 14 % | (-) 59 % |

## INITIAL AMPLITUDE VARIATION TEST

Inspecting broadband Rayleigh waves for the thermoelastic and ablative regime with fixed propagation distance provides a different means to detect the differences in microstructures. Rayleigh wave amplitudes are significantly higher in the ablative regime, making the nonlinear effects important. As previously depicted in Fig. 2-5 in chapter 2, the initial amplitudes determine the degree of waveform distortion in a nonlinear medium. Thus, we analyze the waveforms in the ablative regime from the context of distortion of the waveforms owing to the nonlinear effects that are manifested by the differences in the microstructures. Figures 7-6 (a) – (f) shows the received Rayleigh wave signals at 30 mJ and 120 mJ laser energies for Ti-6Al-4V baseplate, Ti-6Al-4V deposited with nominal process parameters, Ti-6Al-4V

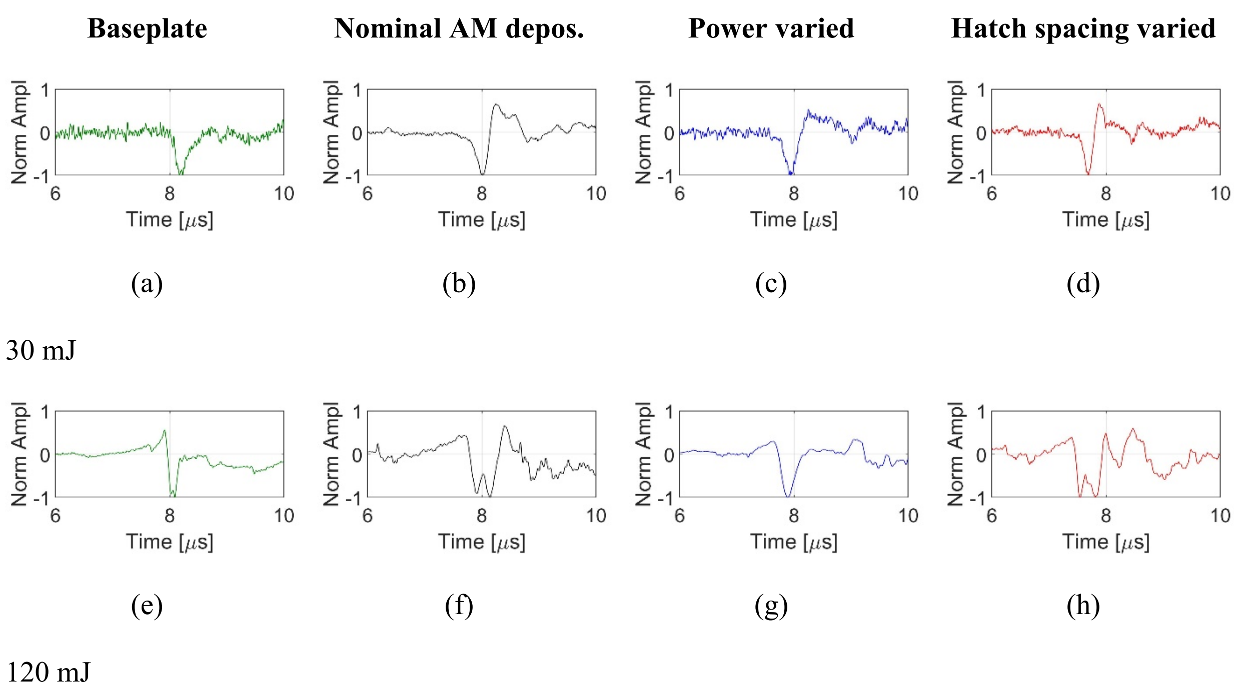


Figure **7-6**. Plots show A-scans at 30 mJ and 120 mJ laser energies at fixed propagation distance for baseplate (green): (a) & (e), nominal Ti-6Al-4V depositions (black): (b) & (f), Ti-6Al-4V deposition with 15% lower depositions power (blue): (c) & (g), and Ti-6Al-4V deposition with 0.1 mm increased hatch spacing (red): (d) & (h).

deposited with 15% lower power, and Ti-6Al-4V deposited with 15% higher hatch spacing. In the thermoelastic regime, the waveform obtained for the baseplate has a monopolar V shape, and the waveforms obtained for the AM depositions have a similar (bipolar) inverted N pulse shape. However, in the ablative regime, the finite-amplitude waves distort differently for each case. As a result, we observe the formation of a steep shock having a bipolar pulse shape and sharp edges for the baseplate. On the other hand, a W-shaped waveform is observed along with shock formation for the nominal AM material and AM deposition with varied hatch spacing. Interestingly, an inversion of the pulse shape (inverted-N to N) is observed for the AM deposition with varied power.

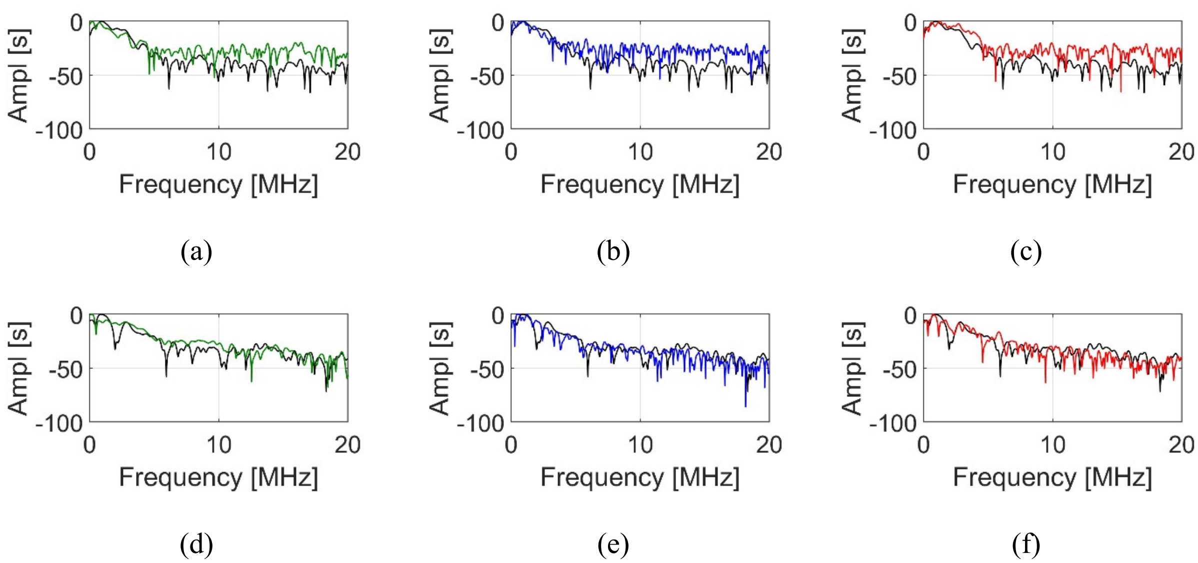


Figure **7-7**. Plots show the frequency spectra for the A-scans shown in Fig 13: Baseplate (green): (a) & (d), Ti-6Al-4V deposited with 15% lower depositions power (blue): (b) & (e), and Ti-6Al-4V deposited with 0.1 mm increased hatch spacing (red): (c) & (f), with the corresponding spectra for Ti-6Al-4V deposited with nominal process parameters overlapped for comparison (black).

The corresponding frequency spectra at the two laser energies for the baseplate, the Ti-6Al-4V deposited with varied power and the Ti-6Al-4V deposited with varied hatch spacing, are shown in Figure 7-7. The corresponding frequency spectrum (black) for the nominal AM deposition is overlapped for comparison. In the thermoelastic regime, the amplitudes in the high-frequency region (5 MHz – 20 MHz) are higher than the nominal AM deposition. However, this effect is not observed in the ablative regime. Note that the directivity patterns are different for the two regimes as depicted in Fig. 2-2 in chapter 2. Furthermore, a reduction in the peak frequencies is observed for each case in the ablative regime. However, the degree of shift in the peak frequencies is different for each case – a reduction of 19 %, 8 %, 1 %, and 42 % is observed for the baseplate, nominal deposition, deposition with varied power, and the deposition with varied hatch spacing, respectively, as seen in Table 7-6.

Table **7-6**. Peak frequencies and precent shift from the frequency spectra shown in Figure 7.7.

| **Laser energy (mJ)** | **Frequency (MHz)** | | | |
|---|---|---|---|---|
| | **Baseplate** | **Nominal deposition** | **Power varied** | **Hatch spacing varied** |
| 30 | 0.211 | 0.9288 | 0.5956 | 1.259 |
| 120 | 0.1715 | 0.8545 | 0.5873 | 0.7352 |
| **% Shift** | (-) 19 % | (-) 8 % | (-) 1 % | (-) 42 % |

### 7.3.3 DED IN-718 depositions with varied process parameters

#### 7.3.3.1 Pulsed wave (PW) deposition

#### PROPAGATION DISTANCE VARIATION TEST

Broadband Rayleigh waveforms having similar temporal and spectral characteristics at lower propagation distances evolve differently with increasing propagation distance for the continuous and pulsed laser deposited IN-718. Figure 7-8 presents the in-situ test results for the nominal (CW) and pulsed wave (PW) AM IN-718 depositions at 23 mm and 39 mm propagation distances. We also note that the differences in the average surface roughness values for the two depositions are minimal, as seen in Table 7-4. For the CW deposition, the amplitude of the right peak of the waveform reduces, and the waveform is marginally compressed (more evidently seen from comparing the width near the tip of the negative part) at the higher propagation distance. A similar reduction in the amplitude of the right peak is observed for PW deposition. However, a significant increase in the left positive peak amplitude and a substantial lengthening of the waveform are observed.

Furthermore, the waveform compression effect observed for the CW deposition is accompanied by an increase in the peak frequency (frequency-up conversion). In contrast, a reduction in the peak frequency (frequency-down conversion) is observed for the PW deposition with the lengthening of the pulse. The increase in the peak frequency for the CW deposition is 1 %, and the reduction in the peak frequency for the PW deposition is 9 %, refer to Table 7-7. In addition, a subtle reduction in the bandwidth for the nominal deposition at the higher propagation distance (noticeable from the dip in the spectrum at approximately 2.4 MHz) and a prominent negative peak in the low-frequency region is observed for the PW deposition.

**Nominal AM depos. (CW)** **PW AM deposition** **Frequency spectra**

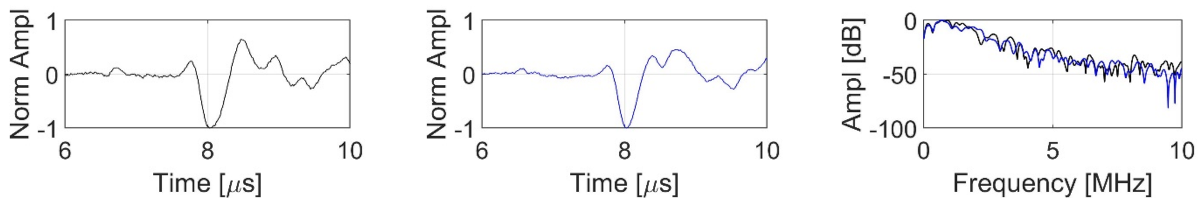


(a) (b) (c)

23 mm

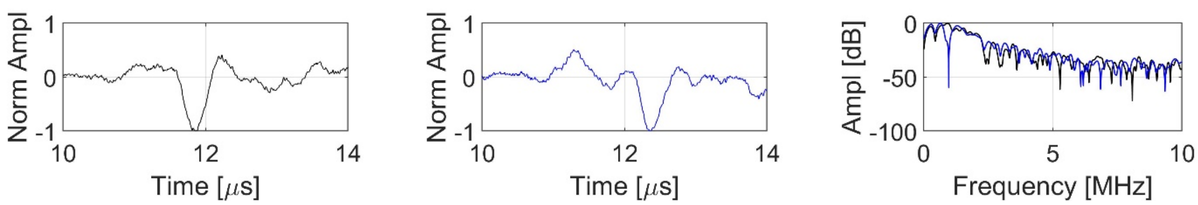


(d) (e) (f)

39 mm

Figure **7-8**. Plots show A-scans at two consecutive locations along the longitudinal scan for Nominal IN-718 deposition (black): (a) & (d), pulsed wave deposition (blue): (b) & (e), and the corresponding spectra: (c) & (f).

Table **7-7.** Peak frequencies and precent shift from the frequency spectra shown in Figure 7.8.

| **Propagation distance (mm)** | **Frequency (MHz)** | |
|---|---|---|
| | **Nominal (CW) deposition** | **Pulsed wave (PW) deposition** |
| 23 | 0.9239 | 0.7052 |
| 39 | 0.9309 | 0.6445 |
| **% Shift** | (+) 1 % | (-) 7 % |

## INITIAL AMPLITUDE VARIATION TEST

The in-situ results obtained in the thermoelastic and ablative regime show significant differences in the waveform evolution for the CW and PW depositions. Figure 7-9 (a)-(f) shows the A-scans and the frequency spectra for the CW and PW depositions at 30 mJ and 120 mJ laser energy. In the thermoelastic regime, the CW deposition has an inverted Mexican hat shape, and the waveform for the PW deposition has a similar shape except a substantially higher right-side positive peak. The peak frequency for the PW deposition is also much lower than the CW deposition at 30 mJ laser energy as seen in Table 7-8.

**Nominal depos. (CW)** **PW deposition** **Frequency Spectra**

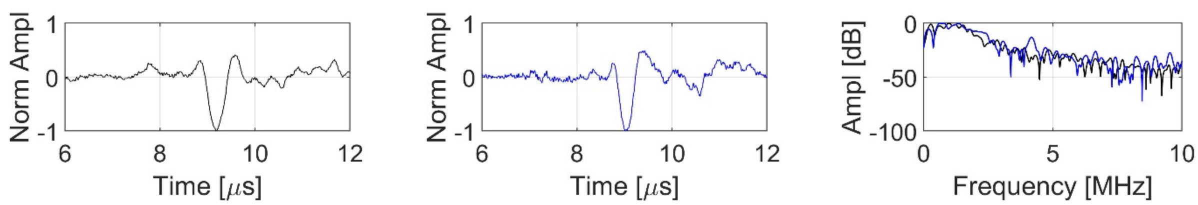


(a) (b) (c)

30 mJ

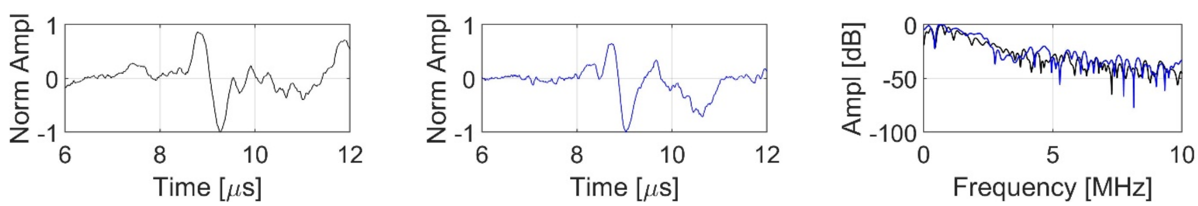


(d) (e) (f)

120 mJ

Figure **7-9**. Plots show A-scans at 30 mJ and 120 mJ laser energies at fixed propagation distance for Nominal IN-718 deposition (black): (a) & (d), pulsed wave deposition (blue): (b) & (e), and the corresponding spectra: (c) & (f).

At higher laser energy, the initial inverted Mexican hat-shaped monopolar pulse evolves into an N-shaped bipolar pulse for both cases. The right peak of the waveform is higher, and the left peak is lower for the PW deposition than the nominal deposition. The reduction in the peak frequency is much higher for the

CW deposition than the PW deposition. Finally, isolated peaks are observed in the PW deposition frequency spectra at approximately 4.5 MHz, refer to Fig. 7-9 (c) and (f). The cause of these peaks is not clear.

Table **7-8.** Peak frequencies and precent shift from the frequency spectra shown in Figure 7.9.

| **Laser energy (mJ)** | **Frequency (MHz)** | |
|---|---|---|
| | **Nominal (CW) deposition** | **PW deposition** |
| 30 | 0.9729 | 0.6218 |
| 120 | 0.658 | 0.6066 |
| **% Shift** | 32 % | 2 % |

#### 7.3.3.2 Processing speed varied

**PROPAGATION DISTANCE VARIATION TEST**

The evolution of broadband waveforms obtained for IN-718 deposition with nominal process parameters and depositions with varied processing speeds are clearly different. Rayleigh waveforms obtained at the 23 mm and 39 mm propagation distance for the nominal deposition, deposition with 9.3 mm/s processing speed, and deposition with 11.8 mm/s processing speed are shown in Fig 7-10. The variations in processing speed have a negligible influence on the average roughness parameters, as seen in Table 7-4. At the lower propagation distance, the positive peaks of the waveforms get blunter from Fig. 7-10 (a) to (c). The right positive peak of the waveform observed in Fig 7-10 (a) has a higher amplitude than the left peak, whereas the waveforms in Fig. 7-10 (b) and (c) have an inverted Mexican hat and V shape. For the higher propagation distance, the waveform for the nominal deposition evolves into an inverted Mexican hat shape due to the reduction of the amplitude of the right peak. A significantly different effect is seen for the AM deposition with 9.3 mm/s processing speed, i.e., evolution from a Mexican hat-shaped waveform to an N-shaped bipolar pulse. For the deposition having 11.8 mm/s processing speed, the initial V-shaped waveform becomes Mexican hat-shaped due to increased amplitudes for the left and the right positive wings (peaks).

**Nominal deposition**

**(Processing speed: 10.6 mm/s)**

**Processing speed: 9.3 mm/s**

**Processing speed: 11.8 mm/s**

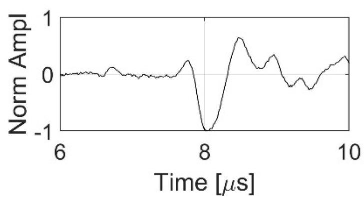


(a)

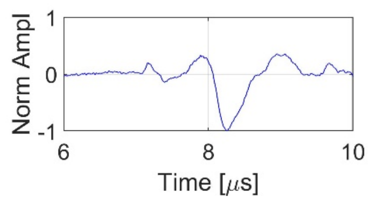


(b)

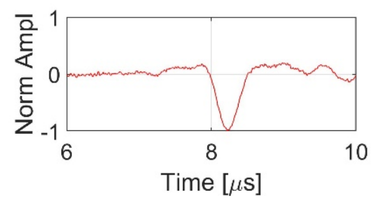


(c)

23 mm

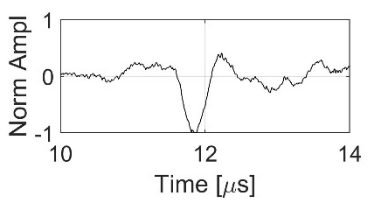


(d)

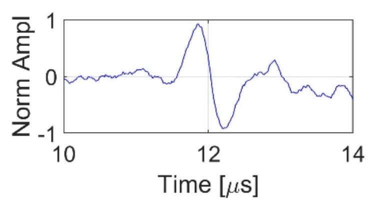


(e)

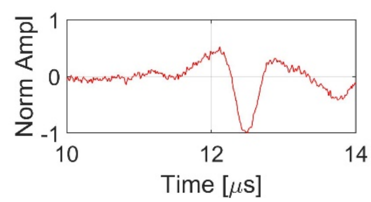


(f)

39 mm

Figure **7-10**. Plots show A-scans at two consecutive locations along the longitudinal scan for nominal IN-718 deposition (black): (a) & (d), depositions having processing speed varied to 22 in/min (blue): (b) & (e), and depositions having processing speed varied to 28 in/min (red): (c) & (f).

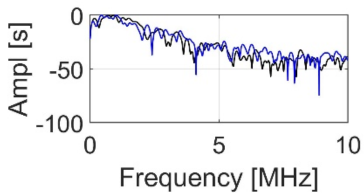


(a)

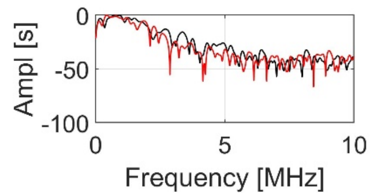


(b)

23 mm

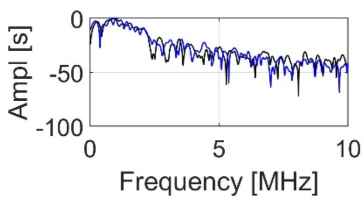


(c)

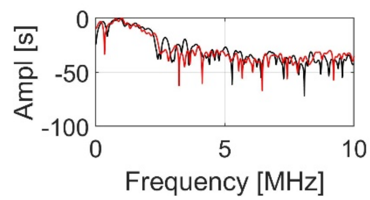


(d)

39 mm

Figure **7-11**. Plots show the frequency spectra for the A-scans shown in Fig 17: Deposition having processing speed varied to 9.3 mm/s (blue): (a) & (c), and deposition having processing speed varied to 11.8 mm/s (red): (b) & (d), with the corresponding spectra for IN-718 deposited with nominal process parameters overlapped for comparison (black).

A common observation from the frequency spectra, shown in Fig 7-11, is the reduction in the bandwidth with increasing propagation distance. We note that the peak frequency for the deposition with 11.8 mm/s processing speed is significantly lower than in the other two cases. Also, a drastic increase of 134 % in the peak frequency is observed for the deposition having 11.8 mm/s processing speed, refer to Table 7-9. On the other hand, a minimal increase of 1 % in the peak frequency is observed for the nominal deposition. Interestingly, the peak frequency for the deposition with 9.3 mm/s remains unchanged at the higher propagation distance.

Table **7-9.** Peak frequencies and precent shift from the frequency spectra shown in Figure 7-11.

| **Propagation distance (mm)** | **Frequency (MHz)** | | |
|---|---|---|---|
| | **Nominal deposition (Processing speed: 10.6 mm/s)** | **Processing speed: 9.3 mm/s** | **Processing speed: 11.8 mm/s** |
| 23 | 0.9239 | 1.014 | 0.427 |
| 39 | 0.9309 | 1.014 | 1.001 |
| **% Shift** | (+) 1 % | 0 % | 134 % |

## INITIAL AMPLITUDE VARIATION TEST

Considerable temporal and spectral differences are observed in the in-situ signals obtained for the nominal and processing speed varied IN-718 depositions in the thermoelastic and ablative regimes. Figure 7-12 shows the results obtained for the 30 mJ (thermoelastic) and 120 mJ (ablative) laser energy with a fixed propagation distance. A Mexican hat-shaped monopolar waveform evolves into an N-shaped bipolar pulse for the nominal deposition. The signal obtained for the 9.3 mm/s processing speed deposition at 30 mJ laser energy also has a Mexican hat shape but a higher left-side positive peak and a blunt right-side positive peak than the nominal deposition. The deposition having 11.8 mm/s processing speed at 30 mJ laser energy has a Mexican hat shape with both the positive peaks blunt. For the depositions with 9.3 mm/s and 11.8 mm/s processing speed at 120 mJ laser energy, the positive left-side peak amplitude grows with a reduction in the negative peak amplitude. However, for the deposition with 11.8 mm/s processing speed, the trough becomes much wider than the deposition with 9.3 mm/s processing speed. This effect is most likely due to the differences in travel speeds of troughs and peaks for the two cases, manifested due to the different nonlinearities. The reduction in the corresponding peak frequencies is 6.2 % and 42.25%, respectively, enlisted in Table 7-10. Highly nonlinear waveforms with sharp edges (discontinuities) and the formation of shocks are observed in Fig. 7-12 (e) & (f). We also note the beginning of the separation of the signals in Fig. 7-12 (f).

**Nominal deposition (Processing speed: 10.6 mm/s)** **Processing speed: 9.3 mm/s** **Processing speed: 11.8 mm/s**

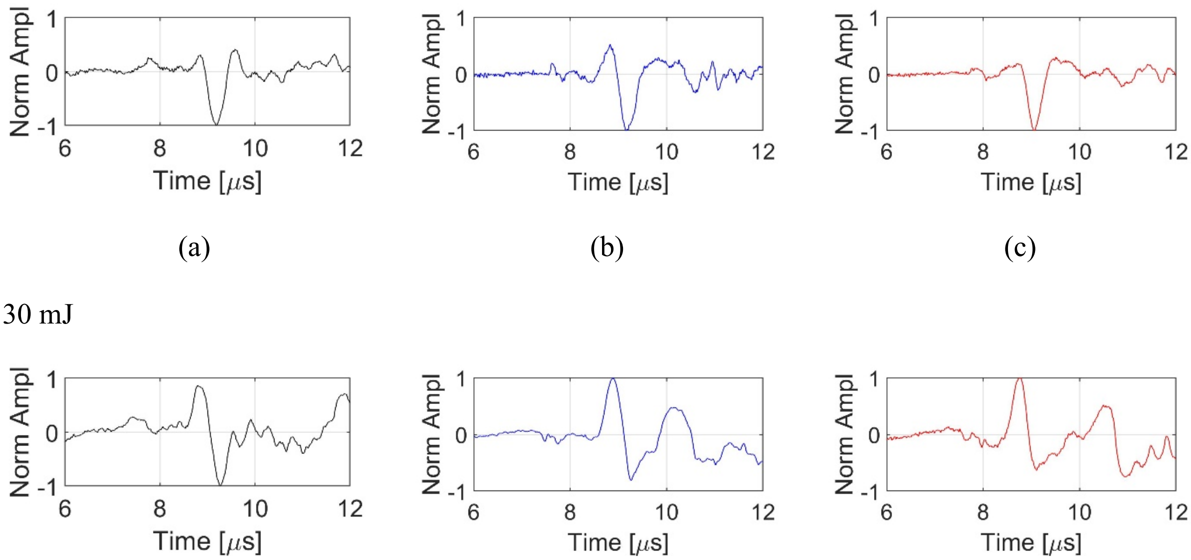


(a) (b) (c)

30 mJ

(d) (e) (f)

120 mJ

Figure **7-12**. Plots show A-scans at 30 mJ and 120 mJ laser energies at fixed propagation distance for nominal IN-718 deposition (black): (a) & (d), depositions having processing speed varied to 9.3 mm/s (blue): (b) & (e), and depositions having processing speed varied to 11.8 mm/s (red): (c) & (f).

Wider frequency bandwidth is observed for the ablative regime than for the thermoelastic regime, which can be interpreted as the leakage of energy to higher frequencies due to the dominant nonlinear effects resulting from the higher amplitudes. The frequency spectra are shown in Fig. 7-13. The bandwidth extension effect is the lowest for the deposition with 9.3 mm/s processing speed. Similarly, the shift in peak frequencies to a lower value is the lowest for the deposition with 9.3 mm/s processing speed. The shift in the peak frequency is – nominal deposition: 32 %, deposition with 9.3 mm/s processing speed: 6 %, and deposition with 11.8 mm/s processing speed: 42 %. The above differences in the time and frequency domain signals demonstrate the capability of the in-situ system to detect changes in the process parameters.


(a) (b)

30 mJ


(c) (d)

120 mJ

Figure **7-13**. Plots show the frequency spectra for the A-scans shown in Fig 19: Deposition having processing speed varied to 9.3 mm/s (blue): (a) & (c), and deposition having processing speed varied to 11.8 mm/s (red): (b) & (d), with the corresponding spectra for IN-718 deposited with nominal process parameters overlapped for comparison (black).

Table **7-10.** Peak frequencies and precent shift from the frequency spectra shown in Figure 7.13.

| **Laser energy (mJ)** | **Frequency (MHz)** | | |
|---|---|---|---|
| | **Nominal deposition (Processing speed: 10.6 mm/s)** | **Processing speed: 9.3 mm/s** | **Processing speed: 11.8 mm/s** |
| 30 | 0.9729 | 0.8384 | 0.9939 |
| 120 | 0.658 | 0.7864 | 0.574 |
| **% Shift** | (-) 32 % | (-) 6 % | (-) 42 % |

#### 7.3.3.3 Hatch spacing varied

**PROPAGATION DISTANCE VARIATION TEST**

Significant changes in the waveform shapes are observed as the propagation distance is increased in IN-718 samples processed with increasing hatch spacing. Figures 7-14 (a)-(f) present the waveforms obtained at 23 mm and 39 mm propagation distances for the nominal deposition and dispositions with 0.75 mm and 0.85 mm hatch spacing. We note that the average surface roughness values are marginally different for the three cases and may have an impact on the rate at which the waveforms evolve.

**Nominal deposition (Hatch spacing: 0.6 mm)** | **Hatch spacing: 0.75 mm** | **Hatch spacing: 0.85 mm**

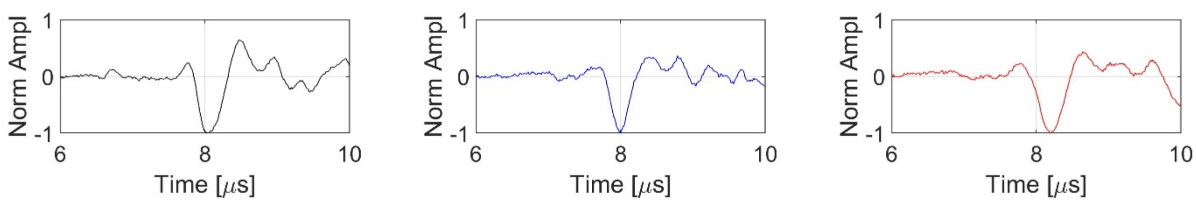


(a) (b) (c)

23 mm

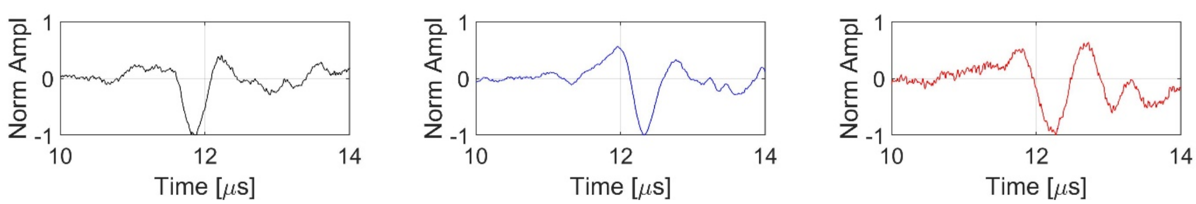


(d) (e) (f)

39 mm

Figure **7-14**. Plots show A-scans at two consecutive locations along the longitudinal scan for nominal IN-718 deposition (black): (a) & (d), depositions having hatch spacing varied to 0.75 mm (blue): (b) & (e), and depositions having hatch spacing varied to 0.85 mm (red): (c) & (f).

However, as the wavelength of the Rayleigh wave pulse at the peak frequency is significantly larger than the maximum deviation in the average surface roughness and the propagation distance is low, we assume that the attenuation effects are insignificant. Thus, we do not perform the attenuation correction in our analysis of waveform evolutions.

The waveforms at the lower propagation distance have similar Mexican hat like monopolar shapes, except a marginally higher right-side peak amplitude for the case of nominal deposition. The trough of the waveform for the deposition with 0.85 mm hatch spacing is relatively broader and has a significantly lower peak frequency, refer to Fig. 7-15 (c) and Table 7-11. At the higher propagation distance, the waveforms for the three cases obtain significantly different shapes. The right-side peak amplitude reduces for the nominal deposition, and the left-side peak amplitude becomes blunt with a minimal increase (1 %) in the peak frequency. An increase in the left-side peak is observed for the deposition with 0.75 mm hatch spacing along with the lengthening of the waveform. The waveform lengthening is manifested with a significant reduction (26 %) in the peak frequency, indicating a negative nonlinearity coefficient. For the deposition with 0.85 mm hatch spacing, the amplitudes of both the positive peaks increase and a further lengthening of the trough are observed. Similar to the deposition with 0.75 mm hatch spacing, the lengthening is accompanied by a reduction in the peak frequency; however, the effect is more prominent (55 %). In addition, the frequency bandwidth increases for the nominal deposition and reduces for the depositions with varied hatch spacing, as seen in Fig. 7-16.

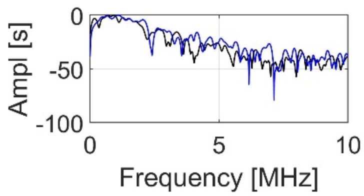


(a)

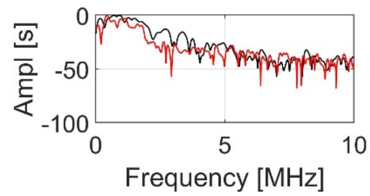


(b)

23 mm

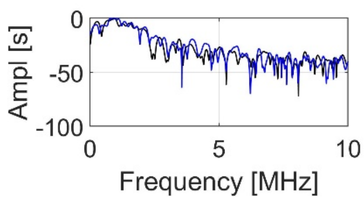


(c)

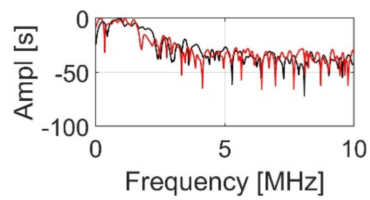


(d)

39 mm

Figure **7-15**. Plots show the frequency spectra for the A-scans shown in Fig 21: Deposition having hatch spacing varied to 0.75 mm (blue): (a) & (c), and deposition having hatch spacing varied to 0.75 mm (red): (b) & (d), with the corresponding spectra for IN-718 deposited with nominal process parameters overlapped for comparison (black).

Table **7-11.** Peak frequencies and precent shift from the frequency spectra shown in Figure 7.15.

| **Propagation distance (mm)** | **Frequency (MHz)** | | |
|---|---|---|---|
| | **Nominal deposition (Hatch spacing: 0.6 mm)** | **Hatch spacing: 0.75 mm** | **Hatch spacing: 0.85 mm** |
| 23 | 0.9239 | 1.085 | 0.4322 |
| 39 | 0.9309 | 0.8007 | 0.1934 |
| **% Shift** | (-) 1 % | (-) 26 % | (-) 55 % |

**INITIAL AMPLITUDE AVRIATION TEST**

The results indicate that the differences in the waveform evolutions obtained in the thermoelastic and ablative regimes can detect subtle changes in the process parameters. Figure 7-16 shows the signals obtained at 30 mJ and 120 mJ laser energy for the nominal deposition, deposition with 0.75 mm hatch spacing, and deposition with 0.85 mm hatch spacing. Figure 7-17 provides the corresponding spectra.

| **Nominal deposition (Hatch spacing: 0.6 mm)** | **Hatch spacing: 0.75 mm** | **Hatch spacing: 0.85 mm** |
|---|---|---|

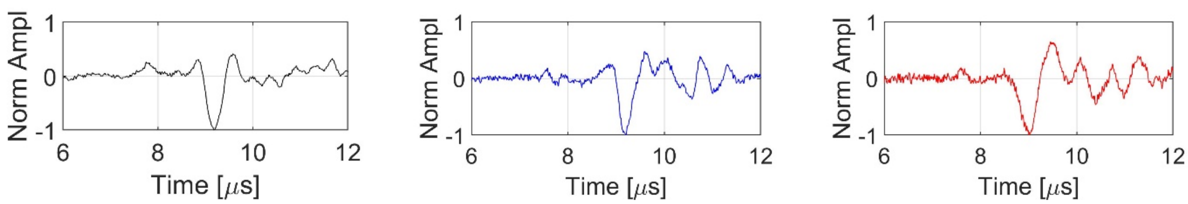


(a) (b) (c)

30 mJ

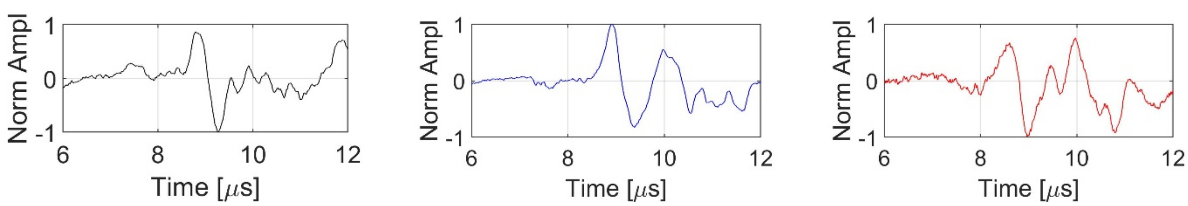


(d) (e) (f)

120 mJ

Figure **7-16**. Plots show A-scans at 30 mJ and 120 mJ laser energies at fixed propagation distance for nominal IN-718 deposition (black): (a) & (d), depositions having hatch spacing varied to 0.75 mm (blue): (b) & (e), and depositions having hatch spacing varied to 0.85 mm (red): (c) & (f).

The initial Mexican hat-shaped waveform evolves into an N-shaped bipolar pulse in the ablative regime. In addition, the formation of several small peaks around 10 $\mu$s is observed along with a significant reduction (32 %) in the peak frequency, refer to Table 7-12. For the deposition with 0.75 mm hatch spacing, the amplitude of the right peak dramatically increases with a gradual reduction and lengthening of the trough in the ablative regime. The lengthening of the peak is accompanied by a reduction (29 %) in the peak frequency. A highly nonlinear signal with discontinuities is formed in the ablative regime for the deposition with 0.85 mm hatch spacing, with two negative and two positive peaks. In contrast to the other depositions, a marginal increase (2 %) in the peak frequency is observed for the deposition with 0.85 mm hatch spacing.

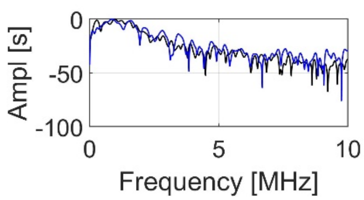


(a)

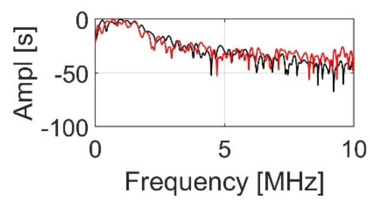


(b)

30 mJ

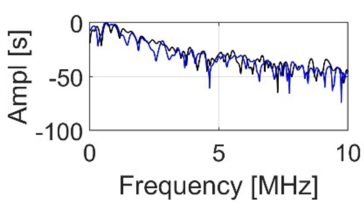


(c)

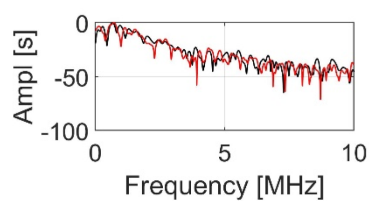


120 mJ

Figure **7-17**. Plots show the frequency spectra for the A-scans shown in Fig 23: Deposition having processing speed varied to 22 in/min (blue): (a) & (c), and deposition having processing speed varied to 28 in/min (red): (b) & (d), with the corresponding spectra for IN-718 deposited with nominal process parameters overlapped for comparison (black).

Table **7-12.** Peak frequencies and precent shift from the frequency spectra shown in Figure 7.17.

| **Laser energy (mJ)** | **Frequency (MHz)** | | |
|---|---|---|---|
| | **Nominal deposition (Hatch spacing: 0.6 mm)** | **Hatch spacing: 0.75 mm** | **Hatch spacing: 0.85 mm** |
| 30 | 0.9729 | 0.8553 | 0.6995 |
| 120 | 0.658 | 0.6066 | 0.7116 |
| **% Shift** | (-) 32 % | (-) 29 % | (+) 2 % |

## 7.4 Conclusions

During the AM deposition, complex physical and metallurgical processes take place that are linked to the process parameters and may lead to undesired microstructure in the final part. Minor variations in the process parameters can induce microstructural changes, which can negatively affect the macroscale mechanical properties. Thus, an in-situ monitoring system sensitive to microstructural changes is required. This chapter demonstrates the nonlinear distortion of broadband Rayleigh waves as a highly sensitive tool to the microstructural changes using the integrated laser ultrasonic system. The nonlinear distortion of broadband Rayleigh waves has not been used for inspecting the material degradation in the literature, which is a key novelty for this research. The results are provided for Ti-6Al-4V depositions with varied deposition power and hatch spacing and IN-718 depositions with varied deposition laser mechanism (continuous wave to pulsed wave), varied deposition speed, and varied hatch spacing and compared with the results obtained for the nominal depositions. In each case, a drastic difference in the evolution of the waveforms is observed for increasing propagation distance as well as increasing initial amplitudes. The evolution of waveforms and their implications on the frequency spectrum, in particular, the shift in the peak frequency, are discussed.

## 7.5 References


1. Song, B.; Dong, S.; Liao, H.; Coddet, C. Process parameter selection for selective laser melting of Ti6Al4V based on temperature distribution simulation and experimental sintering. *Int. J. Adv. Manuf. Technol.* **2012**, *61*, 967–974, doi:10.1007/s00170-011-3776-6.
2. Saboori, A.; Gallo, D.; Biamino, S.; Fino, P.; Lombardi, M. An Overview of Additive Manufacturing of Titanium Components by Directed Energy Deposition: Microstructure and Mechanical Properties. *Appl. Sci.* **2017**, *7*, 883, doi:10.3390/app7090883.
3. Reutzel, E.W.; Nassar, A.R. A survey of sensing and control systems for machine and process monitoring of directed-energy, metal-based additive manufacturing. *Rapid Prototyp. J.* **2015**, *21*, 159–167, doi:10.1108/RPJ-12-2014-0177.
4. Boddu, M.R.; Landers, R.G.; Liou, F.W. Control of laser cladding for rapid prototyping--A review. In Proceedings of the 2001 International Solid Freeform Fabrication Symposium; 2001.
5. Bi, G.; Gasser, A.; Wissenbach, K.; Drenker, A.; Poprawe, R. Identification and qualification of temperature signal for monitoring and control in laser cladding. *Opt. Lasers Eng.* **2006**, *44*, 1348–1359, doi:10.1016/J.OPTLASENG.2006.01.009.
6. Steen, W.M.; Mazumder, J. Laser Automation and In-process Sensing. In *Laser Material Processing*; Springer London: London, 2010; pp. 485–518.
7. Nassar, A.R.; Reutzel, E.W.; Brown, S.W.; Morgan, J.P.; Morgan, J.P.; Natale, D.J.; Tutwiler, R.L.; Feck, D.P.; Banks, J.C. Sensing for directed energy deposition and powder bed fusion additive manufacturing at Penn State University.; Gu, B., Helvajian, H., Piqué, A., Eds.; 2016; p. 97380R.
8. Honarvar, F.; Varvani-Farahani, A. A review of ultrasonic testing applications in additive manufacturing: Defect evaluation, material characterization, and process control. *Ultrasonics* **2020**, *108*, 106227, doi:10.1016/j.ultras.2020.106227.
9. Everton, S.K.; Hirsch, M.; Stravroulakis, P.; Leach, R.K.; Clare, A.T. Review of in-situ process

monitoring and in-situ metrology for metal additive manufacturing. *Mater. Des.* **2016**, *95*, 431–445, doi:10.1016/j.matdes.2016.01.099.

10. Tapia, G.; Elwany, A. A Review on Process Monitoring and Control in Metal-Based Additive Manufacturing. *J. Manuf. Sci. Eng.* **2014**, *136*, doi:10.1115/1.4028540.
11. Smith, R.J.; Hirsch, M.; Patel, R.; Li, W.; Clare, A.T.; Sharples, S.D. Spatially resolved acoustic spectroscopy for selective laser melting. *J. Mater. Process. Technol.* **2016**, *236*, 93–102.
12. Millon, C.; Vanhoye, A.; Obaton, A.-F.; Penot, J.-D. Development of laser ultrasonics inspection for online monitoring of additive manufacturing. *Weld. World* **2018**, *62*, 653–661, doi:10.1007/s40194-018-0567-9.
13. Davis, G.; Nagarajah, R.; Palanisamy, S.; Rashid, R.A.R.; Rajagopal, P.; Balasubramaniam, K. Laser ultrasonic inspection of additive manufactured components. *Int. J. Adv. Manuf. Technol.* **2019**, *102*, 2571–2579, doi:10.1007/s00170-018-3046-y.
14. Pieris, D.; Stratoudaki, T.; Javadi, Y.; Lukacs, P.; Catchpole-Smith, S.; Wilcox, P.D.; Clare, A.; Clark, M. Laser Induced Phased Arrays (LIPA) to detect nested features in Additively Manufactured Components. *Mater. Des.* **2019**, 108412, doi:10.1016/j.matdes.2019.108412.
15. Park, S.-H.; Liu, P.; Yi, K.; Choi, G.; Jhang, K.-Y.; Sohn, H. Mechanical properties estimation of additively manufactured metal components using femtosecond laser ultrasonics and laser polishing. *Int. J. Mach. Tools Manuf.* **2021**, *166*, 103745, doi:10.1016/j.ijmachtools.2021.103745.
16. Yu, J.; Zhang, D.; Li, H.; Song, C.; Zhou, X.; Shen, S.; Zhang, G.; Yang, Y.; Wang, H. Detection of Internal Holes in Additive Manufactured Ti-6Al-4V Part Using Laser Ultrasonic Testing. *Appl. Sci.* **2020**, *10*, 365, doi:10.3390/app10010365.
17. Zou, Y.; Chai, Y.; Wang, D.; Li, Y. Measurement of elastic modulus of laser cladding coatings by laser ultrasonic method. *Opt. Laser Technol.* **2022**, *146*, 107567, doi:10.1016/j.optlastec.2021.107567.
18. Lissenden, C.J. Nonlinear ultrasonic guided waves—Principles for nondestructive evaluation. *J. Appl. Phys.* **2021**, *129*, 021101, doi:10.1063/5.0038340.

19. Nagy, P.B. Fatigue damage assessment by nonlinear ultrasonic materials characterization. *Ultrasonics* **1998**, *36*, 375–381.

20. Walker, S. V.; Kim, J.Y.; Qu, J.; Jacobs, L.J. Fatigue damage evaluation in A36 steel using nonlinear Rayleigh surface waves. *NDT E Int.* **2012**, *48*, 10–15, doi:10.1016/j.ndteint.2012.02.002.

21. Matlack, K.H.; Bradley, H.A.; Thiele, S.; Kim, J.-Y.; Wall, J.J.; Jung, H.J.; Qu, J.; Jacobs, L.J. Nonlinear ultrasonic characterization of precipitation in 17-4PH stainless steel. *NDT E Int.* **2015**, *71*, 8–15, doi:10.1016/j.ndteint.2014.11.001.

22. Liu, M.; Kim, J.Y.; Jacobs, L.; Qu, J. Experimental study of nonlinear Rayleigh wave propagation in shot-peened aluminum platesFeasibility of measuring residual stress. *NDT E Int.* **2011**, *44*, 67–74, doi:10.1016/j.ndteint.2010.09.008.

23. Lardner, R.W.; Tupholme, G.E. Nonlinear surface waves on cubic materials. *J. Elast.* **1986**, *16*, 251–265, doi:10.1007/BF00040816.

24. Shull, D.J.; Hamilton, M.F.; Il'insky, Y.A.; Zabolotskaya, E.A. Harmonic generation in plane and cylindrical nonlinear Rayleigh waves. *J. Acoust. Soc. Am.* **1993**, *94*, 418–427, doi:10.1121/1.407053.

25. Gusev, V.E.; Lauriks, W.; Thoen, J. New evolution equations for the nonlinear surface acoustic waves on an elastic solid of general anisotropy. *J. Acoust. Soc. Am.* **1998**, *103*, 3203–3215, doi:10.1121/1.423036.

26. Gusev, V.E.; Lauriks, W.; Thoen, J. Theory for the time evolution of nonlinear Rayleigh waves in an isotropic solid. *Phys. Rev. B* **1997**, *55*, 9344–9347, doi:10.1103/PhysRevB.55.9344.

27. Kolomenskii, A.A.; Lomonosov, A.M.; Kuschnereit, R.; Hess, P.; Gusev, V.E. Laser generation and detection of strongly nonlinear elastic surface pulses. *Phys. Rev. Lett.* **1997**, *79*, 1325–1328, doi:10.1103/PhysRevLett.79.1325.

28. Lomonosov, A.M.; Hess, P.; Kumon, R.E.; Hamilton, M.F. Laser-generated nonlinear surface wave pulses in silicon crystals. *Phys. Rev. B - Condens. Matter Mater. Phys.* **2004**, *69*, 1–13, doi:10.1103/PhysRevB.69.035314.

29. Dong, Z.; Liu, Y.; Wen, W.; Ge, J.; Liang, J. Effect of Hatch Spacing on Melt Pool and As-built Quality During Selective Laser Melting of Stainless Steel: Modeling and Experimental Approaches. *Materials (Basel).* **2018**, *12*, 50, doi:10.3390/ma12010050.

30. Nečas, D.; Klapetek, P. Gwyddion: an open-source software for SPM data analysis. *Open Phys.* **2012**, *10*, doi:10.2478/s11534-011-0096-2.

31. Corbin, D.J.; Nassar, A.R.; Reutzel, E.W.; Beese, A.M.; Kistler, N.A. Effect of directed energy deposition processing parameters on laser deposited Inconel ® 718: External morphology. *J. Laser Appl.* **2017**, *29*, 022001, doi:10.2351/1.4977476.

32. Kistler, N.A.; Nassar, A.R.; Reutzel, E.W.; Corbin, D.J.; Beese, A.M. Effect of directed energy deposition processing parameters on laser deposited Inconel ® 718: Microstructure, fusion zone morphology, and hardness. *J. Laser Appl.* **2017**, *29*, 022005, doi:10.2351/1.4979702.

33. Kistler, N.A.; Corbin, D.J.; Nassar, A.R.; Reutzel, E.W.; Beese, A.M. Effect of processing conditions on the microstructure, porosity, and mechanical properties of Ti-6Al-4V repair fabricated by directed energy deposition. *J. Mater. Process. Technol.* **2019**, *264*, 172–181, doi:10.1016/j.jmatprotec.2018.08.041.

34. Nassar, A.R.; Reutzel, E.W. Additive Manufacturing of Ti-6Al-4V Using a Pulsed Laser Beam. *Metall. Mater. Trans. A* **2015**, *46*, 2781–2789, doi:10.1007/s11661-015-2838-z.

35. Lomonosov, A.; Mikhalevich, V.G.; Hess, P.; Knight, E.Y.; Hamilton, M.F.; Zabolotskaya, E.A. Laser-generated nonlinear Rayleigh waves with shocks. *J. Acoust. Soc. Am.* **1999**, *105*, 2093–2096, doi:10.1121/1.426814.

# Chapter 8

# CONCLUSIONS

## 8.1 Summary of findings

This thesis investigates the use of laser ultrasound for in-situ component monitoring of metal additive manufacturing.

Chapters 1 laid out the research questions, and Chapter 2 introduced the DED-AM system as the target system for this research and provided the theoretical background for laser generation and reception of ultrasonic Rayleigh waves. The detailed discussion of the current state of laser ultrasonic research for inspecting AM components also brought forth the gap in the literature that presently no laser ultrasonic system is integrated with the AM system to perform in-situ inspections. Chapters 3-6 contribute to the new research studies that address the research questions in Chapter 1.

Chapters 3 and 4 primarily address the surface roughness effects on the distortion of Rayleigh waves. It was identified in the literature survey in Chapter 3 that the surface roughness effects on the linear parameters of Rayleigh waves are well researched; however, there is a gap in the literature for the surface roughness effects on the nonlinearity of Rayleigh waves. Since the as-built AM specimens are highly rough, understanding the surface roughness effects on Rayleigh wave distortion is imperative. However, since the AM surface roughness is complex, Chapter 3 first investigates the surface roughness effects for Aluminum blocks having different roughnesses on self-and mutual interaction of Rayleigh waves. It was found that the surface roughness substantially increased the nonlinearity of the sum and difference frequency waves. A further investigation on the self-interaction of Rayleigh waves having different excitation frequencies showed that the surface roughness effects on Rayleigh wave distortion are frequency dependent. The attenuation correction method alone cannot compensate for the roughness effects on the acoustic nonlinearity parameter measurement. In addition, as the measurement system nonlinearity can hinder the accurate measurement of the material nonlinearity, the system nonlinearity is quantified at various points in the generation of finite-amplitude Rayleigh waves. Finally, it was shown that the mutual interaction of Rayleigh waves can enable material nonlinearities to be received at frequencies free from sensing system nonlinearities only if separate transducers are used to generate the waves that mix only in the waveguide.

Chapter 4 investigates the effect of AM surface roughness and the unique microstructure of AM material on the wave speed and acoustic nonlinearity measurement of Rayleigh waves. Rayleigh waves propagating on polished Ti-6Al-4V baseplate and DED built as-built and glazed Ti-6Al-4V depositions with waves propagating across the hatch, along the hatch, and on the polished region. We first report in Section 4.5.1 that the Rayleigh wave speeds are lower (~3% difference) for AM material than the wrought material and the surface roughness increased the scatter in the wave speed measurements. Then the measured and attenuation corrected relative nonlinearity parameters are reported in Section 4.5.2. It was found that the polished AM material has 4-6 times higher nonlinearity than the wrought material due to the drastically different microstructure characterized by high dislocation density, sharp interfaces, and residual stress.

Chapter 5 investigates the feasibility of laser generated narrowband Rayleigh waves to measure the material nonlinearity. An experimental setup is designed to compare the nonlinearity parameters for laser generation using a microlens array and the conventional angle beam transducer generation of finite-amplitude Rayleigh waves for increasing propagation distance. A similar linearly increasing trend was observed for both the generation methods indicating the cumulative effect of material nonlinearity. However, the slope of the linearly increasing trend was substantially higher for laser generation than the angle beam generation due to the system nonlinearity caused by the laser line array source. It was then shown for the lowest propagation distance that the system nonlinearity could be compensated by characterizing the line array source resulting in comparable slopes for the angle beam and laser generation sources. Furthermore, laser ultrasound was applied to assess the nonlinearity parameter for AISI 4130 steel plates with varying hardness values, and the monotonic increase of the nonlinearity parameter for the hardness levels was observed, which is in agreement with the literature.

In Chapter 6, the laser ultrasound system integrated into a directed energy deposition additive manufacturing (DED-AM) chamber to perform noncontact process monitoring is described. Rayleigh waves are generated by a pulsed laser whose open beam is patterned by a cylindrical lens to actuate a broadband pulse or by a slit mask to actuate a narrowband wave packet. The out-of-plane displacement of the Rayleigh waves is received by an adaptive laser interferometer whose continuous beam is transported to the remote head by optical fiber. Rayleigh waves provide the capability to monitor layer-by-layer deposition for flaws and nonuniformity in the deposited material. In this study, flaws and anomalies were artificially created during processing to demonstrate some of the capabilities of the integrated laser ultrasound system in spite of the presence of significant surface roughness. Flaws associated with skipped hatches were notch-like and reflected a portion of the Rayleigh waves. These flaws were detectable by the decrease in amplitude in through-transmission mode for both broadband and narrowband sources. Varying the hatch spacing resulted in cylindrical voids and surface mounds that created wave scattering. The broadband pulse evolved substantially due to the flaw interaction, strongly suggesting that comparing received waveforms to a nominal baseline would be quite valuable, especially with assistance from machine learning algorithms. Powder impurity caused spherical voids and cracks that also scattered the Rayleigh waves; hence a baseline comparison is also appropriate for this type of flaw.

In Chapter 7, the nonlinear features of laser generated Rayleigh waves are leveraged to gain insight into the material properties through the material microstructure. There has been much interest in second harmonic generation of narrowband Rayleigh waves for early indications of material degradation and microstructure evolution. As described in Chapter 5, one challenge associated with second harmonic generation from a line-arrayed laser source is the large system nonlinearity. On the other hand, a directed broadband laser pulse evolves with propagation distance and as a function of the amplitude and can be used to provide even more information about the material. In this study, microstructural changes in the DED-Ti-6Al-4V and IN-718 depositions are obtained by subtly varying the process parameters such as hatch spacing and deposition source, power, and speed, without creating any material discontinuities. For each study, drastically different evolutions of broadband Rayleigh waveforms are obtained, suggesting the sensitivity of the technique to different material microstructures. Furthermore, the frequency domain implications of the nonlinear waveform distortions are discussed and characterized based on the shift in the peak frequencies.

Thus, the integrated laser ultrasonic system is shown to be capable of monitoring flaws and material microstructures for the DED-AM system. The developed system is not limited to DED processing and should be extendable to powder bed fusion systems.

## 8.2 Future work

1. We envision a re-design of the integrated laser ultrasonic system, in which the generation and reception laser heads are fiber delivered and built into the deposition head to enable interrogation without interrupting the deposition process.
2. Naturally, the above system will require the interrogation of AM parts with temperature gradients. Thus, temperature gradient effects on the laser generation, laser reception, and Rayleigh wave propagations need to be studied.
3. Automation is required for the integrated laser ultrasonic system to monitor the part in-line with the deposition process and prompt the operator if the build is not within the expected tolerance or take corrective action using the closed-loop feedback control. However, due to the lack of standardization of the AM systems, the same detection system might not work in each case. Thus, the detection system should be able to adapt to the different AM systems and develop intelligence in real-time as the build progresses to make intelligent decisions for monitoring the AM part. In addition, a multi-sensor technology will increase the reliability of the detection system and provide sensor invariant decision-making.

**DISCLAIMER**

Any opinions, findings, and conclusions or recommendations expressed in this dissertation are those of the author's and do not necessarily reflect the views of the funding agencies - National Science Foundation (NSF) and the Government.

## NON-TECHNICAL ABSTRACT

Additive manufacturing (AM) is recognized as one of the most innovative technologies in Industry 4.0 due to the many unique advantages over the subtractive manufacturing methods. The increased design freedom due to the layer-wise manufacturing also allows significant weight reductions and enhanced component performance with little or no specialized tooling. However, additive manufacturing technology is still maturing, and subtle changes in the process parameters can lead to defects or undesired microstructure in a part or variability from one part to another. Thus, in-situ material state monitoring techniques are urgently needed to realize the full benefits of additive manufacturing. Laser ultrasonics is a noncontact technique suitable for in-situ monitoring of metal additive manufacturing processes. This research presents a laser ultrasonic system integrated into a directed-energy-deposition additive manufacturing system and demonstrates the in-situ detection of realistic AM defects and microstructural sensing. Laser generation of both narrowband and broadband Rayleigh waves is exploited to detect localized defects created by altering the process parameters in Ti-6Al-4V depositions. Furthermore, the nonlinear waveform distortion of broadband Rayleigh waves is used to detect changes in the material microstructure instilled by marginally varying the process parameters for Ti-6Al-4V and IN718 depositions. The AM surface roughness is a key challenge for laser ultrasound-based in-situ monitoring because it affects both wave reception and the Rayleigh wave propagation. Results demonstrate flaw detection as well as the effect of process parameters on Rayleigh waveform evolution.

# Chaitanya Bakre

411C, EES Building, University Park, PA 16802 Ph: 404-579-1583 Email:chitbak@gmail.com

## Education

| Year | Degree |
|---|---|
| 2017 – 2022 | **Ph.D**. in Engineering Science and Mechanics Dept.<br>Major in **Engineering Mechanics**, Minor in **Acoustics**<br>The Pennsylvania State University<br>University Park, PA, USA |
| 2014 – 2017 | **M.S**. in **Mechanical Engineering** Dept.<br>Indian Institute of Technology Madras<br>Chennai, TN, India |
| 2009 – 2013 | **B.E**. in **Mechanical Engineering**<br>University of Pune<br>Pune, MH, India |

## Scholastic Achievements and Awards

- Second Prize in poster presentation in ESM Today 2018 - an annual graduate research symposium in the department of ESM, Penn State.
- Bronze medal at the Annual Student Poster Competition organized during the 43$^{rd}$ Review of Progress in Quantitative Nondestructive Evaluation (QNDE), Atlanta, GA, USA.
- State bank of India Scholarship for Meritorious students in India (2014 - 2017).
- Ranked among Top 1% (out of 0.2 million candidates) in Graduate Aptitude Test in Engineering (GATE) 2014.

## Publications and Intellectual Property Rights

1. Bakre, C. and Lissenden, C.J., 2021. Surface Roughness Effects on Self-Interacting and Mutually Interacting Rayleigh Waves. Sensors, 21(16), p.5495.
2. Bakre, C., Nassar, A.R., Reutzel, E.W. and Lissenden, C., 2022. Ultrasonic Rayleigh wave interrogation of DED Ti-6Al-4V having a rough surface. Journal of Nondestructive Evaluation, Diagnostics and Prognostics of Engineering Systems, pp.1-31.
3. Bakre, C., et. al, “In-situ laser ultrasound-based Rayleigh wave process monitoring of DED-AM metals”, Research in Nondestructive Evaluation, submitted.
4. Bakre, C., et. al, “Feasibility analysis of material nonlinearity measurement using laser-generated narrowband waves”, in preparation.
5. Bakre, C., et. al, “Laser-based surface wave distortion technique for in-situ microstructural sensing of additive manufacturing”, in preparation.
6. “Laser ultrasonic inspection methodology for gear teeth” by C. Bakre, C.J. Lissenden, A. Isaacson, IDF Submitted, 2021.
7. “A novel combinational mask based grating methodology to employ nonlinear wave mixing using Laser ultrasonics” by C. Bakre, P. Rajagopal and K. Balasubramaniam, Patent ID 201641024213, Granted, 2021.